RAPIDLY SOLIDIFIED MAGNESIUM - NICKEL ALLOYS AS HYDROGEN STORAGE MATERIALS

by **XIAODONG YI**

A thesis submitted to the University of Birmingham for the degree of DOCTOR OF PHILOSOPHY

School of Metallurgy and Materials

College of Engineering and Physical Sciences

The University of Birmingham

June 2013

SYNOPSIS

Due to high hydrogen capacity, good reversibility and low cost, magnesium hydride is one of the most promising hydrogen storage materials. However, the high desorption temperature and slow hydriding kinetics hinder the application of magnesium hydrides. To improve the hydrogen storage characteristics of magnesium hydrides, many effective treatments have been developed and applied, such as ball milling, melt spinning, alloying with other metals, adding catalysts and using thin film technique. In this work, melt spinning and alloying with Ni were the main sample modification methods used to improve hydrogen storage properties for magnesium hydrides. At the beginning of this project, it was found that it was difficult to repeat the methodology of sample preparation in the literature. Therefore, sample synthesis method was developed after numerous preliminary trials and a series of Mg-Ni alloys were melt-spun successfully.

The structural characterization and analysis of hydrogen storage property were performed on the melt-spun Mg-Ni samples in a range of compositions. It was found that a nanocrystalline / amorphous structure was produced by melt spinning, and a metastable intermediate phase, Mg_6Ni, was discovered in the melt-spun materials. The melt-spun Mg-Ni ribbons exhibited fast kinetics of both absorption and desorption at 300 °C, with a high capacity. Moreover, they exhibited low temperature and even room temperature hydrogen sorption, with slow kinetics. γ-MgH_2 phase, which forms usually under high pressure, has been found in the samples, which probably caused the ambient hydrogen absorption.

Mg alloying with other elements (Ti and Ni) has been attempted in the latter stage of this work. Melt-spun ribbons were not produced successfully.

Future work will look at the crystallization behaviour of the metastable intermediate phase Mg_6Ni, and the hydriding/dehydriding process of the unusual γ-MgH_2 phase. In addition, the study of Mg-Ti-based alloys will continue, since some researchers have produced Mg-Ti alloys by other techniques *e.g.* thin film.

ACKNOWLEDGEMENTS

First and foremost, I would like to truly thank my supervisors *Prof. David Book* and *Dr. Allan Walton*. They introduced me to the fantastic research field of hydrogen storage materials, and provided valuable guidance for the melt spinning research. Moreover, they helped me with constructive comments on sample characterization and also with technical support with the development of various methodologies.

Thanks are also due to all the members of *Hydrogen Materials Group, David Book, Allan Walton, Dan Reed, Alex Bevan, John Speight, Ivor Harris, Shahrouz Nayebossadri, Simon Cannon, Vicky Mann, Yinghe Zhang, Lydia Pickering, Guo Sheng, Ruixia Liu and etc.* Special thanks to *Dan Reed* for the help with arrangement of lab experiments and XRD analysis, *Dave Brampton* for the help with DSC, *Steve Tedds* for the help with IGA, *Simon Connon* for the help with equipment issues, and *Vicky Mann* for the help with TGA. There are also many other people who have contributed either directly or indirectly to this study. In addition, I have been benefited greatly from the financial support provided by the department and by *Illica Inc.*.

To my parents, for all your endless understanding and support during all these years. Most important of all, to my wife *Xi*, without whom this would not have been possible, with your encouragement, patience and love.

Praise be to my Lord and Saviour ***Jesus Christ***. Amen.

Table of Contents

LIST OF FIGURES

LIST OF TABLES

1. Introduction

1.1. Background

In modern society, two major issues are energy demand and environmental problems. Due to the developing living conditions of humankind, the demand for energy keeps increasing rapidly. It is expected to grow more than one-third for the energy demand over the time period to 2035, and the developing countries (China, India and the Middle East) is accounting for 60% of the increase (IEA, 2012). Burning these fossil fuels causes large amounts of emissions of greenhouse gases (CO_2, N_2O, CH_4, *etc.*), which contributes towards global warning and subsequent environmental problems. Intergovernmental Panel on Climate Change (IPCC) (2007) has stated: "Most of the observed increase in globally averaged temperatures since the mid-20th century is very likely due to the observed increase in anthropogenic greenhouse gas concentrations". Global CO_2 emissions were increasing greatly in the early 20^{th} century, by more than 3% higher than the value about 1% per year in the 19^{th} centuries (Raupach et al., 2007). In 1990, the global CO_2 emissions from fossil fuel combustion was 20.7 billion tonnes (Gt), compared with 32.5 Gt in 2006 (Guo et al., 2008). Although energy demands will remain increasing, the CO_2 intensity of energy can be reduced by shifting the energy resource away from fossil fuels which contribute the massive CO_2 emissions.

Therefore, in a long future, the clean and sustainable energy (such as wind, solar, *etc*.) will gradually take place of the fossil fuels. In a short time, the renewables can be utilised

with nuclear power, in order to satisfy the world's growing energy demands. However, as renewable energy resources are intermittent, there is a need to store any surplus energy produced in order for it to be utilised during times of high energy demand.

Hydrogen is not a primary energy source, but is generally considered to have the potential to be an "energy carrier" of the future (Dixon, 2007). All kinds of renewable energy from wind or solar can be stored in the form of hydrogen, therefore depending on its production method, hydrogen is a "green" fuel, producing near-zero emissions of greenhouse gases. Moreover, it is compatible with high-efficiency fuel cells, combustion turbines and reciprocating engines to produce power with only water as a combustion product, and able to serve all sectors of the economy *e.g.* transportation, power, industrial, and buildings. To summarise, key elements towards a hydrogen economy would be the development of methods and means of production, storage, transmission and usage of hydrogen.

1.2. Aim and Objectives

This project is focused on solid-state materials for hydrogen storage. Due to the high volumetric hydrogen density, this is of particular interest for transportation applications.

Magnesium alloys are widely known as hydrogen storage materials, and have been studies in ways to improve the storage properties in the view of the application. They are particularly attractive candidates for solid-state hydrogen storage because of properties of MgH_2: low specific weight, a high gravimetric hydrogen storage density of up to 7.6 wt.% H_2, the relatively low cost of magnesium and a comparatively high abundance in the earth's crust. However, it has two drawbacks: high dehydriding temperature and slow hydrogen sorption kinetics.

In order to enhance the hydrogenation and dehydrogenation kinetics, magnesium alloys should have a sub-micrometre crystal size and should contain catalytically active agents such as transition metals, metal oxides, or rare earth elements in order to enhance the dehydrogenation and hydrogenation kinetics. For this reason, melt spinning – a rapid solidification technique – has been applied to achieve nanocrystalline Mg-based alloys. On the other hand, melt spinning Mg with Ni can disperse Ni within the Mg-rich phase, which exhibit an enhanced hydrogenation thermodynamics, due to the catalytic effort of the Ni in reducing the hydrogen dissociation energy. Moreover, alloying with Ni can lead to lower dehydrogenation temperature, because Mg_2NiH_4 has a lower heat of formation than MgH_2 hydride. Therefore, this work aims to improve the hydrogen sorption properties of Mg by achieving melt-spun Mg-Ni alloys as hydrogen storage materials.

2. Hydrogen Storage Review

2.1. Introduction

Science and technology needs energy which can sustain development on earth. Undesirable climate change due to increasing use of energy is the toughest challenge facing the human race. CO_2 emissions from burning fossil fuels has been clearly identified as the main reason for global warming. Global CO_2 emission from fossil fuel combustion increased from 20.7 billion tones (Gt) in 1990 to 32.5 Gt in 2006; currently growing 35 % faster than expected because of inefficiency in fossil fuel use and the weakening of natural carbon sinks (Raupach et al., 2007; Guo et al., 2008).

There are quite a number of available alternative energy sources such as solar, wind, ocean, geothermal and others, and energy storage is another challenge for the applications of the renewable energy. Hydrogen draws much attention as an ideal energy vector, for reforming the current modern economy and society based on fossil fuel system. The concept of the *'Hydrogen Economy'* has been proposed for decade, as an ultimate energy solution which can satisfy the global energy demands whilst reducing emissions of greenhouse gasses. However, before this becomes a reality, there are a number of challenges or obstacles regarding to hydrogen production, storage, convenience for transportation, versatility, utilization, efficiency, safety and environmental compatibility.

Hydrogen Production

Currently, the dominant technology for direct production is steam reforming from hydrocarbons. Methane steam reforming contributes nearly half of the hydrogen production, and 30% from oil-based reforming (Ewan and Allen, 2005). The reaction is performed at high temperature, typically between 1250 °C to 1575 °C, and at high pressures of 20 ~ 100 bars. The products are carbon dioxide and hydrogen gases, and a separation process is then followed to produce high-purity hydrogen gas. It is apparent that current hydrogen production is still highly dependent on fossil fuels with an unfavourable by-product of CO_2.

$$CH_4 + 2H_2O\ (steam) \rightarrow CO_2 + 3H_2 \qquad (Methane\ steam\ reforming)$$

or $$C_xH_y + H_2O\ (steam) \rightarrow CO_2 + H_2 \qquad (Hydrocarbon\ steam\ reforming)$$

There are other methods of hydrogen production, which are environmentally friendly with no harmful emission, such as water electrolysis, photo-electrochemical process or other chemical processes of dissociation of water or steam. It needs high energy to dissociate the water into oxygen and hydrogen, and the electricity used could be from the clean renewable energy sources such like solid bio-mass, solar, wind and tide *etc*.. Currently, the technical problems and high cost hinder the commercialisation of these production methods. Compared with the steam reforming method, these production routes are still in an early stage of research and development, and the former is still the most energy-efficient and cost-effective technology.

Hydrogen Transportation

It is required to deliver hydrogen from the point of production to the locations of the end-user. The method of transportation could be related to the means by which it is being stored. The common methods of transportation include the pipelines, railways, trucks, ships *etc.*

The hydrogen produced is mainly used for upgrading fossil fuels or chemical productions, and the hydrogen production plants are usually concentrated within chemical plants. Therefore, due to the lowest cost of delivery of large capacity of hydrogen, pipelines are currently used widely as the method of hydrogen transportation. The initial cost of the pipeline construction is the majority of the total cost. Thus, the gaseous hydrogen can be delivered at a low cost. For a long distance delivery of hundreds miles, compressed hydrogen or liquid hydrogen can be delivered by other means of transportation, such as ships, trucks, railways. Generally, the delivery system for hydrogen is inconvenient and expensive compared with those of the conventional systems for the fossil fuels.

Hydrogen Applications

Hydrogen has been considered as an ideal energy carrier due to high energy density and clean emission, and can be used in fuel cell for power generation. However, only a small proportion of the hydrogen produced is used as an energy carrier, and the majority is consumed in chemical processing for industrial applications, mainly in fossil fuel processing and ammonia production.

In the petroleum industry, large amount of hydrogen is employed in the hydrocracking process to refine fossil fuels. The hydrogen acts as a hydrogenating agent, in order to increase the level of saturated hydrocarbons from the unsaturated raw materials. The production of ammonia is the second largest consumption of hydrogen in the industry. Nowadays, the ammonia is produced mainly according to the Haber-Bosch process:

$$3H_2 + N_2 \rightarrow 2\ NH_3 \text{ (100 bar, 450 °C)}$$

The Proton Exchange Membrane (PEM) Fuel cell is the main application of hydrogen used as an energy carrier. In such a fuel cell, the hydrogen reacts with oxygen in the air to produce electricity, with the only by-product being water or steam. There are several types of fuel cells, which are categorised by the types of electrolyte and operating temperature, such as PEM fuel cell with a low operation temperature (~80 °C) and the solid oxide fuel cell (SOFC) for high temperatures (~900 °C). Due to the relative low operating temperature of 50 ~ 80 °C, the PEM fuel cell is the most common type used for vehicles, (Schlapbach and Zuttel, 2001).

Unfortunately, the commercialisation of fuel cells suffers primarily from the high cost of the Pt-based catalyst, followed by the membrane, anode and cathode electrodes, and the general poor materials performance such as transport rates, and durability.

Hydrogen Storage

In terms of a *Hydrogen Economy*, hydrogen storage is one of the biggest technical challenges. Hydrogen storage development would be of great benefit to all other sections of *Hydrogen Economy*, including production, transportation and end-use. Currently, the main types of hydrogen storage are compressed hydrogen gas, liquid hydrogen tanks, solid-state hydrides, and high-surface-area absorbents.

For static application, the energy density is not the limiting property. Apart from the compressed tanks, gaseous or liquid hydrogen can be stored underground or in caverns. Geological storage has been used widely for natural gas, and now some projects have been launched to store hydrogen in the underground caverns, such as the European project Hyunder (Hyunder, 2013).

There is also a need for an on-board hydrogen storage systems for automotive applications. To achieve this, a high volumetric and gravimetric density is a crucial requirement, especially for use in light-duty vehicles. To enable a 300-mile driving range, between 5 to 10 kg hydrogen is required, and this should be stored within a light-weight storage system, the total weight of which includes the weight of the H_2 gas. Moreover, hydrogen-driven vehicles should, eventually be competitive with conventional cars in terms of cost, packaging, safety and driving performance and charge/recharge time *etc*.. Therefore, the US Department of Energy (DOE) has amended the performance targets for on-board hydrogen storage system (DOE, 2009) with the following objectives:

- By 2015, to develop and verify a single-use hydrogen storage system for portable power applications achieving 0.7 kWh/kg system (2.0 wt.% hydrogen) and 1.0 kWh/L system (0.030 kg hydrogen/L) at a cost of $90/kWh ($3/g $H_{2\ stored}$).

- By 2017, to develop and verify on-board automotive hydrogen storage systems achieving 1.8 kWh/kg system (5.5 wt.% hydrogen) and 1.3 kWh/L system (0.040 kg hydrogen/L) at a cost of $12/kWh ($400/kg $H_{2\ stored}$).

- To enable an ultimate full-fleet 4 target of 2.5 kWh/kg system (7.5 wt.% hydrogen) and 2.3 kWh/L system (0.070 kg hydrogen /L) at a cost of $8/kWh ($266/kg $H_{2\ stored}$) for on-board automotive hydrogen storage.

Thus, it is crucial to develop effective materials for hydrogen storage which requires:

- high storage capacity and gravimetric/volumetric densities;
- fast kinetics of hydriding and dehydriding;
- appropriate thermodynamics;
- effective heat transfer;
- long cycle lifetime for decomposition /recombination;
- safety under normal use and acceptable risk under abnormal conditions.

Up to now, none of the available storage methods meets all of these criteria. The following literature review will describe briefly research activities into hydrogen storage, including storage methods and materials.

2.2. Gaseous Storage

Hydrogen is a molecular gas, which at room temperature has a density of only 0.0909 kg/m^3. Among other chemical fuels, hydrogen has the highest energy density of about 120 MJ/kg, which is three times higher than that of gasoline with only ~40 MJ/kg. This is one of the main advantages of hydrogen energy which draws the attention of the researchers. However, with regard to volumetric energy density, the gaseous hydrogen has a lower value of ~12.5 MJ/m^3 compared with that of gasoline of ~31.6 MJ/m^3, (Sandí, 2004). Therefore, this represents a key challenge for hydrogen storage research. To increase the energy density by volume, it is possible to compact the gas in a pressure vessel under several hundred atmospheres (up to 700 bar). Nowadays, gas cylinders are used globally, and are made of cheap steel or aluminium and are able to be filled to a pressure of 200 ~ 300 bar (Schlapbach and Zuttel, 2001). A major drawback of the high-pressure gas containers is the very low mass density. A ultra-high-pressure tank can hold 4 wt.%. H_2, and only 1 wt.% for a normal cylinder. However, an advantage is that a gas cylinder can be operated at room temperature.

To achieve the best performance, the materials for gas cylinders should have a high tensile strength, low density and good resistance to the hydrogen absorption/reactions. Therefore, carbon fibre-reinforced 350 and 700 bar compressed hydrogen gas tanks have recently been developed by Quantum Technologies and others, and these can enhance hydrogen density to 30 kg/m^3 at 700 bar, which is about half that of liquid hydrogen (Quantum, 2005; Wang and Ronnebro, 2005). However, the volume efficiency is still relatively poor and much energy is consumed in compressing the non-ideal H_2-gas.

2.3. Liquid Storage

Compared with gaseous storage, liquid hydrogen has a density of 70 kg/m^3. Therefore, storing hydrogen in liquid form has the advantage of significantly increasing its volumetric density, theoretically 8.4 MJ/L (Sandí, 2004). Liquid hydrogen can be stored in cryogenic tanks at 20 K which is its boiling point under ambient pressure, and there is also a critical temperature of 33 K above which no liquid phase exists (Züttel, 2004). Therefore, a cryogenic system is needed for storing the hydrogen, which almost accounts for the total weight and volume of the storage system. Therefore, the cryogenic container materials require the properties of light-weight, low-volume materials with a low heat transfer and high safety factor.

There are, however, some practical problems that limit the use of liquid hydrogen:

- A large amount of energy (about 1/3 of the total energy stored) is required for the liquefaction of the gas
- Hydrogen will be lost continuously by evaporation (the so called ‘boil-off’ effect) as a result of heat losses.

Therefore, due to the issues above, the high cost of cryogenic storage systems limited the use of liquid hydrogen to a narrow range of applications where the cost issue is not such an important consideration and where it consumes the hydrogen in a relatively short time, *e.g.* aerospace applications.

2.4. Solid-state storage

In the future, solid-state hydrogen storage materials are more likely to meet the requirements for onboard storage: appropriate thermodynamics, fast kinetics, high storage capacity, effective heat transfer, light weight, long cycle life, and safety. There are several candidates for hydrogen storage media; including metal hydrides, carbon nanotubes (Züttel et al., 2002; Liu et al., 1999), microporous materials (Pan et al., 2004), inorganic nanotubes, zeolite (Reguera et al., 2008), metal-organic frameworks (MOF) (Ma and Zhou, 2010). Activated and/or nanostructured carbons are capable of physically adsorbing hydrogen due to their high surface areas, as long as the temperature is low enough. A number of zeolites with different pore geometries and composition have been investigated, and a NaY zeolite has been reported with a capacity of 2.1 wt.% at 16 bar at 77 K (Langmi et al., 2003). Metal-organic frameworks (MOF) usually refer to materials in the form of metal ions or metal ion clusters coordinated to multidentate organic linkers, which has a microporous structure with a high surface area – *e.g.* MOF-5 has a hydrogen capacity of 4.5 wt.% at 77 K, and 1 wt.% at room temperature under 20 bar pressure (Rosi et al., 2003).

2.4.1. Metal hydrides

Many metals are capable of storing hydrogen interstitially into the metallic lattice structure or forming a metal hydride phase. Absorption of hydrogen starts with hydrogen dissociated at the surface, and two hydrogen atoms recombine into H_2 in the desorption process. Hydrogen forms compounds with metals like Li, Na, Mg, Ti, which are generally known as metal hydrides. The hydrides have a high volumetric hydrogen density, which is an advantage for mobile energy application (see Table 2-1).

Materials	**H-atoms/cm^3 (×10^{22})**	**wt.% hydrogen**
H_2 gas, 200 bar	0.99	100
H_2 liquid, 20 K (-253 °C)	4.2	100
H_2 solid, 4.2 K (-269 °C)	5.3	100
MgH_2	6.5	7.6
Mg_2NiH_4	5.9	3.6
$FeTiH_{1.95}$	6.0	1.89
$LaNi_5H_{6.7}$	5.5	1.37
$ZrMn_2H_{3.6}$	6.0	1.75
VH_2	11.4	2.10

Table 2-1 Common metal hydrides with volumetric and gravimetric capacity value compared with conventional hydrogen storages. Taken from Selvam *et al.* (1986).

In 1866, Graham first observed the reaction between hydrogen and a metal (Pd) (Graham, 1866). After that, other metals and alloys capable of forming hydrides were found, such as Ca, Mg (Ehlert et al., 1968), Mg_2Ni (Reilly and Wiswall Jr, 1968), and $LaNi_x$ (Buschow and Van Mal, 1972). Many metal hydrides have been studied, and a number of complex hydrides have also been found. Intermetallic compounds, such as AB, usually

form complex hydrides, such as AB-X, where A is a metal element which form hydrides (*e.g.* rare earth metal or transition metal) and B is a metal not reacting with hydrogen (*e.g.* Ni, Co,V, Fe). A summary of common hydrides is given in the Table 2-2.

Type	Metal	Hydride	Structure	Mass%	Pressure	Temperature
Elemental	Pd	$PdH_{0.6}$	Fm3m	0.56	0.02 bar	25 °C
AB_5	$LaNi_5$	$LaNi_5H_6$	P6/mmm	1.37	2 bar	25 °C
AB_2	ZrV_2	$ZrV_2H_{5.5}$	Fd3m	3.01	10^{-8} bar	50 °C
AB	FeTi	$FeTiH_2$	Pm3m	1.89	5 bar	30 °C
A_2B	Mg_2Ni	Mg_2NiH_4	P6222	3.59	1 bar	280 °C
Solid solution	Ti-V-based	Ti-V-H_4	BCC	2.6	1 bar	25 °C

Table 2-2 Key hydrogen storage properties of typical metallic hydrides from (Schlapbach and Zuttel, 2001).

Hydrides come in many forms ranging from metallic elements, which can interstitially store hydrogen within their metallic lattice *e.g.* ($PdH_{0.6}$), to those which chemically react with hydrogen *e.g.* (CH_4). The hydrogen charging and decharging process(es) can be described by pressure-composition isotherms (Figure 2-1), which is often used for thermodynamics analysis of hydride decomposition and formation. When hydrogen is stored interstitially in the metal lattice, the solid solution with diffused hydrogen is called the α-phase. With increasing pressure, the concentration of hydrogen increases dramatically by forming a metal hydride phase (β-phase). The hydrogen atoms in the lattice start reacting with the metal atoms, with the nucleation and growth of the metal hydride phase. While the α- and β-phases coexist, the isotherms exhibit a flat plateau, the length of which determines the amount of hydrogen which can be stored reversibly within a small range of pressure. The plateau pressure (or equilibrium pressure) represents the

thermodynamics of formation of the hydrides. The change of enthalpy (ΔH) and entropy (ΔS) can be calculated from the plateau pressures and the temperatures, using the van't Hoff equation:

$$\ln P_{eq} = \frac{\Delta H}{RT} - \frac{\Delta S}{R}$$

where P_{eq} is for the dehydriding plateau pressure, R for the gas constant, T for the temperature in K, and ΔH and ΔS for the enthalpy and entropy of the hydrides.

The van't Hoff equation is derived from the definition of the Gibbs free energy:

$$\Delta G = \Delta H - T\Delta S \quad \text{and} \quad \Delta G = -RTlnK_{eq}$$

Therefore, the standard van't Hoff equation can be obtained.

$$\ln K_{eq} = -\frac{\Delta H}{RT} + \frac{\Delta S}{R}$$

For the gas-solid reaction of Mg and hydrogen,

$$Mg + H_2 \Leftrightarrow MgH_2$$

The equilibrium constant expression K equals to the equilibrium pressure P_{eq} which is the plateau pressure in the PCT curves in Figure 2-1.

Therefore, for the dehydriding reaction, the Van't Hoff equation can be described as:

$$\ln P_{eq} = \frac{\Delta H}{RT} - \frac{\Delta S}{R}$$

where P_{eq} is for the dehydriding plateau pressure, R for the gas constant, T for the temperature in K, and ΔH and ΔS for the enthalpy and entropy of the hydrides.

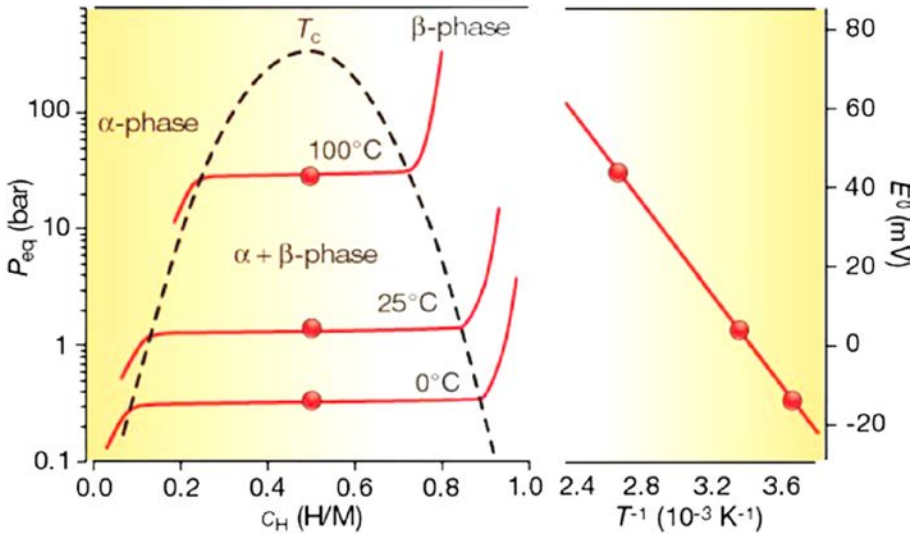

Figure 2-1 Pressure–concentration–temperature plot and corresponding van't Hoff curve. Taken from (Schlapbach and Zuttel, 2001)

The advantage of 'packing' hydrogen within metals is that it allows the hydrogen atoms to be stored much closer together than they would in their molecular form as a compressed gas or as a liquid. This closer packing results in higher volumetric hydrogen storage densities, as showed in Figure 2-2.

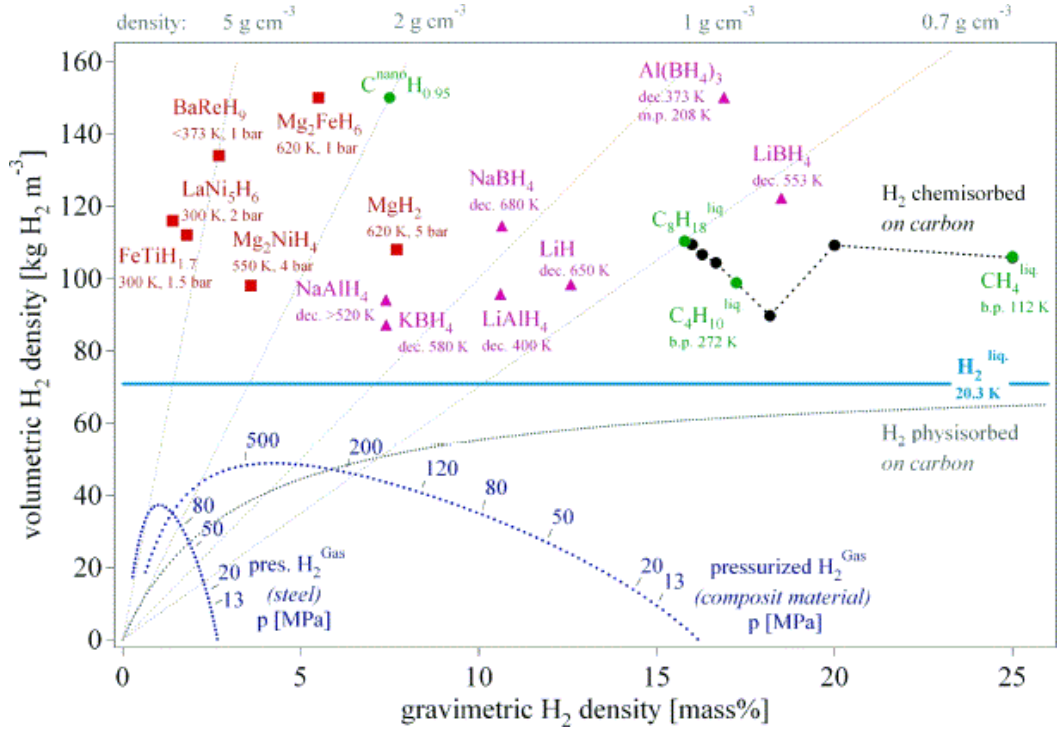

Figure 2-2 Gravimetric and volumetric densities of hydrogen for a number of possible hydrogen storage materials. Taken from Züttel (2003).

Although with high volumetric capacity, the metal hydrides usually have a relatively low gravimetric density, as most of the metals tend to be heavy elements. $LaNi_5$ is a common compound which can form hydrides for hydrogen storage materials. It can absorb and desorb hydrogen under relatively mild conditions of pressure and temperature. Therefore, it has been commercialized in industry as hydrogen storage materials. However, the gravimetric hydrogen density of less than 2 wt.%, means that it does not meet the requirement for transportation and other mobile energy applications.

Metals such as lanthanum are relatively heavy resulting in a low gravimetric capacity, *e.g.* 1.37 wt.% for $LaNi_5$ hydride. Therefore, magnesium has attracted much attention, due to its light-weight and relative abundance. On this basis, Mg has been considered to be a

most promising hydrogen storage material with a low cost and a hydrogen storage capacity of 7.6 wt.% (Selvam et al., 1986).

There are some practical problems hindering the use of MgH_2. One is the high desorption temperature for MgH_2 (> 300 ºC) due to its high stability (ΔH_f = -75 kJ $mol^{-1}H_2$) (Bogdanović et al., 1999). Alloying with other metals can reduce the desorption temperature. Mg_2NiH_4 has a lower heat of formation (-65 kJ $mol^{-1}H_2$) with still relatively high gravimetric capacity of 3.6 wt.% (Reilly and Wiswall Jr, 1968). Another problem is the slow kinetics of hydriding/dehydriding of MgH_2. This can be improved by nano-scale processing, in which an increase in the volume of grain boundary material and particle surface area are generated (Zaluska et al., 2001).

3. Magnesium Hydrides

3.1. Introduction

Hydrogen has attracted worldwide interest as an energy carrier. It has been considered as an ultimate energy solution, due to its abundance, clean combustion and high energy density. One big challenge for hydrogen energy is the attainment of an effective hydrogen storage. Metal hydrides have an important advantage in their high volumetric hydrogen storage densities. However, their gravimetric hydrogen storage densities tend to be low.

A higher gravimetric hydrogen density is only possible with light elements such as calcium and magnesium. In fact, Mg forms ionic MgH_2 and this reaction between magnesium and hydrogen is reversible.

$$Mg + H_2 \Leftrightarrow MgH_2$$

Under normal conditions, magnesium hydride is in the form of α-MgH_2, which has a tetragonal structure of the rutile type. Under high pressure, α-MgH_2 shows a phase transition into two other modifications: hexagonal β-MgH_2 under 80 kbar at 650 °C (Bastide et al., 1980) and orthorhombic γ-MgH_2 under 20 kbar at 800 °C (Bortz et al., 1999).

MgH_2 is of interest for hydrogen storage, due to its high gravimetric capacity of 7.6 wt.% (Selvam et al., 1986), and high energy density of 9 MJ/kg Mg (Bogdanović et al., 1999).

3.2. Limitations

Although magnesium has many advantages as a hydrogen storage material, it has two main disadvantages:

- Slow kinetics of the reaction of Mg hydride formation and decomposition
- High hydrogen sorption temperature (~300 °C) in thermodynamic equilibrium at a plateau pressure of 1 bar.

Several factors cause the slow hydrogen sorption kinetics. One is the slow hydrogen dissociation rate which depends on the metal surface condition. For pure magnesium, the clean surface will require high energy to dissociate the hydrogen molecules into atoms. Catalysts (*e.g.* metal oxides) or other elements (*e.g.* Ni) deposited onto the surface of the magnesium particles in order to reduce the energy for hydrogen dissociation.

Another factor is the slow hydrogen diffusion rate. The diffusion of hydrogen atoms through the magnesium hydride is very slow. As the MgH_2 forms and grows, the reaction rate of hydrogenation decreases due to the long diffusion path through the layer of MgH_2. As a result, MgH_2 usually need an activation treatment for better hydriding kinetics. The grain expands during hydriding and shrink during dehydriding. Several thermal cycles of

hydriding and dehydriding, the grains decrepitate into a smaller particle size, resulting in a larger volume fraction of boundary area which acts as an easy path for hydrogen diffusion. Ball milling is one technique which has been used to reduce the grain size of metal hydrides and also introduce a large number of defects in the lattice structure.

The high dehydrogenation temperature of MgH_2 (and high hydrogenation temperature of Mg) is due to its relative stability: the heat of formation of MgH_2 is -74.5 kJ mol^{-1} H_2 (Stampfer et al., 1960). To reduce the sorption enthalpy of MgH_2, one may consider alloying of the host metal system. When the alloy formation of metal system is exothermic (*e.g.* Mg-Cu, Mg-Al), it could make the net enthalpy change of hydride formation smaller. Alloying magnesium with other elements can form hydrides with lower heat of formation. The compound of Mg_2Ni can form Mg_2NiH_4, which has a heat of formation of -64.5 kJ $mol^{-1}H_2$ (Reilly and Wiswall Jr, 1968). The sorption temperature for Mg_2NiH_4 at 1 bar pressure is decreased to about 250~280 °C. Wagemans *et al.* (2005) showed that the hydrogen desorption energy decreases significantly when the crystal grain size becomes smaller than ~1.3 nm. Theoretically, it has been shown that the hydrogen desorption temperature can drop to about 200 °C when the crystal grain size is 0.9 nm. Ball milling shows the ability to decease the desorption temperature, about 200-240 °C for ball-milled MgH_2 and Mg_2Ni (Zaluska et al., 1999).

Magnesium does not form a binary intermetallic compound with iron, but in the presence of hydrogen it is possible to synthesize the stable ternary hydride Mg_2FeH_6 , which has a hydrogen storage capacity of 5.5 wt.% (Zaluska et al., 2001).

Many synthetic approaches have been used, such as:

1. Reducing grain size (*e.g.* ball milling)
2. Alloying with other transition metals
3. Adding catalyst(s)
4. Depositing as a thin film (hydride)

For instance, Janot (2003) reported a hydrogen sorption temperature of 150 °C with a capacity of 2.6 wt.% for ball milled Mg_2Ni coated with carbon. These improved hydrogen storage properties were achieved by the ball milling technique, alloying with Ni and using a catalyst of carbon.

3.3. Ball-milling

Ball milling is employed to grind down the bulk or granular Mg materials into a fine nanocrystalline structure which exhibit enhanced hydrogen storage properties (Zaluska et al., 1999). The hydrogen sorption properties benefit from a reduction in the grain size, especially into the nano-scale, which can be achieved by ball milling technique.

Reducing the grain size can improve significantly the hydrogen sorption kinetics, in the way of shortening the hydrogen diffusion path. As discussed above, the slowest step of the hydrogenation process is usually the diffusion of hydrogen through the newly formed MgH_2 layers. The diffusion rate decreases with increasing thickness of a MgH_2 layer, reaching zero after a critical thickness is attained (Berlouis et al., 2001).

Beside the reduced grain size, ball-milled samples have several differences compared with conventional hydride powder, including structural defects, phase transformation or transition, and formation of amorphous or nonacrystalline phases.

Usually, hydrogen atoms occupy similar interstitial sites in the amorphous structure to those in the crystalline structure, but the binding energy of the interstitial site varies, due to heavy and varied lattice distortion in the former.

Wagemans (2005) investigated systematically the effect of crystal grain size on the thermodynamic stability of magnesium and magnesium hydride. Both magnesium and magnesium hydride become less stable with decreasing cluster size. However, magnesium hydride destabilizes more strongly than magnesium. As a result, the hydrogen desorption energy decreases significantly when the crystal grain size becomes smaller than ~1.3 nm. An MgH_2 crystallite size of 0.9 nm corresponds to a desorption temperature of only 200 °C.

In high energy ball milling, by controlling the ball to sample ratio, the milling speed and milling time *etc*. a fine powder can be produced. However, there is a limit to the grain size which can be achieved by ball milling, of about 100 nm (Zaluska et al., 2001, Orimo et al., 1997).

There are some other approaches to make materials with a similar grain size to that achieved by ball milling. Melt infiltration of nanoporous carbon with molten magnesium

can be used to produce non-oxidized magnesium crystallites with sizes ranging from 2–5 nm to less than 2 nm (De Jongh et al., 2007). Skripnyuk (2009) reported equal channel angular pressing (ECAP) was applied to a commercial Mg material to improve the hydrogen storage properties. ECAP belongs to the family of severe plastic deformation (SPD) methods in which an intense plastic straining is imparted on a material, chiefly through simple shear. Moreover, it usually causes an increased density of lattice defects and microstructural refinement. Therefore, it increased the hydrogen desorption pressure, changed the slope of the pressure plateau in pressure-composition isotherms, decreased the pressure hysteresis, and accelerated the hydrogen desorption kinetics.

3.4. Alloying with other transition metals

Alloying Mg is another approach to reduce the hydrogen sorption temperature: Mg_2Ni as a typical intermetallic in this category forms a ternary complex hydride Mg_2NiH_4, which contains 3.6 wt.% hydrogen (Reilly and Wiswall Jr, 1968). Mg_2Ni react with hydrogen at 200~300 °C.

$$Mg_2Ni + H_2 \Leftrightarrow Mg_2NiH_4$$

Mg-La or Mg-Ni both have a negative heat of mixing, thus forms stable intermetallic compounds. The alloys Mg_2Ca, Mg_2Cu, and MgAl *etc.* also belong to this category. Ren *et al.* (2009) studied the $Mg_{2-x}La_xNi$ (x=0-6) system, in which Mg was substituted by La, which shows improved hydrogen sorption kinetics and reduced desorption temperature of

200 °C. The hydrogenation of Mg-Al has been studied, and it was observed that the enthalpy of hydride formation is lowered upon alloying with Al (Andreasen, 2008). One example is Mg_2Cu+H_2 which decomposes to MgH_2+MgCu_2 (Reilly and Wiswall, 1967). The enthalpy change of this reaction is -72.8 kJ $mol^{-1}H_2$ which is slightly lower than that of MgH_2. Therefore, the reactions are reversible at relatively high temperature of 300 °C.

The other category is alloy systems with a positive heat of mixing *e.g.* Mg_2FeH_6. Although Mg and Fe do not form a binary alloy, but the Mg_2FeH_6 can be formed with the addition of hydrogen (Porutsky et al., 1990). Another example is the Mg-Ti system. A magnesium based titanium doped hydride was prepared in a high-pressure anvil cell by reacting a mixture of MgH_2 and $TiH_{1.9}$ at 80 kbar and 600 °C (Kyoi et al., 2004). The new hydride, Mg_7TiH_x decomposes into Mg and $TiH_{1.9}$ and releasing 4.7 wt.% hydrogen at around 333 °C.

Apart from those well-known Mg-based compounds, there are also many other alloys which have been studied as potential hydrogen storage materials, *e.g.* Mg_2CoH_5 (Belin et al., 1987), Mg_6IrH_{11} (Černý et al., 2002), Mg_3RuH_6 (Bronger et al., 1993), $MgY_2H_{7.8}$ (Goto et al., 2003), Mg_3MnH_7 (Bortz et al., 1998), Mg_3CrH_6 (Rönnebro et al., 2004), and Mg_3Pr (Ouyang et al., 2009). Although these hydrides have good hydrogen contents, they are usually produced under very high pressures. Therefore, these have not been widely used, due to the difficulty of sample synthesis.

3.5. Adding catalyst(s)

Ni doped onto the magnesium surface can also have a catalytic effect whereby reducing the hydrogen dissociation energy is reduced. Many studies have been carried out to try to improve the hydrogen storage kinetics of magnesium hydrides, by using a variety of catalysts *e.g.* transition metals (Yermakov et al., 2006), metal oxides (Oelerich et al., 2001; Khrussanova et al., 1991), carbon materials (Imamura et al., 2002) and intermetallic compounds (Terzieva et al., 1998).

Hanada *et al.* (2005) tried to ball mill magnesium hydride with several transition metals (Fe, Co, Ni and Cu) as catalysts. In particular, the dispersed Ni nanoparticle exhibits an excellent catalytic effect, enabling ball-milled magnesium hydride to reversibly hydride/dehydride at 150 °C. Dufour (2007) found that a small amount of Pd as a catalyst enhanced the sorption kinetics and shortened the activation of magnesium hydride. Liang *et al.* (1999b) reported that by mechanical milling, the MgH_2+5 at.% V composite, can absorb 2.0 wt.% at room temperature in 1000 s, 4 wt.% hydrogen at 100 °C in 100 s and 5.6 wt.% hydrogen in 250 s at 200 °C under 10 bar of hydrogen pressure. The sample can desorb hydrogen completely at 235 °C under a vacuum within 2000 s. Liang *et al.* (1999a) also studied the catalytic effect of five transition metals, which enhanced the kinetics and reduced the activation energy of desorption, but did not alter the enthalpy and entropy of MgH_2.

Nb_2O_5 shows strong catalyst effect, resulting in very fast kinetics of MgH_2 hydride (Barkhordarian et al., 2004; Aguey-Zinsou et al., 2007). Hanada *et al.* (2006) reported a

remarkable improvement of ball-milled MgH_2 with Nb_2O_5 that absorbed 4.5 wt.% gaseous hydrogen even at room temperature under lower pressure than 10 bar within 15 s and finally its capacity reached more than 5 wt.%. The addition of Cr_2O_3 also causes increased hydrogen sorption kinetics, and it reduces the desorption temperature by 65 °C (Patah et al., 2009). Many kinds of metal oxides as catalysts are sufficient to provide fast sorption kinetics when added a small amount of 0.2 at.% (Oelerich et al., 2001).

The formation of Mg-Graphite composites upon grinding with the organic additives (benzene, cyclohexane or tetrahydrofuran) led to a decrease in the onset temperature of MgH_2 decomposition. Contrastingly, the composites ground without any additives did not show such behaviour (Imamura et al., 2002; Reda, 2009). Shang and Guo (2004) also found that the ball-milled MgH_2 with graphite absorbed about 5 wt.% within 30 min at 250 °C, whereas only 0.8 wt.% for pure MgH_2. It was also found that the hydrogen absorption/desorption kinetics of MgH_2 can be improved by the addition of a small amount of SiC (5 wt.%), while higher levels of doping introduces negative effects (Ranjbar et al., 2009).

Adding intermetallic compounds which absorb hydrogen, is another way of improving the hydrogen sorption properties. It has been shown that the addition of $LaNi_5$ to magnesium improves the absorption-desorption characteristics: the best results are for a composite containing 30 wt.% $LaNi_5$ (Terzieva et al., 1998). The addition of $LaNi_5$ improved the desorption of MgH_2 more than the absorption, and reasonable desorption kinetics can be obtained at 245 °C (Fu et al., 2008). A MgH_2 + 10 wt.%ZrNi composite absorbed about 5 wt.% in less than 3 min and desorbed the same amount in 7 min at 300 °C (Molinas et al.,

2009). In Mg–40 wt.%FeTiMn, the lowest absorption and desorption temperatures were 80 and 240 °C, respectively, with the material absorbing 4 wt.% hydrogen at 80 °C (Vijay et al., 2004). Single-walled carbon nanotubes exhibited a catalytic effect on the hydrogen storage properties of Mg, reaching 6.2 wt.% in 10 min at 300 °C (Wu et al., 2006).

3.6. Using thin film hydrides

The incorporation of hydrogen into a thin film form has been studied for some time. Jain *et al.* (1988) discussed the advantages of thin film metal hydrides. Thin films provide a large surface area with fast charging and discharging rates for hydrogen. Both critical pressure and critical temperature are significantly lower. Heat transfer arrangements and protective surface coating were shown to stop poisoning by oxygen and the activation of thin film hydrides is possible by coating with a layer of catalytic material. Thin films offer an alternative approach for the production of nanostructured materials, with the potential for better control over morphology, stoichiometry and contamination.

Léon *et al.* (2002) studied the hydrogenation characteristics of 30 μm thick air-exposed magnesium films prepared by vacuum evaporation. Those magnesium films absorbed hydrogen at 350 °C under 10 bar of hydrogen pressure and desorbed it at the same temperature under a residual hydrogen pressure of 210 mbar. Pranevicius *et al.* (2006) reported that a 2 μm thick Mg film transformed into MgH_2 under high-flux hydrogen plasma immersion ion implantation at 180 °C after 15 min, while desorption occurred at 260 °C.

Pd/Mg films (Pd (25 nm)-coated Mg (200 nm) films) exhibited hydriding–dehydriding cycles at lower temperatures (< 190 °C) with a capacity of up to 5.6 wt.% (Higuchi et al., 1999). Three layered Pd/Mg/Pd thin films exhibited further improved hydrogen properties in which the hydrogen desorption temperature decreases rapidly with increasing Mg thickness in Pd/Mg/Pd films, down to 100 °C for Pd/Mg (800 nm)/Pd film. Kumar *et al.* (2009) also reported similar improved hydrogen sorption properties at low temperature on MgPd thin films. Room temperature hydrogenation of Mg/Pd films was reported by Yoshimura *et al.* (2004). Mg-4 at.% Fe films exhibited cyclic hydrogen sorption at temperature near 150 °C, with a reduced heat of formation of -66.9 kJ $mol^{-1}H_2$ (Tan et al., 2011). A superior reversible hydrogen storage capacity, along with an excellent rate-capability, was reported for the $Mg_{0.80}Ti_{0.20}$ thin film alloy (Vermeulen et al., 2006). Similarly, there were several other metal` capping Mg thin films that absorbed hydrogen, such as La-Mg (Van Der Sluis et al., 1997), Sm-Mg (Ouwerkerk, 1998), Y-Mg (Nagengast et al., 1999), and Ni-Mg (Richardson et al., 2001).

4. Melt-spun Mg-Ni-based Hydrides

4.1. Introduction

In the previous Chapter, it states that there are mainly, four ways to improve the hydrogen storage properties of MgH_2, which are ball milling, alloying with other metals, using catalyst, and using thin film materials.

However, instead of ball milling, melt spinning has also been applied in this work. Although it has a similar function of producing nanocrystalline materials, melt-spinning does not involve impurity issues compared with ball-milling. Nano-scale processing can produce large volumes of grain boundary material which can acts as active paths for the diffusion of hydrogen. Moreover, it results in a high grain surface ratio, where the hydrogen could react with the metal, and reduce the diffusion through the formed hydride layers. Furthermore, melt spinning is also one of the methods of producing the amorphous phase, which also has a good hydrogen sorption properties, and it is another way of producing nanocrystalline materials by controlling the crystallization of amorphous phase. In view of this, melt spinning has the capability of enhancing the hydrogen sorption kinetics.

Alloying with Ni has also been studied in this work, as Mg_2Ni is a well known hydrogen storage material. Mg_2NiH_4 has a lower heat of formation than MgH_2 with a reduced, but still relatively high, hydrogen capacity of 3.6 wt.%. Therefore, by alloying with Ni, it was hoped that the hydrogen desorption temperature may be reduced.

In conclusion, this project is aiming to improve the hydrogen storage properties of Mg hydrides materials using melt spinning and alloying with Ni. In the past decade, there has been a large number of studies in this field of melt-spun Mg-Ni-based alloys. In the subsequent section, a review of Mg-Ni-based storage materials by melt spinning has been summarized. According to the works of other researchers, the methodology of the present work has been designed and developed, and the results has been analyzed and discussed.

4.2. Mg-based nanocrystalline hydrogen storage materials

Metastable Mg–Ni-based compounds with or without different additives are of interest for the development of H_2 storage materials. Selected alloys prepared by rapid quenching and mechanical alloying are investigated with respect to the thermal phase transformations and their hydrogen absorption and desorption properties, and as well as their electrochemical H_2 charge–discharge behaviour in strong alkaline electrolytes. Research into rapidly solidified Mg-Ni-based hydrides, has been summarized in terms of the hydrogen storage properties, sample synthesis method, amorphous forming ability and activation treatment.

4.2.1. Hydrogen sorption properties

Mg-Ni alloys without additives

Bendersky *et al.* (2011) produced melt-spun $Mg_{100-x}Ni_x$ (x= 0.5, 1, 2,5) binary alloys. The intermediate phase Mg_6Ni was found in the alloys. The alloys show very fast hydrogen absorption kinetics of 4 wt.% in 1 min at 300 °C under 19 bar, and an absorption capacity of 6.5 wt.%. It was also found that about 0.6 wt.% hydrogen can diffuse into the Mg matrix as solid solution which exceeds the solid solubility limit. The limit is usually represented by the hydrogen content at the beginning of hydrogen sorption plateau pressure, which is usually 0.2 ~ 0.4 wt.% H_2 as shown in the PCI result of melt-spun Mg in this work (Figure 6-11).

Kalinichenka *et al.* (2010) produced melt-spun $Mg_{90}Ni_{10}$ ribbons, and directly hydrided and activated the sample without providing any analysis of the as-quenched materials. The hydrogen desorption of the melt-spun $Mg_{90}Ni_{10}$ has been studied for both thermodynamics and kinetics, in spite of the hydrogen absorption. At 250°C under a vacuum, the desorption rate reached 1.3 wt.%·min^{-1}. In addition, the desorption of hydrogen underwent a two-stop process: desorption of HT/LT-Mg_2NiH_4 to $Mg_2NiH_{0.3}$ at 220°C and desorption of MgH_2 to Mg at 350 °C.

Yim *et al.* (2007) studied melt-spun $Mg_xNi_{(100-x)}$ (x = 94, 89, 83) alloys. The Mg–xNi alloys absorbed 90% of the maximum absorption capacity within 15 min.

Friedlmeier *et al.* (1999) produced melt-spun $Mg_{87}Ni_{13}$ and $Mg_{84}Ni_{16}$ ribbons (starting composition), whereas the measured composition is $Mg_{73}Ni_{23}$ and $Mg_{67}Ni_{33}$. Both alloys showed amorphous structure, with crystallization at 160 °C. In the XRD pattern, an unknown metastable phase with peak at 38° crystallized with the Mg phase at that temperature, which is likely to be Mg_6Ni. $Mg_{87}Ni_{13}$ shows a high hydrogen capacity of 5.9 wt.% at 390 °C under 15 bar.

Zhang *et al.* (2009b) reported that melt-spun Mg_2Ni did not exhibit an amorphous phase, but rather a nanocrystalline structure with a grain size of 30 nm. They showed fast kinetics, reaching nearly the saturated capacity of ~3 wt.% in 5 min under 15 bar H_2 at 200 °C. However, it desorbed only 1 wt.% H_2 in one hour under a vacuum at 200 °C.

Mg-Ni alloys with metal oxides

Hong (2008) followed Yim (2007) in adding Nb_2O_5 as a catalyst. The melt-spun Mg-23.5wt%Ni alloy where the addition has been prepared by planetary ball mill and heat treatment at 250°C for 1 hour. The activated 90% (melt-spun Mg–23.5wt%Ni) –10% (Nb_2O_5) alloy absorbs 4.70 wt% H_2 at 300°C under 12 bar H_2 for 10 min, and desorbs 4.75 wt.%. H_2 at 300°C under 1.0 bar H_2 for 25 min.

Mg-Ni alloys with transition metals

Palade *et al.* (2006) produced melt-spun $Mg_{88}Ni_{11}Fe_1$ and $Mg_{88}Ni_{11.4}Fe_{0.6}$ both of which showed that the samples partially contained some amorphous phase. The alloys absorbed around 5 wt.%. H_2 with fast absorption kinetics at 306 °C under 25 bar H_2. Pressure-composition isotherm measurements exhibited two plateaux for both samples, the lower

and wider one corresponding to the MgH_2 phase and the upper and shorter one corresponding to the Mg_2NiH_4 phase.

Mg-Ni alloys with rare-earth elements (RE = Sc, Y, La, Nd)

Spassov and Koster (1999) produced $Mg_{87}Ni_{12}Y_1$ by the same method of melt spinning as described in a previous paper (1998). Melt-spun $Mg_{87}Ni_{12}Y_1$ was in the fully amorphous phase. Two steps of crystallization has been found in DSC studies, that one is the crystallization of Mg phase, followed by the formation of Mg_6Ni from the residual amorphous material.

Kalinichenka *et al.* (2009) produced partial amorphous $Mg_{90}Ni_5Y_5$ and fully amorphous $Mg_{80}Ni_{10}Y_{10}$ ribbon by melt spinning with a very fine nanocrystalline structure in size of 5-20 nm. Two or three exothermic peaks have been reported from the DSC results. The first peak was considered as being due to the crystallization of the Mg_2Ni phase, but others were not analysed, and no metastable phase were mentioned. After three thermal cycles, the activated samples exhibited fast hydriding kinetics of up to 1 wt.%. H_2 per min at 300 °C under 20 bar H_2, with a maximum capacity of 5.3 wt.%.H_2.

Kalinichenka *et al.* (2011b) also produced $Mg_{90}Ni_8RE_2$ by melt spinning, which showed Mg grains of 150 nm and fine Mg(NiY) grains of 5 nm embedded in an amorphous phase. After an activation process of 3 cycles of hydrogen sorption at 385 °C and 30 bar H_2, the sample absorbed 5.5 wt.%. H_2 within 20 min under 20 bar H_2 pressure at 300 °C, and 1.1 wt.%. at 50 °C. The sample remained with a nanoscale microstructure after numerous cycles of hydrogenation.

Tanaka *et al.* (1999) produced a melt-spun ternary alloys of Mg-(15-25 at.%)Ni-5 at.%RE (RE = Nd or La) which were amorphous in the as-quenched state. The activated samples exhibited a nano-crystalline structure of 50-100 nm in diameter. 5.7 wt.% hydrogen was absorbed within 20 min under 35 bar H_2 at 300 °C for the activated Mg-Ni-RE ternary alloys, and 5 wt.% for the $Mg_{85}Ni_{15}$ sample.

By melt-spinning, Lin *et al.* (2012a) produced a series of six Mg-Ni-Ce alloys from $Mg_{94}Ni_3Ce_3$ to $Mg_{88}Ni_9Ce_3$ alloys. Three of them exhibited a nanocrystalline phase embedded in amorphous matrix, two with fully nanocrystalline and one fully amorphous. Apart from the crystalline samples, the alloys exhibited two DSC peaks which may be ascribed to crystallization, firstly of Mg and secondly of Mg_2Ni. Whereas the fully amorphous $Mg_{90}Ni_5Ce_5$ showed a further DSC crystallization peak corresponding to the phase Mg_6Ni. The melt-spun $Mg_{90}Ce_5Ni_5$ ribbons absorbed about 5.0 wt.% H_2 at 300 °C under 25 bar H_2, with a rate of 1 wt.%-H/min, desorbed 4.1 wt.% H_2 within 10 min under a vacuum.

Spassov and Koster (1998) prepared the alloy $Mg_{63}Ni_{30}Y_7$ by melt-spinning and it was found to consist mainly of hexagonal Mg-(Ni;Y) nanocrystals with a size of 2 ~ 3 nm embedded in an amorphous phase. During thermal sorption, the melt-spun materials exhibited crystallization and nanocrystalline growth with an activation energy of 140 ± 7 kJ mol^{-1}. The hydriding properties have been studied by electrochemical methods with a maximum capacity of 3.0 wt.% and relatively fast kinetics comparable to those of the ball-milled Mg_2Ni. Hydrogenation resulted in nanocrystalline growth to 15~20 nm.

Zhang *et al.* (2009b) produced alloys of Mg_2Ni-type $Mg_{2-x}La_xNi$ (x= 0, 2, 4, 6) by melt-spinning. By substituting Mg with La, the ternary alloys exhibited enhanced metallic glass forming ability with a major amorphous phase after melt spinning. The melt-spun alloys exhibited a maximum hydrogen absorption capacity of ~3 wt.% in 5 min under 15 bar at 200 °C, and desorption of 2.5 wt.% H_2 with the highest La content under a vacuum at 200 °C.

Isogai *et al.* (2000) studied the hydrogen absorption of amorphous melt-spun $Mg_{62}Ni_{33}Ca_5$ and crystallized $Mg_{62}Ni_{33}Ca_5$ samples. Under 50 bar H_2, amorphous $Mg_{62}Ni_{33}Ca_5$ exhibited a maximum absorption capacity of 2.3 wt.% at 40 °C and 3.0 wt.% at 100 and 130 °C. On the other hand, the crystallized $Mg_{62}Ni_{33}Ca_5$ exhibited an absorption capacity of 1.3 wt.% at 40 °C, 1.85 wt.% at 100 °C and 2.6 wt.% at 130 °C. The absorption kinetics of the amorphous phase were not faster than those of the crystalline alloy until 400 s, and then increased subsequently. The crystallization behaviour of the amorphous $Mg_{62}Ni_{33}Ca_5$ alloy exhibited a two-step crystallization process, first for the Mg_2Ni phase and secondly for the Mg_2Ca and $MgNi_2$ phases.

4.2.2. Sample Preparation

The sample preparation process was found to be both complex and confusing. As most of the journal articles reported only a very brief description of the sample synthesis process, it is difficult to know how to repeat the experiments based only on the information available. By summarizing a number of articles, it provides some clues but is still not sufficient. In my research work, a large amount of time has been spent on trying to: develop the methodology, in order to replicate results in the literature and then investigating how to most effectively modify the conditions and the configurations.

According to the literature, Mg-Ni melt spinning research generally goes through three steps: preparing the master alloys, melt-spinning, and the follow-up treatment(s). However, it was difficult to establish all the necessary details of the experiments, such as the particular temperature, pressure, cycles and time *etc.*. Moreover when I started the PhD work, the melt-spinning device was newly established in the research group. Therefore, one aim was to determine the detailed experimental conditions and settings needed to achieve the effective melt-spinning of the Mg-based alloys.

The preliminary melt spinning work carried out in the present work, attempted to repeat the reports in the literature. Before melt-spinning, it was necessary to prepare the master alloys. For Mg-based alloys, most researchers employed induction heating due to the evaporation of magnesium. Although Bendersky *et al.* (2011) claimed Mg-Ni alloys were produced by arc melting, they did not provide any more information on the arc-melting conditions used. Therefore, in the present work, induction melting has been used to make

the Mg-Ni compounds. Many researchers have mentioned the evaporation of magnesium, and some have claimed a positive pressure was effective in preventing the losses of magnesium (Huang et al., 2006; Palade et al., 2006), whereas others used low pressure (Zhang et al., 2009b; Lin et al., 2012a). Most workers used the vacuum induction furnace under argon, and a minority employed helium (Zhang et al., 2009b; Zhang et al., 2009c; Friedlmeier et al., 1999). The particular conditions of melt spinning (temperature, pressure *etc*.) varied with the various investigations.

In addition, the selection of an appropriate crucible was another important issue for both induction-melting and melt-spinning. At high temperatures, the crucible materials should be inert to Mg and the additive materials. In the literature, a number of crucibles have been employed, such as steel, graphite, alumina, boron nitride and quartz tube with or without BN coating. Table 4-1 summarises the crucibles used for induction melting and melt spinning. In the present work, due to the low cost, it started with quartz tubes as the crucible,. Subsequently it was found that the quartz tube did not prevent a reaction with Mg and the silicon in the glass, and the BN was used and proved to be an appropriate crucible.

Bendersky *et al.* (2011) used arc-melting to alloy Mg and Ni to form the Mg-Ni alloys. The ingots were then placed in a boron nitride coated quartz tube, and were inductively melted and then ejected by 1 bar He overpressure onto a rotating Cu wheel at a speed of ~30 m/s in an inert gas atmosphere. The melt-spun ribbons were then heated at 450 °C and then ball-milled into powder.

Curcibles used in the Induction Melting	
Steel crucible	(Sugamata et al., 1997) (Tanaka, 2008) (Hong et al., 2009; Hong et al., 2008) (Yim et al., 2007)
Graphite crucible	(Palade et al., 2006) (Friedlmeier et al., 1999)
Quartz tube	(Lin et al., 2012a) boron nitride coated
	(Bendersky et al., 2011)
Alumina crucible	boron nitride coated
	(Kalinichenka et al., 2011b)
Crucibles used in the Melt spinning	
Boron nitride crucible	(Hong et al., 2008) (Hong et al., 2009) (Yim et al., 2007)
Graphite crucible	(Sugamata et al., 1997) (Friedlmeier et al., 1999)

Table 4-1 List of crucibles used for induction heating and melt spinning with corresponding references

Friedlmeier *et al.* (1999) initially pressed Mg and Mg_2Ni powder into pellets, and the pellets were then heated inductively in a graphite crucible above the melting point and then maintained at selected temperatures for about 15 min. Thereafter the melt was quenched by the melt spinner at 700 °C under 300 mbar of He gas atmosphere with 500 mbar overpressure for injection, and the copper wheel speed was 31.4 m/s (3000 rpm). The melt-spun ribbons were collected in air.

Hong *et al.* (2009; 2008) claimed that the preparation of melt-spun Mg-Ni alloys followed the method given by Yim (2007), in which it has been described that pure Mg was heated to 900 °C in a stainless steel crucible and pure Ni was then added to the molten Mg as

chips. The gas atmosphere was CO_2 and SF_6, but no information on the pressure was given in the paper. It is not certain what measures have been carried out to minimize the evaporation and oxidation of the Mg at the high temperature. The gravity cast Mg-Ni ingot was then melt-spun in a boron nitride crucible under 490 mbar pressure through 2.5 mm wide nozzle onto a copper wheel spinning with a velocity of 35 m/s. The conditions of the melt spinning process were not described in detail.

Huang *et al.* (2006; 2009) prepared $(Mg_{60}Ni_{25})_{100-x}Nd_x$ (x = 2, 5, 10, 15) alloy ingots by induction melting a mixture of pure Nd metal and a Mg–Ni alloy in a vacuum furnace under the protection of argon gas. Based on the low melting point and the high vapour pressure of Mg, a special melting technique, that provided a positive pressure protection and repeated melting, was carried out to prevent massive Mg evaporation and ensure composition homogeneity during the preparation of the master alloy ingot. The amorphous or nanocrystalline ribbons were produced by a single roller melt–spun technique (copper quenching disc with a diameter of 250 mm and surface velocity of about 39 ms^{-1}) in an argon atmosphere of 400 mbar. The consequent ribbons were about 2 mm wide and 20 μm thick however, the temperature during the heating in the melt spinner was not given in the paper.

Palade *et al.* (2006) melted Mg pellets, Ni and Fe powder in a graphite crucible under 30 bar argon protection and holding at 1200 °C for 1 hour. The melt was then melt-spun with an injection pressure of 400~600 mbar onto a copper wheel, formed 25~35 μm thick ribbons. They did not mention the melt spinning temperature, wheel speed or the chamber pressure *etc.*

Zhang *et al.* (2009c; 2009b) employed induction melting to produce Mg_2Ni-type ternary MgLaNi and MgCoNi alloys under a pressure of 400 mbar helium atmosphere which was claimed to effectively prevent the volatilization of magnesium. Melt spinning followed the induction heating, with no information on the detailed parameters for melt spinning.

Lin *et al.* (2012a) studied melt-spun Mg-Ni-Ce ternary alloys. Master alloys were prepared by conventional induction melting of a mixture of Ce-Ni intermediate alloys and pure Mg metal in a quartz crucible under an argon atmosphere. Ribbons of 2.5 mm in width and 40 μm in depth were obtained after melt spinning with a wheel velocity of 30 m/s. Prior to the hydrogen storage property measurements, the melt-spun ribbons were ball milled into powders for 30 min.

Spassov and Koster (1998; 1999) used induction melting to alloy the Mg-Ni-Y ternary under 500 mbar argon gas protection. They also claimed special care had been taken to prevent massive Mg evaporation during the melting, but with no further description of what the exact ‘special care’ was provided (Spassov and Koster, 1998). The melt-spun Mg-Ni-Y was then produced by a copper wheel with a diameter of 25 cm and velocity of 35-40 m/s in an atmosphere of helium at 400 mbar. The melt-spun alloy was revealed to be a mixed structure of amorphous and nanocrystalline, with exact chemical composition determined by EDAX analysis to be $Mg_{63}Ni_{30}Y_7$.

A tantalum crucible was used to produce the Mg-Ni-Y ternary alloys (Kalinichenka et al., 2009) and Mg-Ni-Cu-Y alloy (Kalinichenka et al., 2011a) by induction melting at 1000 °C under argon.

For the production of the $Mg_{90}Ni_{10}$, a boron nitride coated crucible was used for induction melting (Kalinichenka et al., 2010). For the $Mg_{90}Ni_8RE_2$ alloy, a boron nitride coated alumina crucible was employed to alloy the master ingots (Kalinichenka et al., 2011b). They did not provide the argon pressure for the induction heating, with no mention of the Mg losses due to sublimation. Besides the 1 bar of Ar for the melt spinning of the $Mg_{90}Ni_8RE_2$, there was no information on the melt spinning temperature, argon pressure *etc.*. Ribbons were collected with a thickness of 35 µm and a width of 10 mm.

Teresiak *et al.* (2009a) described the preparation method in more detail for the alloys $La_{25}Mg_{50}Ni_{25}$ and $La_{20}Mg_{50}Ni_{30}$. The master alloys were prepared by induction melting of the pure elements Ni and La and subsequent cold crucible casting of the re-melted binary alloys with the addition of Mg. It is claimed that, in this way, losses of Mg due to evaporation could be minimized. The melt-spun ribbons were collected with a width of 4mm and a thickness of 30 µm.

Tanaka (2008) prepared MgNiLa and MgNi alloys by melting at 900 °C under an argon atmosphere in a steel crucible for 1 hour. The melt-spun ribbons with dimensions of 20 µm thick and 1 mm wide were then obtained from the master ingots.

4.2.3. Amorphous materials

Rapid solidification technique (*e.g.* melt-spinning) have been well known as a method of producing metallic glass or amorphous phase. The metallic glass phase (amorphous) plays an important role in hydrogen storage research. Not only because the amorphous phase can show a storage capacity of up to 4 wt.%, and also because the amorphous phase can crystallise into a fine nano-crystalline phase which has excellent hydrogen storage properties (Orimo and Fujii, 2001). Therefore, the glass forming ability of Mg-Ni binary and ternary alloys has been studied extensively, and this informs the alloy design to produce amorphous / nanocrystalline Mg-Ni hydrogen storage materials.

Tanaka *et al.* (1999) produced a series of Mg-Ni binary and Mg-Ni-La(or Nb) alloys by melt spinning, with Ni content from 15 to 25 at.% according to the glass forming range of Mg-Ni system (Figure 4-1). The melt-spun $Mg_{70}Ni_{25}La_5$ and $Mg_{70}Ni_{25}Nb_5$ ribbons exhibited an amorphous phase, with 15 at.% Ni content in the glass-forming range.

Bendersky *et al.* (2011) produced melt-spun $Mg_{100-x}Ni_x$ (x= 0.5, 1, 2, 5) binary alloys. All four alloys exhibited a fine crystalline structure with no evidence for any amorphous material. In accordance with the glass forming range shown in Figure 4-1, these particular Mg-Ni compositions are not in the range.

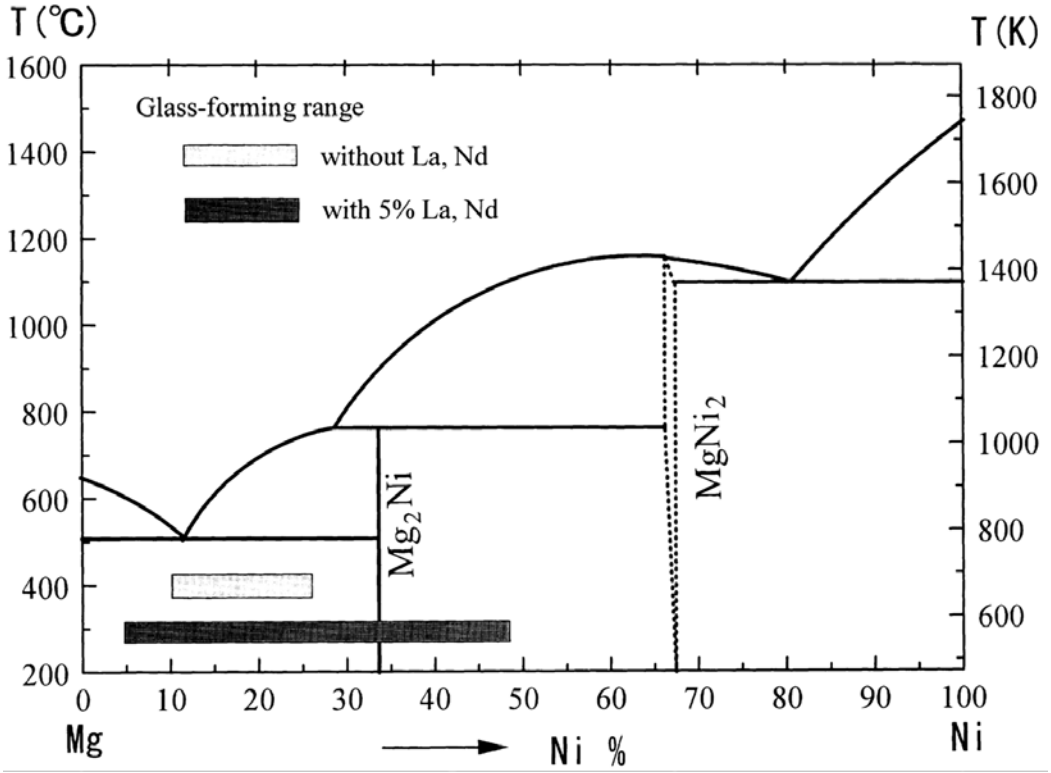

Figure 4-1 Phase diagram of Mg-Ni system including the glass-forming ranges with and without 5 at.% RE. Taken from Tanaka *et al.* (1999)

Friedlmeier *et al.* (1999) tried to melt-spun Mg-Ni binary alloy with the composition in the glass forming range shown in Figure 4-1. The $Mg_{87}Ni_{13}$ and $Mg_{84}Ni_{16}$ samples exhibited the amorphous phase, but the real composition is $Mg_{73}Ni_{23}$ and $Mg_{67}Ni_{33}$ determined by inductively coupled plasma (ICP) atomic emission spectrometry. These workers also mentioned an unknown metastable phase which crystallized during the heat treatment, but it was not identified.

Yim *et al* (2007) claimed that the amorphous phase was observed solely in the eutectic ($Mg_{89}Ni_{11}$) and hypereutectic ($Mg_{83}Ni_{17}$) melt-spun ribbons, and no amorphous phase was found in the hypoeutectic alloy ($Mg_{94}Ni_{6}$).

Spassov *et al.* (2002b) also produced an amorphous of $Mg_{83}Ni_{17}$ with a very fine nanocrystalline of 3-4 nm. The DSC measurement of the melt-spun alloy indicated the evidence of the metastable Mg_6Ni phase which was likely to be crystallized from the amorphous matrix.

Ong *et al.* (1998) reported melt-spun $Mg_{82}Ni_{18}$ which, according to the XRD pattern, exhibited the fully amorphous phase after melt spinning. It was crystallized into the Mg_2Ni phase, the Mg phase and an unknown phase with a d-space value of 2.37 Å, which can be identified as the Mg_6Ni phase.

Zhang *et al.* (2009b) studied a melt-spun Mg_2Ni alloy by both XRD and TEM. The melt-spun Mg_2Ni ribbons did not exhibited the amorphous broad XRD patterns, but TEM indicated a nanocrystalline structure with a grain size of 30 nm.

Song *et al* (2008a) produced amorphous ternary alloys based on the alloy, Mg-23.5wt%Ni ($Mg_{89}Ni_{11}$) by melt spinning. The XRD patterns of (Mg-23.5wt%Ni)-10wt%Cu and (Mg-23.5wt%Ni)-10wt%La exhibited a broad maxima between 35° to 45°.

Lin *et al.* (2012a) reported a fully amorphous $Mg_{90}Ni_5Ce_5$ by melt spinning, and partially amorphous alloys of $Mg_{91}Ni_5Ce_4$, $Mg_{92}Ni_4Ce_4$ and $Mg_{88}Ni_4Ce_8$.

Spassov and Koster (1999) also produced a melt-spun $Mg_{87}Ni_{12}Y_1$ alloy, which was a fully amorphous alloy with a XRD broad peak at 38°. It exhibited a two steps

crystallization process shown by DSC studies. Crystallization of the Mg phase followed with the formation of Mg_6Ni from the residual amorphous material.

Kalinichenka (2009) produced melt-spun amorphous $Mg_{80}Ni_{10}Y_{10}$ alloy which exhibited a typical amorphous XRD pattern with a fine nanocrystalline (5 nm) determined by TEM studies after subsequent crystallization. The melt-spun $Mg_{90}Ni_5Y_5$ alloy exhibited a microstructure of nanocrystalline (20 nm) embedded in an amorphous matrix. Melt-spun $Mg_{90}Ni_8RE_2$ exhibited Mg grains of 150 nm and fine Mg(NiY) grains of 5 nm embedded in an amorphous phase (Kalinichenka et al., 2011b).

Wu *et al.* (2007; 2009) produced $Mg_{88}Ni_{10}Mm_2$ alloys after different solidification conditions with three copper wheel speed of 300, 1000 and 2000 rpm. The melt-spun sample with the highest solidification rate exhibited an amorphous phase with minor nanocrystalline grains of Mg.

Huang *et al.* (2006; 2009) produced amorphous MgNiNb ternary alloys by melt-spinning, which had the compositions $(Mg_{60}Ni_{25})_{100-x}Nd_x$ (x = 5, 10, 15) alloys. $(Mg_{60}Ni_{25})_{95}Nd_5$, $(Mg_{60}Ni_{25})_{90}Nd_{10}$ and $Mg_{60}Ni_{25}Nd_{15}$ exhibited the fully amorphous condition after melt spinning.

Spassov and Koster (1998) produced $Mg_{66}Ni_{30}Y_7$ by melt-spinning, which exhibited mixed structure of amorphous and nanocrystalline.

Zhuang *et al.* (2009b; 2009c) reported that, melt-spun $Mg_{2-x}La_xNi$ (x = 2, 4, 6) with Mg substituted by La and melt-spun $Mg_2Ni_{0.6}Co_{0.4}$ ($Mg_{66.7}Ni_{20}Co_{13.3}$) with Ni substituted by Co formed the amorphous phase in the melt-spun state.

Teresiak *et al.* (2009a) reported work on melt-spun $La_{50}Mg_{50}Ni_{25}$ and $La_{20}Mg_{50}Ni_{30}$ alloys, both of which exhibited solely XRD diffuse maxima. The TEM indicated an amorphous matrix with embedded nanograins of 2~7 nm.

Revesz *et al.* (2012) melt-spun Mg_2Ni-type $Mg_{65}Ni_{20}Cu_5Y_{10}$ alloys. The melt-spun ribbons exhibited the fully amorphous phase. They also reported the crystallization of the Mg_6Ni phase.

4.2.4. Activation Treatment

Several researchers found that the melt-spun Mg-Ni alloys achieved the best hydrogen storage properties after thermal sorption cycling as an activation treatment. This often consisted of 300 °C heat treatment and a high hydrogen pressure of 10~20 bar.

Hong *et al.* (2008) employed 2 cycles of hydriding and dehydriding of H_2 as the activation treatment of the materials studied under 300°C and 10 (and 20) bar hydrogen pressure which is a common set of conditions for hydrogen sorption.

Tanaka *et al.* (1999) claimed that melt-spun ternary alloys of Mg-(15~25 at.%)Ni-5 at.%RE (RE = Nd or La) can be activated, only after three cycles of hydrogenation (under 35 bar H_2) and dehydrogenation (vacuum) at 300 °C. While the melt-spun $Mg_{85}Ni_{15}$ alloy required five such cycles for activation.

Kalinichenka *et al.* discovered that three thermal cycles of hydrogen sorption as a sample activation for an as-quenched $Mg_{80}Ni_{10}Y_{10}$ alloy were required to exhibit excellent hydrogen storage properties (Kalinichenka et al., 2009). Melt-spun $Mg_{90}Ni_8RE_2$ was also activated at 385 ~ 350 °C under a pressure of 30 bar H_2 (Kalinichenka et al., 2011b).

Other researchers employed direct electrochemical charging of the melt-spun ribbons for the electrochemical property investigations. The gas-solid hydrogen absorption differs from that of the electrochemical charging. Therefore, the hydrogen absorption properties from gas-solid reaction were not comparable with the results of electrochemical properties.

Huang's group employed electrochemical measurement for the hydrogen storage property measurements. Melt-spun samples were hydrogen charged under galvanostatic conditions in 6 mol/l KOH electrolyte containing 20 g/l LiOH at room temperature and a cathodic current densities i = 1 mA/cm^2 (Huang et al., 2009; Huang et al., 2006). Spassov (Spassov and Koster, 1998; Spassov and Koster, 1999; Spassov et al., 2002a; Spassov et al., 2002b) employed electrochemical methods to hydrogenate the melt-spun alloys, and studied the hydrogenation properties. Teresiak activated the sample for galvanostatic charging with hydrogen at room temperature in 0.1M NaOH + As_2O_3 solution and with a current density

i of −1 mA/cm^2 for ribbon samples with a length of about 30 mm (Teresiak et al., 2005). Teresiak *et al.* (2009b) studied melt-spun $Mg_{85.7}Ni_{14.3}$, with regard to the effect of H_2 gas or electrochemically charged H_2 on the stability range and on the phase reactions of the Mg-Ni phase and on its crystal structure, respectively.

5. Experimental

5.1. Raw materials

The raw materials used in this project were purchased from several suppliers and in different forms, such as granules, wire and powder. Through an optimisation process, powders were found to be the most suitable form for the raw materials and were used in all the sample presented in this work. The raw materials purchased are listed below with details in Table 5-1.

Material	Company	Purity	Shape	Size
Mg	ALPHA AESAR	99.8%	powder	43.2 μm
Mg	SIGMA-ALDRICH	99.98%	granules	d=1.74 mm
Ni	SIGMA-ALDRICH	99.99%	powder	<150 μm
Ni	SIGMA-ALDRICH	99.9+%	wire	0.5 mm
Ti	UNICORE MATERIALS	99.5%	granulate	0.2-1.5 mm
MgH_2	GOLDSCHMIDT AG	95%	powder	20 μm

Table 5-1 Detailed properties of as-received materials used in this work

5.2. Material Synthesis

Melt spinning Mg-based materials has been studies for some time, but no previous investigations into the melt spinning of Mg-based alloys had been conducted at the University of Birmingham. Therefore, during this project, the material synthesis procedure by several initial trials were developed and optimized.

The initial investigations started by melting the reagents together by induction heating. However, it has been found difficult to attain reliable results, due to the sublimation of Mg.

The optimized approach for the synthesis of the melt spun Mg-Ni alloys is a multi-step process involving powder-pressing to form a compact before melt-spinning and cryo-milling to convert the ribbon into a powder.

5.2.1. Induction Melting

Mg-based ingots were alloyed by induction melting prior to melt spinning. Numerous researchers (Hong et al., 2009; Teresiak et al., 2005; Todorova and Spassov, 2009; Isogai et al., 2000; Wu et al., 2007) used induction melting to alloy Mg-based materials as alloy preparation prior to rapid solidification.

A *Crossley* Induction RF generator (*EC 60*) has been used to produce the Mg-based alloys. About 6~8 grams of the constituent materials were loaded in quartz crucibles or boron nitride (BN) crucibles. The crucibles were then sealed in a quartz tube under an argon atmosphere in order to avoid oxidation. The quartz tube was placed inside the inductive coil for melting. Initial trials used quartz crucibles with BN coating, however, Si was detected within the products, thus indicating that the BN coating did not inhibit completely the reaction between glass and Mg, thus leading to the use of BN crucibles.

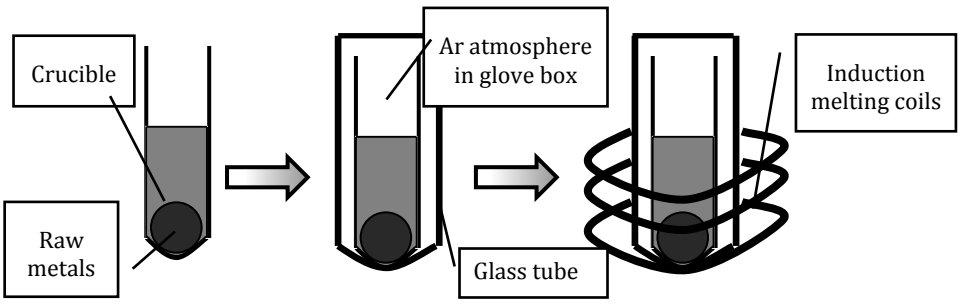

Figure 5-1 Schematic of the material alloying by induction melting

A direct measurement of the temperature of the furnace is not possible; thus, the output power cannot be controlled by setting a target temperature, so a voltage was selected manually. Melting could be achieved with an output power of 30 ~ 35 kW and a frequency of 450 kHz.

The melting point of Mg and Ni is 650 °C and 1455 °C respectively. The melting point of Ni is higher than the sublimation temperature of Mg of only 1090 °C under ambient atmospheric pressure (Ditze and Scharf, 2008). This leads to losses of magnesium due to sublimation. To produce a sample with the target composition, several measures have to be taken. Firstly, extra magnesium was added to compensate for the losses. Secondly, the rate of sublimation, of the magnesium, was dependent on the pressure applied. Zhang (2009c) claimed that 400 mbar pressure effectively prevented the volatilization of the magnesium. Therefore, an argon pressure of 600 mbar was applied when the glass tube was sealed. Thirdly, to enhance the element diffusion and to prevent sublimation, the samples were only melted for 2 min when glowing, and then cooled for annealing. This process was repeated eight times to fully homogenise the samples.

5.2.2. Static-pressing

To avoid the losses of Mg due to sublimation it is necessary to minimize the time of induction melting. A modified procedure, utilizing static-pressing prior to loading in the melt spinner, was adopted in this work. The primary advantage of this approach is that only a single induction melting is required; this occurs immediately before the melt spinning process.

Commercial powders of Mg and Ni, with similar particle size, were loaded in a sealed plastic bottle in glove box. The powders were mixed for half an hour using a mechanical blender (*STR4 General Rotator* by *Stuart Bibby Scintific*). A sausage-like, long modeling balloon was then filled with the mixed powder in the glove box.

The sample balloon has been pressed for about 40 min under a static pressure of 10 tons in a hydraulic press (*Strong-Arm press* by *Clarke*). As a result, the powder sample was pressed into a compacted solid rod, which could be loaded into the induction coil of the melt spinner.

5.2.3. Melt-spinning Technique

The system used in this work is an *Edmund Buelher D-72379 Hechingen* melt spinner which was designed for production of rapid solidified amorphous or microcrystalline ribbons in a high vacuum or inert gas atmosphere. The apparatus has been modified with inert loading and collection tube in order to avoid any air contact because of the high reactivity of Mg at high temperature. A process of melt spinning has been well developed and fine solidified ribbons were achieved successfully.

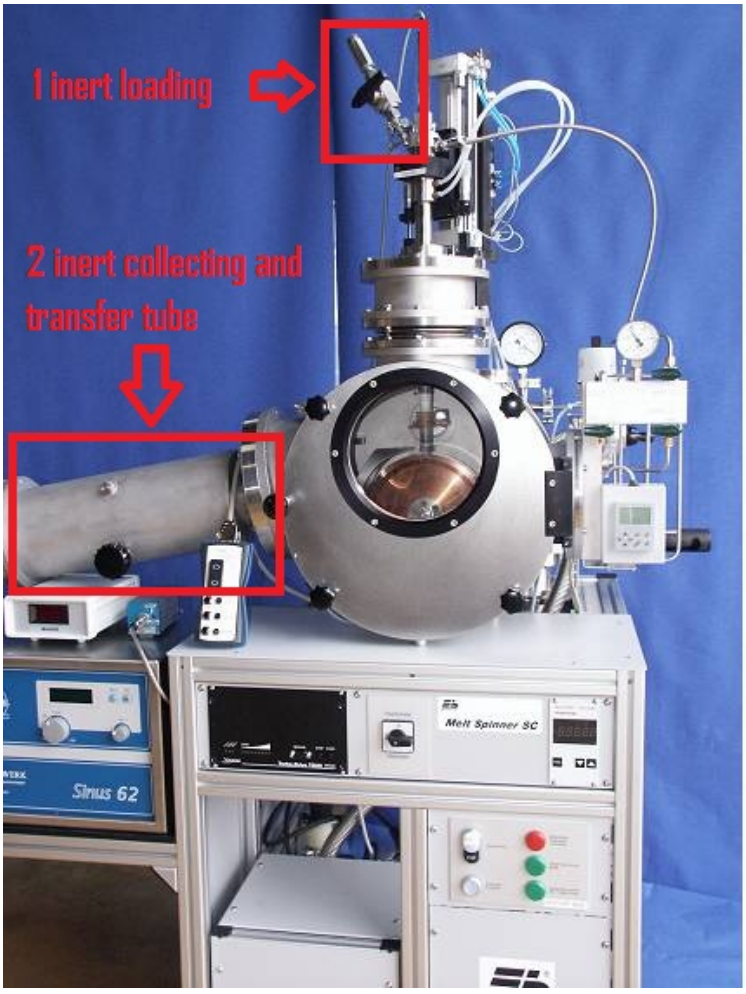

Figure 5-2 Edmund Buelher D-72379 Hechingen Melt-spinner with inert modification.

A BN crucible was employed for the melt spinning of Mg-based materials. The crucible consists of several parts, with an outer diameter of 8 mm and an inner one of 6 mm. The crucible can hold no more than 10 g of a standard metal sample ($Fe_{40}Ni_{40}B_{20}$), suggested by the manufacturer. In this project, a sample of 3 ~ 4 g Mg-based materials resulted in the best melt spinning process. Therefore, for each run of melt spinning, about 3 g samples were loaded into the inert loader in a glove box.

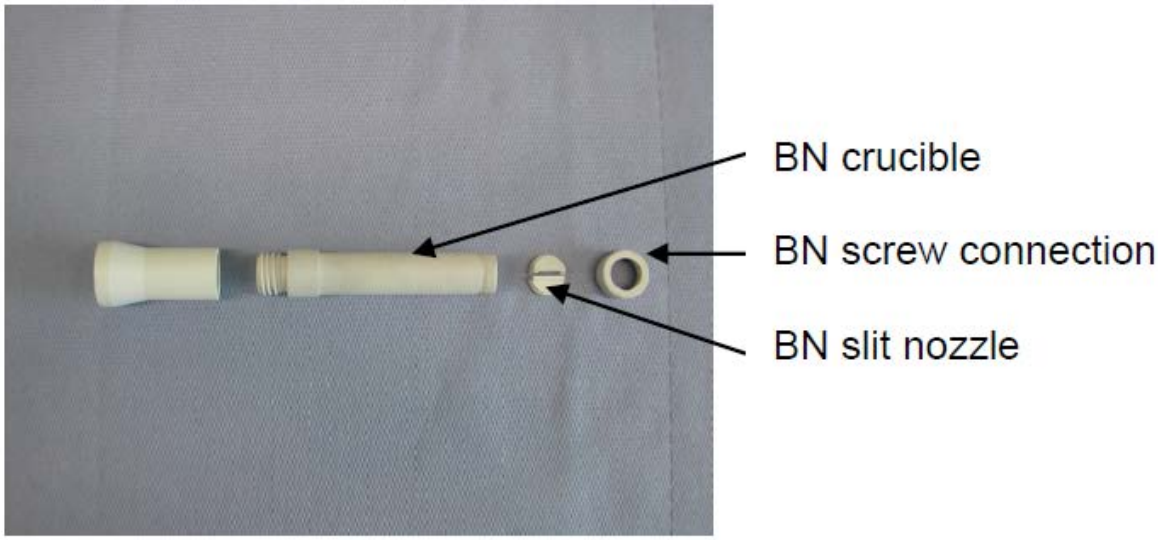

Figure 5-3 BN crucible employed in the melt spinning.

The BN slit nozzle was located in the screw connect, and then fastened to the BN crucible main stem body. The crucible was then screwed to the crucible holder inside the main chamber of the melt spinner. The bottom part of the crucible was inside the induction coil. A 90° gauge was employed to position the slit nozzle at 90° angle against the rim of the wheel. There is a 1° angle vertically off the wheel, thus melt spinning the ribbons directly into the ribbon collection tube on the left hand side. The lowest position of the crucible was set up to be 0.3 mm off the wheel. Therefore, the distance between the slit nozzle and

the wheel was 0.3 mm when the melt was injected during the melt spinning process. 3 grams of Mg-base materials sit in the position fully surrounded by the 5kW coil, which results in a better induction heating and alloying process.

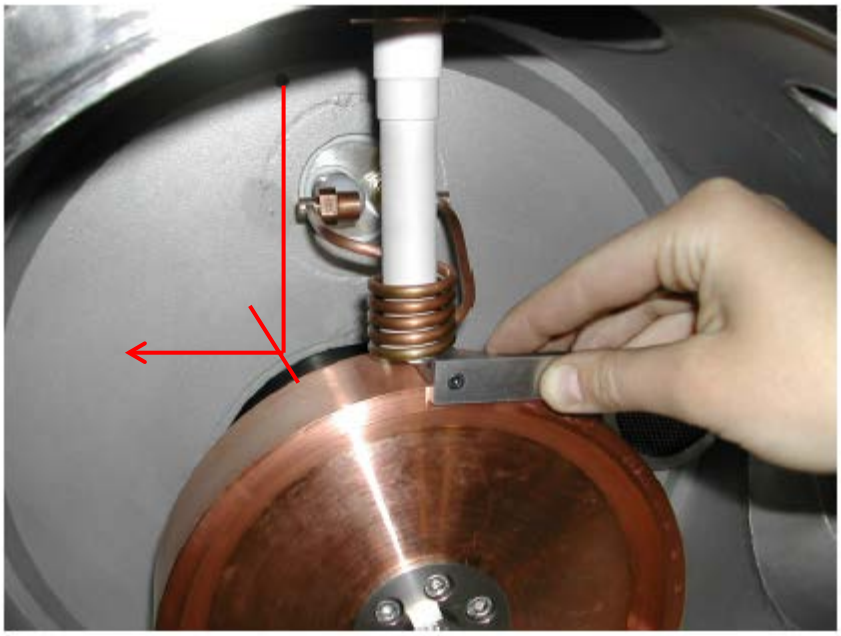

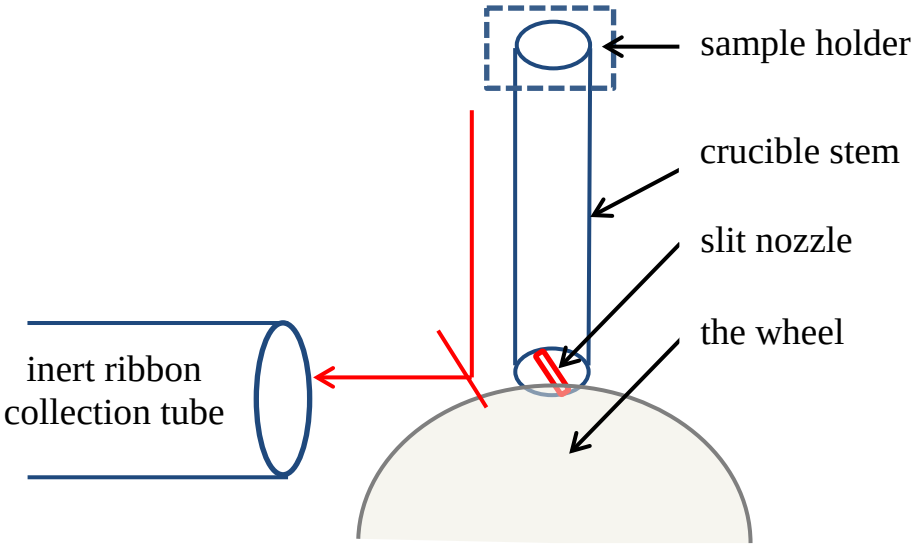

Figure 5-4 Attaching the BN crucible to the crucible holder inside the melt spinner.

Small pieces of compact samples were prepared and loaded into the inert loader in a glove box. The pieces were roughly round in shape with a maximum diameter of 6 mm

because of the dimensions of the inert loader of the melt spinner. The inert loader was re-mounted back on the melt spinner with the gate valve closed. After the main chamber was rinsed several times with argon gas, the gate valve of the inert loader was opened, and the materials were slipped down to the BN crucible. The chamber was then evacuated to a high vacuum of approx. 10^{-6} mbar. The evacuation goes through two steps, initially pumped to ~10^{-2} mbar by a rotary pump, and then to ~10^{-6} mbar by a turbo pump. The chamber was evacuated for two days to produce this high vacuum, and then filled with argon gas for the process of the induction heating and the subsequent melt spinning.

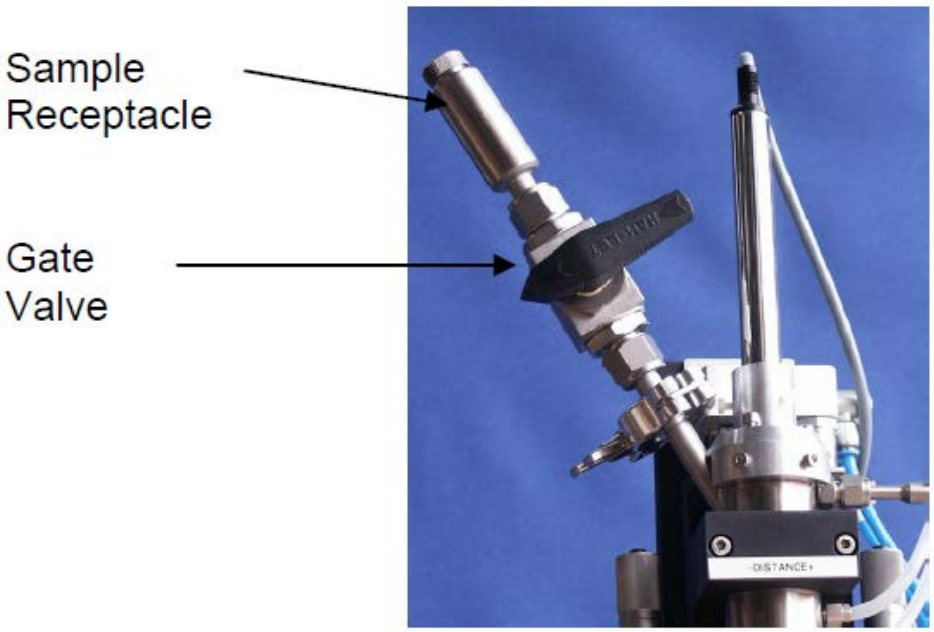

Figure 5-5 The inert loader on the melt spinner.

A pyrometer with a working temperature from 600 °C to 2500 °C was used to measure the temperature of the melt prior to the injection for melt spinning. The pyrometer often failed to reveal the temperature reading in the middle of melt spinning due to the vapour given off by the subliming Mg during induction melting. To minimize the Mg sublimation

effect, many melt spinning trials have been applied, and eventually a heating profile evolved with a prolonged preheating treatment followed by a quick heat-up to the melt-spin temperature. The heating profile varied for the different samples, and the general principle is that a prolonged preheating results in improved diffusion of the starting elements, and the quick heat-up minimizes the side effect of the Mg sublimation.

The configuration of the melt-spinner employed in this work is as follows:

- spacing between the nozzle and wheel is 0.3 mm;
- the wheel rotating speed is 2400 rmp with a surface velocity of 25 $m \cdot s^{-1}$;
- the injection temperature assumed to be 50 °C higher than the melting point (or when the sample glows if temperature measurement is not available);
- the injection overpressure is 200 mbar, with 800 ~ 1000 mbar of argon gas in the main chamber.

All the materials were melt-spun under these conditions.

Approx. 8 ~ 10 mm wide ribbons were produced and spun into the collection tube. The tube was then sealed and transferred into the glove box. The solidified ribbons were collected fully inertly with the modifications of the inert loader and the inert collection tube on the melt spinner. Therefore, reactive materials, such as magnesium, can be processed while avoiding the oxidation issue.

5.2.4. Cryo-milling

The hydrogen sorption measurements require the samples to be in powder form. For Mg, room temperature pulverization is not possible due to its ductility. Mechanical milling therefore needs to take place below the brittle to ductile transition temperature of -180°C (Gandhi and Ashby, 1979). It is possible therefore, to mechanically mill at cryogenic, liquid nitrogen, temperatures.

Melt-spun ribbons were milled under liquid nitrogen with a cryo-mill (*SPEX SamplePrep Freezer Mill*) for a short period. By doing this, the microstructure of samples in the as-quenched state could be maintained without the potential phase transformation caused by milling process. The detailed process of cryo-milling is given below:

- Pre-cooling: 5 min
- Milling: 5min each cycle, and 3 cycle in total
- Rest: 3 min between each cycle.

The melt-spun materials were milled usually for two cycles as described above in liquid nitrogen. The milled powders were then collected in a glove box.

5.3. Structural Characterization

The structural characterizations were performed using a combination of X-ray Diffraction (XRD) and scanning electron microscopy (SEM). The thermal stability of the samples has been investigated using TGA and DSC.

5.3.1. X-Ray Diffraction

Diffraction of X-rays by crystalline materials leads to characteristic diffraction patterns that allows the structure and possibly the composition of a compound or mixture to be determined. Diffraction occurs when parallel beams of monochromatic X-rays interact with an ordered solid, this process can be described by the Bragg's Law.

$$2d \cdot \sin\theta = n\lambda$$

where d is the planar spacing, θ is the angle of incidence of diffraction, n is an integer and λ is the wavelength of X-ray. Figure 5-6 shows the array of crystal lattice with a interplanar spacing, d.

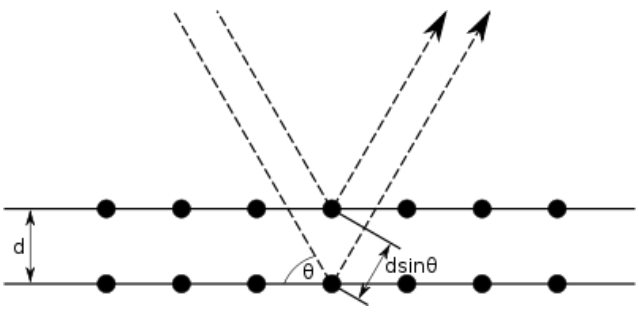

Figure 5-6 X-ray diffraction by a crystal.

A *Bruker D8 Advanced Diffractometer* using CuKα radiation (λ = 1.54056 Å) was used to assess the crystal structure of the melt-spun ribbons and powders. Samples were loaded inertly into a dome-shaped airtight sample holder for room temperature XRD measurement in order to prevent sample oxidation in air.

The diffractometer is able to be modified with a high temperature pressure cell (*Anton Parr XRK900*) under H_2 or He gas, which was employed usually for in-situ X-ray diffraction studies. The in-situ pattern was recorded isothermally, scanning at a particular temperature before heating to the next one. This can be employed to investigate the crystallization behaviour of hydriding or dehydriding of the storage materials. Both powder samples and the ribbons have been examined on the X-ray diffractometer. Powder sample are composed of a very large number of crystallites orientated in a very large number of directions. For the ribbon samples on the other hand, there are possible preferred orientations.

Several databases of the indexed XRD patterns of solids has been established as an XRD analysis reference. In this work, the PDF-2 database by ICDD has been used as a reference. Table 5-2 gives all the references which have been employed to identify the phases recorded in this thesis. For a quantitative analysis, the XRD patterns have been investigated by means of the Rietveld refinement method using the *TOPAS Academic* software package. The Rietveld data can also provide the weight fraction for each phase and also the calculated grain size.

Phase	Lattice type	Reference article
Mg (α-Mg)	Hexagonal	(Malka et al., 2011)
Mg_2Ni	Hexagonal	(Zhang et al., 2009a)
$MgNi_2$	Hexagonal	(Komura and Tokunaga, 1980)
Mg_6Ni	Cubic	(Teresiak et al., 2009b)
MgO	Cubic	(Tsirelson et al., 1998)
α-MgH_2(β-MgH_2)	Tetragonal	(Moser et al., 2009)
γ-MgH_2	Orthorhombic	(Moriwaki et al., 2006)
Mg_2NiH_4 (HT-Mg_2NiH_4)	Cubic	(Zhang et al., 2009a)
$Mg_2NiH_{0.3}$	Cubic	(Noréus and Werner, 1982)
LT-Mg_2NiH_4	Monoclinic	(Zhang et al., 2009a)
Ni	Cubic	(Taylor, 1950)
Ti (β-Ti)	Cubic	(Häglund et al., 1993)
Al_2O_3	Hexagonal	(Ballirano and Caminiti, 2001)

Table 5-2 Reference articles of the crystallographic information source.

The grain size was also calculated using the Scherrer equation. The Scherrer equation is a well known equation which enables a calculation of the grain size of a crystalline material using X-ray diffraction. The Scherrer equation is based on the effect of grain size on peak broadening, and the grain size is calculated using the full width of half maximum values for a number of peaks (FWHM). In the Scherrer equation,

$$\tau = \frac{K\lambda}{\beta\cos\theta}$$

where τ is the average grain size, K is the shape factor which is usually taken as 0.9 for powder sample, λ X-ray wavelength, β the full width of half maximum intensity (FWHM) of a particular peak and θ the Bragg angle.

The Scherrer equation applies especially well for nano-materials, such as the melt-spun samples studied in the present work. The broadening is only manifest for grain size less than 100 nm.

5.3.2. Scanning Electron Microscopy

A scanning electron microscope (*JEOL 6060*) was used in both the Back Scattering Imaging (BSI) and Secondary Electron Imaging (SEI) modes to characterise the morphology and homogeneity of the ribbons and the starting alloys. Energy Dispersive Spectrometry (EDS) analysis has also been conducted to measure the composition of the samples using *INCA Oxford* which is attached to the SEM.

Both melt spun ribbons and the remnants after melt spinning have been mounted and polished for the SEM observation. The melted samples have been sectioned by a cutting machine (*LECO VC-50 Saw*), and mounted in conducting Bakelite. The melt-spun ribbons were also mounted vertically in conducting Bakelite. The samples were then ground by SiC paper with 100,200,400 and 800 grit, followed by mechanical polishing with 6μm, 1μm and 0.25μm diamond suspension on a *Buehler MetaServ® Grinder-Polisher*.

5.3.3. Thermal Gravimetric Analysis

Thermogravimetric analysis (TGA) was conducted on the Mg samples to detect the weight changes that occur during heating. A *Netzsch TG209* was used for a temperature range up to 1000 °C with a heating rate of 2°C/min. The sample was loaded in an alumina crucible in a TGA, under an argon atmosphere, so the weight loss can be ascribed to the

sublimation of Mg material. This gives the sublimation temperature of Mg which explains the composition change which can occur during the synthesis of the alloys.

5.3.4. Differential Scanning Calorimetry

Differential scanning calorimetry (DSC) has also been used for phase analysis. DSC provides the subtle temperature difference between the sample and a reference material, during heating and cooling. The difference of the temperature represents exothermic or endothermic reaction, which could normally be crystallization, phase transformation and transitions.

A *Netzsch DSC204HP* has been employed in this work. The samples have been heated in an argon or hydrogen atmosphere from 30 °C to 450 °C with a heating rate of 2 °C/min with a gas flowing rate of 100 ml/min. A 5 ~ 15 mg sample was loaded in an aluminium pan and placed with a reference pan in the heating pot.

5.4. Hydrogen Sorption Measurements

5.4.1. Thermogravimetric Analysis (IGA)

The hydrogen sorption kinetics of the melt-spun products has been investigated by a thermogravimetric analyzer called an *Intelligent Gravimetric Analyser* (IGA) manufactured by *Hiden Isochema Ltd*. It has a micro-balance connected to a sample holder on one side and a counter weight on the other side (Figure 5-7). The mass was converted from a voltage change caused by the deflection of the balance.

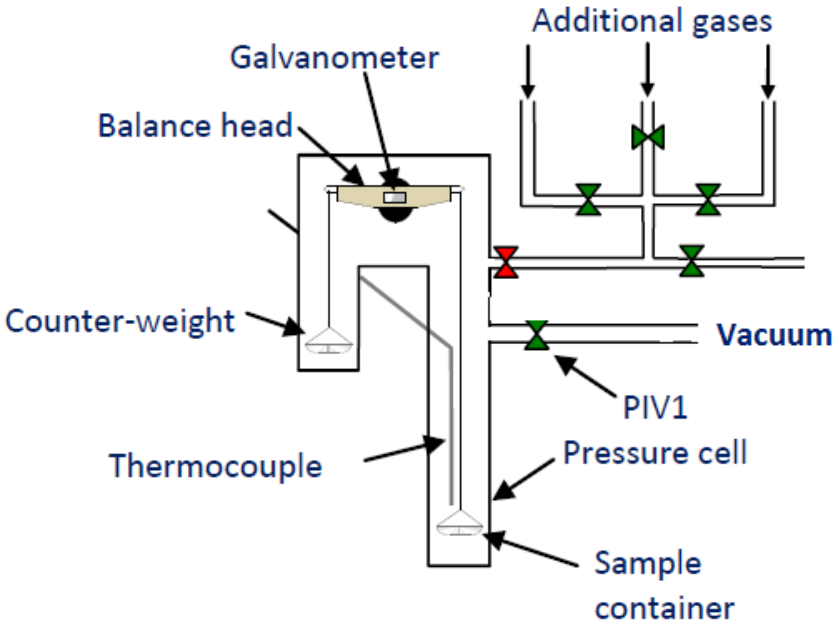

Figure 5-7 Schematic of the thermogravimetric apparatus of Hiden Isochema IGA.

Approximately 100 mg of sample could be loaded in a stainless steel holder which is hooked on the microbalance with a long term stability of ±1 μg. The process of using the IGA, from loading to unloading, is fully under an argon atmosphere to avoid any contact with air. The IGA records the weight change of the sample as a function of time temperature and pressure, thus the sorption kinetics could be investigated.

The pressure cell of the IGA can hold the pressure up to 20 bar, and the pressure barometer has a resolution error of 0.02% of the pressure range. In this project, 10 bar of H_2 pressure with a gas flowing rate of 100 ml/min was applied for the hydriding runs, and for the dehydriding measurements; a high vacuum (~10^{-6} mbar) was achieved with a turbo pump. The IGA system records real-time kinetics which plots pressure, temperature and mass versus time. The temperature was controlled by a thermocouple, and was set to be a fixed value. Both room temperature and high temperature measurement at 300°C have been carried out, and the heating rate to the high temperature was 5K/min.

5.4.2. Thermovolumetric Analysis (HTP)

A *Hiden Isochima HTP S-2* volumetric system is a Sieverts-type apparatus and has been employed to produce Pressure-Composition Isotherms (PCI curves). This is a common method to determine hydrogen concentration and the hydrogen storage properties of a material. The apparatus has a gas dose as a reservoir connected to a sample reactor, and it records the pressure change to determine the gas concentration. The temperature was controlled by a thermocouple in the reactor with water cooling.

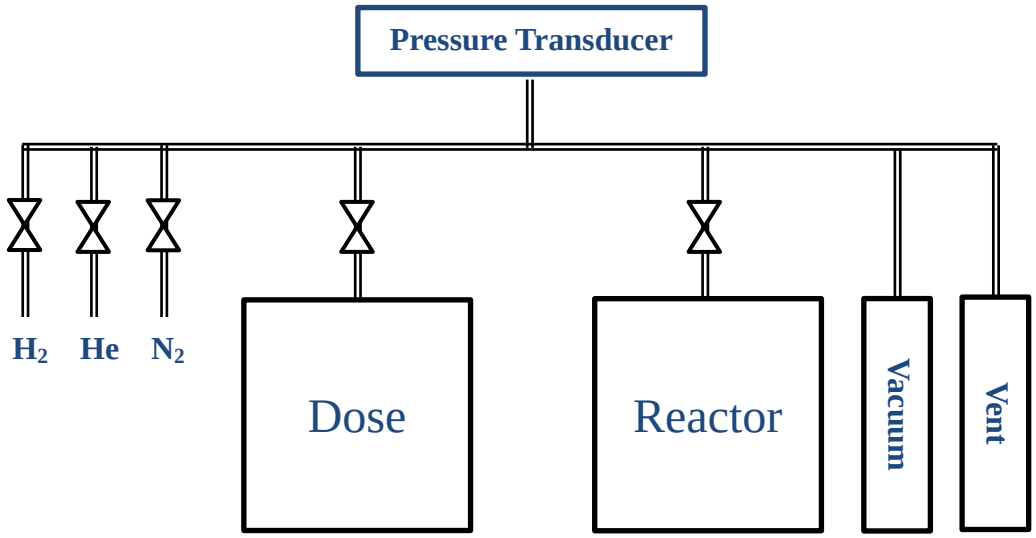

Figure 5-8 Scheme of Sieverts-type apparatus of Hiden Isocheme HTP.

The Sieverts-type apparatus is based on the ideal gas equation:

$$PV = nRT$$

where P is the gas pressure, V the gas volume, n for number of moles of gas, R the universal gas constant and T the absolute temperature.

The apparatus can measure the pressure change during hydriding or dehydriding. By applying the idea gas equation, the starting pressure is P_1 and the starting point of the reaction can be described as:

$$P_1 V = nRT$$

After absorption or desorption, the pressure is changed to P_2, thus we have:

$$P_2 V = nRT$$

Therefore, the absorbed (or desorbed) moles of H_2 Δn can be obtained:

$$\Delta n = n_2 - n_1 = \frac{P_2 V}{RT} - \frac{P_1 V}{RT} = \Delta P \frac{V}{RT}$$

The sample volume was measured prior to the sorption measurements. It is calculated using the same method based on the pressure drop. The dose chamber has roughly the same volume of the reactor chamber, and 5 bar of He gas was introduced into the dose chamber after a system evacuation. Gas was then allowed to flow into the reactor, leading to a pressure drop. Thus the sample volume can be obtained according to the pressure drop.

The absorption and desorption processes were performed isothermally with the gas uptake at numerous pressure. The sample was loaded on the HTP under 10 bar H_2 pressure at a heating temperature range from 250 °C to 375 °C with a heating rate of 5 °C per minute. PCI curves usually exhibit a series of pressure plateaux at different temperatures which can be used to calculate the enthalpy of formation / decomposition of the hydride by using the van't Hoff equation (see page 90).

6. Results and Discussions – Preliminary melt-spinning trials and the melt-spun Mg

This chapter describes the initial experimental trials. It begins with preliminary melt-spinning tests with a FeNiB alloy and a Mg-Cu-based alloy which is a well-known glass forming materials. Subsequently, an initial Mg melt-spinning trial was performed.

6.1. Preliminary Melt spinning Tests

6.1.1. Melt-spun $Fe_{40}Ni_{40}B_{20}$

Since the melt spinner was a newly developed, bespoke piece of equipment, in the *Hydrogen Materials Group*, several test runs were performed on a standard testing material provided by *Edmund Buhler*.

The material used for this work was an alloy, $Fe_{40}Ni_{40}B_{20}$, provided by the melt spinner company for a standard melt spinning test. $Fe_{40}Ni_{40}B_{20}$ is a well know metallic glass forming material (Wei and Cantor, 1989), Tkatch *et al.* (2002) investigated a similar alloy

for their melt-spinning theory studies. The sample was heated to and melt-spun at 1300 °C, and semi-continuous melt spun ribbons were produced and collected (see Figure 6-1).

Four test runs were conducted using this material for the melt-spinning operation exercise and the test running of the equipment of melt spinner. Subsequently, the melt-spun ribbons were produced. The melt-spinning experiments then moved to the Mg-based alloys without any characterization of the melt-spun $Fe_{40}Ni_{40}B_{20}$.

Figure 6-1 The as-received melt-spun $Fe_{40}Ni_{40}B_{20}$ ribbons.

6.1.2. Melt-spun $Mg_{60}Cu_{20}Zn_{20}$

After the practice of melt spinning of the alloy $Fe_{40}Ni_{40}B_{20,}$ the next step was to try to melt-spin Mg-base alloys. This exercise started with a $Mg_{60}Cu_{20}Zn_{20}$ alloy provided by *Dr. Isaac Chang (University of Birmingham)* who used it in this metallic glass materials research. This material was known to form a metallic glass but contained less magnesium than the target alloys in the project.

Due to high reactivity of Mg in air, the Mg-based alloys required inert loading or/and unloading. To achieve that, the $Mg_{60}Cu_{20}Zn_{20}$ sample was loaded into the inert loader of the melt-spinner inside an argon glovebox, and the melt-spun ribbons were also collected inertly in the collection tube of the melt-spinner (see Figure 5-2). The melting point of this alloy was around 600 °C, which was much lower than the minimum working temperature (900 °C) of the original pyrometer attached to the melt-spinner. Therefore, the original pyrometer was replaced with a detector with a lower temperature range. While waiting for the replacement pyrometer, a glowing filament pyrometer camera was employed temporarily for the melt-spinning of the $Mg_{60}Cu_{20}Zn_{20}$ alloy.

The $Mg_{60}Cu_{20}Zn_{20}$ alloy was melt-spun successfully at around 650 °C under an argon atmosphere of 800 mbar pressure. The composition and surface condition of the as-quenched ribbons were investigated by SEM and XRD.

6.1.2.1. SEM of the melt-spun $Mg_{60}Cu_{20}Zn_{20}$

SEM with energy dispersive spectrometry (EDS) was performed on the melt-spun ribbons of $Mg_{60}Cu_{20}Zn_{20}$. The back scattered image (BSI) shows a uniform homogeneity of composition of the melt-spun ribbons, with a few Zn-rich black areas as shown in spectrum 1 in Figure 6-2.

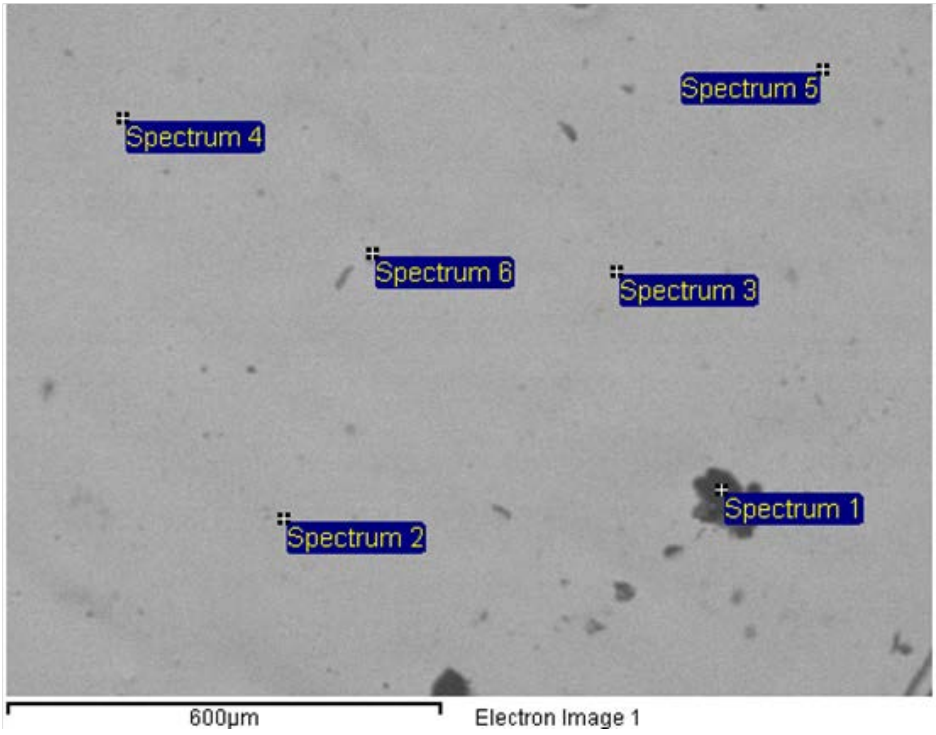

Spectrum	Mg	Cu	Zn
Spectrum 1	71.74	5.98	22.28
Spectrum 2	69.45	18.84	11.71
Spectrum 3	70.27	18.19	11.54
Spectrum 4	69.13	19.03	11.85
Spectrum 5	68.62	19.29	12.09
Spectrum 6	70.86	17.45	11.69
Max.	71.74	19.29	22.28
Min.	68.62	5.98	11.54

* All results in atomic%

Figure 6-2 SEM back scattered image of melt-spun ribbon of $Mg_{60}Cu_{20}Zn_{20}$ with the table of EDS results of the selected areas.

6.1.2.2. XRD result of the melt-spun $Mg_{60}Cu_{20}Zn_{20}$

XRD of the melt-spun ribbons of $Mg_{60}Cu_{20}Zn_{20}$ was performed at room temperature in an inert atmosphere using a dome-shaped crucible loaded inside a glovebox. The holder was spun throughout the X-ray scanning in order to eliminate any effect of preferential orientation of the melt-spun ribbons.

The XRD trace exhibited a broad background between 35° and 45° together with a few relatively sharp peaks. This suggested that the material is comprised of both amorphous and crystalline phases. At this stage, no further analysis was carried out (*e.g.* lattice parameter measurements) as this material was simply used to test the efficiency of the equipment using a relatively high Mg content material which was known to form an amorphous phase during strip casting.

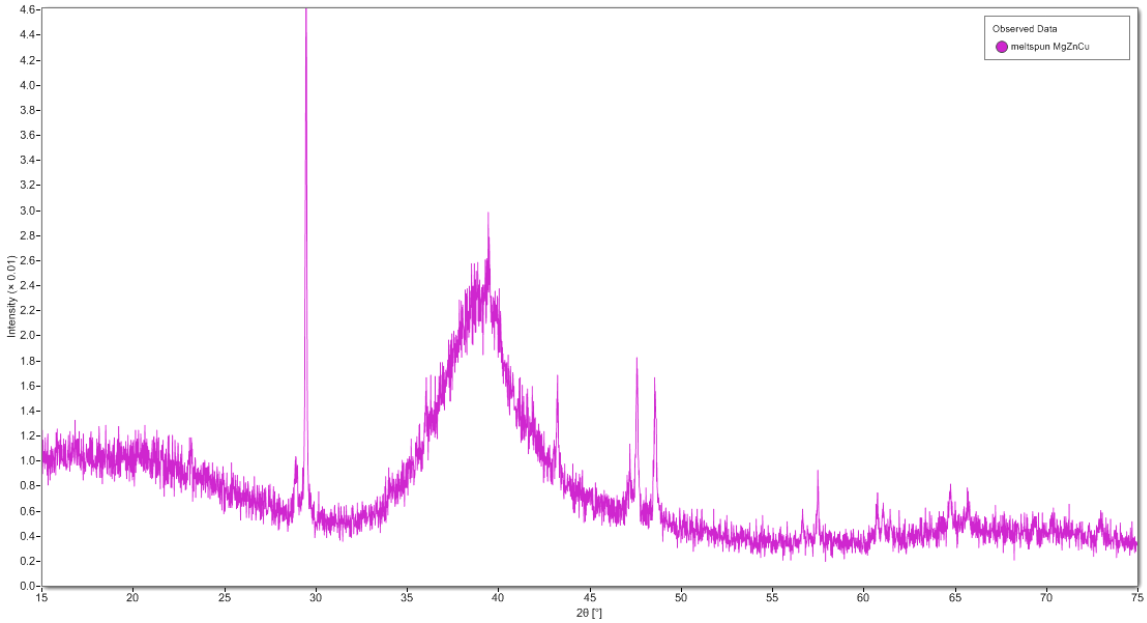

Figure 6-3 XRD pattern of the melt-spun $Mg_{60}Cu_{20}Zn_{20}$.

6.2. Melt-spun Mg

Prior to the melt spinning of the Mg-Ni alloys, melt spinning of pure magnesium was attempted as a reference material. Moreover, it is easier to melt-spin Mg than a binary Mg-Ni alloy such as $Mg_{90}Ni_{10}$ as it has a lower melting point. Therefore this provided a good test sample prior to the study of the more difficult Mg-Ni alloys.

6.2.1. Melt spinning

4 grams of magnesium granules (*SIGMA-ALDRICH*) were loaded into the boron nitride crucible on the melt spinner and processed using the conditions outlined in the experimental section. A new pyrometer was employed in this work, with a temperature range of 600 °C to 2500 °C. The melting point of magnesium is 650 °C, so the material was super-heated to around 700 °C. At 700 °C the Mg could be observed to be glowing orange. The sample was held at this temperature for 10 sec and then ejected in argon using an overpressure of 200 mbar. Semi-continuous melt-spun ribbons were produced (see Figure 6-4). Some of the ribbons stayed in the main body of the chamber and therefore subsequently had to be exposed to air when removed. However, most of the material was collected from the inert collection tube and appeared to be around 5 mm in width with some very thin wire-like material entrained within. The Mg ribbons were transferred into an argon glove box as showed in Figure 6-4.

Figure 6-4 Melt-spun Mg ribbons collected from the inert collection tube inside an argon glove box

6.2.2. XRD of the melt-spun Mg ribbons

For the X-ray diffractometry the melt-spun Mg ribbons were placed in a sample holder. For XRD studies, Friedlmeier *et al* (1999) used silicone grease to fix melt-spun ribbons on a glass sample holder. In the present work, the ribbons were fixed using plasticine. As expected, the XRD pattern (Figure 6-5) shows the presence of Mg, and the peaks appeared to be relatively sharp thus indicating that it is not a nano-scale microstructure.

The XRD pattern shows clearly the Mg phase, but with slightly smaller lattice parameters of a=3.1957 ± 0.0004 Å and c=5.1901 ± 0.0010 Å. The peaks in the pattern exhibited a small amount of broadening. *TOPAS Academic* was used to determine the lattice parameters and the grain size which was calculated to be approx. 10 µm.

Before determining the hydrogen storage properties, the melt-spun material was cryo-milled into a powder sample to facilitate the hydriding / dehydrding reaction. The melt-spun ribbons were pulverized using a cryo-mill, as Mg is ductile at room temperature and therefore it would simply smear using a conventional roller or planetary ball mills. This might significantly alter the microstructure of the materials. To check this, XRD was performed on the as-milled melt-spun Mg, which is shown in Figure 6-6. The XRD pattern exhibited peaks with the same positions as the non-milled material with lattice parameters of a = 3.20945 ± 0.00049 Å and c = 5.21185 ± 0.00088 Å. The calculated grain size was also shown to be 10 μm by means of the *TOPAS Academic* programme. Therefore, it was concluded that the cryo-milling did not cause significant microstructural changes in the material.

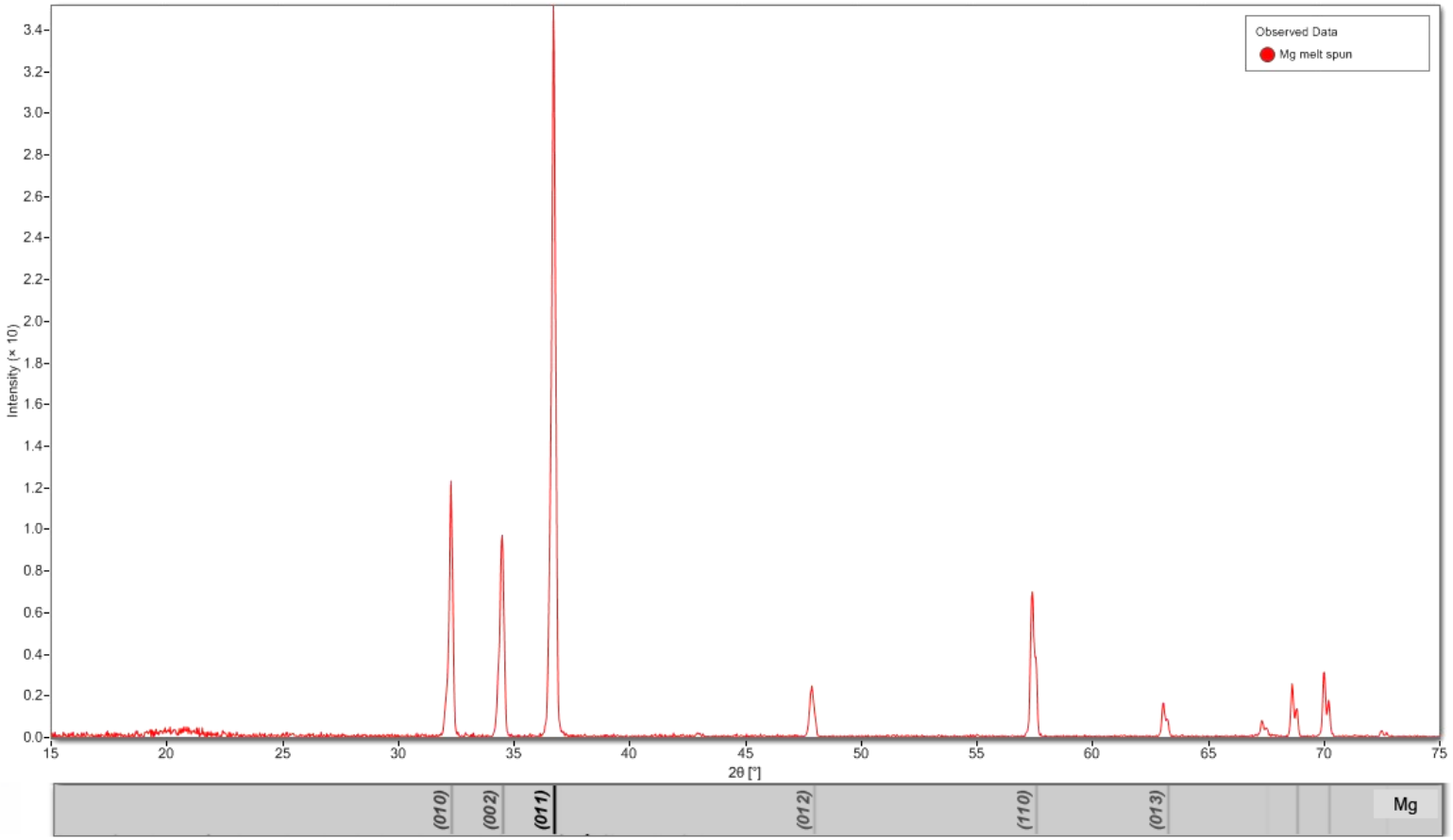

Figure 6-5 XRD pattern of the melt-spun Mg ribbons.

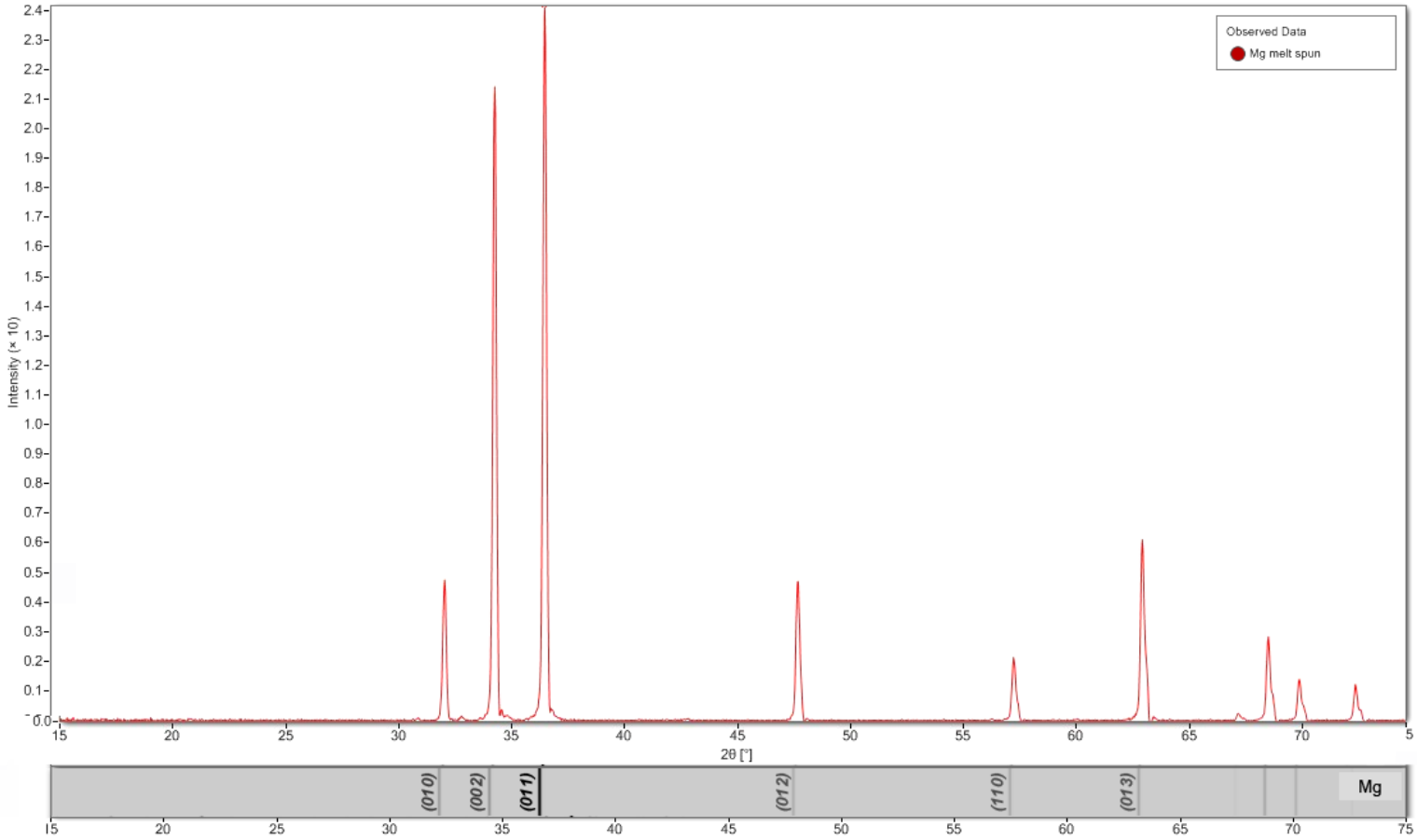

Figure 6-6 XRD pattern of the melt-spun Mg cryo-milled powder.

6.2.3. DSC of the as-received Mg and the melt-spun Mg

Diffzerential scanning calorimetry (DSC) was performed on both the as-received Mg (commercial sample) and the melt-spun Mg ribbons. The samples were heated to 450 °C under both 4 bars of argon and 10 bars of H_2 with a heating rate of 2 °C/min.

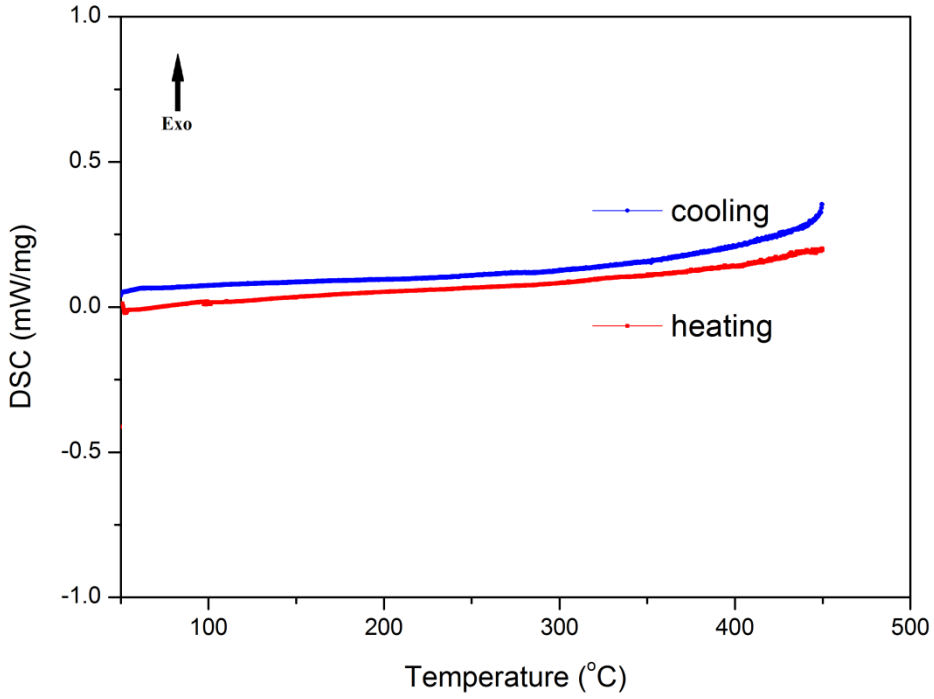

Figure 6-7 DSC of the as-received Mg heated at 2 °C/min under 4 bars of argon.

Figure 6-7 shows the DSC result of as-received Mg granules under 4 bars of Ar gas. No endothermic or exothermic reactions were observed during both the heating and cooling processes.

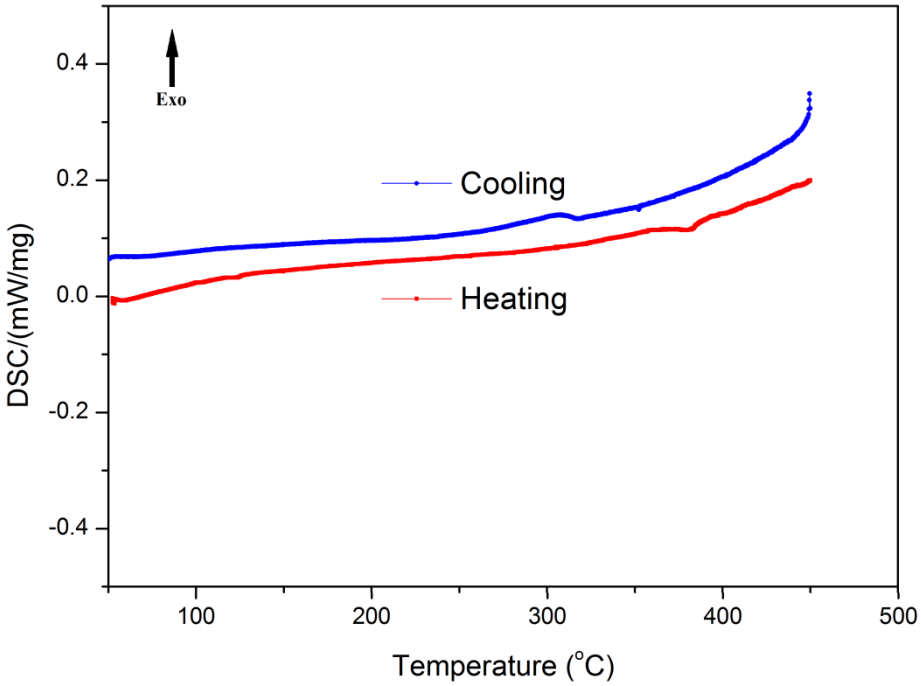

Figure 6-8 DSC of the melt-spun Mg ribbons heated at 2 °C/min under 4 bars of argon.

Figure 6-8 shows the DSC trace of the melt-spun Mg, which is the same as that of the as-received Mg sample shown in Figure 6-7. The DSC trace for the melt-spun Mg did not exhibit an exothermic re-crystallization peak during heating, which was in accordance with the XRD result shown in Figure 6-6, where sharp peaks were observed, representative of a fully crystalline material.

Figure 6-9 shows the DSC profile of the as-received Mg under 10 bars of H_2 gas for three cycles. It has been reported that a three-cycle thermal treatment could act as an activation treatment for the melt-spun Mg-based materials used in hydrogen storage research (Tanaka et al., 1999; Kalinichenka et al., 2009). Endothermic peaks can be observed during the second heating profile, with a peak temperature of ~400 °C and an onset

temperature of ~390 °C. All three cooling profiles exhibit exothermic peaks with peak temperatures of ~335 °C and an onset temperature range of 300 ~310 °C.

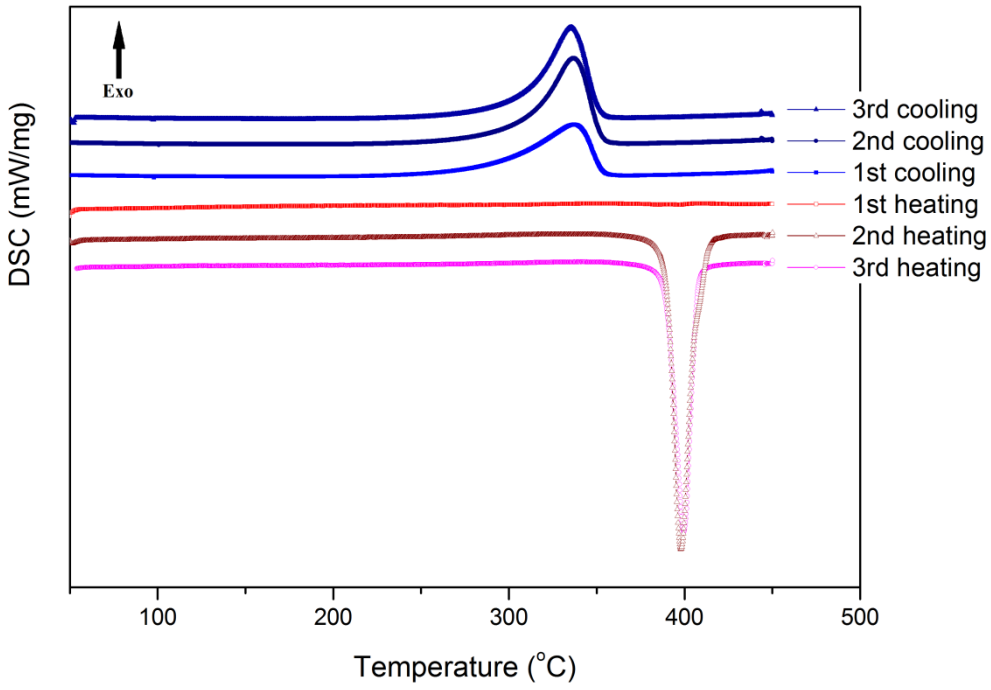

	Area	Peak Temp.	Onset Temp.	End Temp.
Heating 1	N/A	N/A	N/A	N/A
Heating 2	-1583 J/g	399.7 °C	389.2 °C	407.3 °C
Heating 3	-2026 J/g	398.0 °C	389.8 °C	407.4 °C
Cooling1	1139 J/g	336.9 °C	296.4 °C	351.9 °C
Cooling 2	1496 J/g	336.8 °C	308.7 °C	351.3 °C
Cooling 3	1570 J/g	335.4 °C	307.5 °C	351.8 °C

Figure 6-9 DSC of the as-received Mg heated at 2 °C/min under 10 bars of H_2.

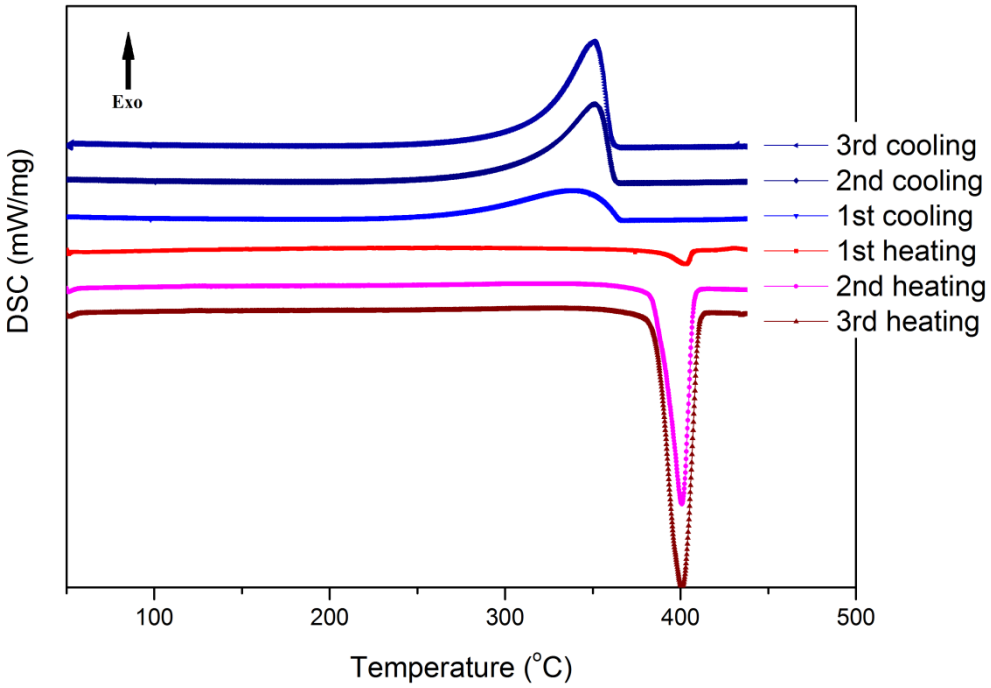

	Area	Peak Temp.	Onset Temp.	End Temp.
Heating 1	-53.83 J/g	403.1 °C	389.0 °C	406.8 °C
Heating 2	-737.5 J/g	400.8 °C	387.5 °C	407.3 °C
Heating 3	-1133 J/g	400.8 °C	386.6 °C	410.1 °C
Cooling 1	491.6 J/g	338.3 °C	281.9 °C	347.8 °C
Cooling 2	811.9 J/g	351.2 °C	308.7 °C	362.0 °C
Cooling 3	958.0 J/g	350.4 °C	310.5 °C	360.9 °C

Figure 6-10 DSC of the melt-spun Mg ribbons heated at 2 °C/min under 10 bars of H_2.

Figure 6-10 shows a similar DSC profile for the melt-spun Mg. The endothermic peaks during heating exhibit a peak temperature of ~400 °C and an onset temperature of ~390 °C, whereas the exothermic peaks during cooling are at ~350 °C with an onset temperature of ~300 °C.

It was interesting to note that, an endothermic peak could be observed on the first heating cycle for the melt spun ribbon sample. Under 10 bar H_2 atmosphere, on the first heating, the magnesium became a hydride and converted back to the pure magnesium at a high temperature ~400 °C, according to the following reactions:

$$Mg + H_2 \rightarrow MgH_2$$
$$MgH_2 \rightarrow Mg + H_2$$

On the subsequent cooling, the dehydrided magnesium hydrided again, and then dehydrided in the same way on heating, and were manifested as the exothermic hydriding peaks on the cooling profiles and the endothermic dehydriding peaks on the heating profiles.

Comparing the DSC results of the as-received Mg and those of the melt spun Mg ribbons, the hydriding / dehydriding behaviour is very similar which would indicate that the melt spinning process does not significantly alter the microstructure of the material. It is however interesting to note that the melt spun magnesium ribbons appear to be more active in hydrogen than the granular material. Both samples showed more active hydrogen absorption behaviour after sorption cycles, as the hydriding peaks grew with increasing DSC cycles (see Figure 6-9 and Figure 6-10). During the hydrogen sorption cycles, the Mg particles expanded during the hydriding reaction and contracted during dehydriding reaction, which resulted in the particles being cracked and broken and lead to their fragmentation into smaller agglomerates and particles.(Hong et al., 2009). Therefore,

these three cycles of hydrogen sorption were likely to act as an activation process for both the Mg samples, resulting in the change in the peaks in the DSC.

6.2.4. PCI of the melt-spun Mg ribbons

To obtain thermodynamic property information regarding the melt-spun Mg, pressure-composition isotherms (PCI) were determined using a Sievert-type system (*Hiden HTP*). The first trial did not show any hydrogen absorption, and the melt-spun ribbons were loaded directly without any grinding. It was deduced that the surface condition of the melt-spun ribbons needed an additional activation treatment, due possibly to a fine oxidation layer.

Therefore, for the second HTP run, the ribbons were cut into small pieces and ground by a pestle and mortar inside an argon glovebox before loading on the HTP. Hydrogen isotherms were measured at 320 °C, 330 °C, 340 °C and 350 °C under a H_2 atmosphere of up to 30 bar.

The Pressure-Composition Isotherms (PCI) (see Figure 6-11) show the hydrogen absorption and desorption in dashed and solid lines, respectively. The melt-spun Mg had a hydrogen capacity of around 6 wt.% which is lower than the theoretical value of 7.6 wt.%. For all temperatures, a flat equilibrium plateau pressure was observed. The desorption plateau pressures were used to calculate the enthalpy of formation according to the van’t Hoff Equation.

$$ln\, P_{eq} = \frac{\Delta H}{RT} - \frac{\Delta S}{R}$$

Where P_{eq} is the equilibrium plateau pressure, R is the universal gas constant, and T is the isothermal temperature in K.

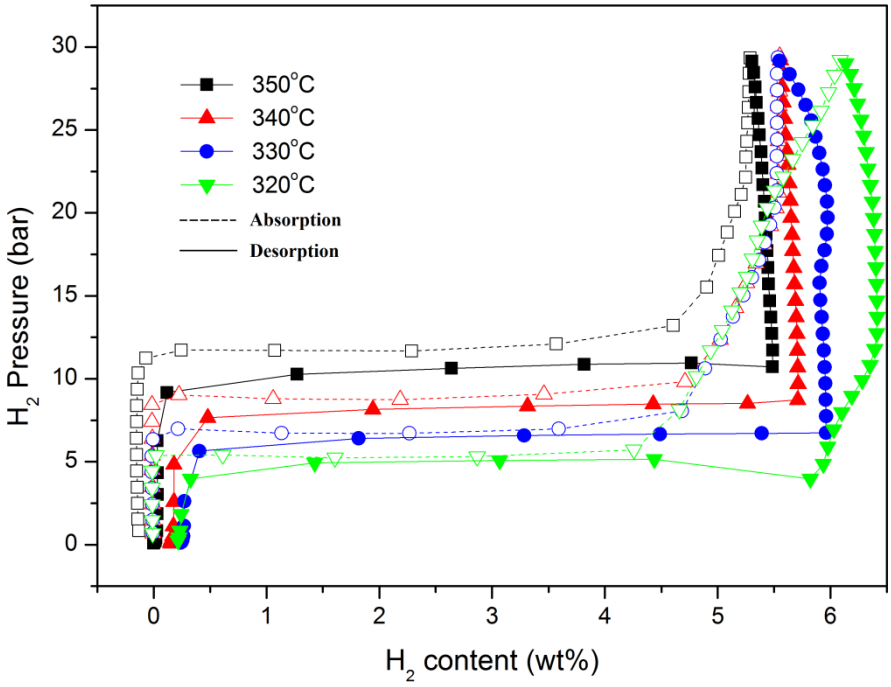

Figure 6-11 Pressure-Composition isotherms of the melt-spun Mg, where solid symbols are the data point of desorption PCI and open ones for the absorptions.

The desorption data of the pressure-temperature isotherms is usually used to calculate the enthalpy and entropy of formation for the hydrides. Figure 6-12 shows the PCI curves for the desorption of the melt-spun Mg.

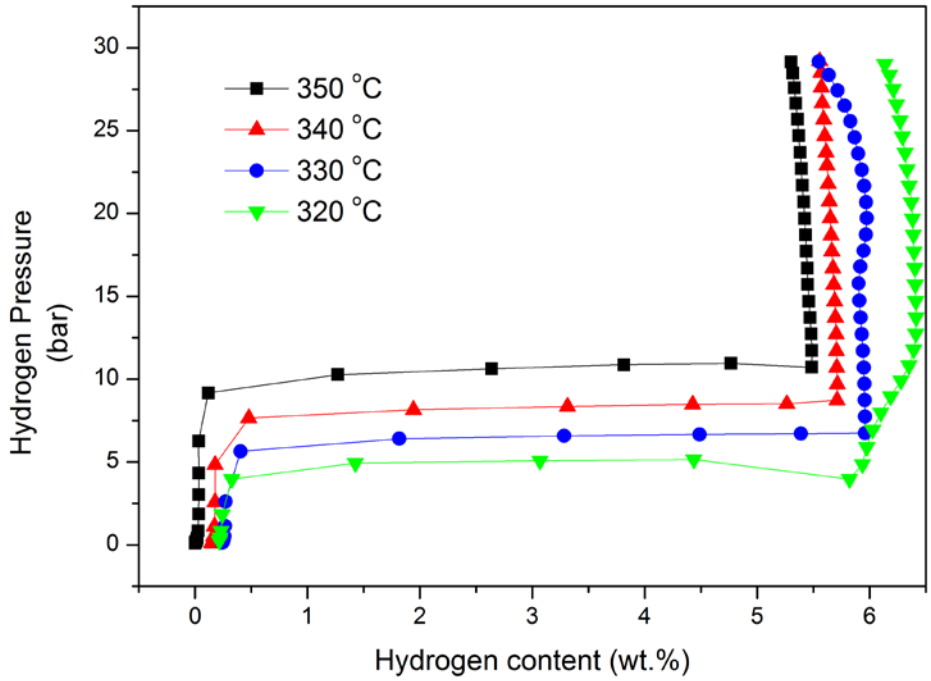

Figure 6-12 Pressure-composition isotherms of the desorptions of the melt-spun Mg.

The value of P_{eq} was taken from the mean value of the data points in the plateau pressure in Figure 6-12. Taking the desorption profile of 350 °C as an example, the plateau pressure was calculated to be 10.69 ± 0.27 bar, which was the best fit result with minimum value of standard deviation. It started with the horizontal linear fit of the middle three points in the plateau region shown in (d) of Figure 6-13. Then the calculated data range extended to 4 or more data points. By comparing the standard deviation value, the best horizontal linear fit can be determined with the minimum SD value, shown in the figures (b) to (d) of Figure 6-13. In figure (d), the data points in red was the data masked off for the linear fit calculation, because they were in the fitting region. Therefore, the P_{eq} of the PCI at 350 °C was taken as the mean value of the fit calculation, with the error value which is the standard deviation. In this thesis, all the P_{eq} values of the PCI results were calculated by the same method.

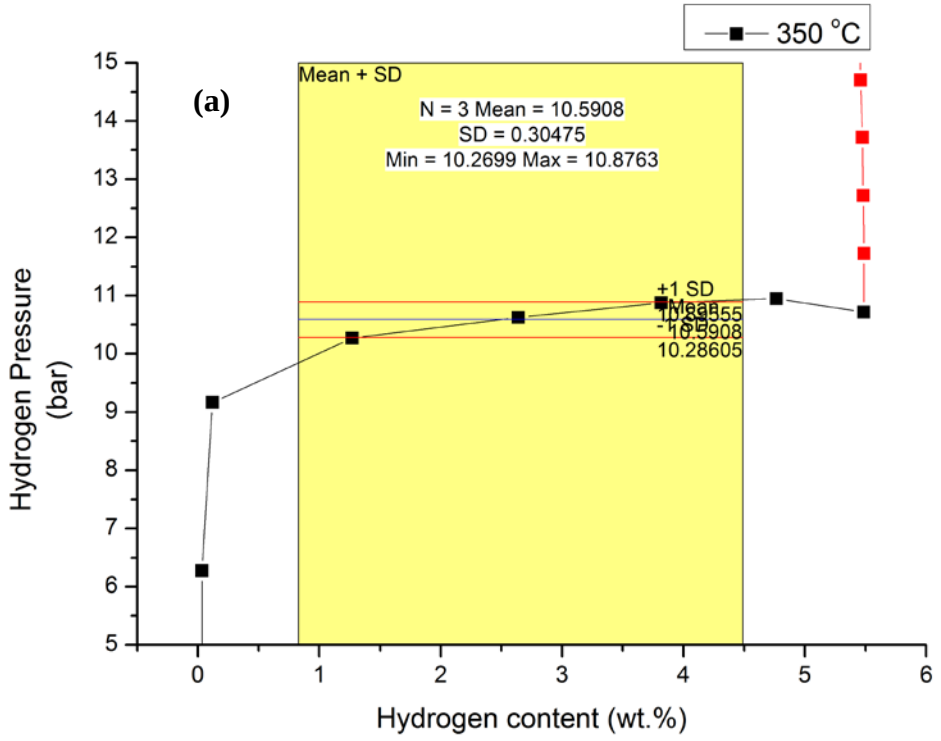

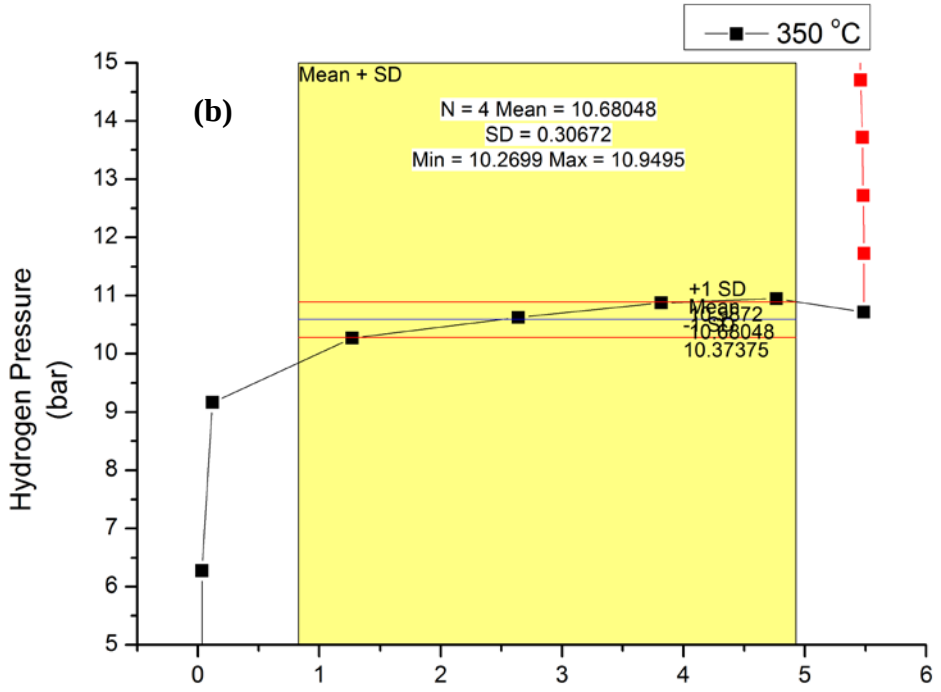

where N for the number of the points calculated in the fit, SD for the standard deviation, blue line for the mean value, rea line for the SD value, the red points for the masked data in the fit calculation.

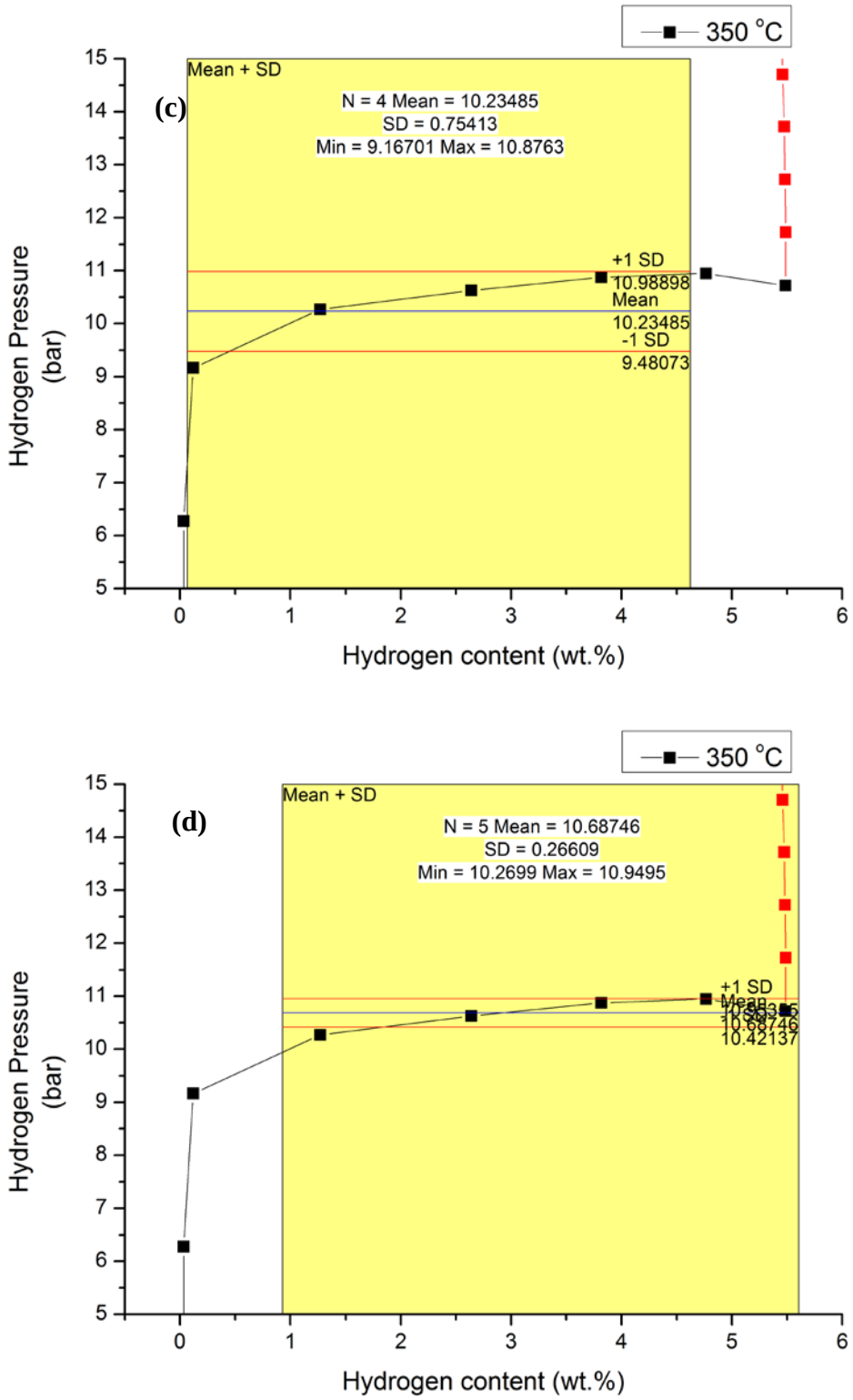

where N for the number of the points calculated in the fit, SD for the standard deviation, blue line for the mean value, rea line for the SD value, the red points for the masked data in the fit calculation.

Figure 6-13 The calculation of pressure plateau in the desorption PCI of melt-spun Mg at 350 °C.

By plotting the value $ln\, P_{eq}$ vs T^{-1}, a linear relationship can be fitted, as shown in Figure 6-14. The enthalpy of formation is determined by the slope of the linear fit, and the entropy by the intercept. The van't Hoff plot showed a good fit with R-value of 0.9996. The enthalpy of formation (ΔH) of MgH_2 was calculated to be -77.03 ± 1.59 kJ·mol$^{-1}H_2$ and entropy (ΔS) of -143.24 ± 2.61 J·K^{-1}mol^{-1}. Stampfer *et al.* (1960) studied the commercial magnesium material by *Dour Chemical Co.* and reported similar values: namely ΔH of MgH_2 of -74.4 ± 0.3 kJ mol$^{-1}H_2$ and ΔS of -135.06 ± 1.9 J·K^{-1}mol^{-1}.

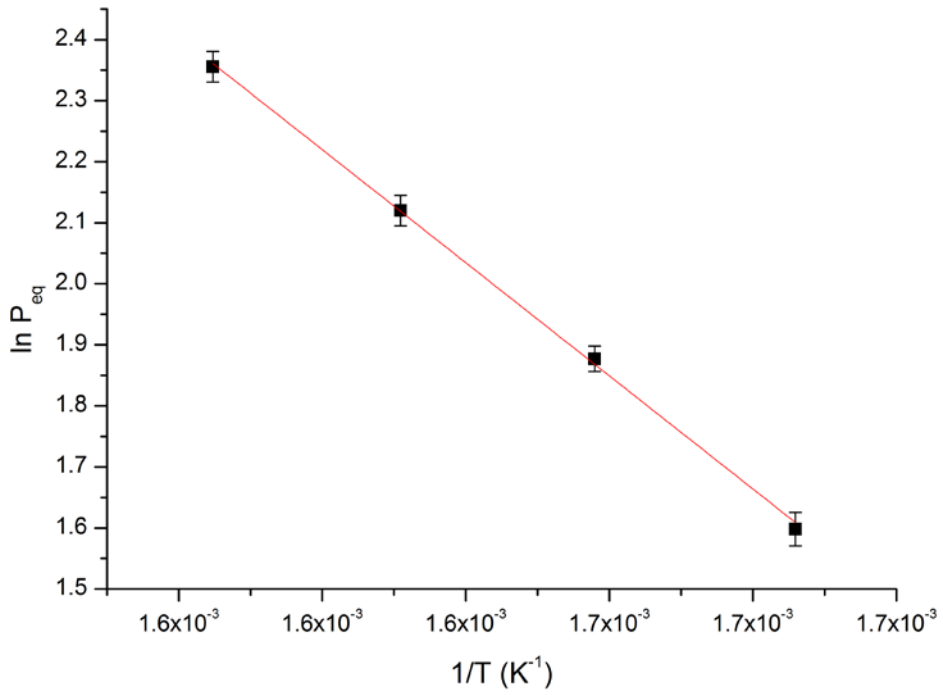

Figure 6-14 Van't Hoff plots of the desorption plateau pressures of the melt-spun Mg.

7. Results and Discussion – Melt-spun pre-cursor Mg-Ni alloys, $Mg_{90}Ni_{10}$ and $Mg_{73}Ni_{27}$

This chapter discusses the melt-spinning trials for Mg-Ni binary alloys. The trials started with the induction melted pre-cursor alloys, and all of them ended with unsuccessful melt-spinning experiments. The failure was examined and analyzed, and was attributed to the method of sample preparation, which was developed and later, changed.

Instead of induction melting, the Mg-Ni mixtures were pressed into pellets using a static press. The pellets were then induction melted once, prior the injection of the melt spinning. As a result, the $Mg_{90}Ni_{10}$ and $Mg_{73}Ni_{27}$ samples were melt-spun successfully, and the melt-spun ribbons exhibited excellent hydrogen storage properties. The characterizations of the melt-spun samples were performed, and, in this chapter the results are discussed in details.

7.1. The induction melted pre-cursor Mg-Ni alloys

After the successful melt-spinning for the Mg-Cu-Zn alloys and pure Mg, the Mg-Ni binary alloys were prepared next in this research timeframe. The aim of this project was to investigate the Mg-Ni alloys with a Mg content as high as 90 at.%. It was intended initially to prepare the Mg-Ni alloys by induction melting. However, magnesium presents a particular problem as its high vapour pressure results in significant losses of Mg even below its melting point.

7.1.1. Induction melted Mg_2Ni with BN coated quartz tubes

It is known that Mg and Ni form two compounds, Mg_2Ni and $MgNi_2$. Since 1968, Mg_2Ni has been investigated as potential hydrogen storage materials, forming Mg_2NiH_4 (Reilly and Wiswall Jr, 1968). Since then, many studies have been carried out on Mg_2Ni-base alloys as hydrogen storage materials, due to relative high storage capacity of 3.6 wt.% H_2 and lower dehydriding temperature (Orimo et al., 1997; Selvam et al., 1988; Spassov and Koster, 1998; Song et al., 2008b; Isogai et al., 2000). Therefore, at the beginning of the present research, the aim was to produce melt-spun Mg_2Ni alloys and then to move on to higher Mg content materials.

Although arc melting is normally used to produce alloys as a pre-preparation treatment for melt spinning, magnesium is not suitable for arc melting due to its high vapour pressure at relatively low temperatures. Therefore, many researchers have used induction melting to alloy Mg-based materials for melt spinning research (Teresiak et al., 2009b; Todorova and Spassov, 2009). As powdered materials do not couple well during induction melting, then magnesium granules and nickel wire were employed (see section 5.1). For a better mixing with the magnesium granules, the nickel wire was cut into small pieces of approx. 2-3 mm long,. Initially quartz tubes were used for the induction melting in accordance with other workers who used quartz tubes as crucibles for melt spinning (Lin et al., 2012a).

During the first few runs, the crucible appeared to react with the Mg-Ni mixtures and cracked at the bottom of the crucible. Therefore, a boron-nitride layer was applied to the inside of the crucible which had been claimed to have been used for the induction melting of Mg-Ni alloys (Bendersky et al., 2011).

An 8 g mixture of magnesium granules and nickel wire was loaded into a glass tube with a boron nitride coating inside. Then the sample tube was placed inside of another glass tube which was sealed under an argon atmosphere at 800 mbar pressure for induction melting.

In an attempt to produce a homogeneous material, the sample was melted 8 times at 3~3.5 kW, and each run held for 2 min and then cooled before the subsequent melting,. During

these runs the quartz tubes stayed intact, and a solid melt was produced. The induction melted Mg_2Ni alloy was assessed using SEM studies of the cross sectioned slugs.

7.1.1.1. SEM & EDS result of the induction melted Mg_2Ni

For SEM observation, cross sections of the induction melted Mg_2Ni slugs were mounted in bakelite and polished. To determine the composition of the melt and the phases in the alloy, back scattered images (BSI) were taken which were analysed further by EDS. The results are shown in Figure 7-1. The melt appeared to contain three phases, with a minority phase comprised of 'needle like' areas which were embedded in the light grey matrix. EDS analysis revealed the phase composition of the three phases (Figure 7-1).

The majority of the material was shown to consist of the Mg_2Ni phase (light grey phase), with a Mg to Ni ratio of 63.15:36.85 equal to $Mg_{1.71}Ni$. It is slightly lower than the starting materials of Mg_2Ni with a ratio of 2:1. The darker boundary area in between the Mg_2Ni phase exhibited the elemental ratio of 87.51:12.49, which is likely to be the Mg-rich component of the eutectic ($Mg_{90}Ni_{10}$ according to the phase diagram Figure 4-1).

Spectrum 1 also showed the presence of Si, thus indicating that contamination was present because of reaction with the quartz glass tube, even with a protective layer of boron nitride. Therefore, the boron nitride coating was shown to be an ineffective barrier layer for these trials. Therefore, pure boron nitride crucibles were used in the remainder of this work.

(a)

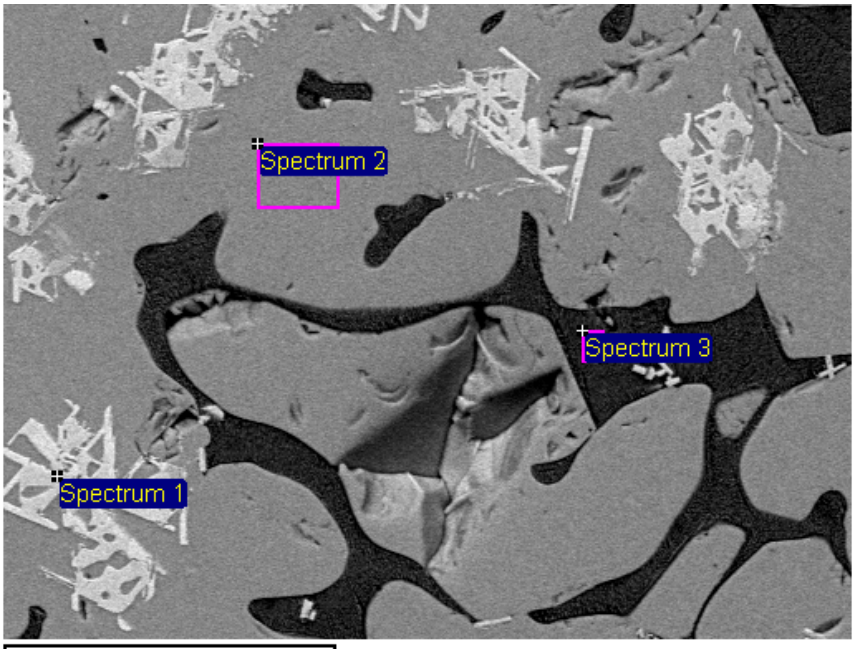

(b)

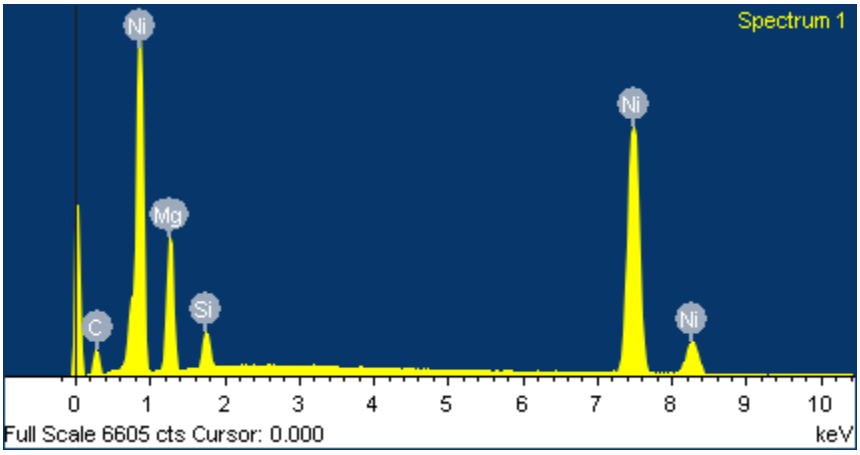

Spectrum	Mg	Si	Ni
Spectrum 1	29.89	4.71	65.40
Spectrum 2	63.15		36.85
Spectrum 3	87.51		12.49
Max.	87.51	4.71	65.40
Min.	29.89	4.71	12.49

*All results in atomic%

Figure 7-1 SEM & EDS results of cross section of induction melted Mg_2Ni by BN coated quartz crucible. (a) backscatter image of the cross section with 3 selected spectrums; (b) EDS profile of the spectrum 1; (c) the atomic fraction of elements in the spectrums 1-3.

7.1.2. Induction melted $Mg_{2.x}Ni$ (x = 0, 1, 2) alloys within BN crucibles

Using boron nitride crucibles, after the failure of the induction melting with the BN coated quartz tubes, a series of induction melting trials were performed. The initial aim was to produce Mg_2Ni ingots. The first run employed magnesium and nickel in an elemental ratio of 2:1. During the induction melting, some magnesium was lost due to sublimation which resulted in a Mg 'lean' material. Therefore, in order to produce a material with the target composition, some excess of magnesium had to be added to compensate for the Mg losses which had occurred.

Excess magnesium was added by increments of 5 and 10 at.% to the starting Mg-Ni mixture which was already at a ratio of Mg_2Ni. Therefore, these starting samples were noted as Mg_2Ni, $Mg_{2.1}Ni$ and $Mg_{2.2}Ni$. The solid mixtures were loaded into the boron nitride crucible, and melted eight times in the same way as previously mentioned. To assess the alloys, SEM was performed as shown in Figure 7-2 ~ Figure 7-5.

7.1.2.1. SEM & EDS of the induction melted $Mg_{2-x}Ni$ (x=0, 1, 2) alloys

Cross sections of the induction melted slugs were prepared in the same way as described previously.

Mg_2Ni sample

At ×200 magnification, the induction melted Mg_2Ni sample was shown to consist of three phases (Figure 7-2). Two light grey majority phases can be observed which appeared to be surrounded by a eutectic phase. The EDS spectra are shown in Figure 7-3. The brighter phase (Spectrum 1~3 in Figure 7-3) was shown to be $MgNi_2$ with a Mg-Ni ratio close to 30:70. As expected, the majority of the melt was shown to be Mg_2Ni (Spectrum 4 in Figure 7-3), with an Mg to Ni ratio slightly lower than 2:1. The boundary area (Spectrum 5 in Figure 7-3) had an Mg-Ni ratio of around 86:14, corresponding to the composition of the eutectic reported to be at a ratio of 90:10 in Mg-Ni binary phase diagram Figure 4-1.

It was evident that the induction melted slugs were not completely homogeneous and that most of the alloy was made up of the phases, Mg_2Ni and $MgNi_2$. Therefore, the total composition of the melt was shown to be lower than that of the starting materials (2:1). This is likely to be due to magnesium loss during heating.

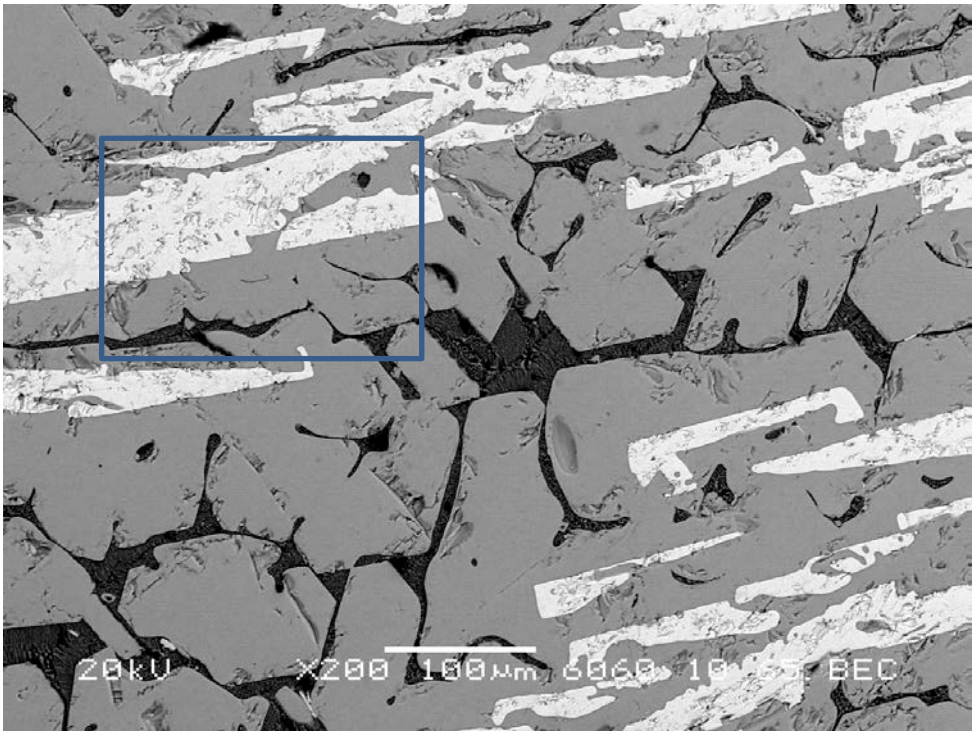

Figure 7-2 Back scattered image of the induction melted Mg_2Ni at ×200 magnification.

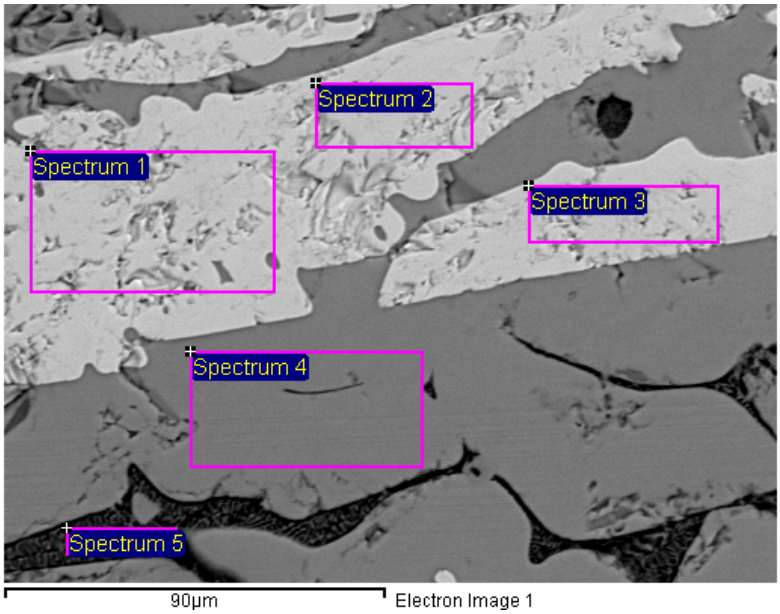

Spectrum	Mg	Ni
Spectrum 1	30.23	69.77
Spectrum 2	28.39	71.61
Spectrum 3	28.63	71.37
Spectrum 4	62.28	37.72
Spectrum 5	86.51	13.49
Max.	86.51	71.61
Min.	28.39	13.49

All results in atomic%

Figure 7-3 Back scattered image of an enlarged area of the induction melted Mg_2Ni at ×700 magnification with EDS analysis of 5 spectrums.

$Mg_{2.1}Ni$ and $Mg_{2.2}Ni$ samples

To compensate for the magnesium losses and to achieve better compositional control, two more Mg_2Ni samples were prepared by adding 5, 10 at.% excess Mg into the mixture of Mg granules and Ni wires with a ratio of 2:1. The induction melting followed the same route. After that, the cross sections of these two samples were mounted and assessed by SEM. They showed similar results compared with the induction melted Mg_2Ni alloy above. Both the melts of $Mg_{2.1}Ni$ and $Mg_{2.2}Ni$ consisted of primary Mg_2Ni and $MgNi_2$ phases surrounded by eutectics (see Figure 7-4 and Figure 7-5). The formation of the $MgNi_2$ could be ascribed to the incomplete diffusion of Ni into Mg. These induction melted alloys were used initially as the precursor materials for melt spinning (Teresiak et al., 2005).

The induction melted alloys consisted mainly of Mg_2Ni which is the target compound. However, the $MgNi_2$ phase is also present, despite the fact that excess Mg was added. SEM could not provide a reliable value of the fraction of the different phases in the melt, so XRD was employed to quantify the amount of each phase.

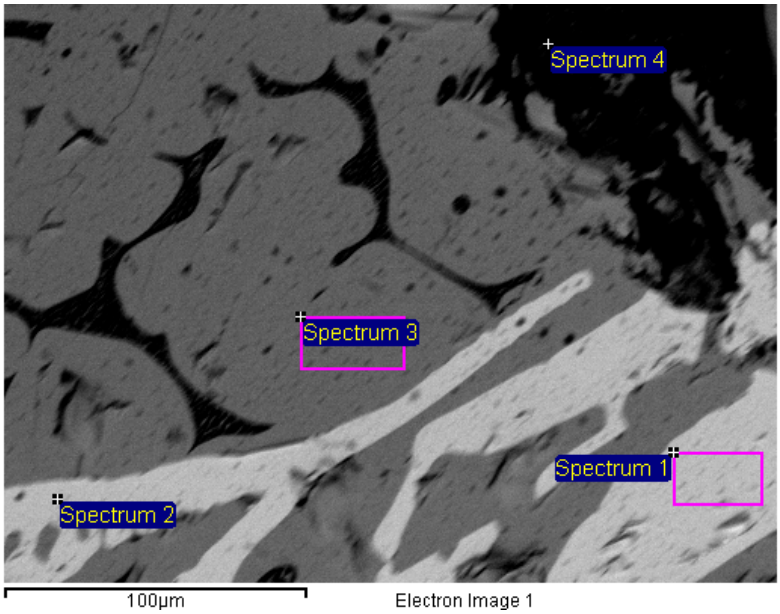

Spectrum	Mg	Ni
Spectrum 1	34.91	65.09
Spectrum 2	34.89	65.11
Spectrum 3	65.75	34.25
Spectrum 4	87.10	12.90
Max.	87.10	65.11
Min.	34.89	12.90

All results in atomic%

Figure 7-4 Back scattered image of cross section of the induction melted $Mg_{2.1}Ni$ at ×1000 magnification, with elemental fraction by EDS.

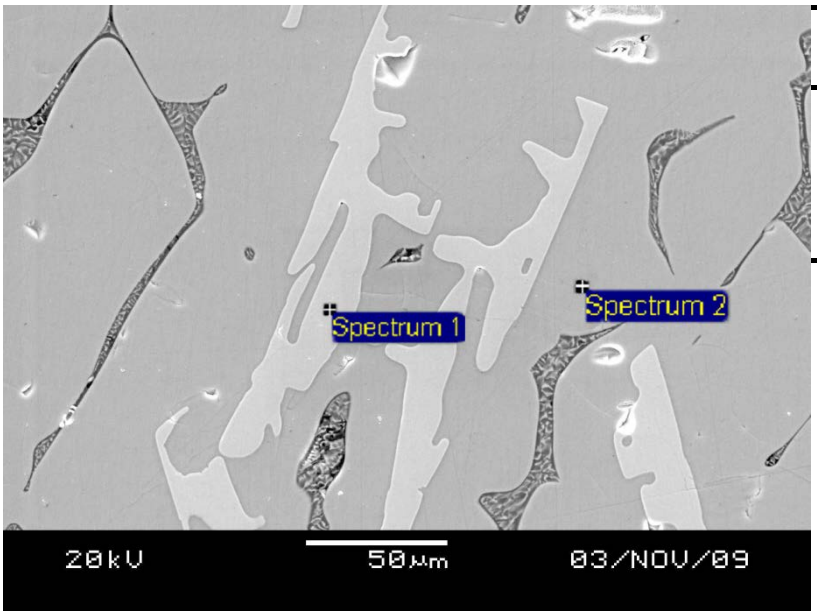

Spectrum	Mg	Ni
Spectrum 1	32.04	67.96
Spectrum 2	64.47	35.53
Max.	r47	67.96
Min.	32.04	35.53

All results in atomic%

Figure 7-5 Back scattered image of cross section of the induction melted $Mg_{2.2}Ni$ at ×1000 magnification, with elemental fraction by EDS.

7.1.2.2. XRD of the induction melted $Mg_{2-x}Ni$ (x=0, 1, 2) precursor alloys within BN crucibles

Room temperature XRD was performed on the cross sections of the induction melted alloys of $Mg_{2-x}Ni$ (x= 0, 1, 2). The cross sections were mounted on a holder on the X-ray diffractometer, and they were then rotated throughout the XRD run in order to eliminate possible effects of preferential orientation within the materials.

In Figure 7-6, all three XRD patterns of the induction melted $Mg_{2-x}Ni$ (x= 0, 1, 2) alloys indicate very similar constitutions, consisting mainly of the Mg_2Ni phase, with some $MgNi_2$ phase and a small proportion of a Mg-rich phase. This agrees well with the results obtained from the SEM studies described in the previous section.

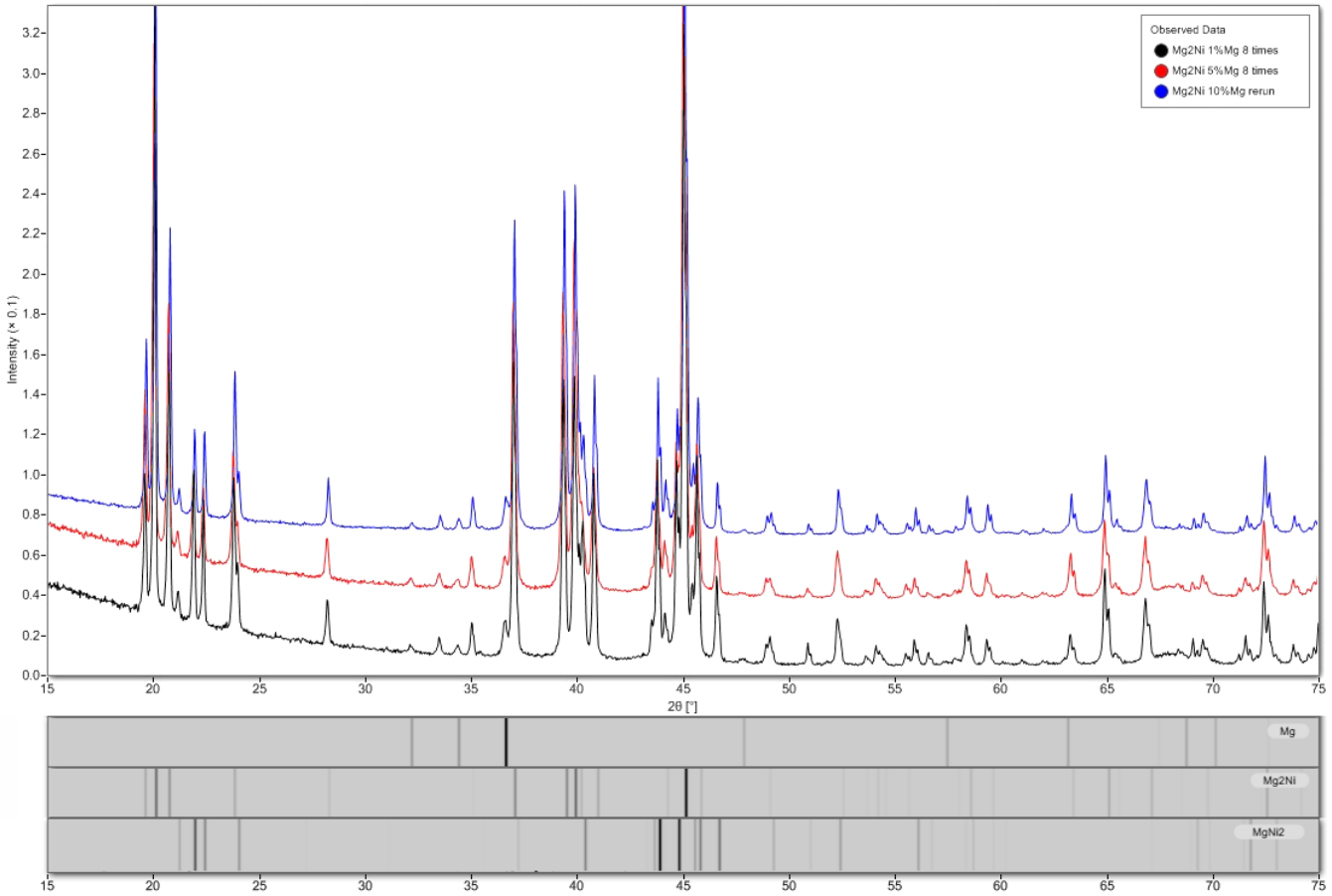

Figure 7-6 XRD patterns of the induction melted $Mg_{2-x}Ni$ (x=0, 1, 2) alloys.

The peak intensities for each of these phases differed between the samples, indicating a different ratio of these phases. *TOPAS Academic* was used to calculate the weight fraction of each phase using the Rietveld Refinement. The pattern (a) in Figure 7-7 shows for each phase the Rietveld refinement of the XRD pattern of the melted Mg_2Ni sample. The red curve is the refined pattern and the grey is the residual difference. The refined pattern of the Mg_2Ni melt has a goodness of fit (GOF) of 3.389 which was the lowest value obtained. The weight fraction of each phase is Mg_2Ni 71.57 ± 0.37 %, $MgNi_2$ 25.35 ± 0.30 % and Mg 3.08 ± 0.33 %. These calculated values agree with the analyses of SEM observations, showing nearly three quarters of the melt consisted of the Mg_2Ni phase. With about one quarter is the $MgNi_2$ phase and with smaller quantities of Mg-rich eutectic phase.

GOF is a measure of goodness which describe the sum of differences between observed data and expected XRD data. In Rietveld analysis, R-factor is used to describe how the observed data fit to a calculated model. R_{wp} is the most straightforward value, which stands for the weighted profile R-factor.

$$R_{wp} = \sqrt{\frac{\sum w_m (Y_{o,m} - Y_{c,m})^2}{\sum w_m {Y_{o,m}}^2}}$$

where $Y_{o,m}$ and $Y_{c,m}$ for the observed and calculated Y-axis intensity of the data point m, w_m for the weighting value given to the data point m and $w_m = 1/\sigma(Y_{o,m})^2$ where $\sigma(Y_{o,m})^2$ is the uncertainty in $Y_{o,m}$

If an ideal model is found, which perfectly indicates each value of $Y_{o,m}$, thus the R_{wp} in this model is the best possible value which can be obtained. Therefore, this R_{wp} is called the expected R-factor, R_{exp}. It is obvious that in this model, $w_m(Y_{o,m} - Y_{c,m})^2$ equals to 1. Therefore, using N as the total number of data point, the R_{exp} can be obtained as:

$$R_{exp} = \sqrt{\frac{N}{\sum w_m {Y_{o,m}}^2}}$$

GOF can be considered as the 'chi square' in statistics in the Rietveld refinement, and it can be obtained from:

$$GOF = \frac{R_{wp}}{R_{exp}}$$

Therefore, when the GOF decreases, it indicates the model used is in better agreement with the XRD data obtained. Therefore, the best phase combination can be found when the GOF reaches its minimum value.

Figure (b) shows the refined XRD pattern of the induction melted $Mg_{2.1}Ni$ sample with a GOF of 2.845. The weight fractions of each phase are Mg_2Ni of 79.29 ± 0.30 %, $MgNi_2$ of 17.94 ± 0.20 % and Mg of 2.77 ± 0.28 %.

The results of the sample of $Mg_{2.2}Ni$ indicate nearly the same result as those of the $Mg_{2.1}Ni$ sample. The GOF is 3.846. Mg_2Ni contributes to 80.25 ± 0.28 % of the mass (see Figure b in Figure 7-7).

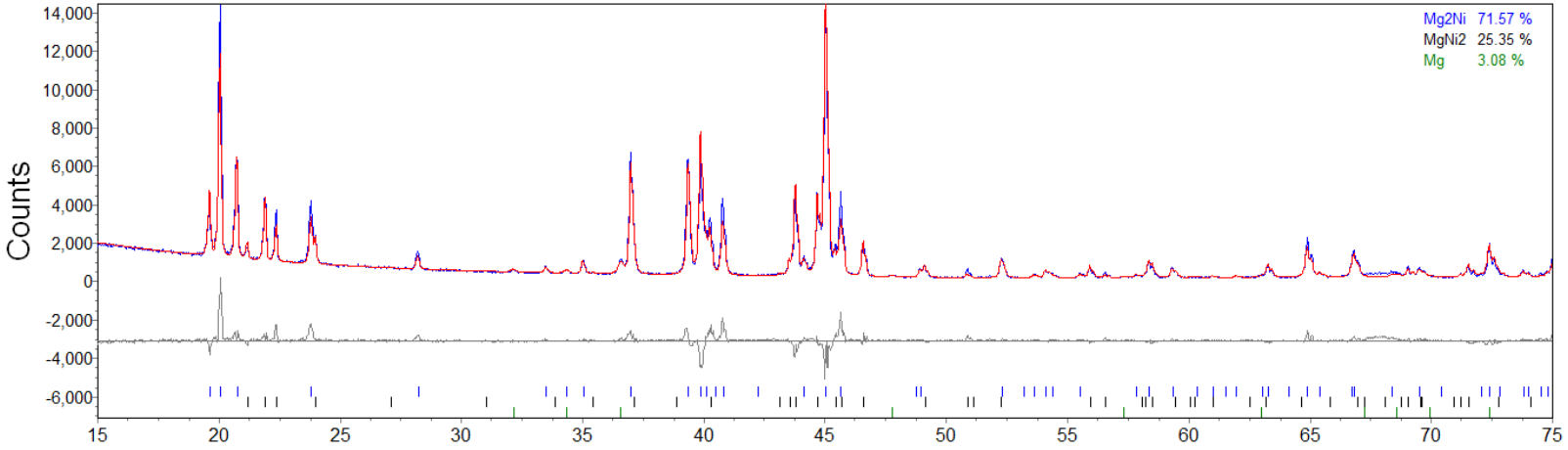

(a) Weight fractions of the induction melted Mg_2Ni sample from the Rietveld refinement.

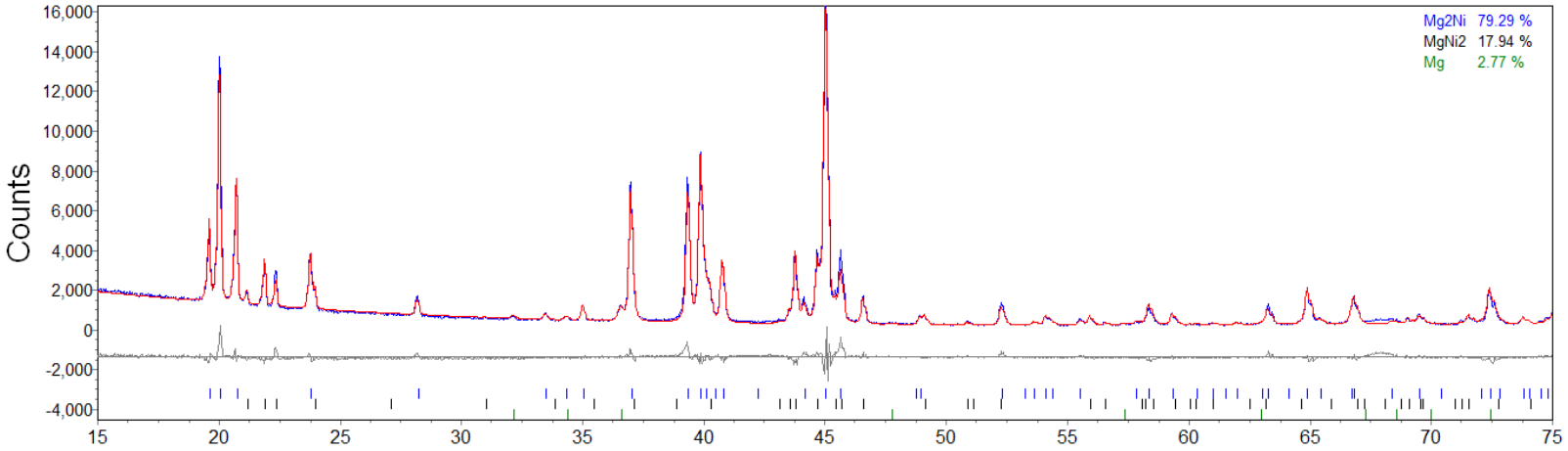

(b) Weight fractions of the induction melted $Mg_{2.1}Ni$ sample from the Rietveld refinement.

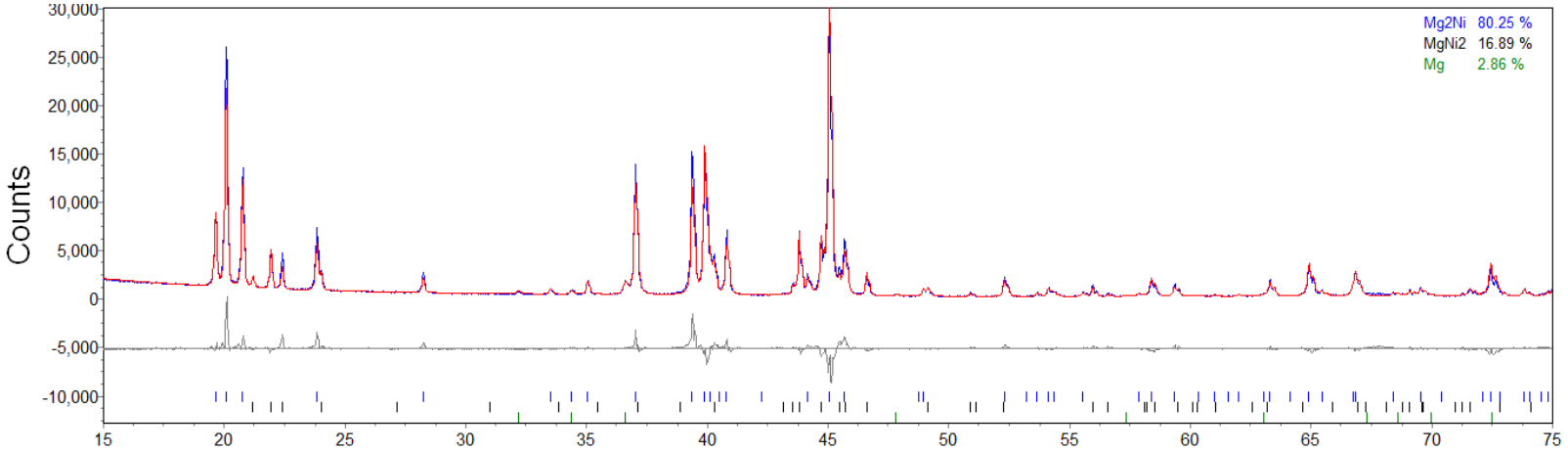

(c) Weight fractions of the induction melted $Mg_{2.2}Ni$ sample from the Rietveld refinement.

Figure 7-7 The Rietveld refinement analysis of the XRD patterns of the induction melted $Mg_{2-x}Ni$ (x=0, 1, 2) samples.

To summarize, adding excess of Mg did compensate for some of the Mg losses which occurred during melting, and resulted in less $MgNi_2$. However, there was no large difference between the $Mg_{2.1}Ni$ and $Mg_{2.2}Ni$ alloys. The target alloy was $Mg_{66.7}Ni_{33.3}$ and by adding up all the phases it was clear that significant Mg loss had occurred during the induction melting (Table 7-1). In terms of the Mg losses, 7.7 at.% Mg was lost for the Mg_2Ni mixture, 6.4% for the $Mg_{2.1}Ni$ mixture and 7.3% for the $Mg_{2.2}Ni$ mixture.

	Weight Percentage			**Mole Percentage**			**Real Composition**
	Mg_2Ni	$MgNi_2$	Mg	Mg_2Ni	$MgNi_2$	Mg	
Mg_2Ni alloy	71.57%	25.35%	3.08%	68.58%	18.39%	13.03%	$Mg_{61.54}Ni_{38.46}$
$Mg_{2.1}Ni$ alloy	79.29%	17.94%	2.77%	75.44%	12.92%	11.64%	$Mg_{63.40}Ni_{36.60}$
$Mg_{2.2}Ni$ alloy	80.25%	16.89%	2.86%	75.95%	12.10%	11.95%	$Mg_{63.73}Ni_{36.27}$

Table 7-1 Summary of the calculated composition from the Rietveld refinement of the XRD patterns of the induction melted $Mg_{2-x}Ni$ (x=0, 1, 2) samples.

7.1.2.3. Melt spinning of the induction melted $Mg_{2.x}Ni$ (x=0, 1, 2) alloys within BN crucibles

The induction melted $Mg_{2.x}Ni$ (x=0, 1, 2) ingots were used as feedstock for the melt spinner. As the melting point of Mg_2Ni is around 760 °C, the materials were heated and melt spinning was attempted at 850 °C and 950 °C.

Unfortunately, none of the $Mg_{2-x}Ni$ alloys could be ejected through the nozzle of the melt spinner. Even at 950 °C., when the crucible appeared to be glowing yellow (and the material looked fully molten), no material could be ejected from the nozzle during pressurization. All the melt spinning trials ended in failure, and the nozzle of the crucible appeared to be completely blocked with material. To discover the reason for the failures and to modify the method of melt spinning, the material residue in the crucibles were characterized by SEM analysis.

7.1.2.4. Failure analysis of the melt spinning of the induction melted $Mg_{2.2}Ni$ alloys

After unsuccessfully melt spinning the highest Mg-containing alloy, $Mg_{2.2}Ni$, the material left in the melt spinning crucible was removed and then cross sectioned across the slug. The BSI and EDS results are shown in Figure 7-8. It can be observed that a larger amount of $MgNi_2$ phase is present compared to that of the original induction melted material (see Figure 7-5). It is notable that the Mg-Ni eutectic phase disappeared, and the area of

$MgNi_2$ phase increased significantly. This indicated that the Mg loss was even more significant in this particular step and that a different experimental approach was required.

From the SEM Figure 7-8, it is evident that the Mg_2Ni phase constituted approximately half of the material in this part of the slug which was removed. In this case, the Mg losses during the melt spinning process were much more significant than those of ~7 at.% losses during the induction melting of the mixtures. The significant losses may be due to the high heating temperature, as the temperature reached 950 °C, or the fact that the standard induction melting for alloy preparation was carried out in sealed tubes which would minimize the Mg losses.

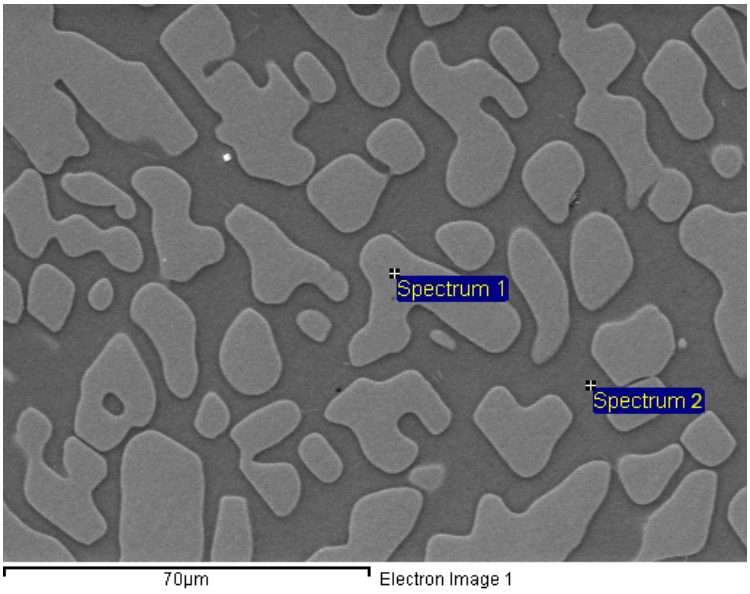

Spectrum	Mg	Ni
Spectrum 1	29.15	70.85
Spectrum 2	62.20	37.80
Max.	29.15	70.85
Min.	62.20	37.80

All results in atomic%

Figure 7-8 Back scattered image and EDS of the cross section of the remnant of $Mg_{2.2}Ni$ alloy after melt spinning.

To determine the temperature at which significant Mg losses would occur, a thermogravimetric analysis (TGA) measurement was performed. The induction melted $Mg_{2.2}Ni$ alloy was placed in an alumina (Al_2O_3) crucible in a furnace. The sample was

then heated from room temperature to 950 °C, with a heating rate of 5 °C/min. In Figure 7-9, the Differential Thermal Analysis (DTA) curve reveals a small peak at an onset temperature of 757.4 °C corresponding to the melting of the Mg_2Ni phase at approx. 760 °C. The thermogravimetric analysis (TGA) curve shows an onset temperature of ~700 °C with a significant weight drop at around 780.7 °C, indicating the sublimation of Mg from the induction melted $Mg_{2.2}Ni$ alloy. From ~700 up to 950 °C, the sample lost nearly 10 wt.%, which is about 20 at.% of the Mg, in agreement with the SEM image of the remnants of $Mg_{2.2}Ni$ after heating at 950 °C after melt spinning.

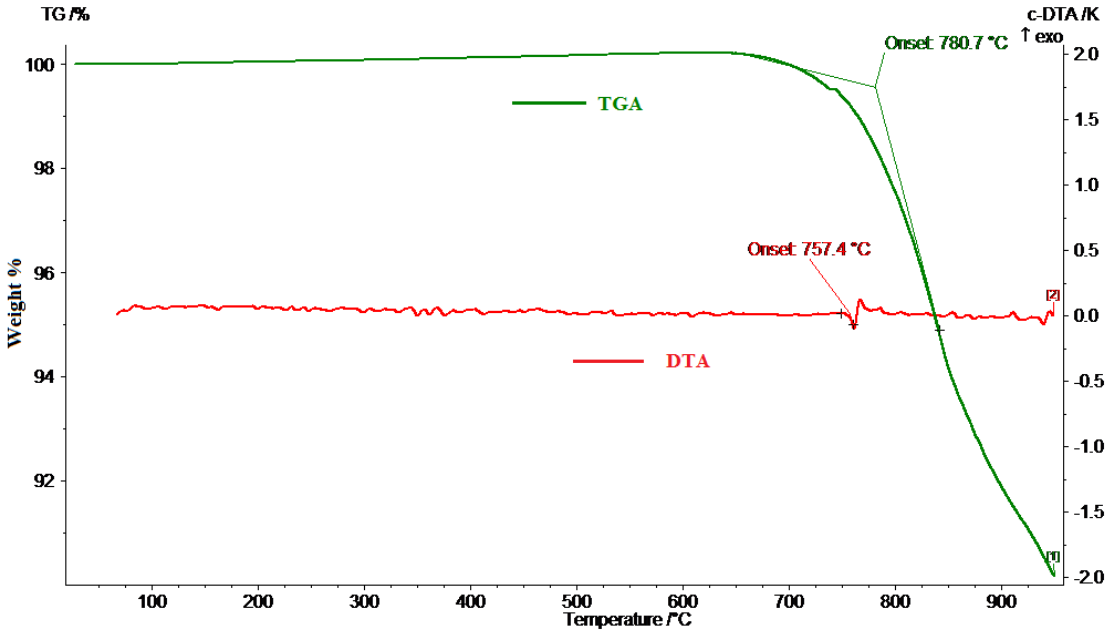

Figure 7-9 TGA result of the induction melted $Mg_{2.2}Ni$ sample.

So far, the failure of the melt spinning trials can be explained in term of the massive losses of Mg by sublimation during the induction melting. The evaporation of Mg occured at ~700 °C, and caused Mg losses during the melting. The magnesium losses push the alloy composition towards the Ni-rich side, thus forming more $MgNi_2$ phase in

the Mg_2Ni material. Because the melting point of $MgNi_2$ is around 950°C., this phase will remain solid during induction melting and subsequent injection which would result in the nozzle becoming blocked.

It was obvious from these initial trials that an alternative approach to induction melting for sample preparation was required. It should also be noted that, with regard to sample preparation prior to the melt spinning, few details are provided in the literature, therefore it was unclear how previous workers had synthesized the magnesium based alloy ribbons. To avoid the problems associated with a lack of homogeneity in the induction melted alloys, the alloys were prepared by mixing Mg and Ni powders and then pressing the powders into green compacts. The green compacts were then alloyed the induction field and it also meant that the Mg and Ni did not have far to diffuse. In theory, this means that the hold times and ultimate temperatures could be reduced.

7.2. Melt-spun $Mg_{90}Ni_{10}$ and $Mg_{73}Ni_{27}$ alloys

It has been shown previously that hydrogen storage properties of Mg-based materials can be enhanced by obtaining an ultrafine microstructure. It has also previously been showed that, for the Mg-Ni system, the metallic glass forming range is from $Mg_{90}Ni_{10}$ to $Mg_{75}Ni_{25}$ (Tanaka et al., 1999). Yim *et al* (2007) reported the $Mg_{90}Ni_{10}$ eutectic alloy exhibits better hydriding properties than the hypoeutectic or hypereutectic alloys. Therefore, in this work alloys were prepared within this compositional range, specifically $Mg_{90}Ni_{10}$ and $Mg_{80}Ni_{20}$ by melt spinning.

7.2.1. Sample preparation for the Mg-Ni compacts

It was evident that standard induction melting of wires failed to produce a homogeneous Mg-Ni alloy for melt spinning. Therefore, the sample preparation method had to be modified and developed to prepare the master alloys of Mg-Ni prior to the induction melting on the melt spinner.

Friedlmeier *et al.* (1999) reported an alternative method of preparing precursor Mg-Ni material for melt spinning. In his work, a mixed powder of Mg and Ni was pressed into pellets, followed by melt spinning. Therefore, this powder-pellet method was used to prepare Mg-Ni alloys in this work.

The $Mg_{90}Ni_{10}$ and $Mg_{80}Ni_{20}$ compacts were produced in the conditions described in Section 5.2.2. Unlike the previous work by Friedlmeier *et al.* (1999), the whole process in the present work was conducted under argon.

7.2.2. Melt-spinning

It was evident from the work on standard induction melting of Mg-Ni alloys that significant losses of Mg were encountered and that an inhomogeneous mixture of phases was produced. Therefore, during the induction melting process which occurred on the melt spinner for the $Mg_{90}Ni_{10}$ compact, a tailored heating profile was used. This involved holding the Mg-Ni compact for a prolonged period of time at a relatively low power, and therefore temperature, in order to allow the Mg and Ni to diffuse without significant loss of Mg which would occur at higher temperatures. The power was then increased rapidly in order to superheat the material above its melting point to allow ejection of the melt through the nozzle. To avoid Mg losses, the material was only held for a short period of time at this maximum temp. The detailed heating processes of melt-spun $Mg_{90}Ni_{10}$ is shown in Table 7-2.

From 15% to 20% power input, the $Mg_{90}Ni_{10}$ compacts were heated for 10 min to enable Mg-Ni inter-diffusion, with a temperature around 600 °C given by the pyrometer. However, the temperature reading was lost when the power increased to 20%, due to the magnesium vapour which blocks the signal to the pyrometer. Because the crucible was heated to a glowing orange at this moment, and vapour could be seen gushing out of the crucible nozzle. Therefore, the power was increased rapidly to 25% for 6 min, which overheated the materials and made the sample molten for melt-spinning injection. The $Mg_{90}Ni_{10}$ sample was melt-spun after a total of 18-min induction melting, and continuous ribbons were obtained. Some melt-spun ribbons were collected from the main chamber of the melt spinner in air.

Table 7-2 shows the heating process for the $Mg_{80}Ni_{20}$ compacts during melt spinning, which is slightly different from that of the $Mg_{90}Ni_{10}$ sample. When the power was increased to 20%, the crucible did not glow orange. The power was then increased to 23% when the crucible started to glow and vapour could be seen gushing out. Due to the higher Ni-content, the $Mg_{80}Ni_{20}$ sample was melt-spun after a total of 24-min heating. This turned out to be a successful melt-spinning, and all the melt-spun ribbons were collected inertly from the collection tube.

$Mg_{90}Ni_{10}$		$Mg_{80}Ni_{20}$	
Power	Time	Power	Time
15%	2 min	15%	2 min
16%	2 min	16%	2 min
17%	2 min	17%	2 min
18%	2 min	18%	2 min
19%	2 min	19%	2 min
20%	2 min	20%	2 min
		21%	2 min
		22%	2 min
		23%	2 min
25%	6 min	25%	6 min
Total 18 min		Total 24 min	

Table 7-2 Induction heating profiles during melt spinning of the $Mg_{90}Ni_{10}$ and$Mg_{80}Ni_{20}$ sample.

7.2.3. Cryo-milling

For subsequent measurements, the melt-spun ribbons were cryo-milled into a powder material. The cryo-milling process followed the same process as in section 5.2.4. The melt-spun $Mg_{90}Ni_{10}$ and $Mg_{80}Ni_{20}$ ribbons were cryo-milled under liquid nitrogen for two cycles for 10 min in total.

7.2.4. SEM of melt-spun $Mg_{90}Ni_{10}$ and $Mg_{80}Ni_{20}$ ribbons

The Mg-Ni ribbons were 5 ~ 10 mm wide and around 50 μm thick. The composition of the as-quenched ribbons was investigated by scanning electron microscopy (SEM) with energy dispersive spectrometry (EDS).

Melt-spun $Mg_{90}Ni_{10}$ ribbons

Figure 7-10 shows the surface condition of the melt-spun ribbons of $Mg_{90}Ni_{10}$. The surface of the ribbons appeared rough but homogeneous. The surface composition is exactly $Mg_{90}Ni_{10}$, the same as that of the starting composition. Spectrum 5 in Figure 7-10 shows a higher Ni content area. This could be explained by incomplete diffusion of the Ni into Mg. Generally, the melt-spun ribbons indicate successful melt-spinning.

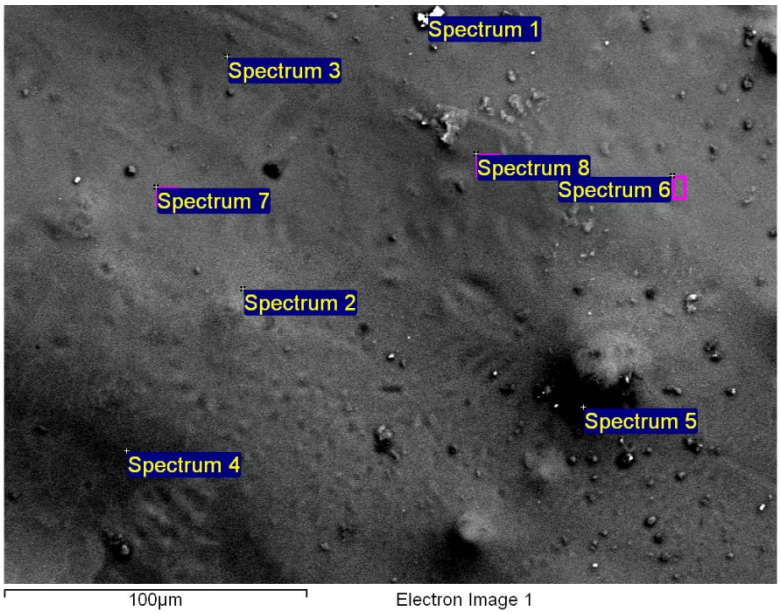

Spectrum	Mg	Ni
Spectrum 1	90.83	9.17
Spectrum 2	91.49	8.51
Spectrum 3	90.89	9.11
Spectrum 4	91.03	8.97
Spectrum 5	83.44	16.56
Spectrum 6	90.78	9.22
Spectrum 7	91.61	8.39
Spectrum 8	90.77	9.23
Mean	90.10	9.90
Std. deviation	2.71	2.71
Max.	91.61	16.56
Min.	83.44	8.39

All results in atomic%

Figure 7-10 SEM&EDS results of the surface of the melt-spun $Mg_{90}Ni_{10}$ ribbon.

Several sections of the melt-spun ribbons were mounted vertically and then polished. Figure 7-11 shows SEM & EDS analysis of five pieces of the melt-spun $Mg_{90}Ni_{10}$ sample. The average composition was measured as $Mg_{89}Ni_{11}$ with the Mg content of 89 ± 2.7 at.%, and this sample will be noted as '$Mg_{90}Ni_{10}$' in this work. This composition means that no significant Mg loss has occurred under these processing conditions.

The first piece of ribbons in Figure 7-11 appeared to exhibit high homogeneity but with a slightly higher Ni-rich composition of approx. $Mg_{85}Ni_{15}$. However, both the second and third samples had a composition of $Mg_{90}Ni_{10}$. Surprisingly, a multi-layer segregation has been observed in the fifth image in Figure 7-11. It can also be seen in another piece in the fourth image in Figure 7-11. It is not clear why this segregation has taken place and this has not been shown before in the literature, and the same segregation was not found in the $Mg_{80}Ni_{20}$ sample. Mishima *et al* (1993) observed the cross section of the rapidly solidified La-Ni-Al ternary ribbons, and reported a columnar structure. This was not found to be the case in the melt-spun samples investigation in this work.

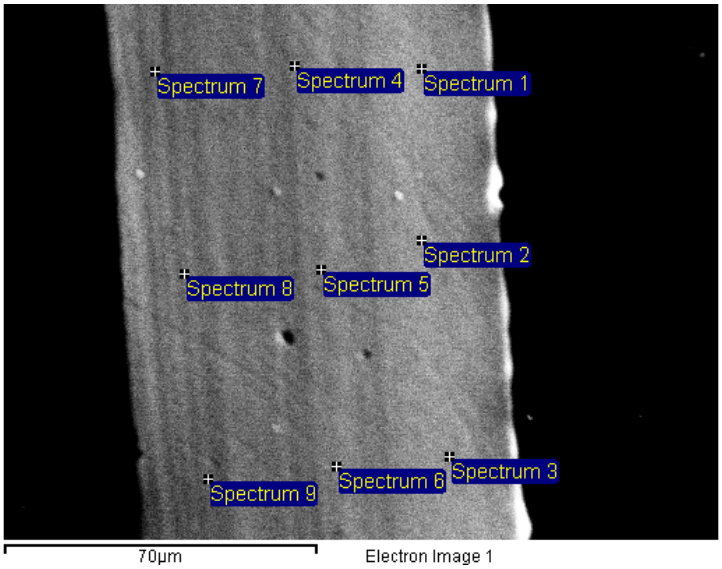

Spectrum	Mg	Ni
Spectrum 1	84.82	15.18
Spectrum 2	84.57	15.43
Spectrum 3	84.46	15.54
Spectrum 4	85.18	14.82
Spectrum 5	84.70	15.30
Spectrum 6	84.80	15.20
Spectrum 7	85.73	14.27
Spectrum 8	85.97	14.03
Spectrum 9	85.75	14.25
Mean	85.11	14.89
Std. deviation	0.57	0.57
Max.	85.97	15.54
Min.	84.46	14.03

All results in atomic%

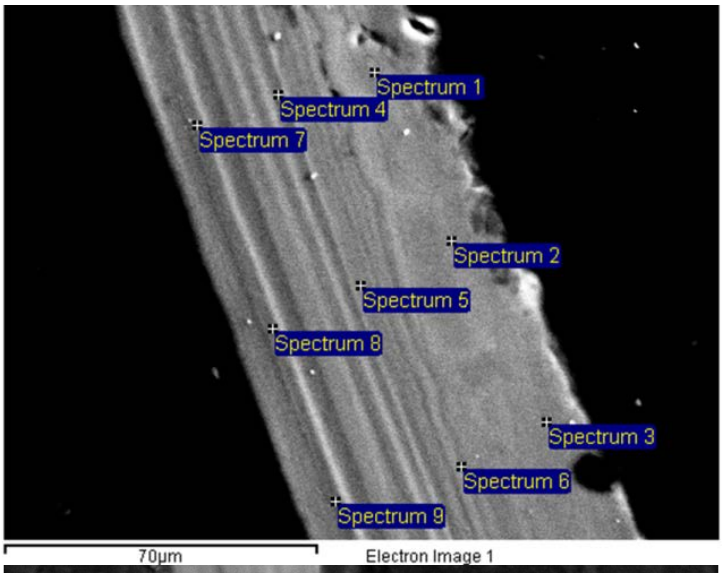

Spectrum	Mg	Ni
Spectrum 1	89.33	10.67
Spectrum 2	90.19	9.81
Spectrum 3	89.88	10.12
Spectrum 4	88.53	11.47
Spectrum 5	88.75	11.25
Spectrum 6	88.94	11.06
Spectrum 7	90.07	9.93
Spectrum 8	89.21	10.79
Spectrum 9	90.68	9.32
Mean	89.51	10.49
Std. deviation	0.73	0.73
Max.	90.68	11.47
Min.	88.53	9.32

All results in atomic%

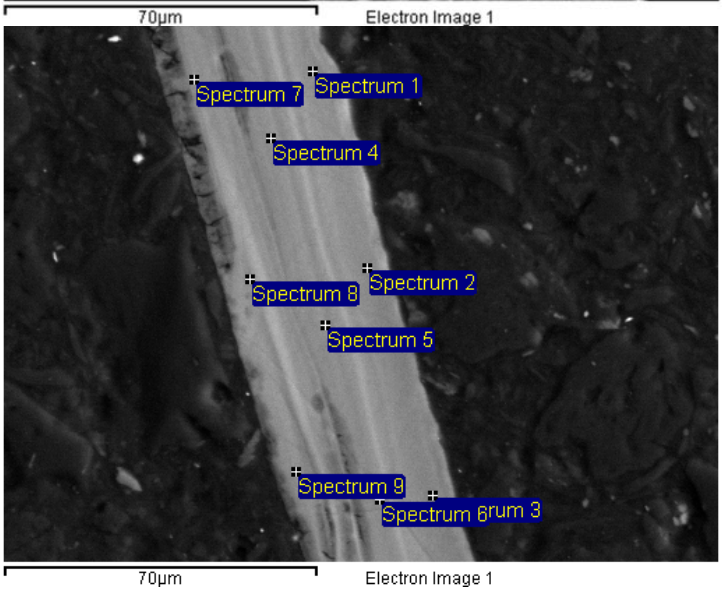

Spectrum	Mg	Ni
Spectrum 1	88.73	11.27
Spectrum 2	88.77	11.23
Spectrum 3	88.78	11.22
Spectrum 4	89.30	10.70
Spectrum 5	89.09	10.91
Spectrum 6	87.98	12.02
Spectrum 7	89.33	10.67
Spectrum 8	89.64	10.36
Spectrum 9	90.95	9.05
Mean	89.17	10.83
Std. deviation	0.82	0.82
Max.	90.95	12.02
Min.	87.98	9.05

All results in atomic%

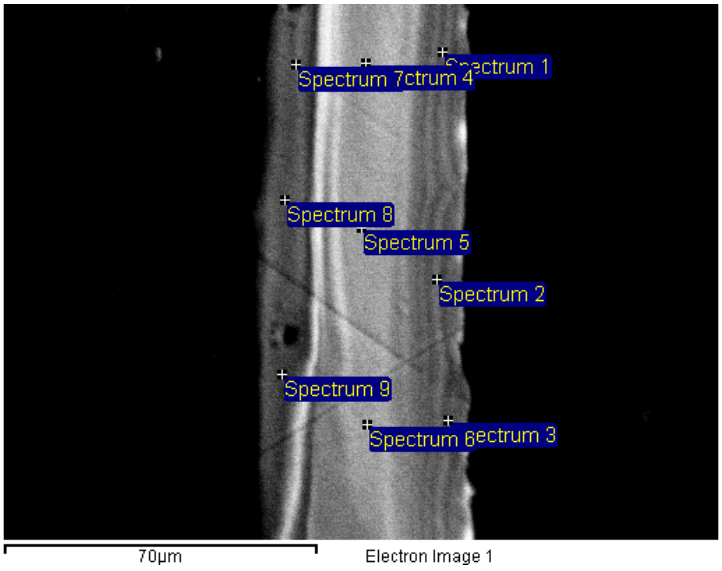

Spectrum	Mg	Ni
Spectrum 1	91.70	8.30
Spectrum 2	91.21	8.79
Spectrum 3	91.38	8.62
Spectrum 4	86.81	13.19
Spectrum 5	86.62	13.38
Spectrum 6	86.48	13.52
Spectrum 7	91.70	8.30
Spectrum 8	92.78	7.22
Spectrum 9	94.61	5.39
Mean	90.37	9.63
Std. deviation	2.98	2.98
Max.	94.61	13.52
Min.	86.48	5.39

All results in atomic%

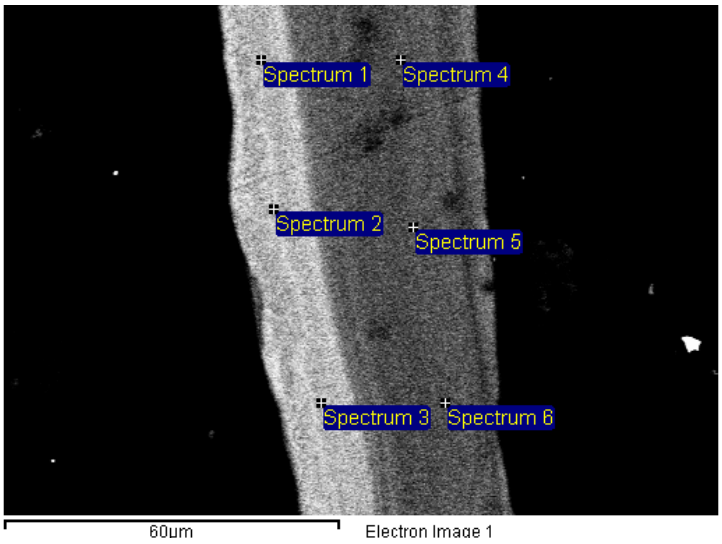

Spectrum	Mg	Ni
Spectrum 1	87.49	12.51
Spectrum 2	87.02	12.98
Spectrum 3	86.99	13.01
Spectrum 4	93.78	6.22
Spectrum 5	93.57	6.43
Spectrum 6	93.18	6.82
Mean	90.34	9.66
Std. deviation	3.48	3.48
Max.	93.78	13.01
Min.	86.99	6.22

All results in atomic%

Figure 7-11 SEM&EDS results of five pieces of the melt-spun $Mg_{90}Ni_{10}$ ribbons after cross sectioning and polishing.

Melt-spun $Mg_{80}Ni_{20}$ ribbons

The Figure 7-12 shows the SEM & EDS results of the cross-sectioned melt-spun $Mg_{80}Ni_{20}$ ribbons. Unlike the melt-spun $Mg_{90}Ni_{10}$, three pieces of melt-spun $Mg_{80}Ni_{20}$ showed a single homogeneous composition throughout the ribbon. However, after melt spinning the composition of the $Mg_{80}Ni_{20}$ compact was shown to be depleted in Mg. The average composition was approximately $Mg_{73}Ni_{27}$, and therefore, ~9 at.% of the Mg was lost compared to the starting materials. For the rest of the thesis this material will be referred to as "$Mg_{73}Ni_{27}$".

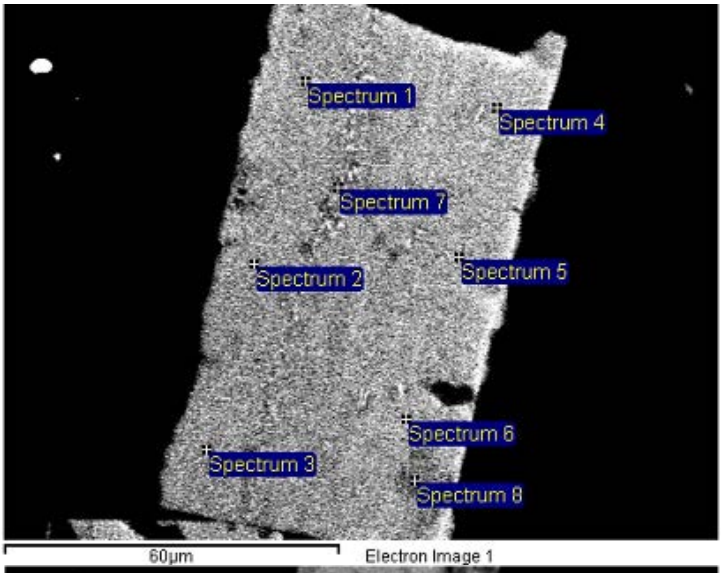

Spectrum	Mg	Ni
Spectrum 1	73.67	26.33
Spectrum 2	73.86	26.14
Spectrum 3	74.00	26.00
Spectrum 4	73.19	26.81
Spectrum 5	73.54	26.46
Spectrum 6	73.77	26.23
Mean	73.67	26.33
Std. deviation	0.57	0.57
Max.	74.00	26.81
Min.	73.19	26.00

All results in atomic%

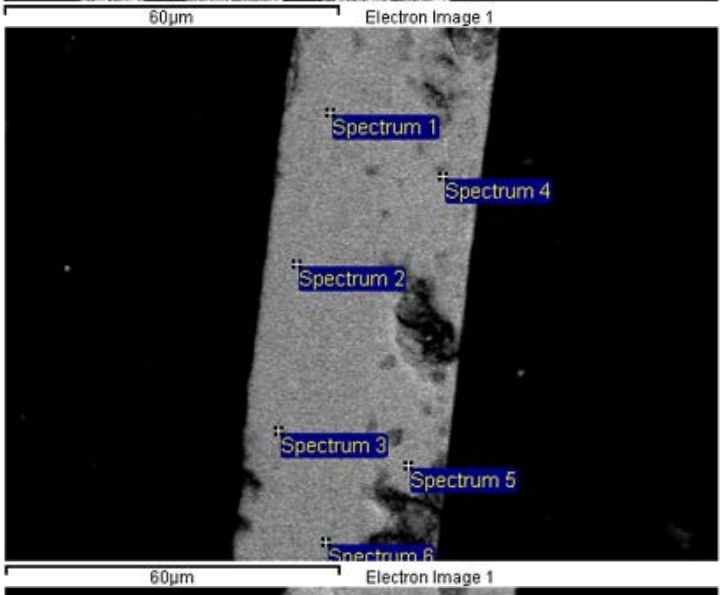

Spectrum	Mg	Ni
Spectrum 1	74.21	25.79
Spectrum 2	74.36	25.64
Spectrum 3	74.16	25.84
Spectrum 4	73.41	26.59
Spectrum 5	72.20	27.80
Spectrum 6	74.34	25.66
Mean	73.78	26.22
Std. deviation	0.85	0.85
Max.	74.36	27.80
Min.	72.20	25.64

All results in atomic%

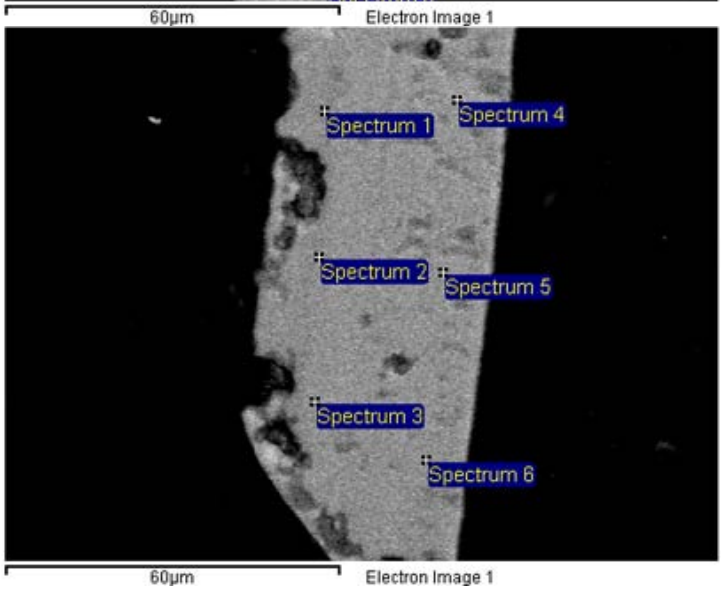

Spectrum	Mg	Ni
Spectrum 1	73.21	26.79
Spectrum 2	72.92	27.08
Spectrum 3	72.45	27.55
Spectrum 4	72.45	27.55
Spectrum 5	72.88	27.12
Spectrum 6	72.84	27.16
Mean	72.79	27.21
Std. deviation	0.30	0.30
Max.	73.21	27.55
Min.	72.45	26.79

All results in atomic%

Figure 7-12 SEM&EDS results of three sites of the cross section of the melt-spun $Mg_{80}Ni_{20}$ ribbons.

Remnants of $Mg_{90}Ni_{10}$ melt

It was evident that, during induction melting of the $Mg_{90}Ni_{10}$ and $Mg_{80}Ni_{20}$ samples before the molten material was ejected, Mg vapour could be observed subliming from the end of the nozzle. After melt-spinning, some of the alloy also solidified in the nozzle of the BN crucible and resulted in some of the material being retained in the crucible. The remaining material was removed and cross sectioned. Figure 7-13 shows the remnants of the $Mg_{90}Ni_{10}$ sample after the melt spinning operation, and it is apparent that the Mg to Ni ratio dropped significantly compared to that of the starting mixture. In the first image of Figure 7-13, the average Mg content is only 41.85%. Two phases were observed based upon a composition of approximately Mg_2Ni and $MgNi_2$ (Figure 7-13). It would appear therefore that, the sublimation of Mg during induction heating has pushed the composition of some of the material to the Ni-rich side of the phase diagram. As this has occurred, the melting point of the more Ni rich phases will increase and therefore this material is likely to solidify. It is likely therefore that, this material becomes blocked in the nozzle and that is why the whole melt does not pass through onto the wheel.

It is evident therefore that, despite the very controlled conditions used to induction-melt the pressed pellets, there is still some magnesium loss, although this is observed to a lesser degree than with pre-prepared induction melted alloys shown previously in section 7.1.2.4.

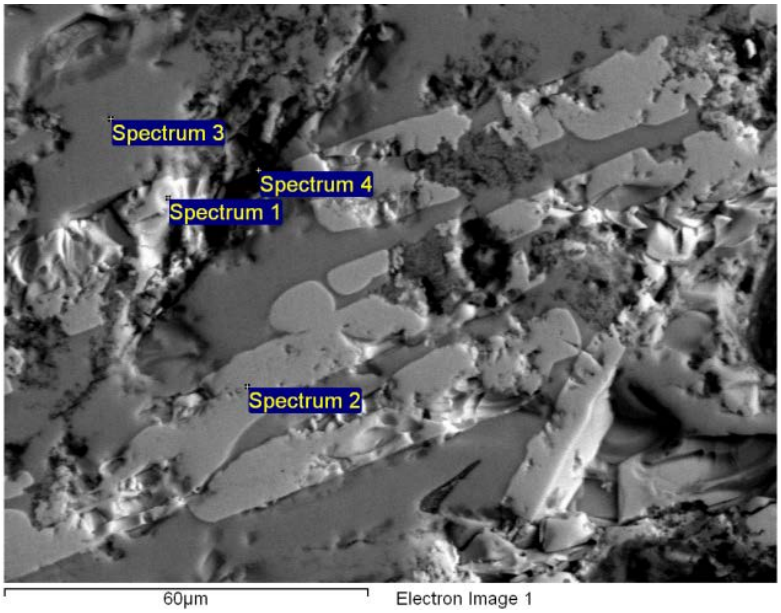

Spectrum	Mg	Ni
Spectrum 1	36.11	63.89
Spectrum 2	28.69	71.31
Spectrum 3	60.50	39.50
Spectrum 4	42.10	57.90
Max.	60.50	71.31
Min.	28.69	39.50

All results in atomic%

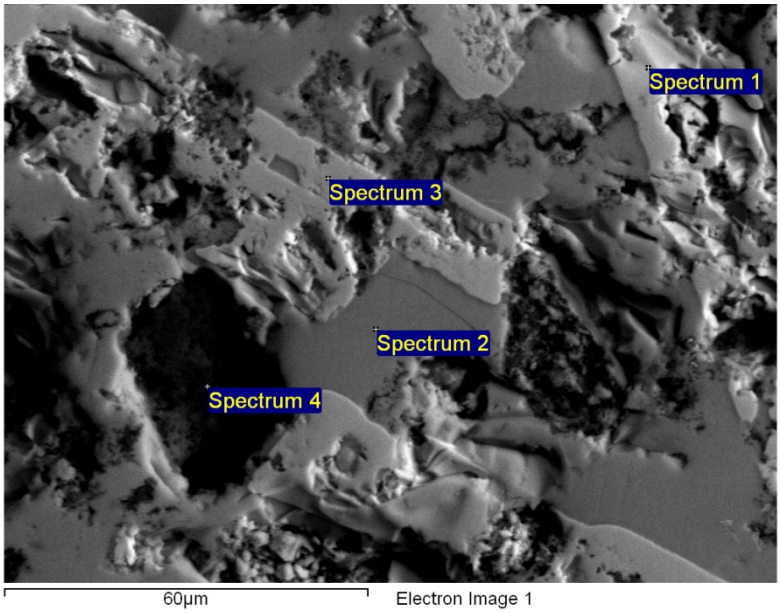

Spectrum	Mg	Ni
Spectrum 1	32.26	67.74
Spectrum 2	61.21	38.79
Spectrum 3	28.87	71.13
Spectrum 4	85.90	14.10
Max.	85.90	71.13
Min.	28.87	14.10

All results in atomic%

Figure 7-13 SEM&EDS results of the remnants of the $Mg_{90}Ni_{10}$ sample in the crucible after melt spinning

7.2.5. XRD of the melt-spun $Mg_{90}Ni_{10}$ and $Mg_{73}Ni_{27}$ samples

XRD was performed on the melt-spun $Mg_{90}Ni_{10}$ and $Mg_{73}Ni_{27}$ powders in the as-quenched state. The XRD has been conducted in accordance with the procedures outlined in Section 5.3.1.

Melt-spun $Mg_{90}Ni_{10}$ sample

XRD of both the as-spun ribbons and the cryo-milled powders for the alloy $Mg_{90}Ni_{10}$ was performed (Figure 7-14). Comparing with the XRD results shown in Figure 6-5 for the melt-spun Mg ribbon, it is clear that the melt-spun $Mg_{90}Ni_{10}$ exhibited broad peaks, thus indicating that the melt spinning technique produced a much finer microstructure, potentially amorphous or nano-crystalline, by adding Ni to the Mg.

In Figure 7-14, both patterns show the same general peaks, where the main peaks represent the pure Mg phase with smaller amounts of Mg_2Ni. Aside from the Mg peaks for the as-spun ribbons (red pattern), there is one small peak at about 38°. The peak is near the (020) peak of Mg_2Ni at 40°, but it is more likely to represent the Mg_6Ni phase, which will be discussed in more detail at the end of this chapter.

For the cryo-milled powders for the $Mg_{90}Ni_{10}$ sample (magenta pattern), the peaks of Mg_2Ni are more obvious. Moreover, in the XRD pattern, a small background hump can be seen from 35° ~ 45°, whereas the small 38° peak becomes hardly detectable.

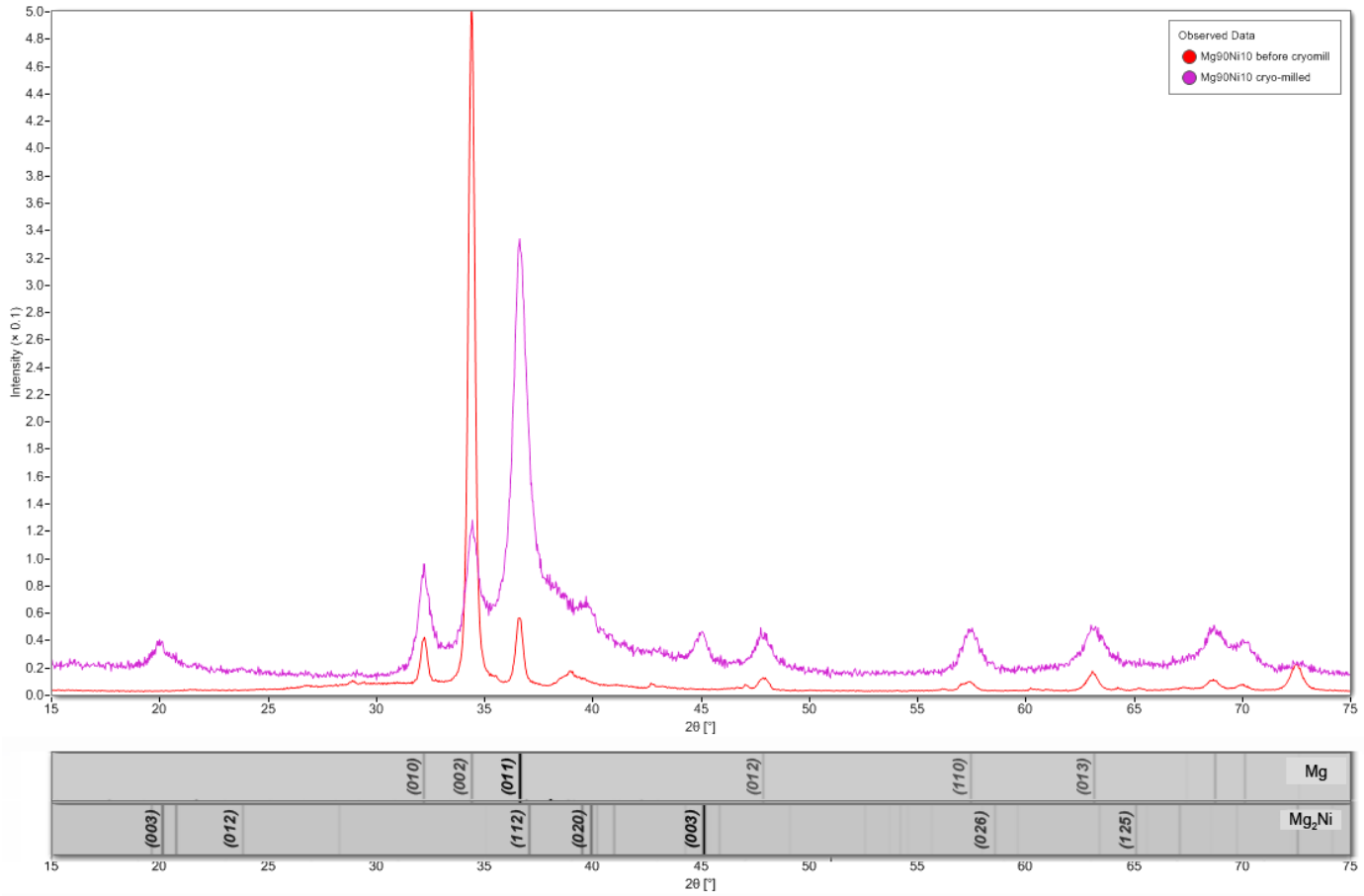

Figure 7-14 XRD patterns of the as-spun ribbons (red) and the cryo-millled powder (megenta) of the $Mg_{90}Ni_{10}$ sample.

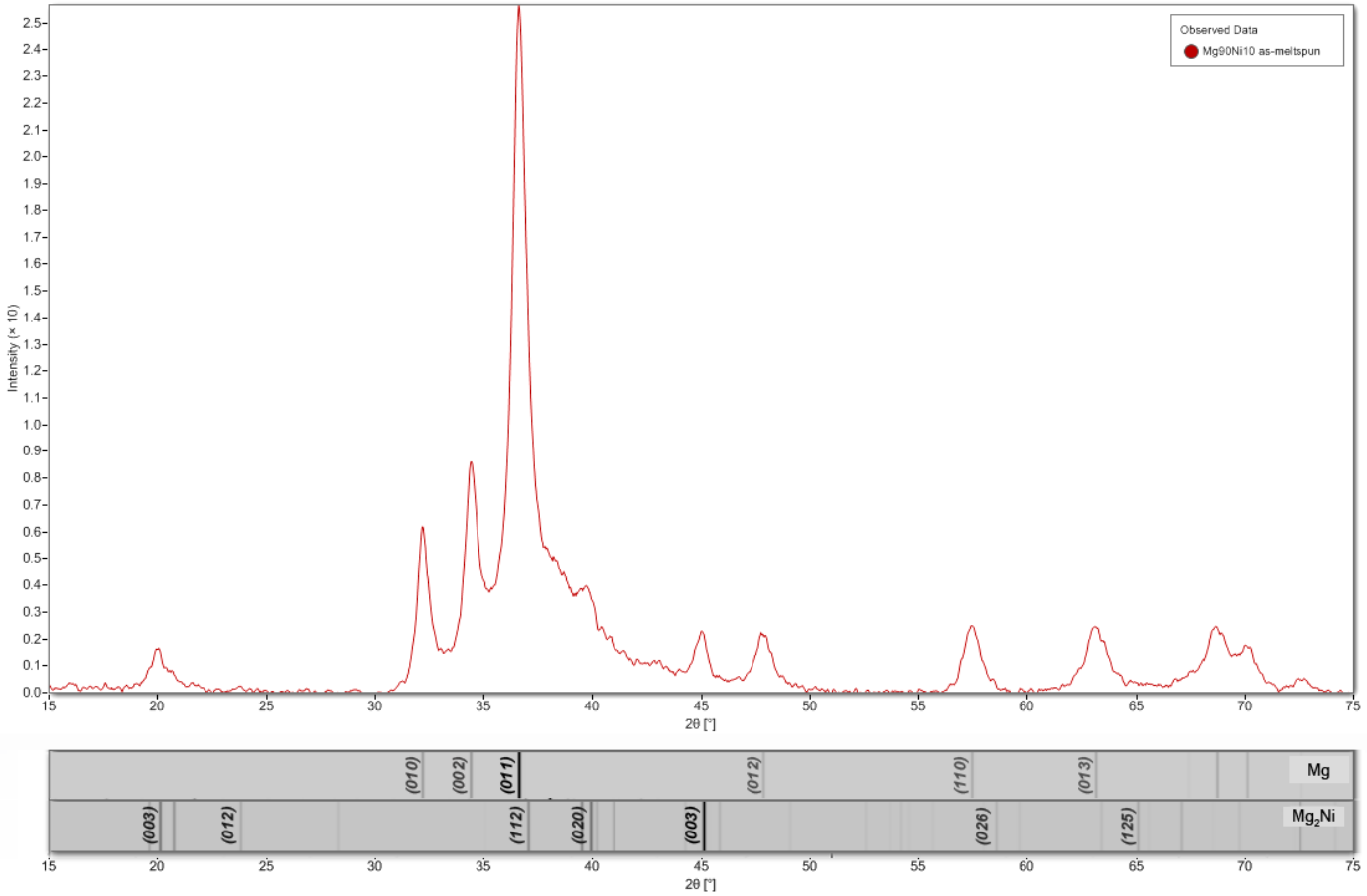

Figure 7-15 XRD pattern of the cryo-milled powder of the melt-spun $Mg_{90}Ni_{10}$.

Moreover, it was seen that the non-milled ribbons exhibited a preferred orientation of the (002) reflection (in Figure 7-14), which was not the case for the cryo-milled powder shown in Figure 7-15. Kalinichenka *et al.* (2011b) found that the XRD pattern of melt-spun $Mg_{90}Ni_8Re_2$ ribbons exhibited the same preferred orientation of Mg (002) reflection.

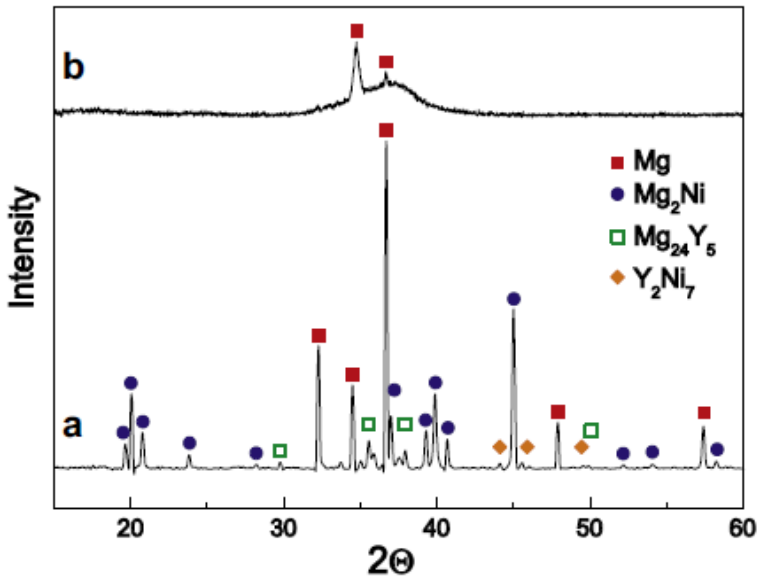

Figure 7-16 XRD patterns of (a) as-cast and (b) as-melt-spun $Mg_{90}Ni_8Y_2$ sample. Taken from Kalinichenka (2011b).

Teresiak *et al.* (2009b) reported a similar result, and claimed that it disappeared after milling the sample for a short time after cooling. It can be explained in terms of the crystals formed by the fast cooling when making contact to the copper wheel in the vertical direction. It is apparent therefore that directional solidification occurs as the molten material strikes the copper wheel. However, the cryo-milled powder did not exhibit any preferred orientation effect.

Figure 7-15 shows the XRD pattern for the melt-spun $Mg_{90}Ni_{10}$ cryo-milled powder. Mg and Mg_2Ni peaks are apparent in the pattern. The majority of the powder demonstrates

broad peaks for the Mg with a much stronger intensity than those for the Mg_2Ni phase. Moreover, there is a large background hump from 30° to 45°, indicating a partially amorphous phase or possibly the presence of a metastable phase of Mg_6Ni.

Kalinichenka *et al.* (2011b) showed a very similar XRD pattern for melt-spun $Mg_{90}Ni_8Y_2$ with a large background hump (see pattern b in Figure 7-16). It was concluded that as-spun $Mg_{90}Ni_8Y_2$ consisted of an amorphous phase together with Mg and $Mg_2(Ni,Y)$ nanocrystals with an average size of 150 nm and 5 nm, respectively. It is likely that the material produced in this project has a similar mixture of both amorphous and nanocrystalline material.

Bendersky *et al.* (2011) described a Mg_6Ni phase in a melt-spun Mg-Ni binary alloys. A series of $Mg_{100-x}Ni_x$ (x= 0.5, 1, 2, 5) alloys were melt-spun and observed by XRD. The XRD pattern appeared sharper with no amorphous background. In Bendersky's work, as the Ni content was increased through the range of samples, then a Mg_6Ni phase became apparent, especially in the $Mg_{95}Ni_5$ sample with a peak at 38°.

Palade *et al.* (2006) reported a very similar XRD pattern for melt-spun $Mg_{88}Ni_{11}Fe_1$ and $Mg_{88}Ni_{11.4}Fe_{0.6}$, indicating the presence of an amorphous phase with Mg and a metastable Mg_6Ni phase. The composition of the samples is very close to the melt-spun $Mg_{90}Ni_{10}$ samples studied in this work. Therefore, it is likely that Mg_6Ni could be present in the melt-spun $Mg_{90}Ni_{10}$ sample.

Rietveld refinement was applied to the XRD data of the melt-spun $Mg_{90}Ni_{10}$ by *TOPAS Academic*, with and without simulating the Mg_6Ni phase. Figure 7-17 shows that the refined data exhibited a better fit when the Mg_6Ni phase was added to the refinement. Without including the Mg_6Ni phase, the goodness of fit (GOF) value was 2.765. Conversely, when the Mg_6Ni phase was included, the refined pattern had a reduced value of 1.379. The lower GOF indicated the R-value of the refinement with the information on Mg_6Ni phase was closer to the R_{exp} value, thus referring to be closer to the perfect refinement model. Therefore, it is very likely to indicate the presence of the Mg_6Ni phase in the melt-spun $Mg_{90}Ni_{10}$ sample.

the Rietveld refinement without the information on the Mg_6Ni phase included

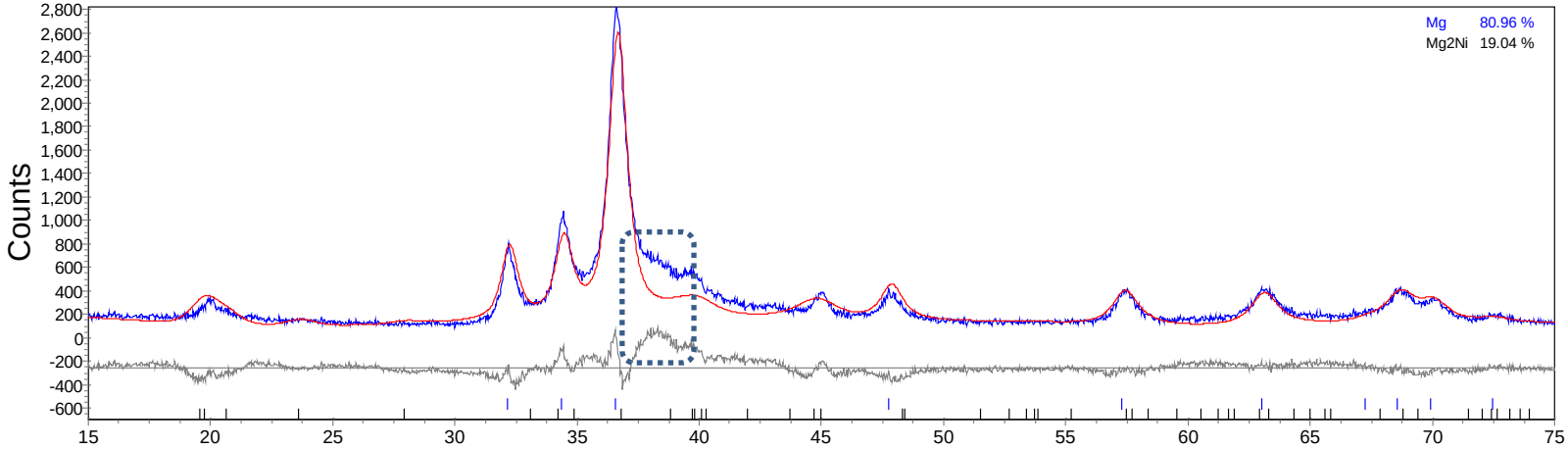

the Rietveld refinement with the information on the Mg_6Ni phase included

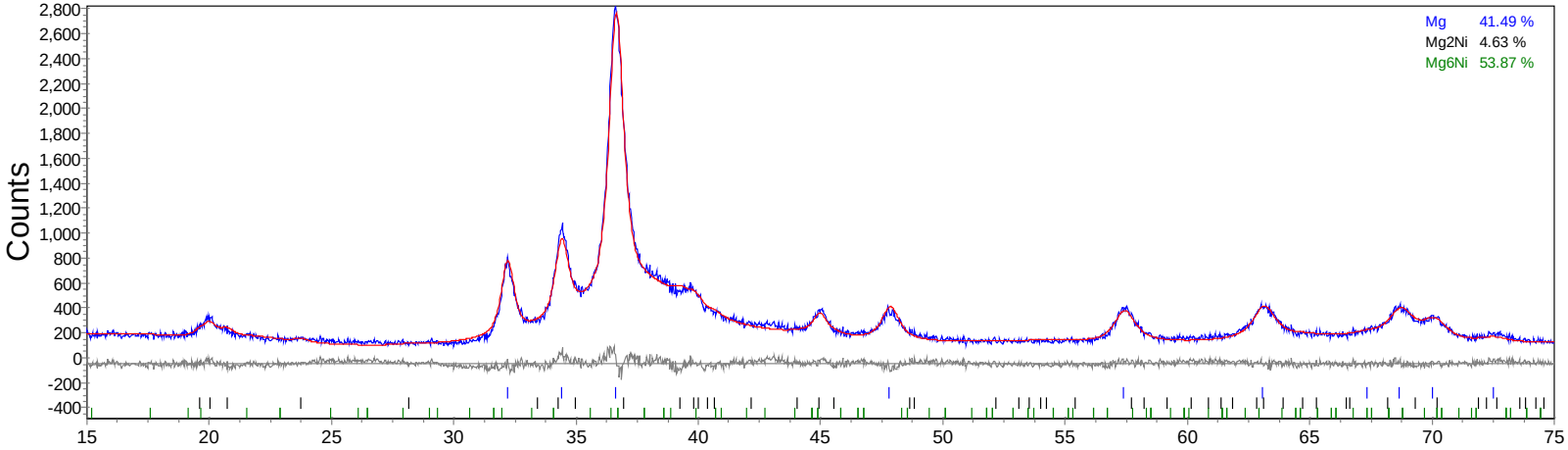

Figure 7-17 The Rietveld refinement of the XRD pattern of the melt-spun $Mg_{90}Ni_{10}$ powder (red: calculated pattern, blue: raw pattern, grey: residual curve).

Melt-spun $Mg_{73}Ni_{27}$ sample

In contrast to the previous pattern for $Mg_{90}Ni_{10}$, shown in Figure 7-18, the $Mg_{73}Ni_{27}$ sample exhibited strong Mg_2Ni peaks together with much lower intensity Mg peaks, thus indicating that the Mg_2Ni phase constituted a larger volume fraction of this sample. Moreover, the peak at 38° for the $Mg_{73}Ni_{27}$ sample is much more apparent which would indicate a greater proportion of the metastable Mg_6Ni phase in this material (see Figure 7-18).

Spassov *et al.* reported this same result in several of his studies, where the XRD pattern showed a background hump indicating the presence of an amorphous phase and a peak at 38° for the Mg_6Ni phase (Spassov and Koster, 1999; Spassov et al., 2002b; Rangelova and Spassov, 2002).

The presence of Mg_6Ni was confirmed by the Rietveld refinement analysis using the *TOPAS* software. Similar to the refinement of the patterns for the melt-spun $Mg_{90}Ni_{10}$ sample (Figure 7-17), Figure 7-19 exhibited that a better fit was achieved when the Mg_6Ni phase was used in the calculations. According to the Rietveld refinement, without incorporating the Mg_6Ni phase, the refined pattern had a goodness of fit (GOF) of 2.485, whereas a better fitted pattern had a GOF of 2.026 when Mg_6Ni was included. The grain sizes were also calculated by the Rietveld refinement, and the values for both the Mg and Mg_2Ni were around 10 nm.

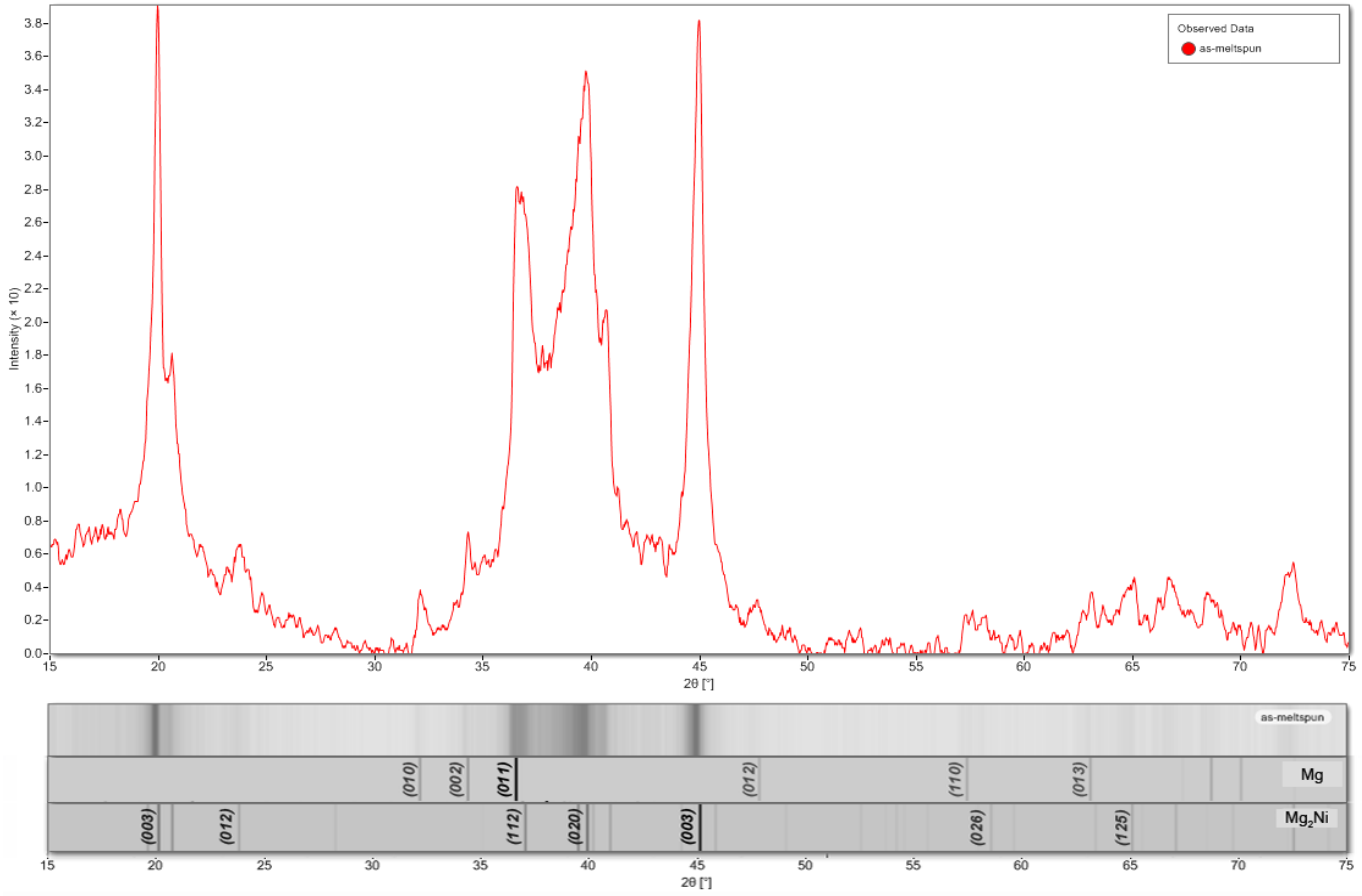

Figure 7-18 XRD pattern of the cryo-milled powder of the melt-spun $Mg_{73}Ni_{27}$ sample.

the Rietveld refinement without the information on the Mg_6Ni phase included

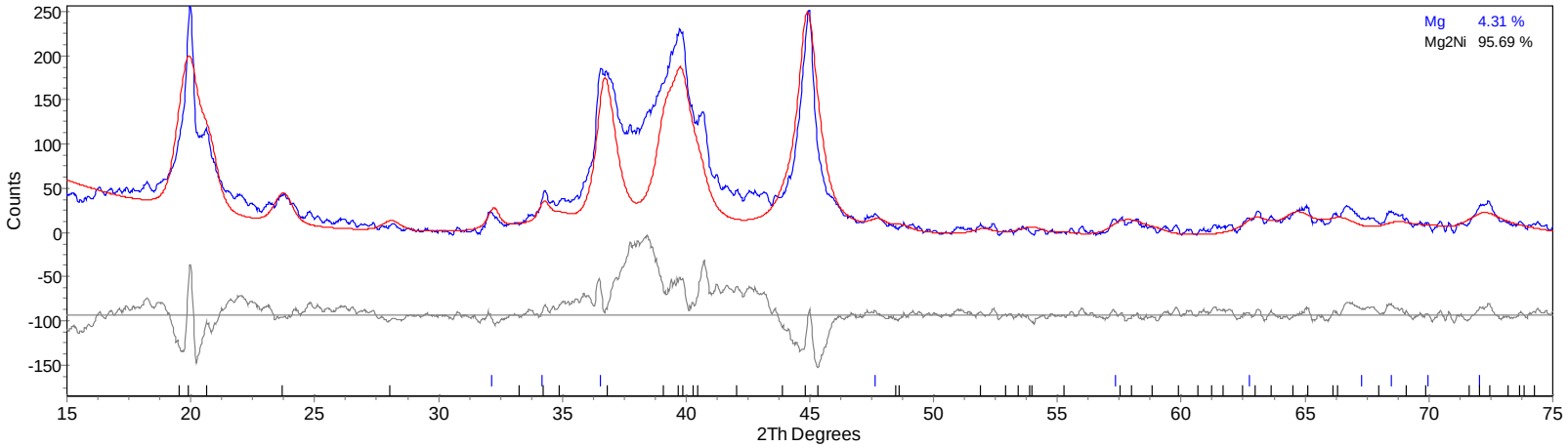

The Rietveld refinement with the information on the Mg_6Ni phase included

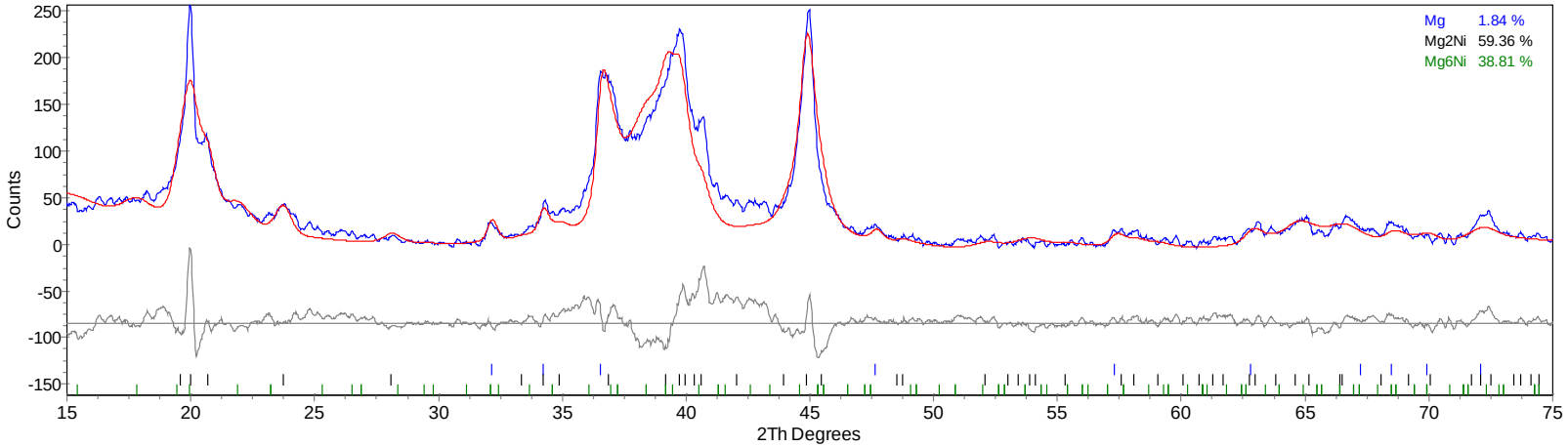

Figure 7-19 The Rietveld refined XRD patterns of the melt-spun $Mg_{73}Ni_{27}$ (Blue: raw data, Red: calculated profile; Grey: difference curve).

7.2.6. Thermal stability of the as-melt-spun alloys

DSC studies of the melt-spun $Mg_{90}Ni_{10}$ and $Mg_{73}Ni_{27}$ were performed up to 400 °C with a heating rate of 2 °C/min separately under both Ar and H_2 gas atmospheres. The aim was to identify possible re-crystallization peaks and to characterize the hydriding / dehydriding behaviour of the material.

Ar DSC measurements

The DSC profiles for both the melt-spun $Mg_{90}Ni_{10}$ and $Mg_{73}Ni_{27}$ samples are shown in Figure 7-20. Both samples exhibited exothermic peaks in a low temperature range of between 120~160 °C on heating, and no reaction occurred when cooling. These peaks are likely to relate to the re-crystallization behaviour of the amorphous phase. The melt-spun $Mg_{90}Ni_{10}$ exhibited only one small peak at 160 °C, whereas the $Mg_{73}Ni_{27}$ sample exhibited two exothermic peaks at slightly lower temperatures.

The first exothermic peak in the DSC studies for both samples is likely to be due to the re-crystallization of the amorphous phase. According to the XRD studies in Figure 7-15 and Figure 7-18, $Mg_{73}Ni_{27}$ has a much larger amorphous background when compared to that of the $Mg_{90}Ni_{10}$ sample, which would indicate a larger volume fraction of the amorphous phase. This could explain the larger exothermic peak in the DSC trace for the

$Mg_{73}Ni_{27}$ sample. On crystallization it has been shown previously that the Mg phase or Mg_2Ni phase was produced (Spassov and Koster, 1999).

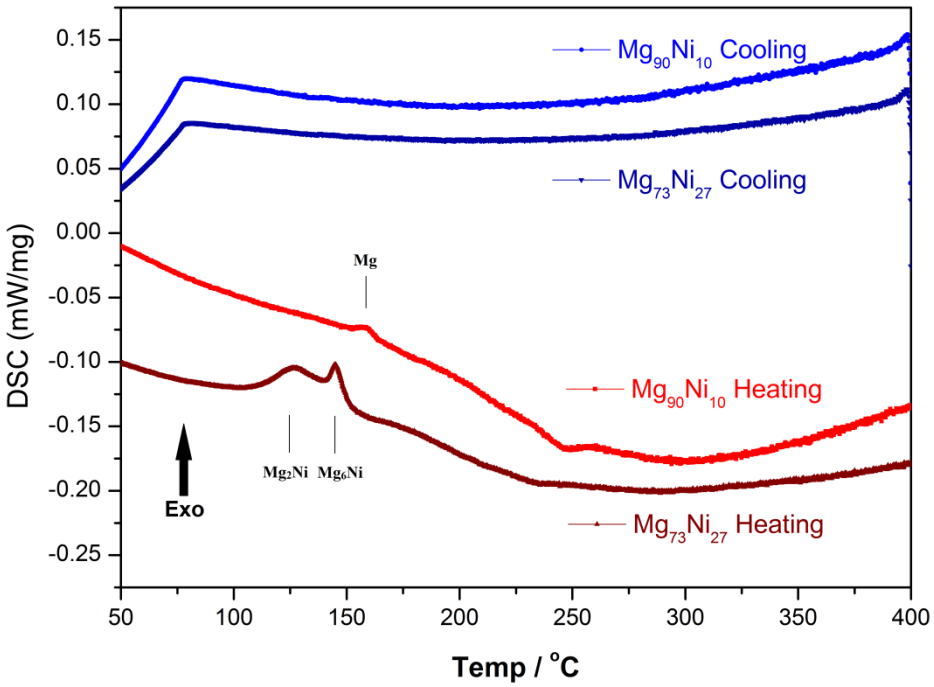

$Mg_{90}Ni_{10}$	Area	Peak Temp.	Onset Temp.	End Temp.
Heating	1.502 J/g	158.8 °C	147.2 °C	159.4 °C
Cooling	N/A	N/A	N/A	N/A

$Mg_{73}Ni_{27}$	Area	Peak Temp.	Onset Temp.	End Temp.
Heating	(in total)	127.6 °C	105.7 °C	170.1 °C
	30.47 J/g	145.1 °C	133.8 °C	151.3 °C
Cooling	N/A	N/A	N/A	N/A

Figure 7-20 DSC profiles of the $Mg_{90}Ni_{10}$ and $Mg_{73}Ni_{27}$ samples for heat treatment up to 400°C heated at 2°C/min under 4 bars of Ar atmosphere.

Song *et al.* (Song et al., 2008b) reported DSC results for the melt-spun Mg-23.5wt.%Ni alloys and this work exhibited two exothermic peaks at 160°C and 190°C, and it was claimed that they were crystallization peaks, but they did not discuss the exact crystallization behaviour. In another paper (Song et al., 2008a), melt-spun (Mg-23.5wt.%Ni)-10wt.%Cu was studied and was shown to be amorphous in the as-spun state, and showed an exothermic peak at 157°C during the DSC measurement. The crystallization peaks were later confirmed by the presence of the crystalline phases of Mg, Mg_2Ni and Mg_2Cu formed after the heat treatment and were identified by XRD.

Spassov and Koster (1999) reported DSC results for melt-spun $Mg_{87}Ni_{12}Y_1$, which showed two distinct exothermic peaks for the re-crystallization of the amorphous state. It was claimed that on heating, primary crystallization of the Mg phase accounted for the first peak at 158 °C, then followed by a second peak for the Mg_6Ni at ~40 °C higher temperature. Therefore, in this work the peak of 160 °C for the melt-spun $Mg_{90}Ni_{10}$ sample was likely to be due to the re-crystallization for Mg phase, although no peak for Mg_6Ni was detected.

Teresiak *et al.* (2009b) studied melt-spun $Mg_{85.7}Ni_{14.3}$ alloy which corresponds exactly to the Mg_6Ni in composition. Their studies showed a direct crystallization of the Mg_6Ni phase from the amorphous phase at 150 °C (from the in-situ XRD patterns). Spassov *et al.* (2002b) reported a DSC trace for the melt-spun $Mg_{83}Ni_{17}$, with only one crystallization peak at 180°C corresponding to the formation of Mg_6Ni. Ong *et al.* (1998) reported a main peak with a shoulder peak from the DSC profile for a $Mg_{82}Ni_{18}$ alloy. The XRD analysis showed that, at 160 °C, an unknown phase and the Mg_2Ni phase were

observed which was then followed by the crystallization of Mg. The unknown phase had a d-spacing of 2.37 nm which resulted in a XRD peak at 38°. Therefore, the unknown phase could be identified as Mg_6Ni.

Spassov and Koster (1999) performed DSC studies on melt-spun $Mg_{75}Ni_{20}Mm_5$ (Mm=Ce, La-rich mischmetal) which showed a two-step crystallization with the first exothermic peak for Mg_2Ni and the other for the phase $Mg_{17}Mm_2$. Spassov *et al.* then studied the DSC profiles for melt-spun $Mg_{76}Ni_{19}Y_5$ and $Mg_{78}Ni_{18}Y_4$, which also exhibited two exothermic peaks. The first peak was due to the crystallization of Mg_2Ni at ~190 °C followed by a broader and wider peaks (200 ~ 240 °C) for the Mg_6Ni phase (Spassov et al., 2002a; Rangelova and Spassov, 2002). The Mg_6Ni phase transforms into the Mg and Mg_2Ni phases at a higher temperatures with a small enthalpy change which usually is not able to be detected by the DSC measurement (Spassov et al., 2004). Todorova and Spassov (2009) claimed that the decomposition of Mg_6Ni cannot be detected at low heating rates (<40 K/min) by the DSC measurement. Therefore, in this work, no peak was observed for the decomposition process at higher temperature for both samples.

Teresiak *et al.* (2005) studied the crystallization of melt-spun $Mg_{77}Ni_{18}Y_5$, showing a similar result to Spossov's work above. The Mg_2Ni-type MgNiY phase crystallized first from the amorphous phase, followed by Mg_6Ni formed at a slightly higher temperature.

With substitution of Ca with Mg, Isogai *et al.* (2000) produced melt-spun $Mg_{62}Ni_{33}Ca_5$ which was a Mg_2Ni-type ternary alloy. It was shown that, during heating on the DSC, two exothermic peaks could be observed. The first one at 200 °C was related to the

crystallization of the Mg_2Ni phase, and the second one at 233 °C was for the Mg_2Ca and $MgNi_2$ phases.

Zhang *et al.* (2009b) reported that Mg_2Ni-type $Mg_{1-x}La_xNi$ ternary alloys exhibited two exothermic peaks during heating, corresponding to two crystallization reactions. The first at 210 °C corresponding to the crystallization of the Mg_2Ni phase from the amorphous phase. Another Mg_2Ni-type melt-spun alloy $Mg_{20}Ni_6Co_4$ ($Mg_{66.7}Ni_{20}Co_{13.3}$) studied by Zhang *et al.* (2009c), exhibited an exothermic peak at 232 °C, which was claimed to be the crystallization peak for the formation of the Mg_2Ni phase.

Therefore, from the previous works, it would appear that, the primary crystallization reaction under Ar, is usually that for Mg or Mg_2Ni,, followed by the crystallization of the Mg_6Ni phase. If the Mg-Ni ratio is higher than 6:1, the Mg phase will be crystallized first.

In the case of the $Mg_{90}Ni_{10}$ sample studied in this work, it can be assumed that the primary crystallization of the Mg phase was related to the predominant peak, with no peak for the formation of Mg_6Ni detected by the DSC measurement as of the Ni content which was likely to be too small to form the Mg_6Ni phase (Spassov et al., 2004; Spassov et al., 2002b). Mg_6Ni was likely to be decomposed into the Mg and Mg_2Ni phases over a broad high temperature range above 300 °C, and the exothermic peak associated with this transformation was rather small and cannot be detected by DSC measurement (Spassov and Koster, 1999; Spassov et al., 2002a; Spassov et al., 2002b). For the $Mg_{73}Ni_{27}$ sample, the primary exothermic reaction was likely to be due to the crystallization of the Mg_2Ni phase at 105 ~135 °C, followed by the crystallization of Mg_6Ni with a sharper peak at

145 °C. According to the Rietveld refinement (Figure 7-19), the $Mg_{73}Ni_{27}$ sample had a certain amount of the Mg_6Ni phase, thus a possible peak attributed to Mg_6Ni was exhibited in the DSC measurements.

H_2 DSC measurements

Figure 7-21 shows the DSC curves for the melt-spun samples of $Mg_{90}Ni_{10}$ and $Mg_{73}Ni_{27}$, cryo-milled powders. The crystallization behaviour shown during the DSC measurements under an Ar atmosphere would also be expected to occur during heat treatment under H_2. On further heating it would be expected that the hydriding reaction would also occur. As a result, the H_2 DSC curve on heating, exhibits the consequence of overlapping peaks of both the hydriding and crystallization behaviour. When cooling, the DSC curve exhibits the dehydriding reaction of the alloys.

For the $Mg_{90}Ni_{10}$ sample on heating, a very broad peak can be observed at 200 °C with an onset temperature of 130 °C compared to that in the Ar DSC (Figure 7-20). For the $Mg_{73}Ni_{27}$ sample, one broad peak can also be seen at ~140 °C.

In Figure 7-21 of the $Mg_{73}Ni_{27}$ sample, only one exothermic peak was observed during heating and became bigger and broader than those two peaks in the Ar DSC results, possibly due to the result of overlapping exothermic peaks of the hydrogenation reaction with the crystallization processes. The crystallization process has been discussed in the previous paragraphs, and consists of the formation of the Mg_2Ni and Mg_6Ni phases. The hydriding reactions usually correspond to the formation of the hydrides of MgH_2 and

Mg_2NiH_4. The hydriding reactions for the $Mg_{73}Ni_{27}$ at these temperatures (<200 °C) were investigated further using in-situ XRD and are discussed in section 7.2.7.

$$Mg + H_2 \rightarrow MgH_2$$

$$Mg_2Ni + 2H_2 \rightarrow Mg_2NiH_4$$

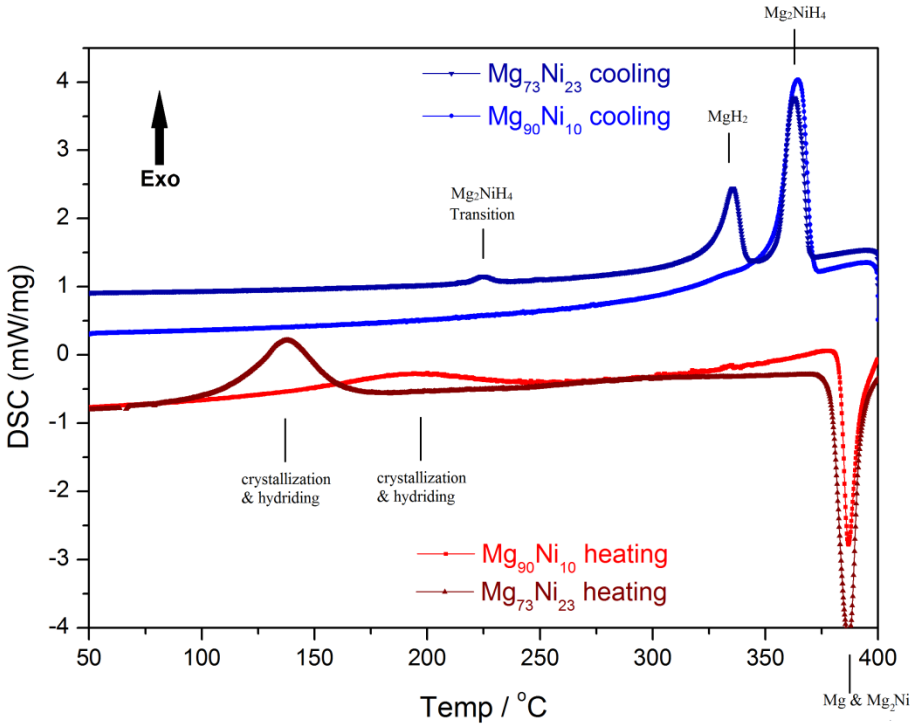

$Mg_{90}Ni_{10}$	Energy	Peak Temp.	Onset Temp.	End Temp.
Heating	491.8 J/g	200.0 °C	129.9 °C	259.4 °C
	-569.0 J/g	386.9 °C	383.0 °C	391.8 °C
Cooling	1170 J/g	364.3 °C	354.0 °C	370.6 °C

$Mg_{73}Ni_{27}$	Energy	Peak Temp.	Onset Temp.	End Temp.
Heating	892.6 J/g	137.6 °C	78.8 °C	160.9 °C
	-1020 J/g	386.7 °C	379.4 °C	392.0 °C
Cooling	625.8 J/g	362.7 °C	355.9 °C	369.2 °C
	384.6 J/g	335.6 °C	326.7 °C	341.0 °C
	17.64 J/g	224.2 °C	222.2 °C	227.7 °C

Figure 7-21 DSC profiles of the $Mg_{90}Ni_{10}$ and $Mg_{73}Ni_{27}$ samples for heat treatment up to 400°C, heated at 2°C/min under flowing 10 bars of H_2 gas.

At higher temperatures of around 380 °C, there is a sharp endothermic peak for both samples which relates to the dehydrogenation of the hydrided samples. A decrease of 20 °C in the temperature for H_2 desorption is observed when compared to that obtained from the DSC result for the melt-spun Mg ribbons under the same conditions. During cooling in H_2, the DSC curve shows a major exothermic peak (~360 °C) which for both samples is expected to be due to the formation of MgH_2. However, the $Mg_{73}Ni_{27}$ sample shows another exothermic peak at a slightly lower temperature (~340 °C) which suggests that another phase is hydriding. This is likely to be due to the formation of the phase Mg_2NiH_4, as the XRD studies have shown that a large proportion of the material is comprised of the Mg_2Ni phase.

Mg_2NiH_4 hydride has two forms: a high temperature (HT) phase with the cubic Mg_2NiH_4 form and a low temperature (LT) phase which consists of the monoclinic Mg_2NiH_4 form. At lower temperatures of around 220 °C, there is a very small exothermic peak for the $Mg_{73}Ni_{27}$ sample (see Figure 7-21). This could be as a result of the phase transition from HT-Mg_2NiH_4 to LT-Mg_2NiH_4 forms.

$$HT\text{-}Mg_2NiH_4 \rightarrow LT\text{-}Mg_2NiH_4$$

Selvam *et al.* (1988) reported that the transformation between LT- and HT-Mg_2NiH_4 occurs at 240 °C. Kalinichenka *et al.* (2009) found LT-Mg_2NiH_4 in the XRD pattern of hydrided melt-spun Mg-Ni-Y samples. Moreover, Kalinichenka *et al.* (2010) also reported the Mg_2NiH_4 transition in a melt-spun $Mg_{90}Ni_{10}$ sample, whereas this transition was not detected in the H_2 DSC of the $Mg_{90}Ni_{10}$ sample reported in the present work.

Cyclic DSC measurements

To confirm the crystallization process on heating of the melt spun ribbons, cyclic DSC studies of the $Mg_{73}Ni_{27}$ powder were performed in both atmospheres of Ar and H_2. Figure 7-22 provides conclusive support for the findings obtained by Ar DSC shown in Figure 7-20. The exothermic peaks did not appear again after the 2nd cycle in Ar DSC, thus revealed that the exothermic peaks in the Ar DSC correspond to the crystallization behaviour of the melt-spun $Mg_{73}Ni_{27}$ sample.

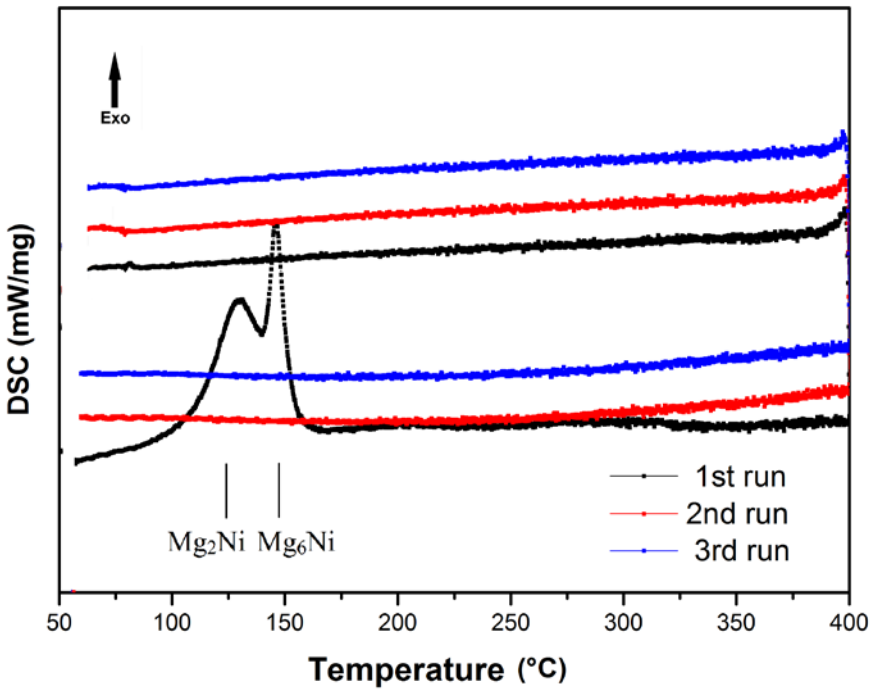

$Mg_{73}Ni_{27}$	Area	Peak Temp.	Onset Temp.	End Temp.
Heating 1	(in total)	131.2 °C	107.2 °C	158.8 °C
	43.15 J/g	146.0 °C	140.3 °C	152.9 °C
Heating 2	N/A	N/A	N/A	N/A
Heating 3	N/A	N/A	N/A	N/A
Cooling 1	N/A	N/A	N/A	N/A
Cooling 2	N/A	N/A	N/A	N/A
Cooling 3	N/A	N/A	N/A	N/A

Figure 7-22 Three cycle DSC profiles of the $Mg_{73}Ni_{27}$ sample, heated at 2°C/min under flowing 4 bar Ar.

Figure 7-23 shows three cycles of H_2 DSC for the melt-spun $Mg_{73}Ni_{27}$ sample. For the first cycle, a broad exothermic crystallization peak was obtained at low temperatures on heating, and it did not appear again after the 1st cycle. This is in accordance with the cyclic Ar DSC result reported in the previous paragraphs which indicates that it would not exhibit an exothermic crystallization peak after the 1st cycle. In addition, it would not exhibit exothermic hydriding peaks, because the sample was already hydrided when cooled from high temperatures.

At higher temperatures (>300 °C), the cyclic H_2 DSC studies shows the hydriding / dehydriding behaviour of the melt-spun $Mg_{73}Ni_{27}$. During heating on the first cycle, a large endothermic peak could be observed at 384 °C which is likely to correspond to the dehydriding of MgH_2 and possibly of some Mg_2NiH_4. With increasing cycles, the dehydriding peak at 384°C divides into two peaks corresponding to the dehydriding of Mg_2NiH_4 and MgH_2. The same finding has been reported by Selvam *et al* (1988) who identified the new endothermic peak as the dehydriding peak for Mg_2NiH_4.

Moreover, on cooling, the DSC curves show two distinct exothermic peaks. The peak at 364 °C is likely to correspond to the formation of MgH_2 and the peak at 336 °C to the Mg_2NiH_4 hydride. The peak believed to relate to Mg_2NiH_4, increases with increasing cycles, which would indicate that the full hydriding of this phase required an activation process.

Friedlmeier *et al.* (1999) found a similar cyclic H_2 DSC result for melt-spun $Mg_{87}Ni_{13}$. The hydriding and dehydriding of Mg and MgH_2 phases occurred at 390 °C and 420 °C

during cooling and heating, respectively. Moreover, the peaks grow with increasing number of cycles, which was also found in this work (Figure 7-23).

On heating and cooling, small peaks at around 220 °C were very apparent, thus indicating the transition between HT&LT Mg_2NiH_4 phases which is a reversible reaction (Selvam et al., 1988).

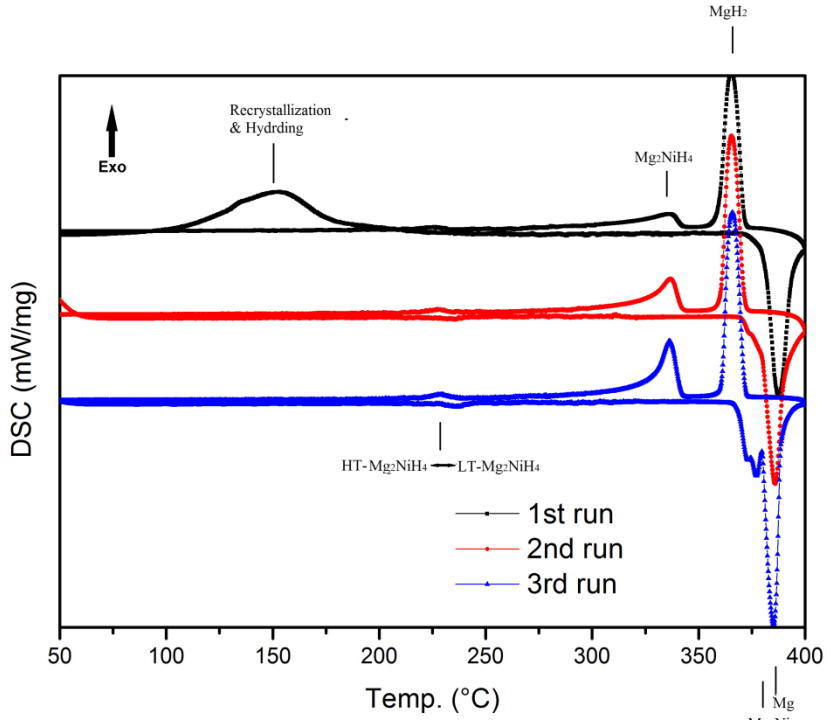

Crystallization Peak	Area (J/g)	Peak Temp. (°C).	Onset Temp. (°C)	End Temp. (°C)
Heating 1	712.8	162.1	139.9	177.4
Cooling 1	N/A	N/A	N/A	N/A
Dehydriding on heatings				
Heating 1	-824.8	387.0	380.6	391.9
Heating 2	-1052	384.5	376.7	387.3
Heating 3	-1169	384.1	379.3	386.6
Hydriding on coolings				
Cooling 1	580.5	364.1	358	369.5
	335.3	336.3	327.6	341.6
Cooling 2	565.5	363.9	358.3	369.6
	441.7	336.0	329.4	341.0
Cooling 3	566.7	364.3	359.1	370.0
	538.2	335.6	329.5	341.0
Mg_2NiH_4 Transition				
Heating 1	N/A	N/A	N/A	N/A
Heating 2	-15.33	234.3	228	237.9
Heating 3	-21.64	235.8	227.9	237.7
Cooling 1	14.42	225.5	215.8	228.0
Cooling 2	32.46	226.8	219.2	226.8
Cooling 3	26.21	228.5	222.9	236.0

Figure 7-23 Three cycles DSC profiles of the $Mg_{73}Ni_{27}$ heated at 2°C/min under flowing 10 bar H_2.

7.2.7. Crystallization and hydrogenation behaviour of the melt-spun $Mg_{90}Ni_{10}$ and $Mg_{73}Ni_{27}$ alloys

XRD of the melt-spun $Mg_{90}Ni_{10}$ and $Mg_{73}Ni_{27}$ samples after DSC

XRD scans were performed for both samples after the Ar and H_2 DSC treatments. As discussed in the previous section, after one cycle of Ar DSC, the samples exhibited no further crystallization peaks. Figure 7-24 showed the XRD patterns of the samples after Ar DSC, consisting of peaks due to the Mg and Mg_2Ni phases only. The major peaks of $Mg_{90}Ni_{10}$ were Mg peaks and those due to $Mg_{73}Ni_{27}$ are Mg_2Ni. The grain size increased up to 40 nm calculated by the FWHM values and using the Scherrer equation.

After the DSC measurement in 10 bars of H_2, both the melt-spun $Mg_{90}Ni_{10}$ and $Mg_{73}Ni_{27}$ samples were left in the hydrided state. As expected, the XRD patterns (Figure 7-25) for both samples showed peaks due to MgH_2 and Mg_2NiH_4 hydrides, in agreement with the discussion of the H_2 DSC results. However, the $Mg_{90}Ni_{10}$ and $Mg_{73}Ni_{27}$ samples exhibited slightly different hydrogenation behaviour.

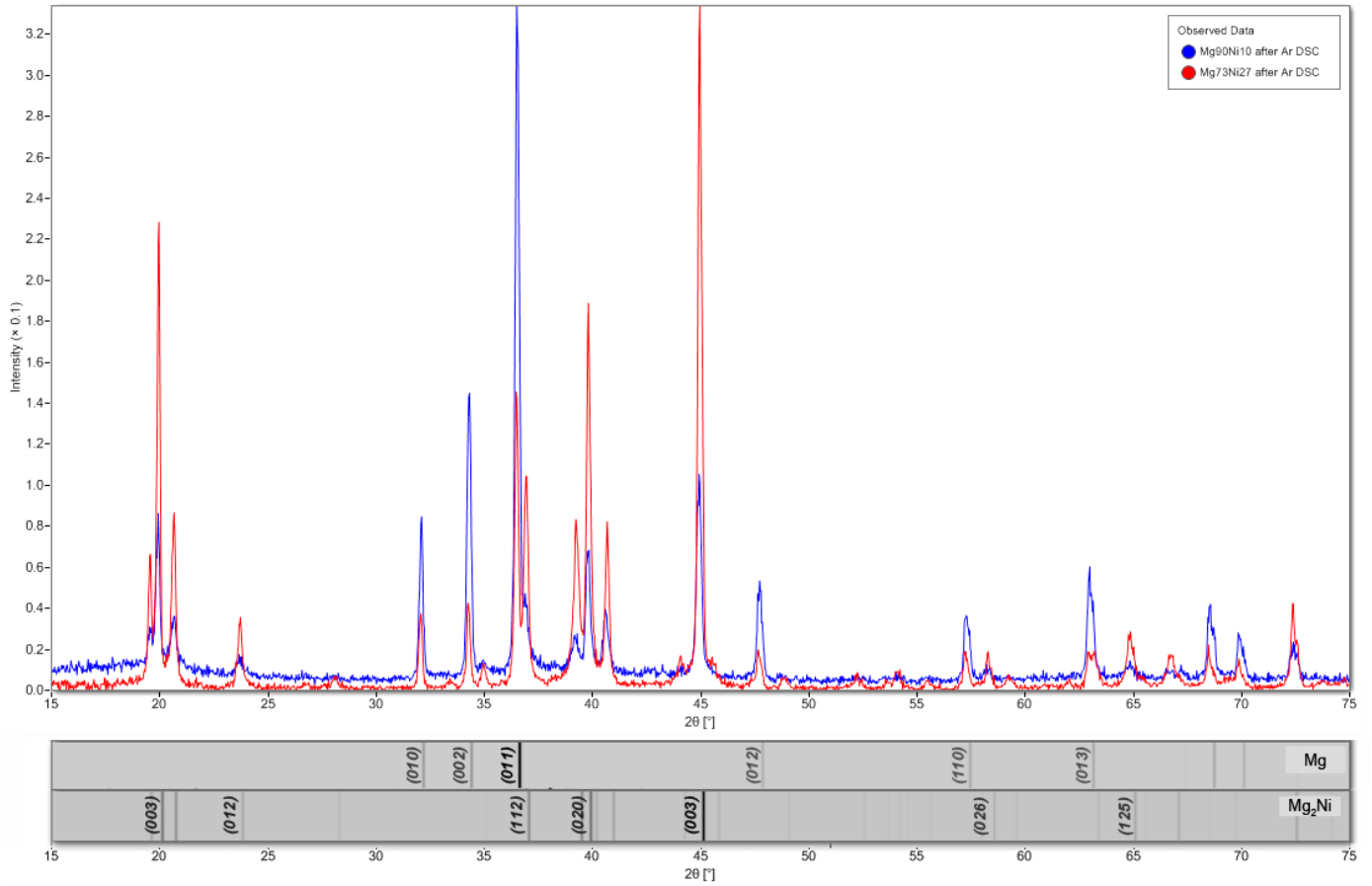

Figure 7-24 XRD patterns of the melt-spun $Mg_{90}Ni_{10}$ (blue) and $Mg_{73}Ni_{27}$ (red) samples after DSC in 4 bar Ar.

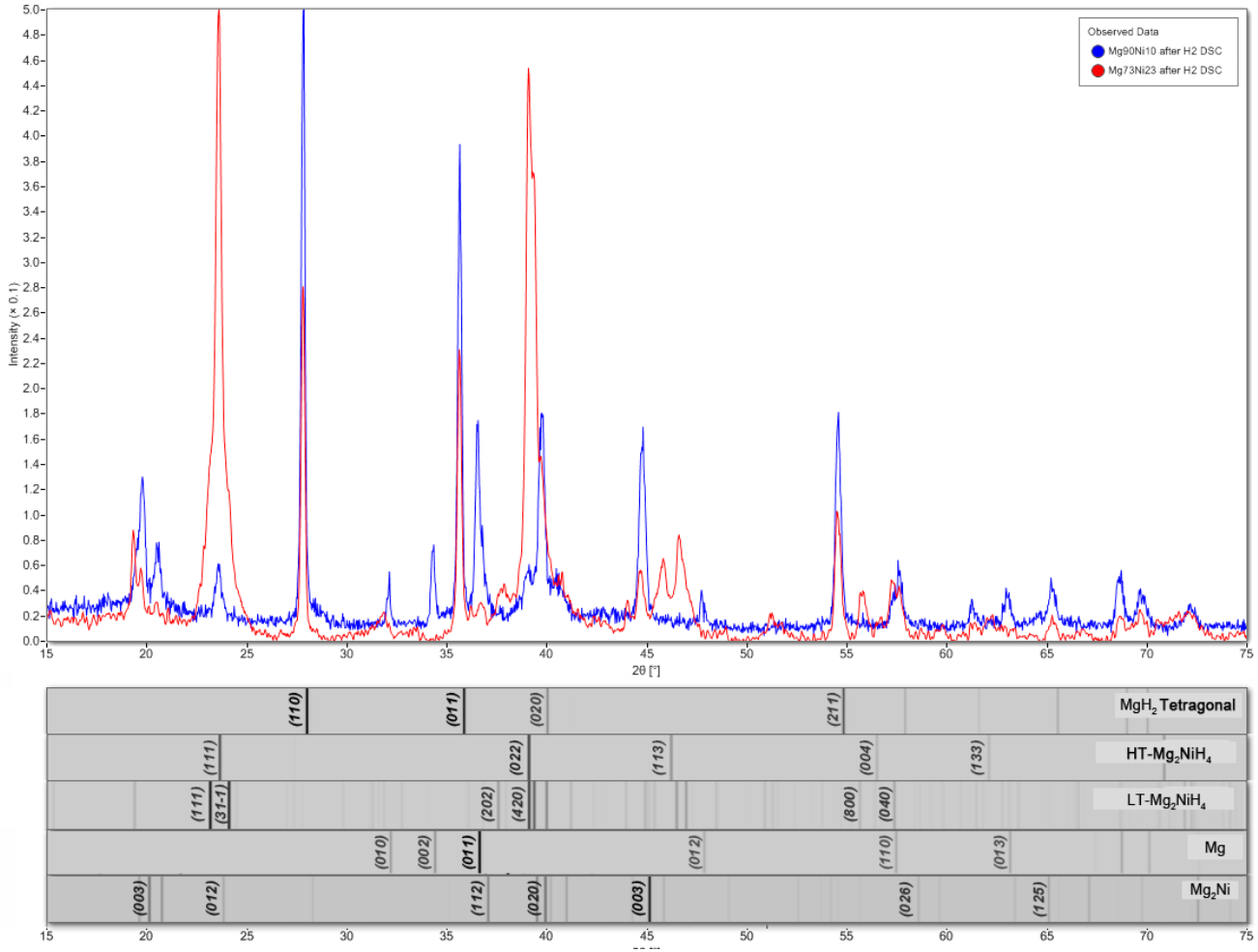

Figure 7-25 XRD patterns of the melt-spun $Mg_{90}Ni_{10}$ (blue) and $Mg_{73}Ni_{27}$ (red) powders after DSC in 10 bars of H_2.

For the $Mg_{90}Ni_{10}$ sample in the XRD pattern, the tetragonal magnesium hydride α-MgH_2 (also called β-MgH_2) was the predominant phase, although some smaller peaks relating to the Mg phase could also be clearly identified, indicating an incomplete reaction of the sample with hydrogen. However, the peaks of Mg_2NiH_4 were very small, and the other peaks were likely to be attributable to the Mg_2Ni phase. The XRD pattern revealed that the $Mg_{90}Ni_{10}$ sample was not fully hydrided. Most of Mg phase hydrided into α-MgH_2, but the hydriding of Mg_2Ni had hardly begun.

However, when the Rietveld refinement was applied (Figure 7-26), the refined pattern had a better fit when the H-diffused Mg_2Ni (also called $Mg_2NiH_{0.3}$ solid solution phase) was introduced instead of the Mg_2Ni phase. Therefore, according to the Rietveld refinement result, it indicates the presence of MgH_2, $Mg_2NiH_{0.3}$ and Mg_2NiH_4 phase with the weight fraction of each phase. This Rietveld refinement result is in good agreement with the results of Wu *et al.* (2009) who analysed the XRD pattern of hydrided melt-spun $Mg_{88}Ni_{10}Mm_2$ (see Table 7-3).

Sample	**MgH_2**	**$Mg_2NiH_{0.3}$**	**Mg_2NiH_4**	**Others**	**Source**
$Mg_{90}Ni_{10}$	51.66 %	25.04 %	13.22 %	10.07 % (Mg)	Rietveld refinement
$Mg_{88}Ni_{10}Mm_2$	55.9 %	24.8 %	12 %	7 % (MmH_3)	(Wu et al., 2009)

*all the values are in weight percentage.

Table 7-3 Weight fractions of $Mg_{90}Ni_{10}$ after H_2 DSC by Rietveld refinement, in comparison with the result of hydrided $Mg_{88}Ni_{10}Mm_2$.

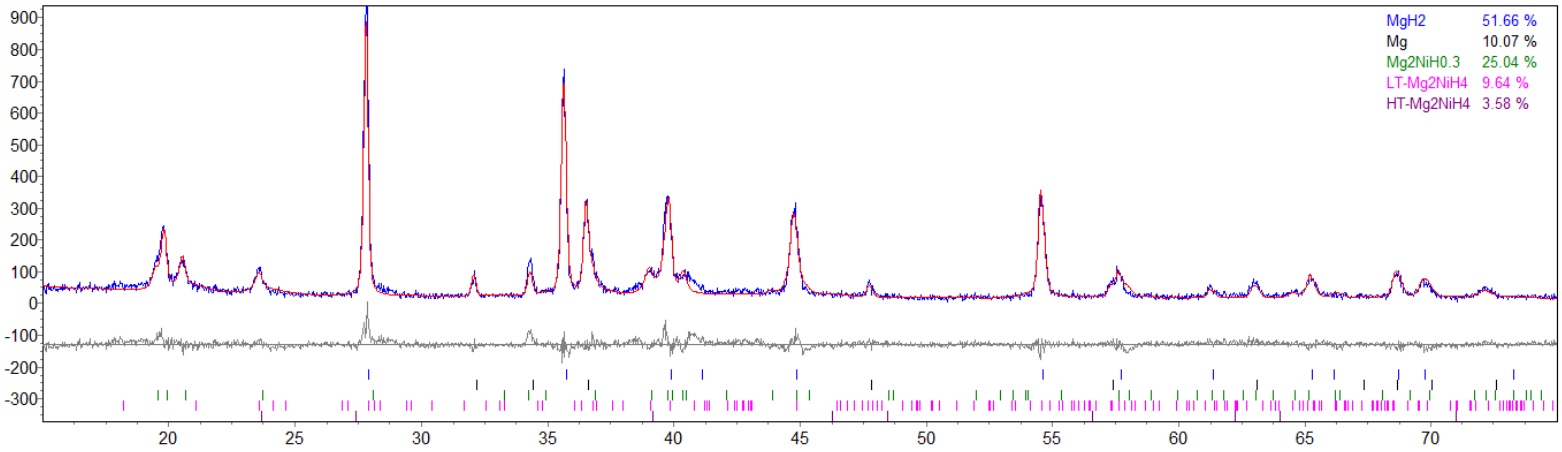

Figure 7-26 The Rietveld refinement of the XRD pattern of the melt-spun $Mg_{90}Ni_{10}$ powder after 10 bar H_2 DSC.

(red: calculated pattern, blue: raw pattern, grey: residual curve)

In contrast to the $Mg_{90}Ni_{10}$ XRD pattern, the pattern of $Mg_{73}Ni_{27}$ (shown in Figure 7-25) does not exhibit peaks due to Mg or Mg_2Ni, thus indicating a complete hydriding process after H_2 DSC. This indicates that this sample has enhanced hydriding kinetics compared to those of the $Mg_{90}Ni_{10}$ sample. The main peaks in the XRD pattern related to the Mg_2NiH_4 phase, with the peaks of the α-MgH_2 phase being of a lower intensity. The LT-Mg_2NiH_4 phase could also be identified in the XRD pattern but with even weaker intensity peaks compared to those for the α-MgH_2 phase. This suggests that the LT-Mg_2NiH_4 phase contributes only a small fraction of the sample. According to the results of the cyclic H_2 DSC for the $Mg_{73}Ni_{27}$, in the 1st cycle the peak of LT/HT-Mg_2NiH_4 is small, and it increases in the 2nd and 3rd cycle. Therefore, after 1 cycle of H_2 DSC, the phase transition was incomplete and on further cycling it was more pronounced.

In addition, it is worth pointing out that, for both samples, no peak for γ-MgH_2 phase has been found in the XRD patterns. Teresiak *et al.* (2009b) found that γ-MgH_2 could be identified in the in-situ XRD for the melt-spun $Mg_{85.7}Ni_{14.3}$ when hydrided at 180 °C and 5 bar H_2, but it transformed into α-MgH_2 at higher temperatures (316 °C). Therefore, on the DSC it is not expected that the γ-MgH_2 phase would be observed after the heat treatment at high temperature (400 °C).

In Figure 7-25, the peaks appear broader than those in the XRD of samples after Ar DSC shown in Figure 7-24, especially when comparing the peaks for the Mg phase. The peak broadening suggests a smaller grain size, which has been calculated to be 25 nm as opposed to 40 nm after Ar DSC. It is well known that when H atoms are dispersed within a crystal structure they can inhibit the crystallization and hence slow further grain growth.

140 °C in-situ isothermal XRD of the melt-spun $Mg_{90}Ni_{10}$ sample

Over a range of pressure and temperature, in-situ XRD analysis was performed on the melt-spun Mg-Ni powders in a gas cell. A melt-spun $Mg_{90}Ni_{10}$ cryo-milled powder sample was loaded into a *Bruker* XRD inside the gas cell. The sample cell was evacuated and, over the course of 2 hours, purged three times with H_2. The cell was then pressurised to 10 bar H_2 gas and the sample was heated to 140 °C with a heating rate of 2 °C/min. It was therefore possible to monitor the crystallographic changes which occurred at the temperature where crystallization and hydrogen uptake was observed from the DSC data (Figure 7-21).

The XRD scan started as soon as the temperature reached the set temperature of 140 °C, and it scanned the sample continuously 10 times with the same settings as those for the room temperature XRD scans. Each run took around 25 min, so the total scanning time was 4 hours.

The first and 10^{th} XRD scan for the $Mg_{90}Ni_{10}$ milled sample under 10 bar H_2 gas are shown in Figure 7-27. Both patterns look very similar, but on closer inspection it was revealed that Mg_2Ni, α-MgH_2 and γ-MgH_2 appeared at 140 °C in the 10 bar H_2 atmosphere runs.

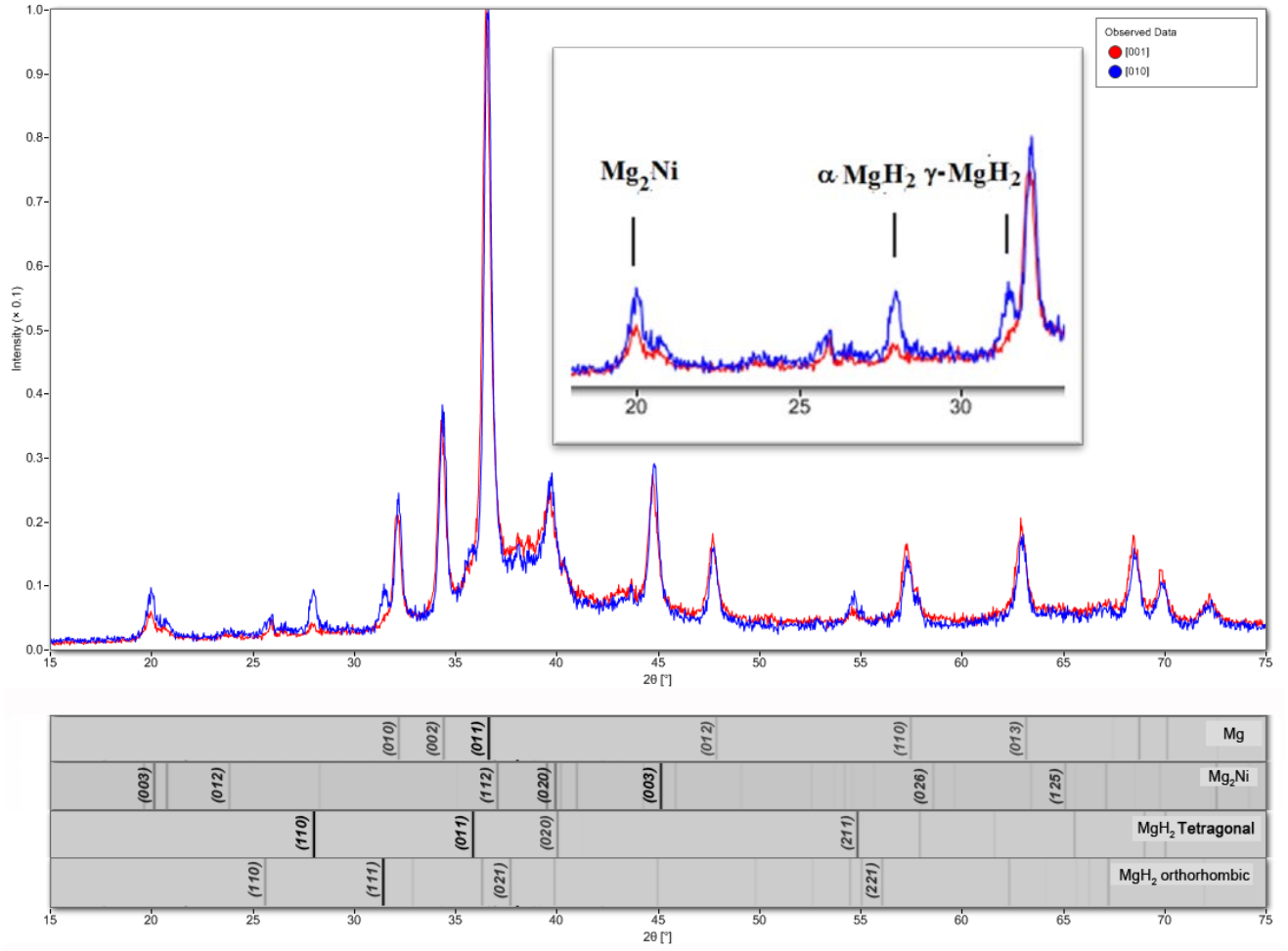

Figure 7-27 XRD patterns for the 1st and 10th scans for the $Mg_{90}Ni_{10}$ cryo-milled powder sample at 140 °C under 10 bar H_2 gas with an enlarged area of the pattern for a close inspection.

By using *TOPAS Academic*, the weight fraction of each phase can be calculated from the Rietveld refinement, according to the standard cif files. It should be pointed out that the amount of the amorphous phase cannot be calculated from the Rietveld refinement. For the melt-spun $Mg_{90}Ni_{10}$ sample, the difference will be subtle, as according to the XRD pattern of the as-spun powder (Figure 7-15), it is not expected to have large amounts of the amorphous phase.

The presence of the Mg_6Ni phase has been discussed in the Section 7.2.5. By using the same method, the presence of the intermediate metastable phase Mg_6Ni, has again been confirmed. Taking the second run [002] as an example, the grey curve is the difference between the observed data and the calculated data from the Rietveld refinement. Without incorporating the crystallographic information on the phase Mg_6Ni, the calculated curve (red) does not fit well with a goodness of fit (GOF) of 5.195. The grey curve shows a broad peak around 35° ~ 40°, which corresponds to the peak due to Mg_6Ni. By introducing the crystallographic information on the Mg_6Ni phase, the calculated curve fits much better with a GOF of 1.521, and the differential grey curve is nearly flat. Therefore, it is believed that, in hydrogen the Mg_6Ni exists in the melt-spun $Mg_{90}Ni_{10}$ powder.

As shown in Figure 7-28, the weight fraction can be calculated from the Rietveld refinement using *TOPAS Academic*. By listing all the weight fractions of all 10 XRD scans in Table 7-4, the change of weight for each fraction can be plotted in Figure 7-29 indicating the phase transformation of the melt-spun $Mg_{90}Ni_{10}$ sample at 140 °C under 10 bar H_2 atmosphere.

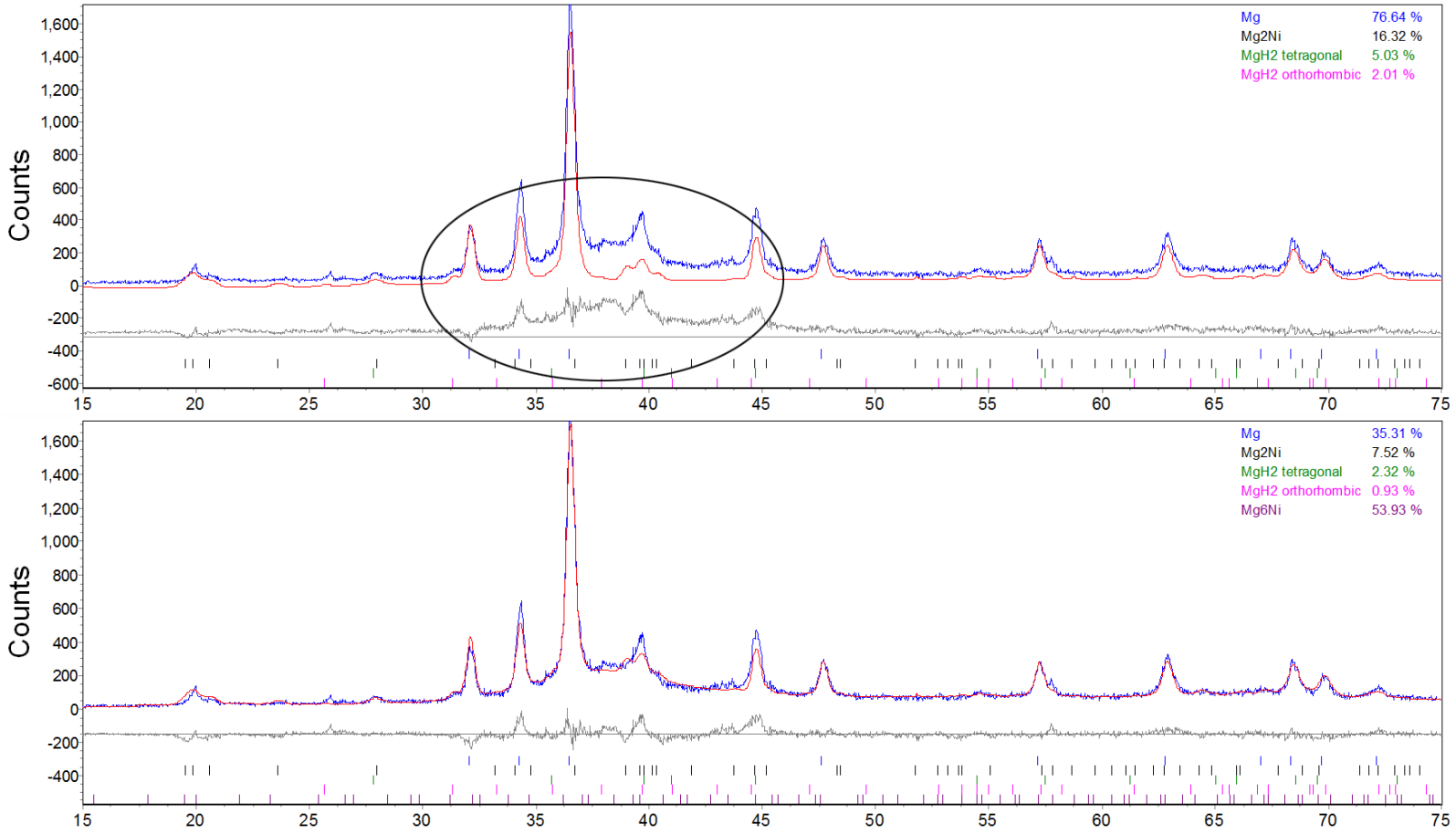

Figure 7-28 The Rietveld refinement of the 2nd pattern of 140 °C isothermal XRD of the melt-spun $Mg_{90}Ni_{10}$ pattern with/without Mg_6Ni refined.

(Blue: raw data, Red: calculated pattern; Grey: difference curve)

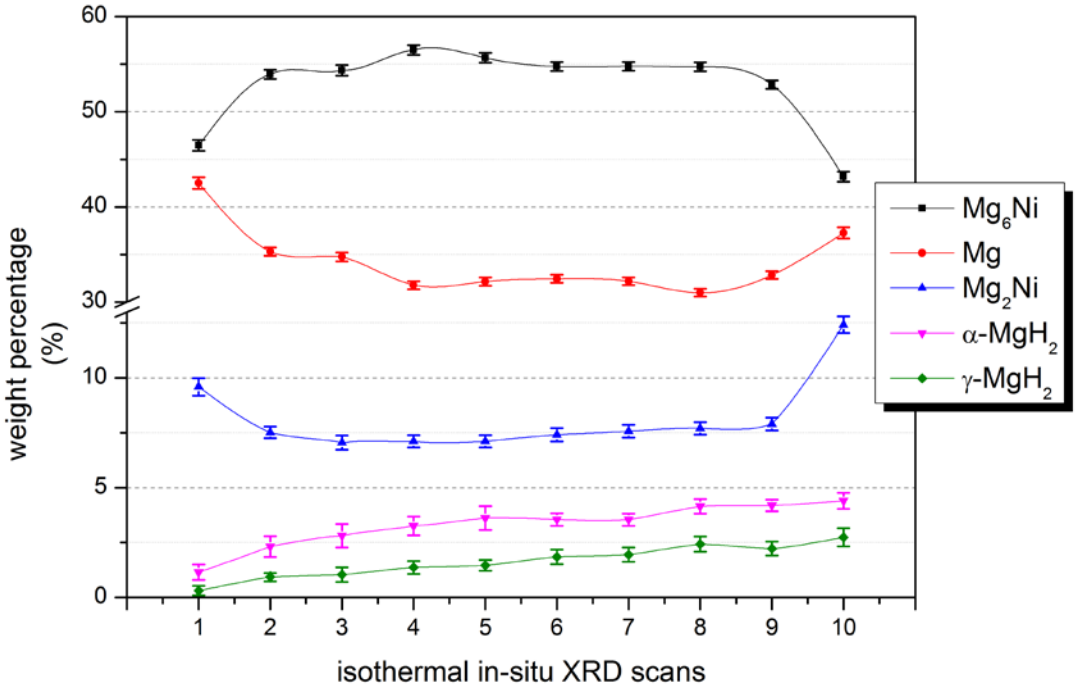

Figure 7-29 Weight fraction as a function of scans for the melt-spun $Mg_{90}Ni_{10}$ cryo-milled powder at 140 °C under 10 bars of H_2.

Scans	Mg_6Ni	Mg	Mg_2Ni	α-MgH_2	γ-MgH_2	GOF
[001]	46.46	42.5	9.59	1.15	0.31	2.028
[002]	53.93	35.31	7.52	2.32	0.93	1.521
[003]	54.35	34.75	7.05	2.81	1.04	1.538
[004]	56.50	31.76	7.11	3.26	1.37	1.531
[005]	55.67	32.15	7.11	3.62	1.46	1.536
[006]	54.76	32.44	7.41	3.55	1.85	1.539
[007]	54.77	32.18	7.57	3.54	1.95	1.563
[008]	54.72	30.98	7.70	4.15	2.43	1.545
[009]	52.84	32.84	7.90	4.19	2.23	1.545
[010]	43.18	37.26	12.42	4.40	2.74	1.636

*all the values are in weight percentage (wt.%)

Table 7-4 Weight fractions calculated from the 140 °C isothermal XRD using the Rietveld refinement.

Figure 7-29 shows that, as soon as the XRD scan started, the α-MgH_2 was the hydride that formed first. In addition, to a lesser degree the γ-MgH_2 was also formed at 140 °C. Gennari *et al.* (2001) also reported that by ball milling, the formation of γ-MgH_2 was observed even at room temperature. At the 10th run, the decrease of Mg_6Ni occurred along

with the increase of both Mg and Mg_2Ni, which agrees with the work of Teresiak *et al.* (2009b) who reported that, in 5 bar H_2, the decomposition of Mg_6Ni started at 210 °C for the melt-spun $M_{85.7}Ni_{14.3}$. Teresiak *et al.* also explained that the presence of Mg_6Ni phase lead to the formation of the γ-MgH_2 phase under H_2 gas but at higher temperatures (180 °C). This is discussed in more detail later in this chapter.

In the 140 °C XRD pattern, the Mg_2NiH_4 phase was not found which is surprising as it has been reported to be easier to activate and has a lower enthalpy of formation compared to that of MgH_2 (Reilly and Wiswall Jr, 1968). Mg_2NiH_4 was shown to form for the $Mg_{90}Ni_{10}$ sample measured in H_2 on the DSC (Figure 7-21). This must have occurred at much higher temperatures. Thus, there are some other hydriding reactions which occur in a higher temperature range than 140 °C. Subsequently, variable temperature in-situ XRD was performed to investigate further the nature of the hydrogenation reactions.

Variable temperature in-situ XRD of the melt-spun $Mg_{73}Ni_{27}$

For both samples, in-situ XRD under 10 bar H_2 was performed at every 20 °C from room temperature to 420 °C, in order to study the crystallization and hydrogenation behaviour.

Melt-spun $Mg_{90}Ni_{10}$

The in-situ XRD patterns for the $Mg_{90}Ni_{10}$ sample showed no significant crystallographic changes on heating from RT to 420 °C. However on cooling, hydriding peaks could be observed in the XRD patterns. Therefore, for comparison, the patterns between 380 °C 340 °C and 300 °C have been shown in Figure 7-30. The XRD patterns at all temperatures are listed in the appendix.

At 340 °C, the hydriding of α-MgH_2 could be observed, with an increase of the peak intensity and the corresponding decrease of the intensity of the peaks for the Mg phase. The peak changes became more significant at 300 °C. This hydriding behaviour is in good agreement with the results of the H_2 DSC for the $Mg_{90}Ni_{10}$ sample which showed one hydriding peak at 360 °C.

At all three temperatures, the Mg_2Ni phase did not exhibit any hydriding reactions. The cyclic H_2 DSC for the $Mg_{73}Ni_{27}$ sample has shown that the Mg_2Ni phase was not active during the first cycle of hydrogen sorption, and it contributed only a small amount of the volume fraction for the $Mg_{90}Ni_{10}$ sample.

The Al_2O_3 phase also appeared in the XRD patterns in Figure 7-30. This was because there was not enough powders to fill the XRD sample holder with the melt-spun $Mg_{90}Ni_{10}$ and hence it was mixed with Al_2O_3 power for the in-situ XRD scans.

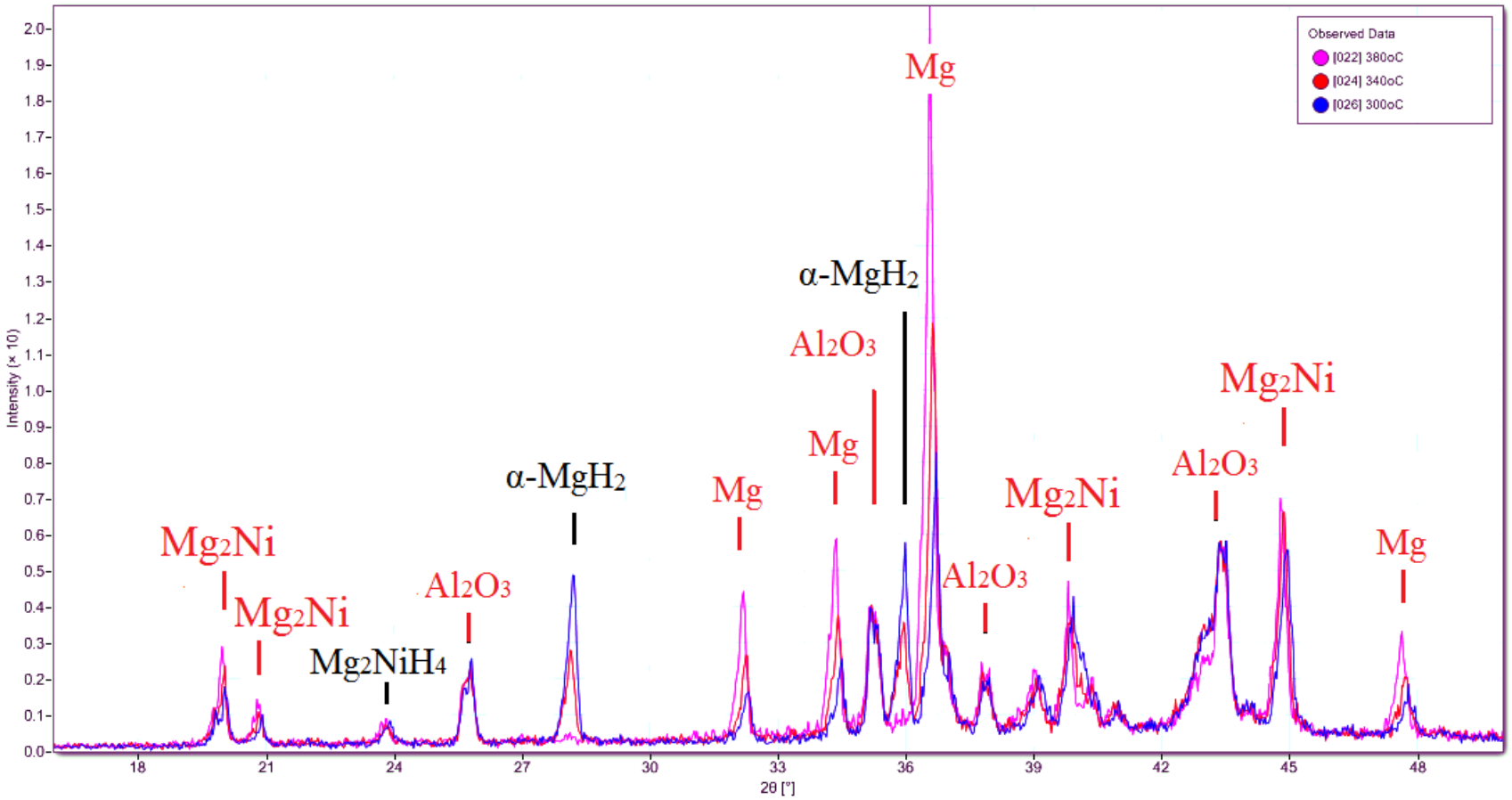

Figure 7-30 Various temperature in-situ XRD of the melt-spun $Mg_{90}Ni_{10}$ sample under 10 bars of H_2 at 380 °C, 340 °C and 300 °C in 2θ range of 16° to 50°.

Melt-spun $Mg_{73}Ni_{27}$

For the melt-spun $Mg_{73}Ni_{27}$ powder, at temperatures up to 140 °C, no significant crystallographic changes could be observed. Therefore, the XRD patterns are shown from 160 °C onwards. In order to make comparison easier, the patterns between RT, 160 °C and 220 °C were shown together and then from 300 °C to 380 °C. All of the scans at all temperatures are shown in the appendix.

Figure 7-31 shows the XRD patterns for the melt-spun $Mg_{73}Ni_{27}$ powder under 10 bar H_2 at RT, 160 °C, and 220 °C. The XRD patterns for the 160 °C and 220 °C traces show a progressively lower content of Mg and Mg_2Ni. The amorphous background was shown to shrink at 160 °C (shown as the arrow in Figure 7-31), thus indicating crystallization and phase transformation of the metastable Mg_6Ni. At 160 °C, both α-and γ-MgH_2 can be observed.

At 220 °C, the intensity of the XRD peak due to γ-MgH_2 phase increases further compared to the trace at 160 °C. The increase in the amount of γ-MgH_2 is likely to be due to the transformation of the Mg_6Ni phase under a H_2 atmosphere. Teresiak *et al.* (2009b) found that the Mg_6Ni phase transformed into γ-MgH_2 at 180°C under H_2 for a melt-spun $Mg_{85.7}Ni_{14.3}$ material.

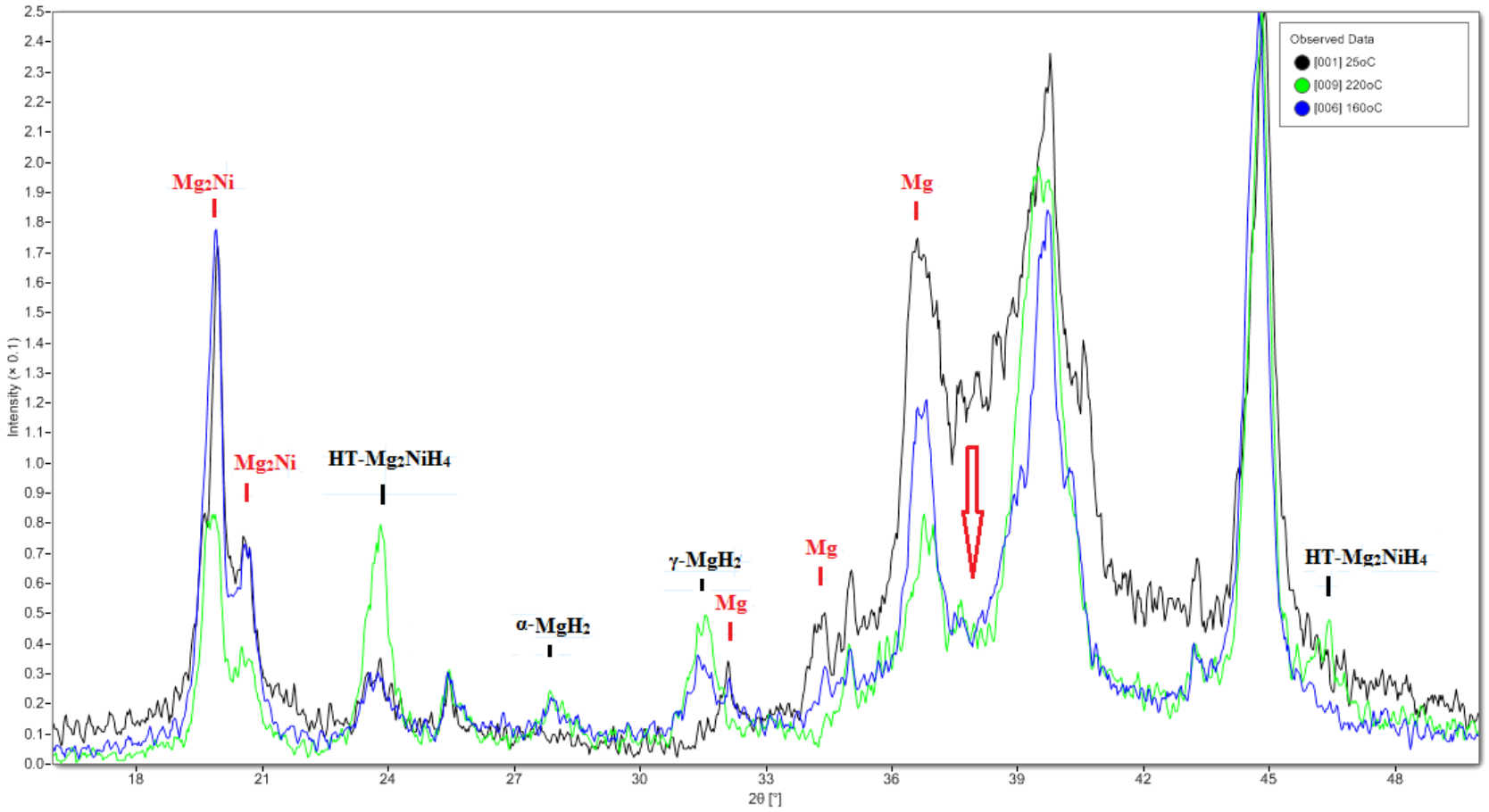

Figure 7-31 Various temperature in-situ XRD of melt-spun $Mg_{73}Ni_{27}$ sample under 10 bar H_2 at room temperature, 160 °C and 220 °C in 2θ range of 16° to 50°.

In addition, besides the MgH_2 phases, the hydriding of HT-Mg_2NiH_4 started at 220°C, while the peaks for Mg_2Ni became smaller at 220 °C. However, the peaks for Mg_2Ni at 160 °C did not show any significant change compared to those at RT, indicating that the hydriding of Mg_2NiH_4 occurred at higher temperatures. The XRD patterns of the Mg_2Ni phase indicates expanded lattice parameters of a= 5.27 ± 0.04 Å, c=13.48 ± 0.11 Å compared to the standard Mg_2Ni lattice (a= 5.219(1) Å and c= 13.225(1) Å). This indicates that the solid solution phase of Mg_2Ni (~ $Mg_2NiH_{0.3}$) was formed.

Figure 7-32 shows the XRD traces for the melt-spun $Mg_{73}Ni_{27}$ cryo-milled powder measured in 10 bars of hydrogen at 300 °C and 380 °C. At 300 °C, the sample was not fully hydrided and peaks due to the Mg_2Ni phase could be seen in the XRD pattern. The peaks for the Mg phase and Mg_6Ni disappeared at this temperature, indicating that the Mg_6Ni phase decomposed at 300 °C (Spassov et al., 2002a) and Mg hydrided into α- and γ-MgH_2. At 380 °C, the sample could be observed to desorb hydrogen as the intensity of the Mg and Mg_2Ni peaks grow at the expense of those due to the MgH_2 and Mg_2NiH_4 phases. This agrees with the H_2 DSC result where dehydriding was shown to occur at 380 °C (Figure 7-21). However, under these conditions the sample was not fully dehydrided, which would indicate slow kinetics. Even at 420 °C, there were still peaks present for both hydrides but with relatively small intensities.

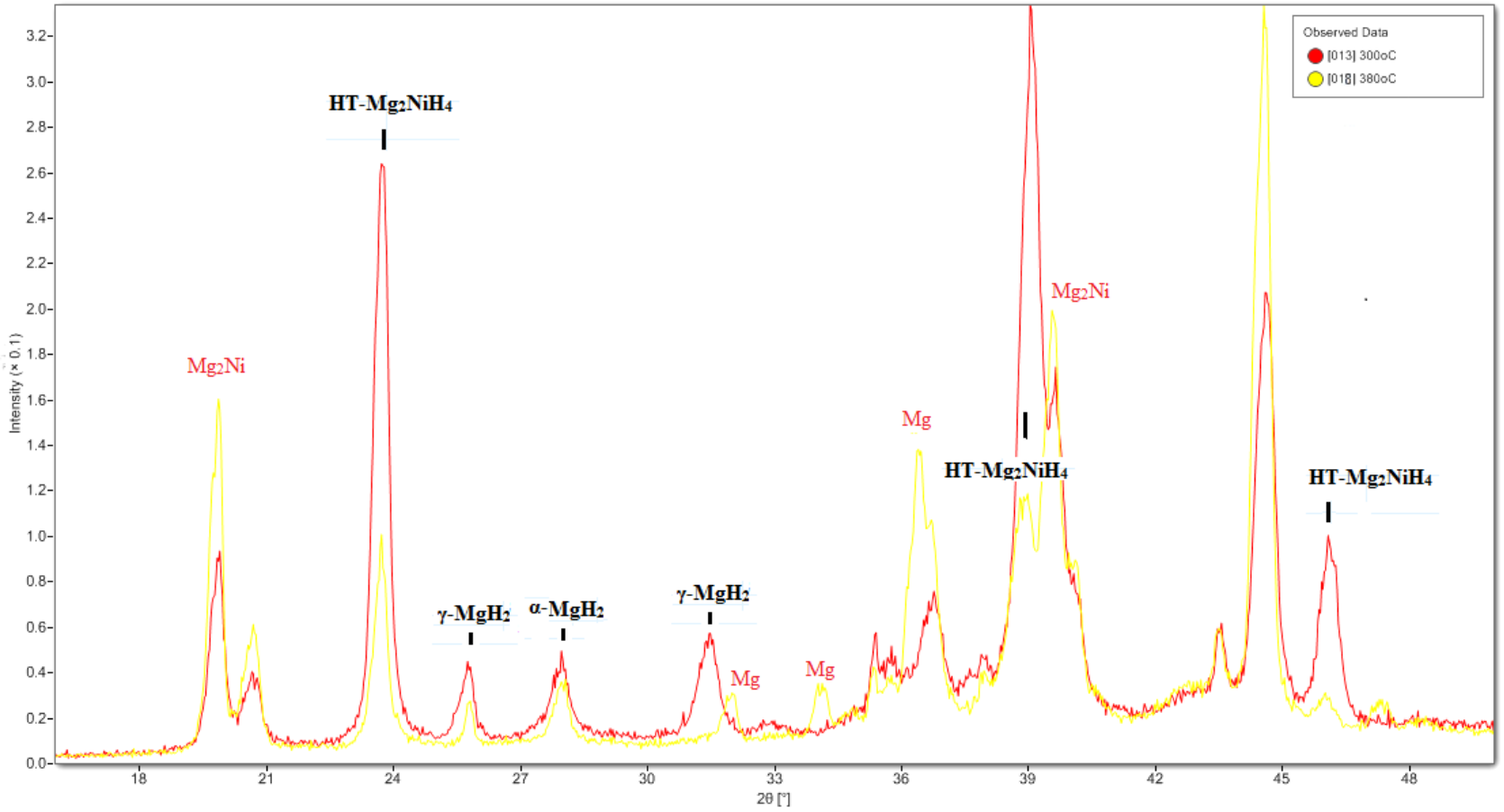

Figure 7-32 Variable temperature in-situ XRD of the melt-spun $Mg_{73}Ni_{27}$ sample under 10 bar H_2 at 300 °C and 380 °C in 2θ range of 16° to 50°.

The DSC result for the $Mg_{73}Ni_{27}$ sample in H_2 showed two exothermic hydriding peaks for the $Mg_{73}Ni_{27}$ sample at 360 °C and 335 °C on cooling from 400 °C. The in-situ XRD analysis in hydrogen was continued from 420 °C during cooling. XRD patterns were again recorded every 20 °C down to 300 °C. The formation of hydrides was observed in the XRD patterns shown in Figure 7-33.

At 380 °C, pure Mg peaks could be observed clearly, but they disappeared at 340 °C. The pattern shown at 340 °C clearly indicates the formation of α-MgH_2, but the peaks for the Mg_2NiH_4 phase are very small. The pattern at 300 °C shows obvious formation of the HT-Mg_2NiH_4 phase, while the peaks of α-MgH_2 continued to increase in size. The temperature of hydriding for the Mg_2NiH_4 was also lower than that shown in the H_2 DSC trace at 336 °C. It is surprising that the γ-MgH_2 phase remained unchanged at the higher temperatures. Teresiak *et al.* (Teresiak et al., 2009b) reported that, for a melt-spun $Mg_{85.7}Ni_{14.3}$ sample, γ-MgH_2 transformed into α-MgH_2 at 316 °C, with an enthalpy of 46.3 kJ mol^{-1}. Further work to investigate the γ-MgH_2 phase is requried.

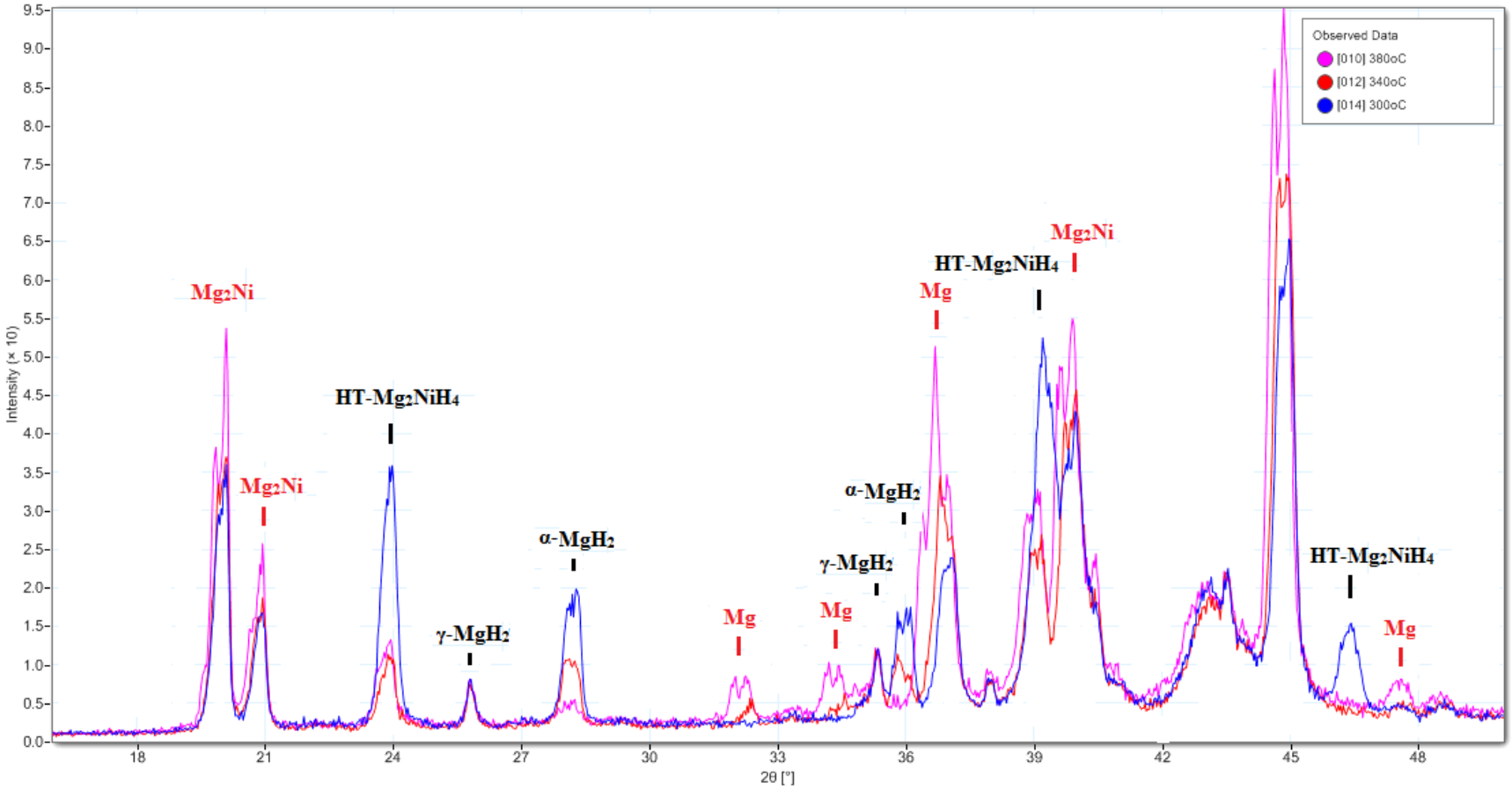

Figure 7-33 Variable temperature in-situ XRD of the melt-spun $Mg_{73}Ni_{27}$ sample under 10 bar H_2 on cooling at 380 °C 340 °C and 300 °C in 2θ range of 16° to 50°.

7.2.8. Hydrogen Sorption Properties of the melt-spun $Mg_{90}Ni_{10}$ and $Mg_{73}Ni_{27}$ alloys

High temperature hydrogen sorption

In this work, the hydrogen sorption measurements were conducted in a range of temperatures from RT to 300 °C. Initially the hydrogen sorption measurements were conducted at 300 °C (573 K) under 10 bars of hydrogen pressure for absorption or at low pressure (50 mbar) or in a vacuum, for desorption. These are common conditions for hydrogen sorption measurements used by many researchers both within the group and externally (Hong et al., 2008; Kalinichenka et al., 2011b; Kalinichenka et al., 2009).

Hong *et al.* (2008; 2009) discussed that the activation of the melt-spun Mg23.5wt.%-Ni has been completed after three cycles of hydriding-dehydriding. Kalinichenka *et al.* (2011b) also activated melt-spun $Mg_{90}Ni_8RE_2$ (RE = Y, Nd, Gd) samples by three cycles of hydrogen sorption runs at 350 °C ~ 370 °C under 30 bars for absorption and 2 bars for desorption. The samples produced in this work were shown by cyclic DSC measurements to be more active over several cycles (Figure 7-23). Therefore, the first three cycles have been considered as the activation of the melt-spun Mg-Ni alloys, and the kinetics are shown from the 4^{th} cycle onwards.

Melt-spun $Mg_{90}Ni_{10}$ sample

Activation cycles

The $Mg_{90}Ni_{10}$ sample was activated by three hydrogen sorption cycles in a Hiden IGA at 300 °C under 10 bars of hydrogen pressure. Due to an equipment failure, the data for the first cycle was not collected. Figure 7-34 shows the activation cycles (2^{nd} and 3^{rd} absorption runs) for the $Mg_{90}Ni_{10}$. Within 120 min, the $Mg_{90}Ni_{10}$ absorbed 4.8 wt.% H_2 during the 3^{rd} cycle, compared to only 0.2 wt.% H_2 during the second run, and it attained 4.8 wt.% in 8000 min. There was no significant improvement for the hydrogen desorption during the activation cycles, which exhibited the same kinetics as the subsequent cycles in Figure 7-36. Therefore, an activation treatment was required, especially for hydrogen absorption.

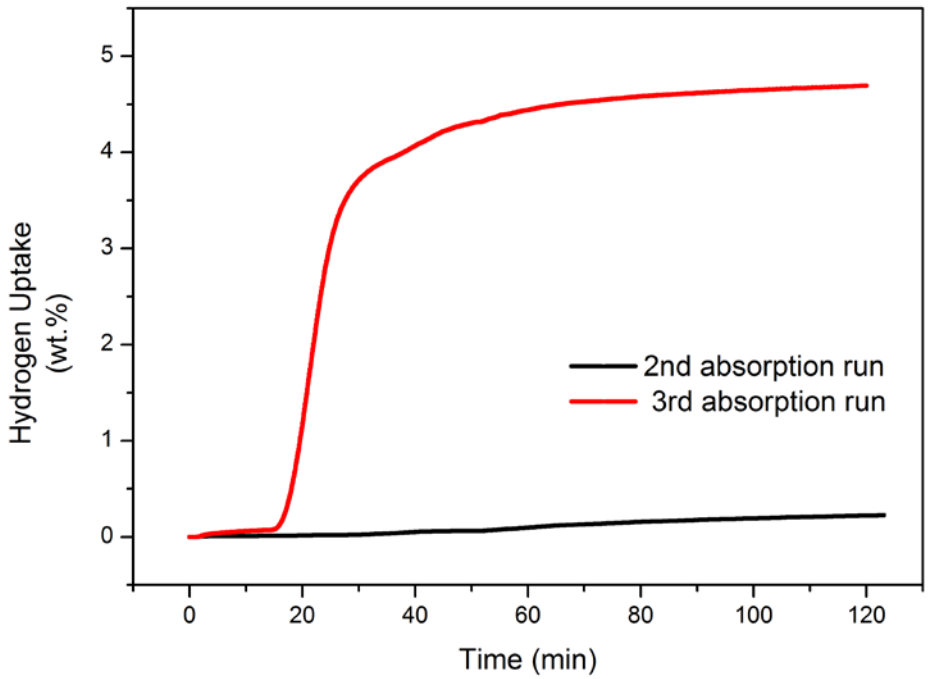

Figure 7-34 The 2nd and 3rd IGA absorption cycles for the melt-spun $Mg_{90}Ni_{10}$ cryo-milled sample at 300 °C under 10 bars of H_2 as an activation treatment.

300 °C Hydrogen sorption cycles for the melt-spun $Mg_{90}Ni_{10}$

Figure 7-35 exhibits the behaviour of six cycles for the absorption after the activation cycles. The $Mg_{90}Ni_{10}$ sample showed a H_2 capacity ~5 wt.%, and relatively fast kinetics reaching 4.5 wt.% capacity in <20 min. Figure 7-36 showed the desorption of $Mg_{90}Ni_{10}$ at 300 °C under 50 mbar H_2 which also showed fast kinetics, nearly fully desorbing in 10 min.

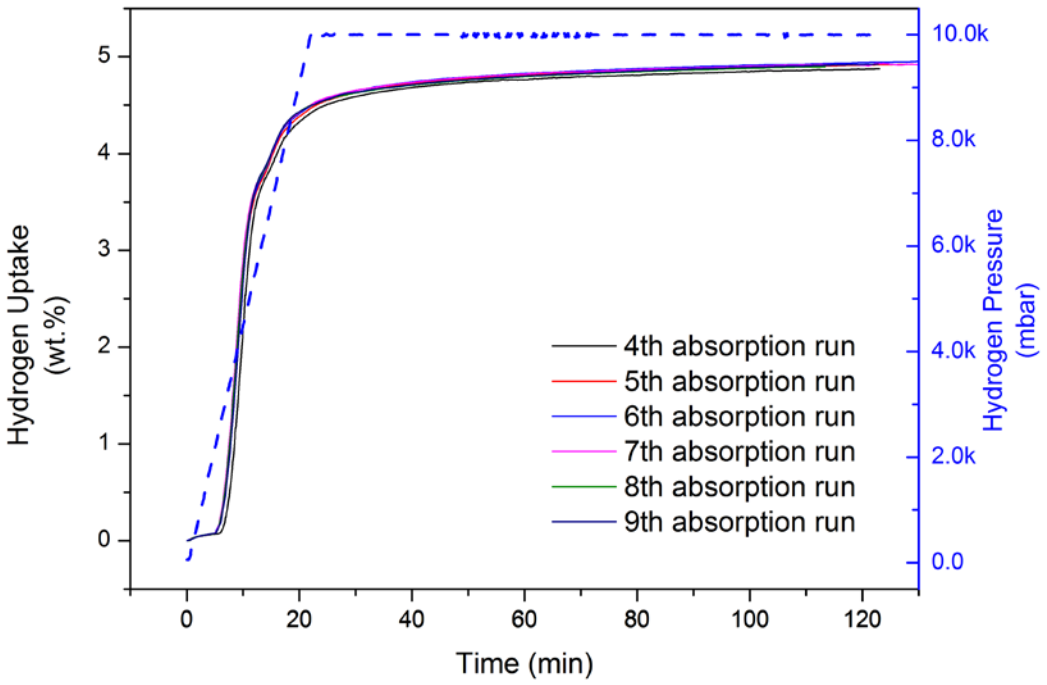

Figure 7-35 The 4th~9th IGA absorption runs for the melt-spun $Mg_{90}Ni_{10}$ cryo-milled sample at 300°C under 10 bar H_2 (500 mbar/min) with dashed pressure curve(blue).

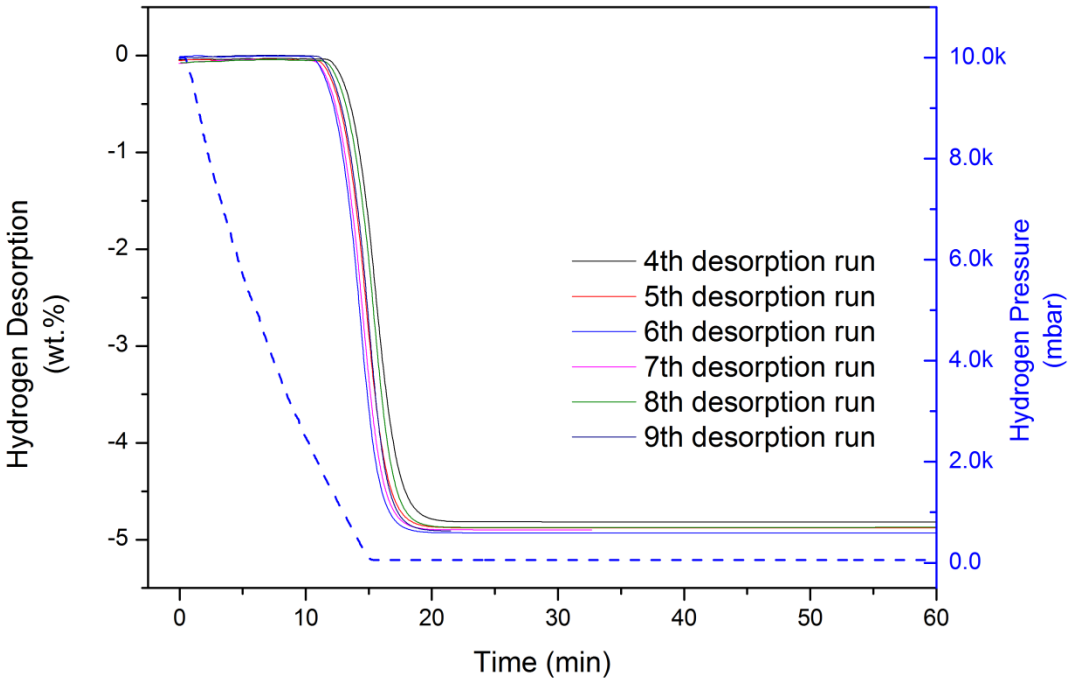

Figure 7-36 4th~9th IGA desorption runs of the melt-spun $Mg_{90}Ni_{10}$ cryo-milled sample at 300°C under 50 mbar H_2 (500 mbar/min) with dashed pressure curve (blue).

In the literature, several researchers during the timeframe of this project have reported fast kinetics for the melt-spun Mg-Ni alloys of a similar composition. Bendersky *et al.* (2011), for example, reported excellent kinetics for melt-spun $Mg_{95}Ni_5$ sample reaching 4 wt.% H_2 under 1 min at 19 bar H_2 and desorbed 3 wt.% within 4.4 min at 300 °C under a vacuum. It should be noted that the rate of pressure increase on the IGA system used in this work is limited and therefore this will decrease the rate of mass increase during hydrogen ingress.

Kalinichenka *et al.* (2011b) also reported that the activated $Mg_{90}Ni_8RE_2$ melt-spun ribbons absorbed 5.5 wt.% H_2 within 20 min under 20 bar H_2 pressure at 300 °C. The activated $Mg_{90}Ni_5Y_5$ and $Mg_{80}Ni_{10}Y_{10}$ alloys demonstrated a similar capacity of 5.4 wt.% H_2 under 20 bar at 280°C, and fully desorption under vacuum (Kalinichenka et al., 2009).

Song *et al.* (2008b) reported a very similar result for the melt-spun Mg-23.5wt%Ni sample (equal to $Mg_{89}Ni_{11}$) which absorbed 3.92 wt.% H_2 for 10 min at 300 °C under 12 bar H_2 and desorbed 3.58 wt.% H_2 for 20 min at 300 °C under 1 bar H_2.

Hong *et al.* (2009) reported similar results for the Mg–23.5wt.%Ni ($Mg_{89}Ni_{11}$) melt-spun samples, and the slope for the absorption curve at 300 °C was steeper than that for the desorption. The activated 90% (Mg–23.5wt%Ni) –10% (Nb_2O_5) alloy absorbed 4.70 wt.% H_2 at 300 °C under 12 bar H_2 for 10 min, and desorbed 4.75 wt.% H_2 at 300 °C under 1.0 bar H_2 in 25 min. In addition, another sample, the activated (Mg–23.5Ni)–$10Ta_2O_5$ alloy, absorbs 4.64 wt.% H in 5 min at 300 °C, and desorbed 5.11 wt.% H in 40 min at 300 °C.

Palade *et al.* (2006) reported that a melt-spun $Mg_{88}Ni_{11}Fe_1$ alloy had a hydrogen capacity of 5 wt.%, with slower kinetics at 306 °C under 25 bar H_2 than the melt-spun $Mg_{90}Ni_{10}$ sample examined in this work.

The fast kinetics observed in this work can be explained by the nanocrystalline structure of the material, which was produced by the melt spinning technique. Similar results have been observed for high velocity ball milled Mg samples (Huot et al., 2001). The grain boundaries in the material can act as pathways for rapid diffusion of the hydrogen. As discussed in the work, the hydrided melt-spun samples have a fine structure with a grain size of approx. 25 nm.

Melt-spun $Mg_{73}Ni_{27}$ sample

Activation cycles

The melt-spun $Mg_{73}Ni_{27}$ alloy has also been cycled for three cycles, but it did not show an activation effect. The hydrogen sorption cycles exhibited the same behaviour as the subsequent cycles (shown in Figure 7-37 and Figure 7-38). Therefore, the figures have not been represented here.

The $Mg_{90}Ni_{10}$ sample exhibited an activation effect during the initial hydrogen sorption cycles at 300 °C, which was not apparent for the $Mg_{73}Ni_{27}$ sample. This is likely to be the result of the hydrogen sorption measurements at low temperatures. For both samples, the measurements at 300 °C were performed after hydrogen sorption cycles at low temperatures which are discussed in the subsequent section. It is believed that, during low temperature runs, the $Mg_{73}Ni_{27}$ sample had been already activated prior to the measurements at 300 °C, because a the low temperature hydrogen sorption cycles exhibited a maximum absorption capacity of ~3 wt.%. On the other hand, it was not the case for the $Mg_{90}Ni_{10}$ sample at low temperature, which exhibited an activation effect during the 300 °C sorption cycles.

300 °C hydrogen sorption cycles for the melt-spun $Mg_{73}Ni_{27}$

Figure 7-36 and Figure 7-37 shows 5 cycles of thermal sorption for the melt-spun $Mg_{73}Ni_{27}$ cryo-milled sample. The activated $Mg_{73}Ni_{27}$ sample exhibited nearly 3 wt.% capacity but with very fast kinetics. The $Mg_{73}Ni_{27}$ sample showed very fast kinetics and

its absorption behaviour also indicated a two-step absorption process. In order to increase this effect, the pressure ramp rate was decreased to 200 mbar/min from 500 mbar/min for the $Mg_{90}Ni_{10}$ sample (Figure 7-35). It is very likely that the two-step absorption was due to the result of the MgH_2 and Mg_2NiH_4 absorbing at different pressures (Song and Park, 1998). It is interesting to note that the $Mg_{90}Ni_{10}$ sample did not exhibit such an obvious two-step absorption due to the low fraction of Mg_2Ni phase, and this could be confirmed by pressure-composition isotherms (PCI) measurements. The $Mg_{73}Ni_{27}$ sample also exhibited the same two steps on the desorption trace which, in this case, was performed in a vacuum (Figure 7-38).

Zhang *et al.* (2009b) reported that melt-spun Mg_2Ni does not produce any amorphous material, but consisted solely as a nanocrystalline structure with grain sizes of around 30 nm. The sample reached nearly a saturation capacity of ~3 wt.% in around 5 min under 15 bar H_2 at 200 °C. However, it desorbed only 1 wt.% H_2 in one hour under a vacuum at the same temperature (200 °C). Zhang's result is similar to those of the melt-spun $Mg_{73}Ni_{27}$ sample which has been shown to contain a considerable amount of the Mg_2Ni phase.

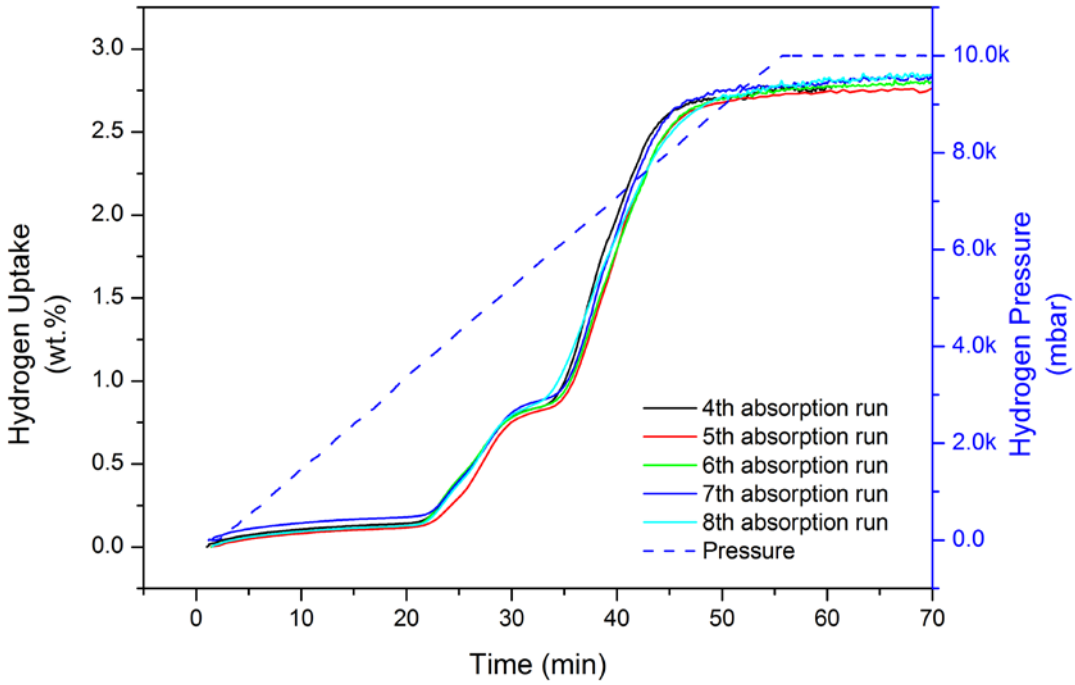

Figure 7-37 The 4th~8th IGA absorption runs for the melt-spun $Mg_{73}Ni_{27}$ sample at 300 °C under 10 bar H_2.

;

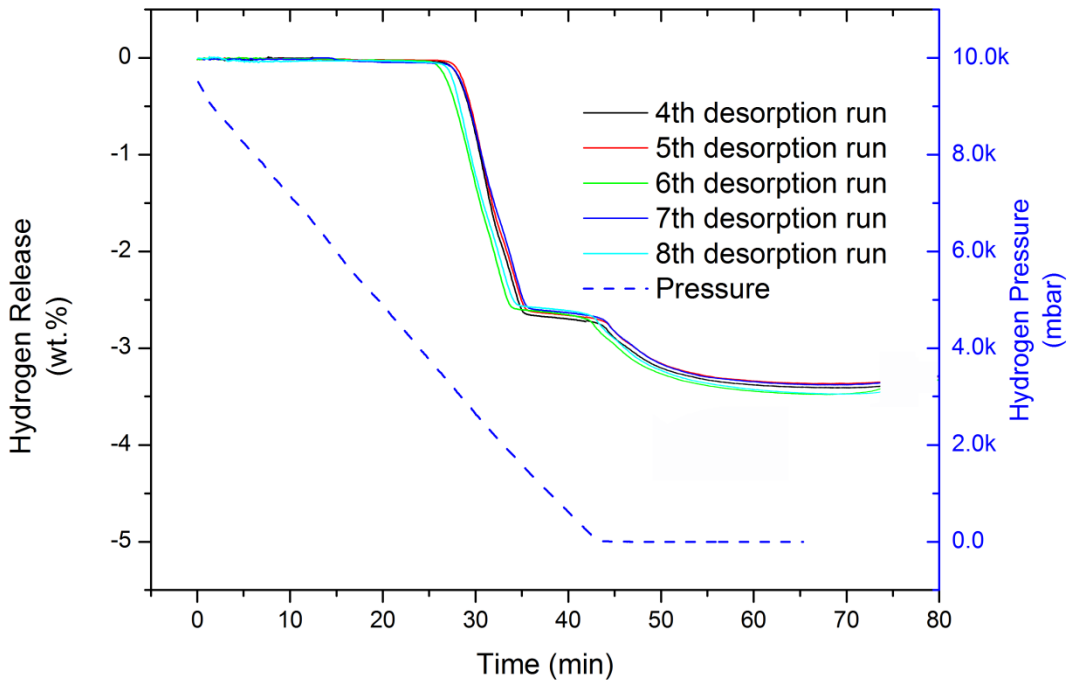

Figure 7-38 The 4th~8th IGA desorption runs for the melt-spun $Mg_{73}Ni_{27}$ sample at 300 °C under a vacuum.

To try to show the absolute hydrogen absorption kinetics, the IGA studies of the absorptions were carried out at successively higher pressure ramp rates of 1000, 1500 and 2000 mbar/min. The results are shown in Figure 7-39. It is apparent that the time for complete absorption is highly dependent upon the pressurization rate. The faster the pressure is increased, then the quicker the sample reaches the maximum hydrogen capacity. Saturation is achieved in around 3 min for the $Mg_{73}Ni_{27}$ sample with a ramp rate of 2000 mbar/min. This is the maximum ramp rate for the equipment. It is likely that even faster kinetics could be recorded if the ramp rate could be increased further.

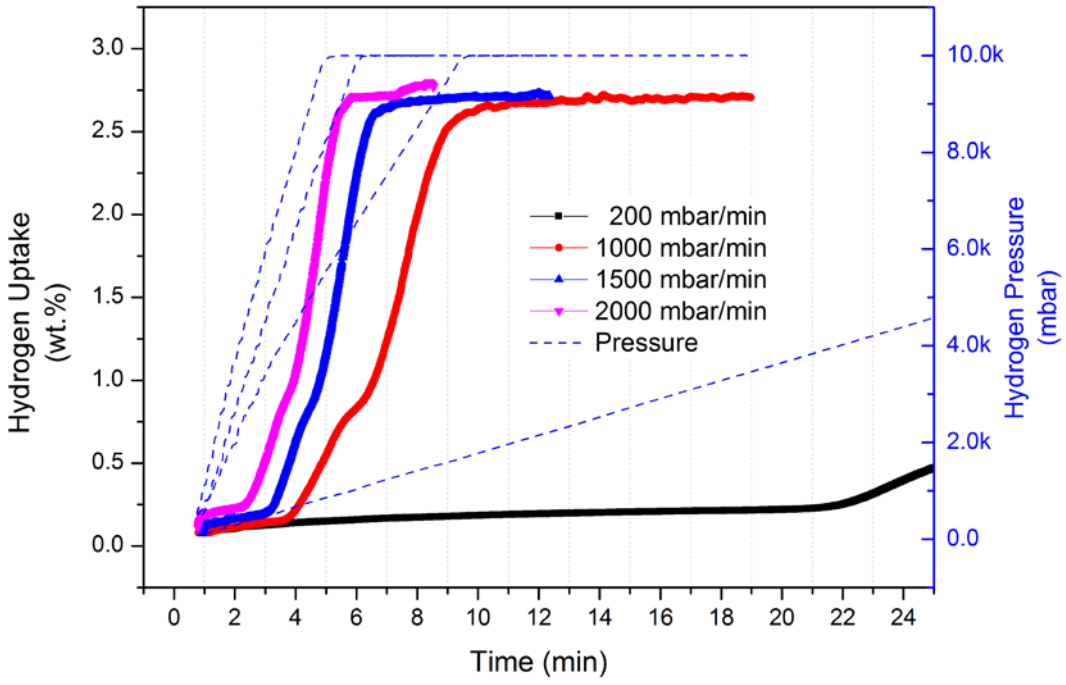

Figure 7-39 IGA thermal sorption measurement of the melt-spun $Mg_{73}Ni_{27}$ sample under 10 bar H_2 at 300 °C, pressurized at 200, 1000, 1500 and 2000 mbar/min.

For both samples, it is unclear why the theoretical saturation absorption is not reached. However it is evident from the XRD data that some of the material does not hydride. This could be due to the fact that larger grained material exists within the nanocrystalline structure.

Low temperature hydrogen sorptions

Melt-spun $Mg_{90}Ni_{10}$ sample

An attempt was made to hydride the milled $Mg_{90}Ni_{10}$ sample below the temperature for crystallization. Figure 7-40 shows an initial test carried out at 110 °C under 10 bars of H_2 pressure. The maximum H_2 uptake was nearly 3.6 wt.% with slow kinetics for absorption. Kalinichenka *et al.* (2011b) reported that crystallized $Mg_{90}Ni_8RE_2$ (Re= Y, Nd, Gd) after activation at 400 °C, exhibited a hydrogen concentration of 3 wt.% at 100 °C and 3.8 wt.% at 150 °C within 60 min under 20 bar H_2 pressure. The $Mg_{73}Ni_{27}$ sample examined in this work showed a similar hydrogen capacity (~3.6 wt.%) but with slower kinetics.

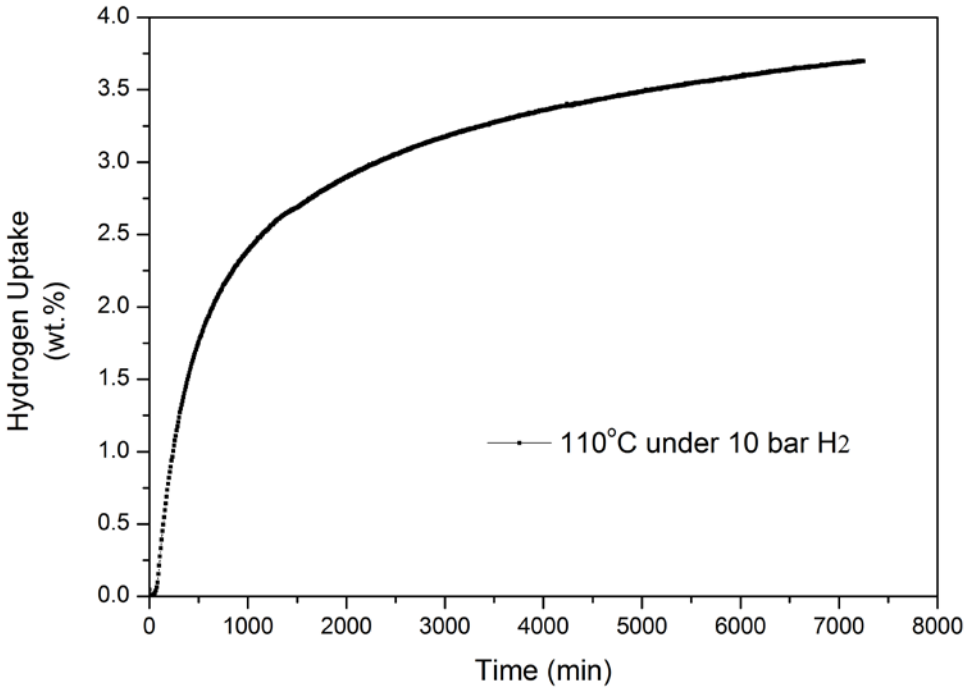

Figure 7-40 IGA absorption for the melt-spun $Mg_{90}Ni_{10}$ sample at 110 °C under 10 bar H_2 gas.

It was not possible to desorb the sample in a vacuum or at 50 mbar at the same temperature. Therefore, the sample was heated to 140 °C at which point desorption began to occur. The desorption reached about 2.2 wt.% capacity after nearly 8000 mins and appeared to show a slight kink. Due to constraints on equipment time, it was not possible to fully dehydride the sample.

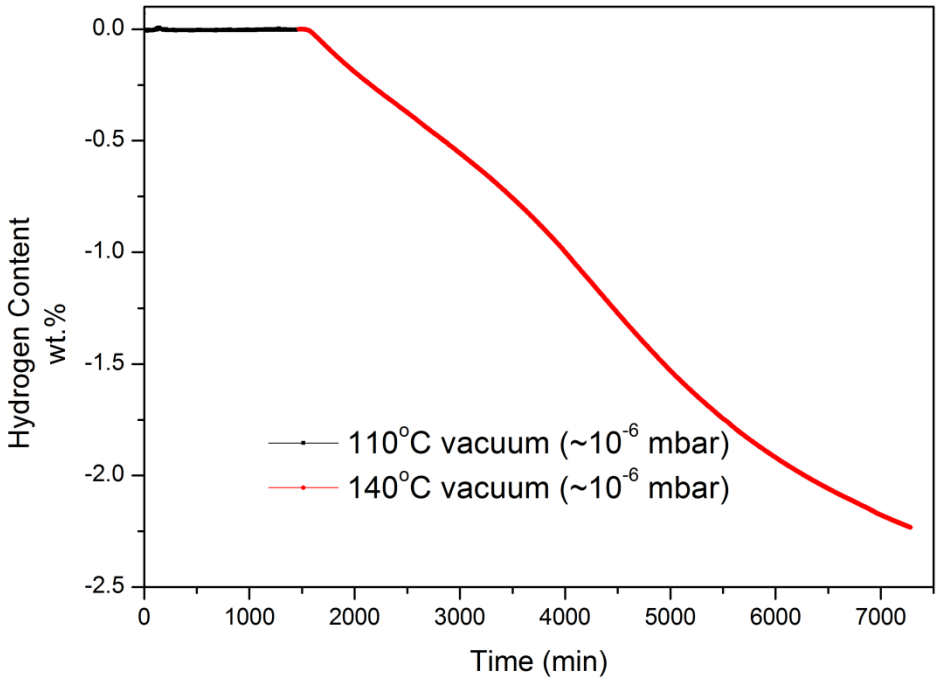

Figure 7-41 IGA desorption for the melt-spun $Mg_{90}Ni_{10}$ sample at 110 and 140 °C under a vacuum.

After the desorption run at 140 °C, the sample was held at 140 °C, and the pressure was increased to 10 bar H_2 in order to investigate whether it was possible to cycle the sample. In Figure 7-42, the absorption capacity is shown to be lower than that of the first absorption at 110 °C, and this can be attributed to the incomplete absorption during the second hydriding run. It was interesting to note that the hydriding kinetics at 140 °C were slower than those observed on the first cycle at 110 °C. This may be due to the incomplete dehydriding, because the kinetics decrease as the sample hydrides.

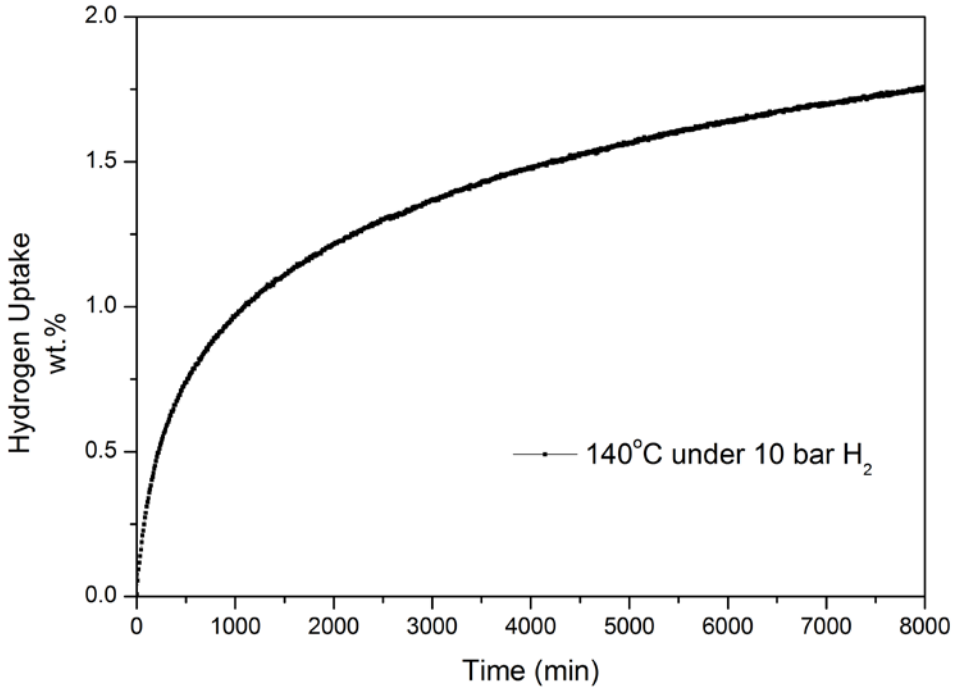

Figure 7-42 IGA absorption for the the melt-spun $Mg_{90}Ni_{10}$ cryo-milled sample at 140 °C under 10 bars of H_2 gas.

Melt-spun $Mg_{73}Ni_{27}$ sample

The melt-spun $Mg_{73}Ni_{27}$ sample was loaded on an IGA, and the sorption kinetics were measured initially at low temperatures under the same conditions as those employed for the $Mg_{90}Ni_{10}$ sample. Figure 7-43 shows the absorption of the melt-spun $Mg_{73}Ni_{27}$ sample at both 110 and 140 °C under 10 bar pressure. At 110 °C, the melt-spun $Mg_{73}Ni_{27}$ sample saturated at 2.5 wt.% and most of the reaction had occurred within 20 min. Similar kinetics were observed for the sample measured at 140 °C with a slightly higher capacity of ~2.8 wt.%. The kinetics observed here were very similar to those observed for the same sample at 300 °C.

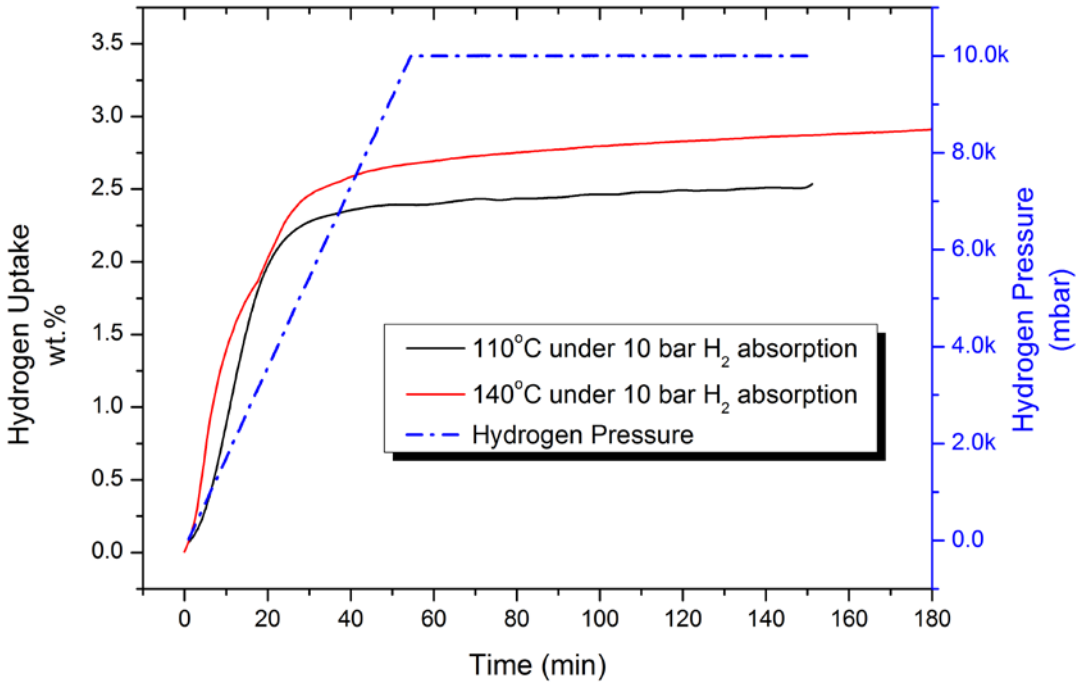

Figure 7-43 IGA absorption for the melt-spun $Mg_{73}Ni_{27}$ sample at 110 and 140 °C under 10 bar H_2 gas.

The hydrogen sorption of the Mg_2Ni-type alloys at low temperatures has also been reported. Isogai *et al.* (2000) studied the hydriding process of as-melt-spun $Mg_{62}Ni_{33}Ca_5$ in the amorphous phase at 100 °C and 130 °C under 50 bar pressure. It exhibited a maximum capacity of 3 wt.% H_2. The kinetics at 130 °C under 35 bar H_2 was about 2.1 wt.% H_2 absorbed in 60 min. The crystallized sample after heat treatment at 400 °C for 24 hours, exhibited slightly improved kinetics of 1.85 wt.% and 2.6 wt.% at 100 and 130 °C in 60 min, respectively.

At low temperatures, the melt-spun $Mg_{90}Ni_{10}$ alloy did not show such excellent hydrogen sorption kinetics as those of the $Mg_{73}Ni_{27}$ alloy. The $Mg_{90}Ni_{10}$ sample did not show hydrogen uptake after several hours. In contrast, the hydrogen absorption for the $Mg_{73}Ni_{27}$ alloy nearly reached saturation when the pressure increased to 10 bars of H_2. This may indicate that the Mg_2Ni phase has a positive impact on the fast kinetics, as the

melt-spun $Mg_{73}Ni_{27}$ has been shown to contain a considerable amount of the Mg_2Ni phase.

Figure 7-43 shows the hydrogen desorption measurements at 140 °C under a vacuum, after the absorptions at 110 °C and 140 °C. The sample only desorbed 2 wt.% of hydrogen after 2000 min during the first desorption run and ~2.6 wt.% during the second run. Although the kinetics for absorption were fast, the $Mg_{73}Ni_{27}$ sample exhibited slow desorption at 140 °C in a vacuum.

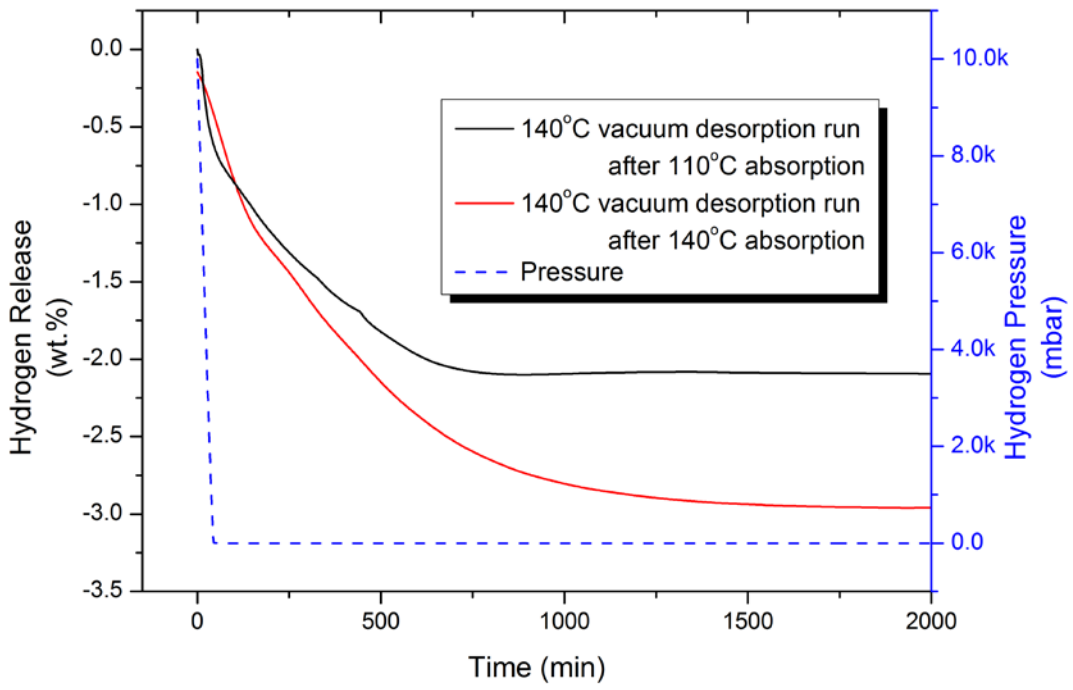

Figure 7-44 IGA desorption for the melt-spun $Mg_{73}Ni_{27}$ sample at 140 °C under a vacuum.

Room Temperature (RT) Measurements

Both the melt-spun $Mg_{90}Ni_{10}$ and $Mg_{73}Ni_{27}$ alloys demonstrated the ability to absorb hydrogen at room temperature in 10 bars of H_2 albeit with slow kinetics (Figure 7-45 and Figure 7-46). The first RT-absorption for the $Mg_{90}Ni_{10}$ was extremely slow, and it was not saturated within 10k min. However, the second run shows much quicker kinetics which did not improve further in the following 3rd cycle. This may indicate that initial hydrogen sorption cycle has an impact on the hydrogen absorption kinetics. Although the RT-kinetics were slow, the absorption capacity of the $Mg_{90}Ni_{10}$ sample reached nearly 2 wt.%. This is relatively high compared to other literature values for similar materials (Lin et al., 2012b), but not as good as ~3.6 wt.% which was demonstrated at 110 °C.

Figure 7-46 indicates much faster kinetics than the $Mg_{90}Ni_{10}$ sample, with 2 wt.% H_2 absorbed within 500 min. Although faster kinetics have been observed at RT for catalysed $Mg_{62}Ni_{33}Ca_5$ ribbons (Isogai et al., 2000), it has not been reported yet in term of the kinetics for the Mg-Ni ribbons on their own, which has been demonstrated clearly in this work.

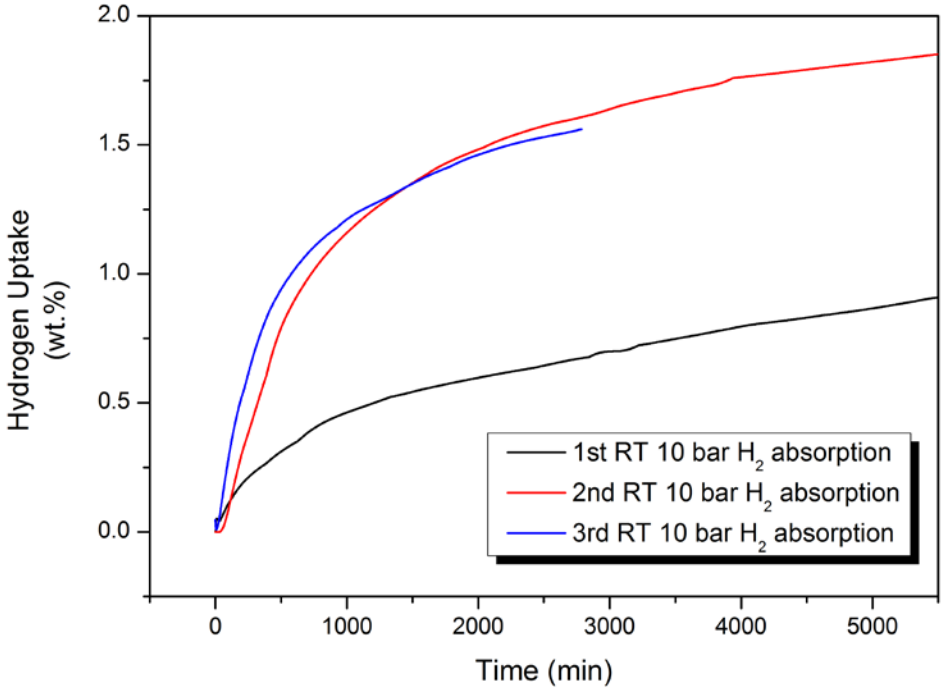

Figure 7-45 IGA absorptions for the melt-spun $Mg_{90}Ni_{10}$ powder under 10 bar H_2 at RT.

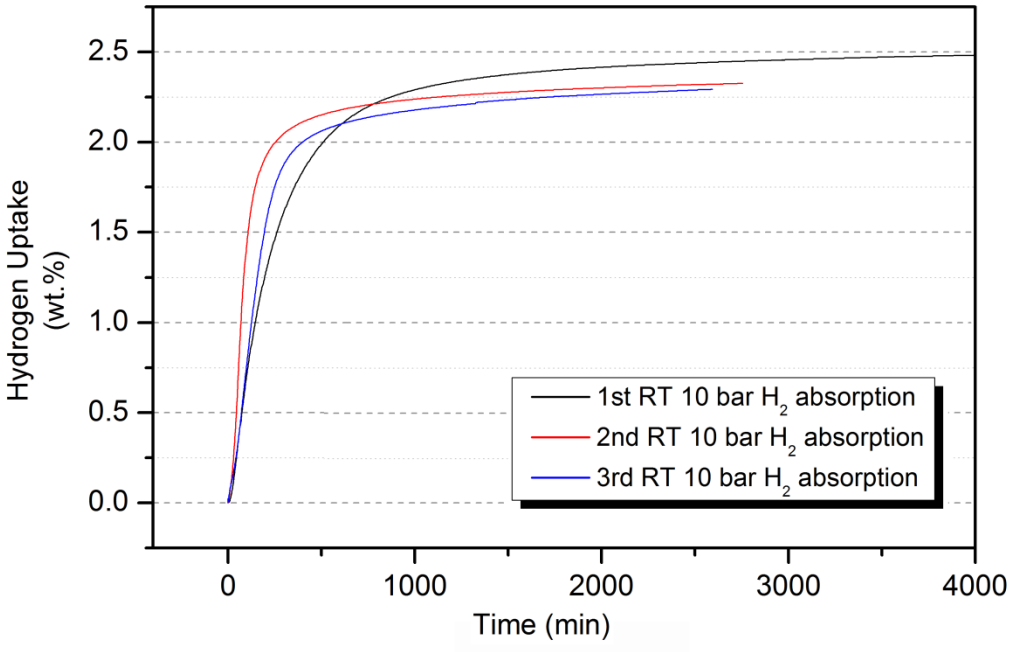

Figure 7-46 3 cycles of IGA absorptions for the melt-spun $Mg_{73}Ni_{27}$ sample at RT under 10 bar H_2.

Desorption of both the $Mg_{90}Ni_{10}$ and $Mg_{73}Ni_{27}$ samples occurred only at 140 °C or above under a vacuum. The kinetics for the desorption was extremely slow for the $Mg_{90}Ni_{10}$ sample with the mass dropping by 1 wt.% H_2 in around 4 days. The $Mg_{73}Ni_{27}$ sample dehydrided a little faster, dropping by 1 wt.%. H_2 in around 1 day and then fully dehydriding in a week.

It is quite surprising that the melt-spun Mg-Ni alloys exhibited absorption at room temperature, although such behaviour has already been reported in the literature. Hanada *et al.* (2006) reported room temperature sorption of ball-milled Mg activated by addition of Nb_2O_5 catalyst. Liang *et al.* (1999b) reported that, by mechanical milling, MgH_2+5at.% V composite absorbed 2.0 wt.% hydrogen at room temperature in 1000 s, 4 wt.% at 100 °C in 100 s and 5.6 wt.% in 250 s at 200 °C under a pressure of 10 bar hydrogen. After ball milling the ternary Mg-V-Nb alloys were able to relatively quickly absorb hydrogen at room temperature at a pressure of 1 bar and over 20 sorption cycles, with a capacity of about 3 wt.% (Tan et al., 2012). Mg-7Cr-13V alloy absorbed hydrogen at room temperature under a pressure of 2 bar, reaching about 4 wt.% H_2 (Zahiri et al., 2011).

Zhou *et al.* (2013) reported that a ball-milled MgH_2 sample catalysed with $TiMn_2$ exhibited hydrogen absorption capability (~3 wt.%) at room temperature and 1 bar hydrogen pressure. Bobet *et al.* (2003) reported that ball-milled Mg_2Ni with a small amount of V, absorbed less than 0.5 wt.% H_2 within 30 min under a pressure of 10 bar at room temperature.

Lin *et al.* (2012b) claimed that Mg-Ce-Ni melt-spun alloys exhibited RT-absorption of 0.2~0.4 wt.% H_2 under a pressure of 23 bar H_2. Kalinichenka *et al.* (2011b) found 1.1 wt.% H_2 absorption of activated melt-spun $Mg_{90}Ni_8RE_2$ at 50 °C under 20 bar H_2. In comparison, the melt-spun $Mg_{90}Ni_{10}$ sample studied in this work exhibited a higher hydrogen capacity of nearly 2 wt.% at room temperature, although the kinetics are not fast.

Isogai *et al.* (2000) reported a H_2 absorption capacity at 50 °C of 2.3 wt.% for amorphous melt-spun $Mg_{62}Ni_{33}Ca_5$ and 1.3 wt.% for crystallized $Mg_{62}Ni_{33}Ca_5$ under 50 bar pressure. The melt-spun $Mg_{73}Ni_{27}$, as Mg_2Ni-type material, exhibited similar hydrogen kinetics and capacity compared to the literature values (to my knowledge). Melt-spun Mg-Ni binary ribbons on its own have not been reported. Therefore, this is a novel finding, and requires further investigations.

Pressure-Composition Isotherms

This section reports the pressure-composition isotherms for the $Mg_{90}Ni_{10}$ and $Mg_{73}Ni_{27}$ alloys which were measured using a Sievert-type system (*Hiden HTP*) in the temperature range from 250 °C ~ 375 °C with H_2 pressures up to 30 bar.

Figure 7-47 and Figure 7-48 show the PCI absorption curves of the melt-spun $Mg_{90}Ni_{10}$ and $Mg_{73}Ni_{27}$ alloys respectively. The maximum hydrogen capacity was shown to be ~6.5

wt.% for $Mg_{90}Ni_{10}$ and 3.8 wt.% for $Mg_{73}Ni_{27}$, which were higher than those obtained from the IGA result measured at 10 bars of H_2.

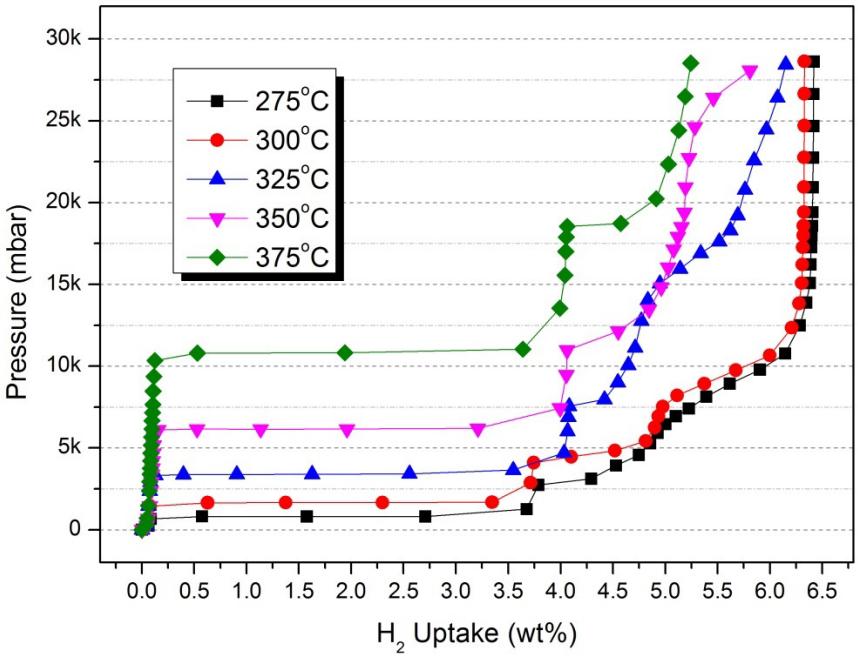

Figure 7-47 PCI absorption curves for the melt-spun $Mg_{90}Ni_{10}$ sample.

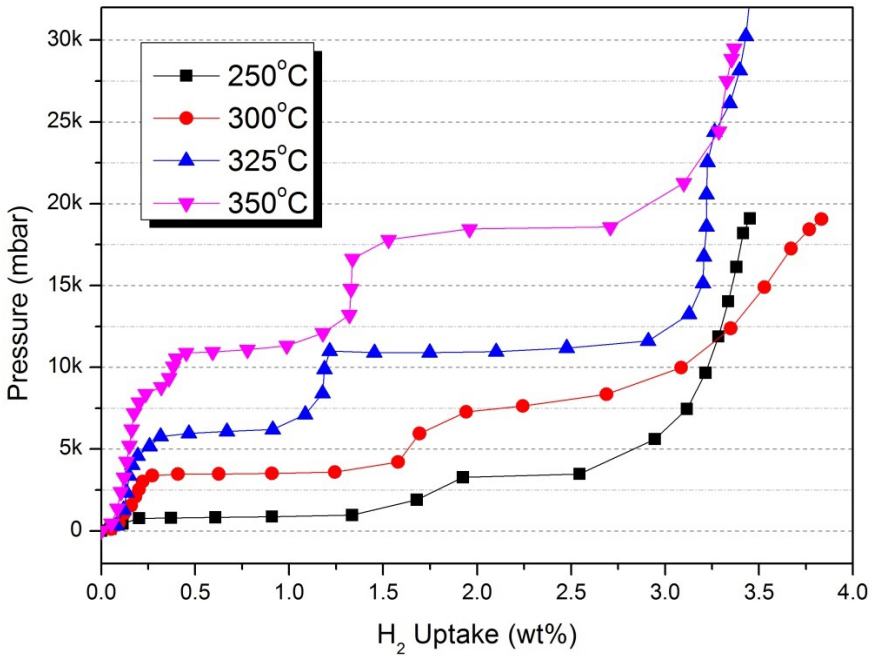

Figure 7-48 PCI absorption curves for the melt-spun $Mg_{73}Ni_{27}$ sample.

Figure 7-49 and Figure 7-50 show the PCI desorption curves for the melt-spun $Mg_{90}Ni_{10}$ and $Mg_{73}Ni_{27}$ alloys. The PCI desorption isotherms are used typically to calculate the heat of formation of hydrides. Several steps can be observed in the PCI desorption curves, indicating that a number of different hydrides are likely to have formed.

Multi-plateaux has been reported by many researchers (Hong et al., 2008; Tanaka et al., 1999; Hong et al., 2009; Palade et al., 2006; Friedlmeier et al., 1999). For Mg-Ni alloys, two plateaux are very common, corresponding to the MgH_2 phase and the Mg_2NiH_4 phase. Hong *et al.* (2008; 2009) found that there were two plateaux for absorption of hydrogen and only one plateau for desorption. The plateaux pressures have been reported in several papers about melt-spun Mg-23.5wt.%Ni containing many kinds of catalysts (Song et al., 2008b; Hong et al., 2009; Hong et al., 2008; Song et al., 2008a; Song et al., 2009). Melt-spun $Mg_{88}Ni_{11}Fe_1$ and $Mg_{88}Ni_{11.4}Fe_{0.6}$ also showed two plateaux pressures in PCI curves (Palade et al., 2006).

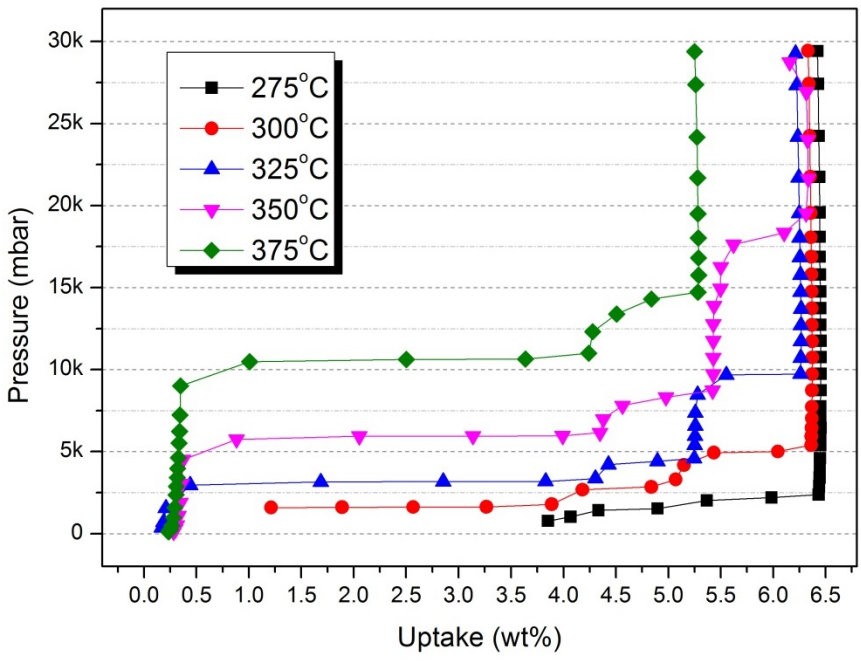

Figure 7-49 PCI desorption curves for the melt-spun $Mg_{90}Ni_{10}$ sample.

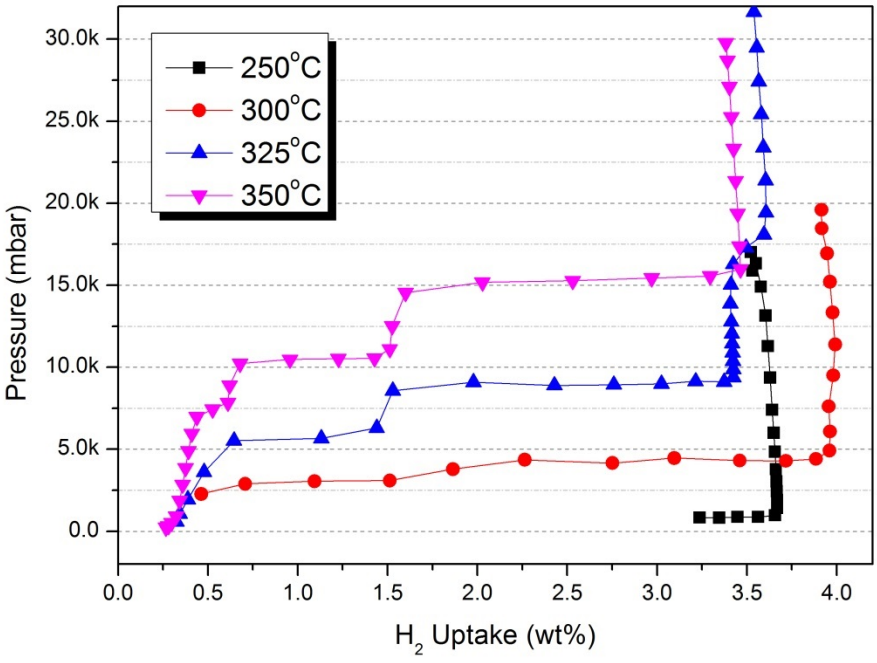

Figure 7-50 PCI desorption curves for the melt-spun $Mg_{73}Ni_{27}$ sample.

Tanaka *et al.* (1999) found very similar PCI results with those reported in this work. Figure 7-51 shows similar PCI curves with two plateaux, the lower one corresponding to the decomposition of MgH_2 and higher to Mg_2NiH_4. Moreover, Mg-rich $Mg_{80}Ni_{15}Nd_5$ showed a similar PCI curve, where the lower plateau pressure was longer than the higher one. This can be attributed to the larger fraction of H_2 release was due to the decomposition of MgH_2. Conversely, Ni-rich $Mg_{70}Ni_{25}Nd_5$ exhibits a longer and higher plateaux, which can also be observed in Figure 7-50 for the Ni-rich $Mg_{73}Ni_{27}$ sample. Therefore, the plateaux in the PCI curves of $Mg_{90}Ni_{10}$ and $Mg_{73}Ni_{27}$ are likely to correspond to the phases of MgH_2 and Mg_2NiH_4. However the $Mg_{90}Ni_{10}$ sample exhibits three plateaux as in Figure 7-52.

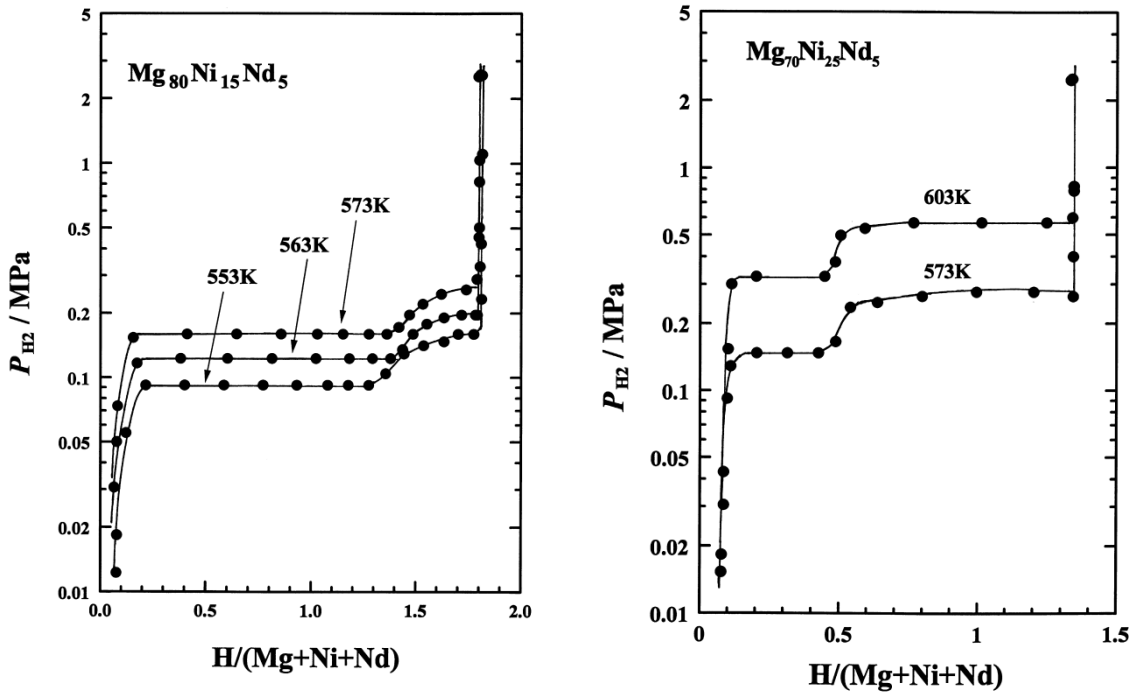

Figure 7-51 PCI desorption curves of $Mg_{80}Ni_{15}Nd_5$ and $Mg_{70}Ni_{25}Nd_5$, showing two plateau pressures. Taken from Tanaka *et al.* (1999)

The enthalpy of formation for the desorption reaction can be determined from the plateau pressures using the van't Hoff equation. Taking the PCI desorption plateaux for the $Mg_{90}Ni_{10}$ marked as Plateau 1, 2 and 3 from low to high pressure in Figure 7-52, the van't Hoff plots are plotted in Figure 7-53. The enthalpy and entropy can then be determined by the slope and intercept of the fitted linear line.

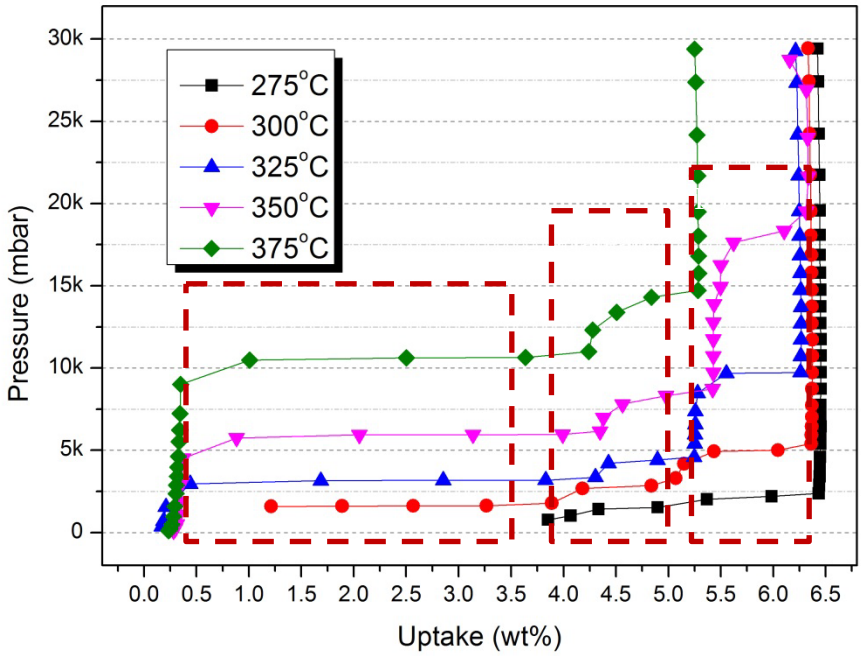

Figure 7-52 PCI desorption curves for the melt-spun $Mg_{90}Ni_{10}$ sample with three marked regions of plateau pressures, noted as plateau 1 to 3 from low to high.

As showed in Figure 7-53, ΔH_1 of $Mg_{90}Ni_{10}$ was -77.45 ± 0.11 kJ $mol^{-1}H_2$, and entropy ΔS_1 was -139.05 ± 0.19 $J \cdot K^{-1}mol^{-1}$, which are comparable to the value of melt-spun pure Mg in section 6.2.4 and ΔH of -77.9 kJ $mol^{-1}H_2$ with ΔS of 139.7 $J \cdot K^{-1}mol^{-1}$ in the literature (Lin et al., 2012a).

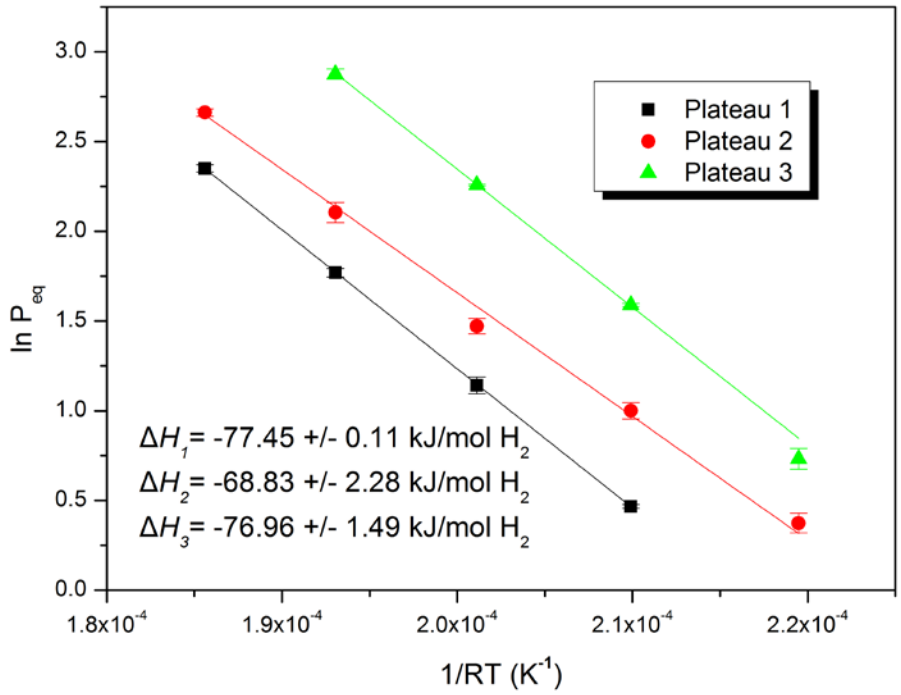

Figure 7-53 Van't Hoff plots of desorption PCI for the melt-spun $Mg_{90}Ni_{10}$ sample

ΔH_2 was calculated to be -68.83 ± 2.28 kJ $mol^{-1}H_2$, with ΔS_2 of -128.23 ± 3.68 $J{\cdot}K^{-1}mol^{-1}$. This ΔH value can be compared with the values of −64.5 kJ $mol^{-1}H_2$ for bulk Mg_2NiH_4 where the ΔS was not mentioned (Reilly and Wiswall Jr, 1968). Tanaka *et al.* (1999) also reported a comparable thermodynamics values of Mg_2NiH_4 where ΔH was 69 kJ $mol^{-1}H_2$ and ΔS was 129 $J{\cdot}K^{-1}mol^{-1}$ with no error range provided.

ΔH_3 was -76.96 ± 1.50 kJ $mol^{-1}H_2$., with ΔS_3 of -147.48 ± 2.52 $J{\cdot}K^{-1}mol^{-1}$.ΔH_3 was believed to be attributable to the γ-MgH_2, because γ-MgH_2 has nearly the same enthalpy as α-MgH_2 (Cui et al., 2008; Vajeeston et al., 2012). On the other hand, Gennari *et al.* (2001) found direct dehydrogenation of γ-MgH_2 prior to transition into α-MgH_2.

In the same way, PCI desorption curves of $Mg_{73}Ni_{27}$ have also been analysed in the same method. The enthalpy of formations from the lower plateaux (Figure 7-50) were

calculated to be ΔH_1 = -75.00 ± 2.84 kJ/mol^{-1} H_2, with ΔS of -139.77 ± 4.66 J·K^{-1}mol^{-1}, which is comparable to the enthalpy and entropy of formation for the MgH_2 hydride determined from the PCI curves of the $Mg_{90}Ni_{10}$ sample.

According to the higher platueax for the $Mg_{73}Ni_{27}$ (Figure 7-50), ΔH_2 is calculated to be -80.53 kJ/mol^{-1} H_2, with ΔS_2 of -152.70 ± 4.76 J·K^{-1}mol^{-1}, which are higher than the values reported for Mg_2NiH_4. It is not clear what caused the increase of the heat of formation of Mg_2NiH_4 for the melt-spun $Mg_{73}Ni_{27}$, so further work is required. However, Tanaka *et al.* (2008) also reported an increased ΔH of Mg_2NiH_4 of -73.3 kJ mol$^{-1}H_2$ for a melt-spun $Mg_{85}Ni_{10}La_5$ sample, and this was attributed to the large amounts of the grain boundary area. He studied the nano-boundary region, and reported a ΔH value of -95 kJ mol$^{-1}H_2$ for the grain boundary. Therefore, he claimed that the increase in ΔH for the Mg_2NiH_4 was caused by the larger amounts of nano-grain boundary area.

8. Conclusions

The aim of the work described in this thesis was to study the hydrogen storage properties of Mg-based alloys produced by melt spinning on a newly installed melt spinner with an unique inert transfer capability. Several methods were used to prepare the starting materials for melt spinning, but by far the most successful route was to powder blend the materials and to induction melt the material directly on the melt spinner. Below, separate conclusions are given for each material investigated.

Melt-spin Mg sample

Pure melt spun Mg ribbons were produced, which, from the XRD patterns, were shown to be comprised of a fine crystalline material with grain sizes of around 10 μm. This was in agreement with previous studies which showed that, on rapid quenching pure Mg does not form an amorphous material. It was evident that the ribbons required surface activation in order for the material to take up hydrogen. Cryo-milling was employed for the melt-spun ribbons. Although it can act as a surface treatment, it has been shown by the XRD analysis that, it will not lead to significant structural changes in the material. The DSC studies showed the hydriding and dehydriding temperatures at 350 °C and 400 °C respectively, which is in agreement with the behaviour of other forms of Mg. It was also evident that hydrogen cycling increased the activity of the material. The pressure-composition isotherms demonstrated that, up to 30 bars of H_2, the pure Mg ribbons had a hydrogen capacity of 6 wt.%. Using the van't Hoff equation, the heat of formation of MgH_2 has been calculated to be -77.03 ± 1.59 $kJ \cdot mol^{-1}H_2$, with an entropy ΔS of -143.24

± 2.61 $J \cdot K^{-1} mol^{-1}$ which are comparable with the published value: namely ΔH of MgH_2 of -74.4 ± 0.3 kJ $mol^{-1} H_2$ and ΔS of -135.06 ± 1.9 $J \cdot K^{-1} mol^{-1}$ (Stampfer et al., 1960).

Melt-spun Mg-Ni samples

The Mg-Ni powder mixtures in ratios of 90:10, 80:20 and 70:30 were pressed into pellets and melt spun. In order to optimise the conditions and to produce ribbons from the $Mg_{90}Ni_{10}$ sample and the $Mg_{80}Ni_{20}$ sample, many melt-spinning trials were performed under different conditions. For each composition, an induction heating profile was developed which started with a prolonged time at low power in order to aid inter-diffusion of Mg and Ni with a shorter time at higher power to guarantee some superheat in the material prior to the melt spinning. It was evident immediately that the sublimation of Mg was a major problem and caused significant problems in reading the temperature and in producing ribbons. The melting point for the alloys increased with increasing Ni content and consequently it became increasingly more difficult to produce a ribbon from the powder compacts. This was evident particularly in the case of the $Mg_{70}Ni_{30}$ sample which did not produce sufficient melt-spun materials for further analysis. However, melt spun ribbons were produced with a composition of $Mg_{90}Ni_{10}$ and $Mg_{73}Ni_{27}$.

XRD analysis showed that both these samples exhibited an amorphous background and nanocrystalline peaks. For both samples, both Mg and Mg_2Ni nanocrystalline phases were observed in the XRD patterns. The Mg phase formed a larger volume fraction for the melt-spun $Mg_{90}Ni_{10}$ sample compared to the $Mg_{73}Ni_{27}$ sample where Mg_2Ni was the

predominant phase. In both melt-spun samples, Rietveld refinement showed evidence for a metastable Mg_6Ni phase.

For both samples, the DSC analysis in an argon atmosphere showed crystallization peaks at around 160 ^oC which is in agreement with similar works reported in the literature. There was only one small exothermic re-crystallization peak observed for the $Mg_{90}Ni_{10}$ sample, whereas the $Mg_{73}Ni_{27}$ sample exhibited two peaks which relate to the Mg_2Ni and the Mg_6Ni phases. For both samples, H_2 DSC studies showed peaks for hydrogen desorption at 387 °C, and two hydriding peaks at 364 °C and 336 °C for the formation of the MgH_2 and Mg_2NiH_4 phases. The phase transition from high temperature to low temperature Mg_2NiH_4 was also observed in the H_2 DSC studies.

The 140 °C in-situ XRD for the melt-spun $Mg_{90}Ni_{10}$ material demonstrated the crystallization and hydriding behaviour at this temperature under 10 bars of H_2. The metastable Mg_6Ni phase was also observed in the XRD patterns, and the decomposition into Mg and Mg_2Ni was also observed. It is noted that the γ-MgH_2 phase was also shown in the XRD pattern at140 °C, as it was not observed in the XRD pattern after the H_2 DSC treatment.

The variable temperature, in-situ, XRD investigation for the melt-spun $Mg_{73}Ni_{27}$ sample reveals the re-crystallization and hydriding behaviour with increasing temperatures. The metastable Mg_6Ni was shown to be crystallized at 160 °C and decomposed at around 300 °C. The α- and γ-MgH_2 formed at relatively low temperatures (<160 °C), and exhibited a marked increase in concentration at around 220 °C. The hydriding of

Mg_2NiH_4 started at higher temperatures of around 220 °C. In accordance with the DSC peaks, the dehydriding occurred at 380 °C. On cooling, MgH_2 was shown to hydride first, followed by Mg_2NiH_4 at lower temperatures.

The hydrogen sorption kinetics for both samples were extremely fast and comparable to those of high energy ball milled samples. The melt-spun $Mg_{90}Ni_{10}$ sample was shown to absorb >5 wt.% H_2 within 20 min, and the kinetics could be relatively fast with a higher ramp rate of hydrogen pressure. On hydrogen absorption at 300 °C, the melt-spun $Mg_{73}Ni_{27}$ sample exhibited two distinctive steps, which was not found for the $Mg_{90}Ni_{10}$ sample. At a low temperature of 140 °C and even at room temperature, both samples showed hydrogen sorption, and the kinetics were improved with increasing hydrogen sorption cycles. The pressure-composition isotherms (PCI) exhibited multi-step hydrding-dehydriding for both samples. The $Mg_{90}Ni_{10}$ sample exhibited three steps with three desorption plateau pressures, according to the heat of formations which were calculated using van't Hoff equation, corresponding to the dehydriding of α- & γ-MgH_2 and Mg_2NiH_4. The $Mg_{73}Ni_{27}$ exhibited similar PCI curves, but with an increased heat of formation for the Mg_2NiH_4 phase, the reason of which remains uncertain.

As the hydrogen storage material for the light-duty vehicles, the melt-spun Mg-Ni samples meet the gravimetric capacity target of 5.5 wt.% which is the target for 2017 by DOE US. At a high temperature such as 300 °C, the melt-spun Mg-Ni alloys exhibited very fast kinetics, especially under high hydrogen pressure. However, for practical applications, hydriding or dehydriding at a lower temperature range is more realistic. For both samples, hydrogen absorption at a low temperature (140 °C) and even room

temperature, were observed, however, with slow kinetics. The hydrogen desorption was observed only at the temperature of 140 °C or above. Therefore, the kinetics at a lower temperature does not meet the requirement for a short time of hydrogen charging. Due to the relative high hydrogen capacity, potential good kinetics and low cost, further development for the Mg-Ni alloys as hydrogen storage material is required.

Mg-Ni-Ti alloys

It proved impossible to melt spin the Mg-Ni-Ti alloy outlined in this work. This is not entirely surprising given the difficulties which arose when melt spinning the Mg-Ni samples, the immiscibility of Ti in Mg and the high melting point for Ti.

Others

During the course of this study, several other authors also published similar work on the same or similar alloy systems. It was encouraging to note that similar hydrogen sorption properties were observed in these studies. The inert sample transfer and cryo-milling performed in this work distinguished it from the other reports. It was interesting to note that, in this study, the kinetics observed at low temperatures were on a par with catalysed samples reported by other authors.

It is evident that by the melt spinning of Mg-Ni alloys, it is possible to produce a nano-crystalline sample which can be cycled in hydrogen with very fast sorption kinetics, on a par with those of the high velocity ball-milled powders. As opposed to the particles size of the powders, this proves that the grain size of the particular material has the largest impact on hydrogen sorption kinetics. Melt spinning can really be scaled up and is used

on an industrial scale for other applications (*e.g.* the production of nano-crystalline NdFeB ribbons for permanent magnets). The melt spinning route should be a more cost effective way of producing large quantities of Mg-alloys (or other alloys) for hydrogen storage applications compared with that of high energy milling.

9. Future Work

In this study, it proved very difficult to produce the Mg-Ni ribbons with a target for the elemental composition. In order to widen the compositional range of the materials which can be produced, further work is required to try to minimise the Mg losses. If this can be achieved then more of the variables can then be altered including wheel speed, nozzle diameter, distance of crucible from wheel *etc*..

Further work is required to investigate the phase segregation which was apparent in the melt-spun $Mg_{90}Ni_{10}$ ribbons but not found in the melt-spun $Mg_{73}Ni_{27}$ sample. More melt-spun ribbons could be produced with various cooling rates due to different wheel speed, and an investigation is required to explain whether the cooling rate is the cause of the phase segregation.

More work is required for the investigation on the metastable Mg_6Ni phase. An in-situ XRD at a temperature up to 160 °C under a helium atmosphere could be performed, to investigate the re-crystallization behaviour and phase transformation of the melt-spun samples, where potentially, the Mg_6Ni phase plays a crucial role. This in-situ XRD on the same sample could be repeated to investigate re-crystallization behaviour of the amorphous phase within the melt-spun sample. The SEM observation could then be performed to compare the as-quenched and fully-crystallised samples.

In the present study, the γ-MgH_2 phase was observed during the hydriding process, and it requires more investigation of the MgH_2 hydride. In the present work, the in-situ XRD

was conducted from room temperature to 400 °C, where the γ-MgH_2 phase was observed at a low temperature range and did not appear when cooled from 400 °C. Therefore, a low temperature in-situ XRD (< 250°C) could be performed to investigate the phase stability of the γ-MgH_2 and any possible γ-MgH_2-related hydriding or dehydriding processes. This in-situ XRD measurement should also be repeated. Moreover, the studies of the in-situ XRD under H_2 could also focus on the changes of the intensity of the peaks due to the presence of the Mg_6Ni phase, and the possible relationship between the Mg_6Ni and the γ-MgH_2 phases, or the possible hydriding of Mg_6Ni phase can be discussed. SEM or even TEM observation on the hydrided or dehydrided samples could also provide important information for the investigation on the hydriding or dehydriding behaviour of the γ-MgH_2 phase.

The hydrogen absorption at 300 °C for the $Mg_{73}Ni_{27}$ sample exhibited a two-step process, which is likely to correspond to the hydriding of the MgH_2 and Mg_2NiH_4 phase. The hydrogen sorption process requires further investigation. Mathematical simulation models can be applied to the observed data to analyse the kinetics of the hydrogen sorption process. The two-step absorption was not observed at a low temperature (140 °C), and therefore, it requires more studies on the hydrogen sorption measurements in a low temperature range, to study the hydrogenation behaviour at such temperatures.

For both $Mg_{90}Ni_{10}$ and $Mg_{73}Ni_{27}$ samples, the activation treatment exhibited a positive effect for the kinetics of hydriding at a high temperature. It requires more investigation into the changes during the activation treatment, such as phase transformation related to a possible amorphous phase, metastable Mg_6Ni phase, unusual γ-MgH_2 phase *etc*.. A

detailed XRD analysis could be conducted to compare the sample before and after the hydrogen sorption cycles. Moreover, a cyclic hydrogen sorption measurement at a low temperature could be performed in the same way as the high temperature IGA measurements for 10 cycles. These measurements could indicate whether the low temperature sorption cycles have an effect on the activation of the hydrogen sorption properties.

In the present work, the room temperature absorption is one of the novel findings, which is an important hydrogen storage property for possible on-board mobile applications. The hydrogen sorption at room requires more investigation. For both $Mg_{90}Ni_{10}$ and $Mg_{73}Ni_{27}$ samples, they exhibited room temperature absorption in the as-quenched state, and it should be confirmed whether it is the case for the sample after a heat treatment. Therefore, for a sample after the DSC measurements or cyclic hydrogen sorption measurements at high temperatures (>300 °C), a room temperature hydrogen sorption measurement is required.

Further investigation on the PCI system using HTP is required, in order to analyse the multiple steps of the plateaux in the PCI curves. The enthalpy and entropy of the related hydrides are required to be determined, with comparison with the values reported in the literature.

It would also be very beneficial to investigate the effect of catalysts on the Mg-Ni system, such as Y and Nd, in accordance with other workers. Moreover, it is also necessary to reproduce the samples studied in the thesis and repeating some experiments which

provided the key findings, in order to examine the reproducibility of those observations with an analysis of the statistical significance.

10. Appendix

10.1. $Mg_{70}Ni_{30}$ sample

In line with the previous samples, an attempt was made to melt spin a $Mg_{70}Ni_{30}$ pressed pellet. A wide range of processing conditions were investigated with power ratings from 15% ~ 45% (see Table 10-1). During these melting trials, it was evident that, before the material became molten, a large quantity of Mg vapour was being lost through the nozzle of the BN crucible. The Mg vapour prevented the pyrometer from providing a reliable temperature reading and therefore, the material was taken to a temperature where it appeared to be molten before pouring was attempted.

Power	Time	Power	Time
15%	2 min	25%	1 min
16%	2 min	30%	1 min
17%	2 min	35%	1 min
18%	10 min	40%	1 min
19%	2 min	45%	1 min
20%	2 min		

Table 10-1 Induction heating profile during the melt spinning of the $Mg_{70}Ni_{30}$ sample.

Because of these problems, only a very small amount of very thin ribbons were produced (< 0.1 grams) The cross section of the melt-spun $Mg_{70}Ni_{30}$ ribbon was observed by SEM in the same way as that carried out for the $Mg_{90}Ni_{10}$ and $Mg_{73}Ni_{27}$ samples. Figure 10-1 shows the BSI image and EDS result of the melt-spun $Mg_{70}Ni_{30}$ ribbons.

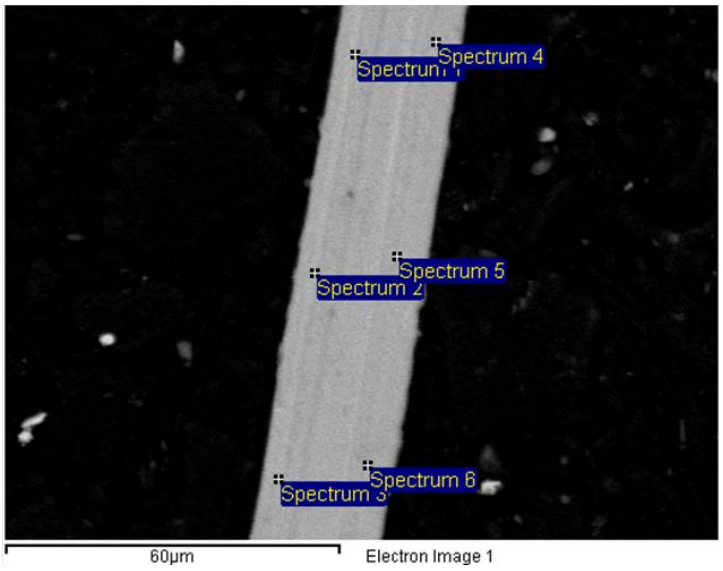

Spectrum	Mg	Ni
Spectrum 1	71.42	28.58
Spectrum 2	71.67	28.33
Spectrum 3	70.81	29.19
Spectrum 4	72.36	27.64
Spectrum 5	70.16	29.84
Spectrum 6	71.26	28.74
Mean	71.28	28.72
Std. deviation	0.75	0.75
Max.	72.36	29.84
Min.	70.16	27.64

All results in atomic%

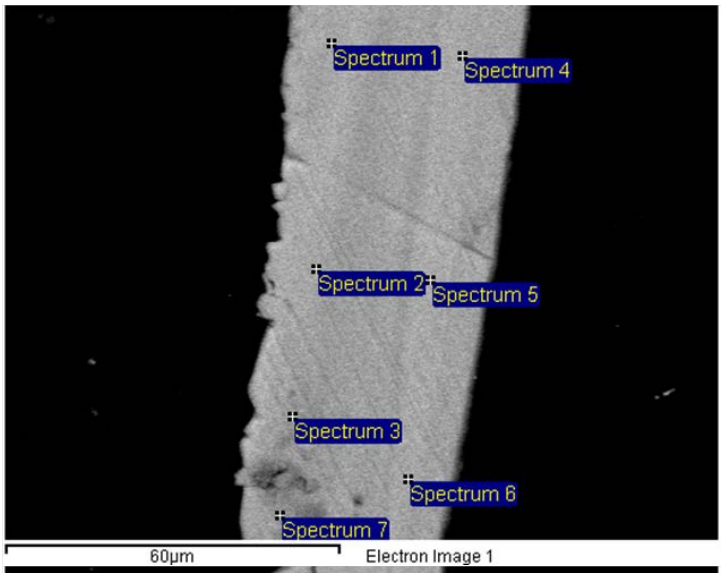

Spectrum	Mg	Ni
Spectrum 1	70.43	29.57
Spectrum 2	70.50	29.50
Spectrum 3	68.61	31.39
Spectrum 4	69.72	30.28
Spectrum 5	68.99	31.01
Spectrum 6	69.31	30.69
Spectrum 7	60.60	39.40
Mean	68.31	31.69
Std. deviation	3.47	3.47
Max.	70.50	39.40
Min.	60.60	29.50

All results in atomic%

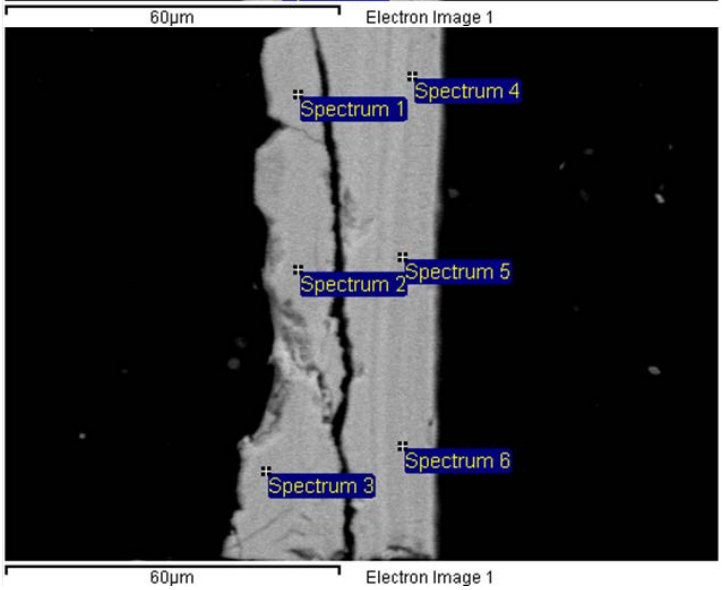

Spectrum	Mg	Ni
Spectrum 1	61.73	38.27
Spectrum 2	61.31	38.69
Spectrum 3	58.52	41.48
Spectrum 4	62.28	37.72
Spectrum 5	62.02	37.98
Spectrum 6	62.02	37.98
Mean	61.31	38.69
Std. deviation	1.41	1.41
Max.	62.28	41.48
Min.	58.52	37.72

All results in atomic%

Figure 10-1 SEM & EDS results of cross sections of the melt-spun $Mg_{70}Ni_{30}$ ribbons.

Surprisingly the material which was ejected from the nozzle was almost exclusively the same composition as the initial composition. However, the amount of material was so small that further analysis could not be performed. Despite many repeated attempts using these conditions, and modified processing conditions, it was not possible to produce an appreciable amount of material.

The failure of the melt spinning process is again likely to be due to the losses of magnesium. The melting point of the $Mg_{70}Ni_{30}$ alloy should be around 760 °C (see Figure 4-1), therefore the material has to be taken to a higher temperature in the first instance. The higher temperature will result in the loss of further Mg due to sublimation and therefore the melting point will increase even further as $MgNi_2$ is likely to form. . In order to investigate the reason for the failed melting trials, the remaining material in the crucible was extracted and examined in cross section. This was then examined by SEM combined with EDS.

For the $Mg_{70}Ni_{30}$ alloy after melt spinning, Figure 10-2 and Figure 10-3 show the BSI of the top and bottom section of the remaining material in the crucible. The EDS measurements showed the elemental ratio of the inspected area in the SEM images. It was evident that the material at both the top and the bottom of the crucible, especially for the top area, was Mg 'lean' compared to that of the starting composition and the small amount of the melt-spun ribbons. Few of the publications on melt spinning of Mg-Ni based systems reveal how the starting materials are prepared and melted. Therefore it was unclear how some of the workers had managed to produce alloys close to the composition of $Mg_{70}Ni_{30}$.

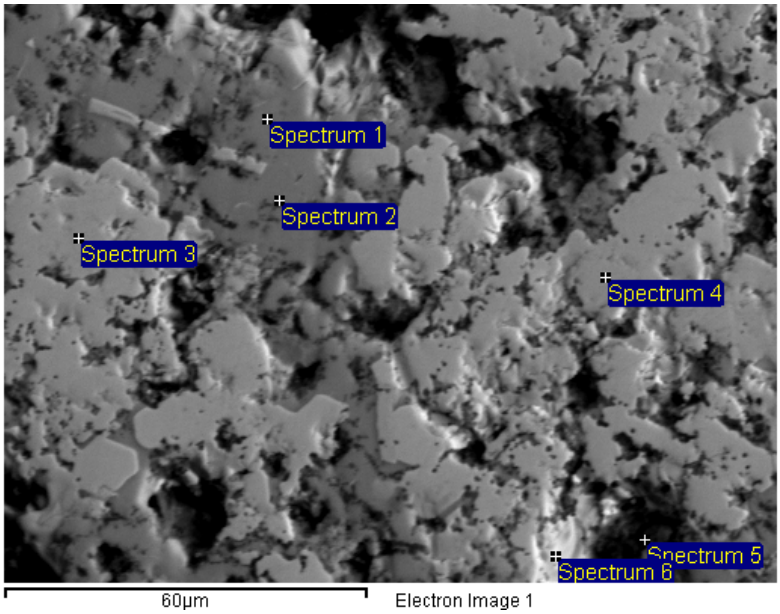

Spectrum	Mg	Ni
Spectrum 1	59.88	40.12
Spectrum 2	62.53	37.47
Spectrum 3	27.84	72.16
Spectrum 4	27.10	72.90
Spectrum 5	92.68	7.32
Spectrum 6	38.49	61.51
Max.	92.68	72.90
Min.	27.10	7.32

All results in atomic%

Figure 10-2 SEM of the top part of the remnants of $Mg_{70}Ni_{30}$ after melt spinning.

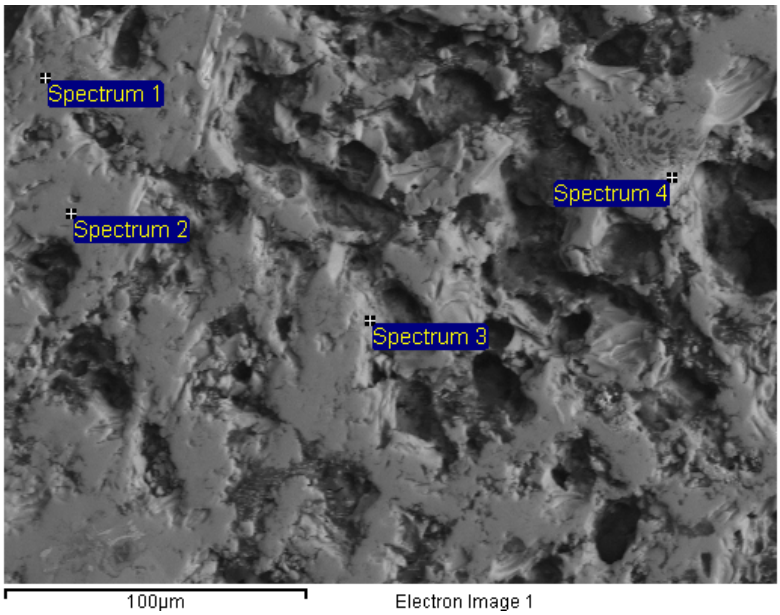

Spectrum	Mg	Ni
Spectrum 1	61.33	38.67
Spectrum 2	60.77	39.23
Spectrum 3	71.77	28.23
Spectrum 4	60.86	39.14
Max.	71.77	39.23
Min.	60.77	28.23

All results in atomic%

Figure 10-3 SEM of the bottom part of the remnants of $Mg_{70}Ni_{30}$ after melt spinning.

10.2. MgNiTi alloy

In the final year of this PhD, an attempt was made to melt spin a Mg-Ni-Ti alloy. Titanium is another light-weight element which can form stable hydrides with a relatively high capacity of ~4 wt.%. However, in thermodynamic equilibrium, Mg and Ti are immiscible elements. Some researchers produced successfully Mg-Ti-based alloys using non-equilibrium techniques such as sputtering and ball milling *etc.* (Baldi et al., 2009; Choi et al., 2008). Gremaud *et al.* (2007) formed ternary Mg-Ti-Ni combinatorial thin film materials by sputtering, and used an optical technique called 'hydrogenography' to investigate the hydrogen storage properties. One composition, namely $Mg_{0.69}Ti_{0.26}Ni_{0.05,}$ was proposed as exhibiting a promising enthalpy of formation, $\Delta H = -40$ kJ $mol^{-1}H_2$ which is much lower than that of magnesium hydride (–76 kJ $mol^{-1}H_2$). This means that a much lower temperature should be required for the desorption of hydrogen from the hydride. Therefore, in this work, this composition was chosen for melt spinning.

10.2.1. Ball milling of MgH_2-Ni-Ti

An attempt was made to make pre-cursor materials with an intimate mixture of Mg, Ni and Ti by ball milling the elements together. However, as magnesium is ductile, magnesium hydride was used instead of metallic Mg. Hydrogen would be degassed after ball milling.

20 g powders of MgH_2, Ni and Ti were weighted out in an atom-ratio of $(MgH_2)_{69}Ni_{26}Ti_5$ and then fully mixed with a blender. The mixed powder was then loaded inertly into two 50 cm^3 stainless steel milling pots in a glove box. Each of these two pots held 10 g of mixed powder with 12 stainless steel balls, with a ball-sample mass ratio of 10:1. The two pots were then located on opposite position in the planetary ball mill (*Retsch PM400*). The milling proces was set to be with a rotating speed of 200 rpm and a milling time of 5 hours. As hydrogen is released from the MgH_2 on milling the milling pot was sporadically opened inside a glovebox to avoid over-pressurising within the pot. This was performed after 1, 3 and 6 hours of milling.

Before the melt spinning, the ball-milled sample has been degased to release H_2. It has been heated at 400°C for 24 hours in a stainless steel crucible in a furnace under 1 bar argon atmosphere with a flowing rate of 100 ml/min.

10.2.2. XRD of ball-milled MgH_2-Ni-Ti sample and degassed Mg-Ni-Ti sample

Room temperature XRD was conducted on both the as-ball-milled sample and the degassed sample. Figure 10-4 shows the phases which were present in the as-milled sample, including MgH_2, Ni, Ti, and Mg. The MgH_2, Ni and Ti were the starting materials, and the Mg was formed due to the degassing of MgH_2 as a result of the ball milling.

Rietveld refinement was performed on the XRD data for the MgH_2, Ni, Ti and Mg phase (in Figure 10-5). The refined data fitted very well with the raw data with a goodness of fit (GOF) of 1.294. Moreover, there was no significant change of the phase ratio after ball milling.

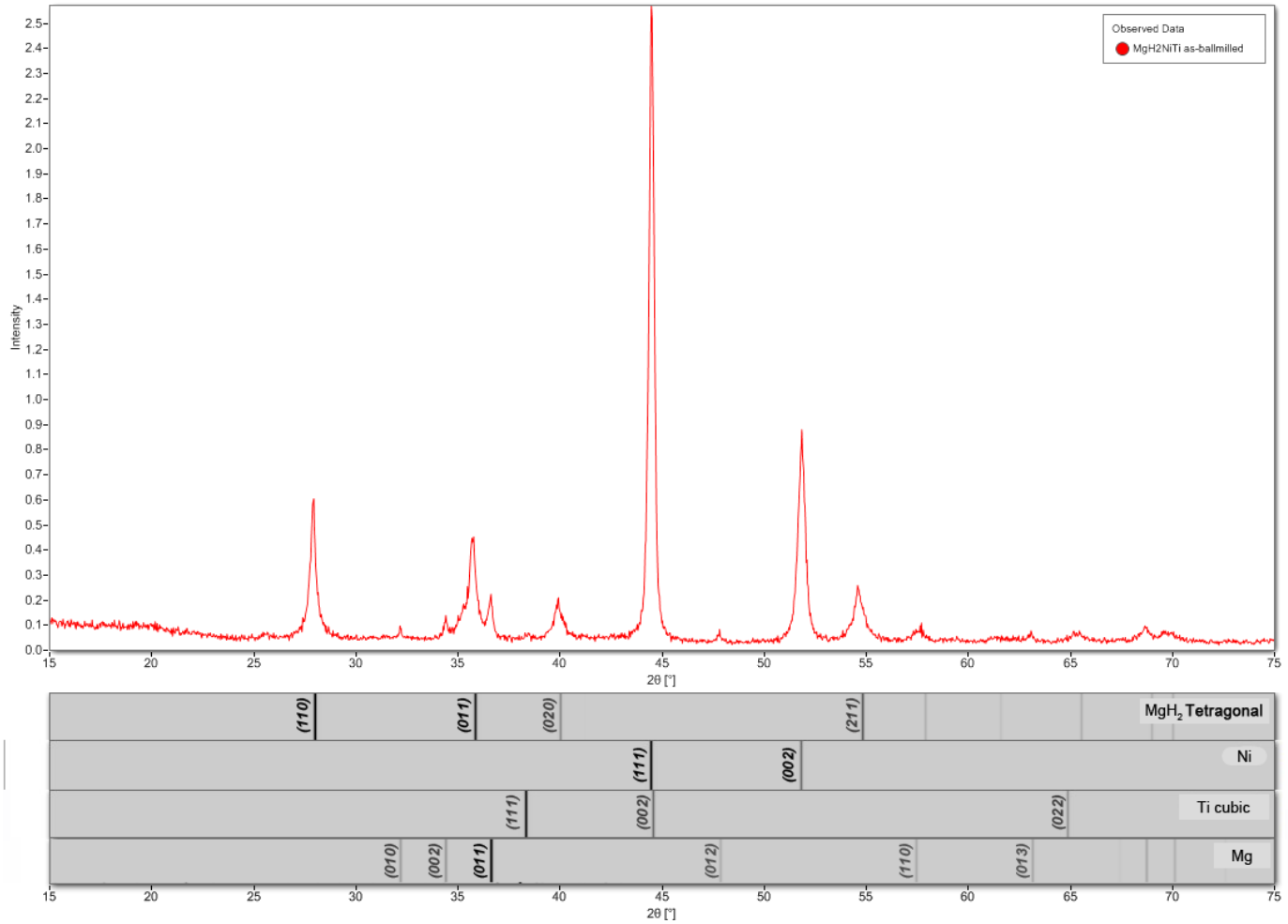

Figure 10-4 XRD pattern for the as-ball-milled MgH_2-Ni-Ti powder.

Starting Ratio	Mass Ratio				Mole Ratio			
	MgH_2	Ni	Ti	Mg	MgH_2	Ni	Ti	Mg
$(MgH_2)_{69}Ni_{26}Ti_5$	40.16%	46.82%	9.49%	3.52%	57.24%	29.90%	7.43%	5.43%

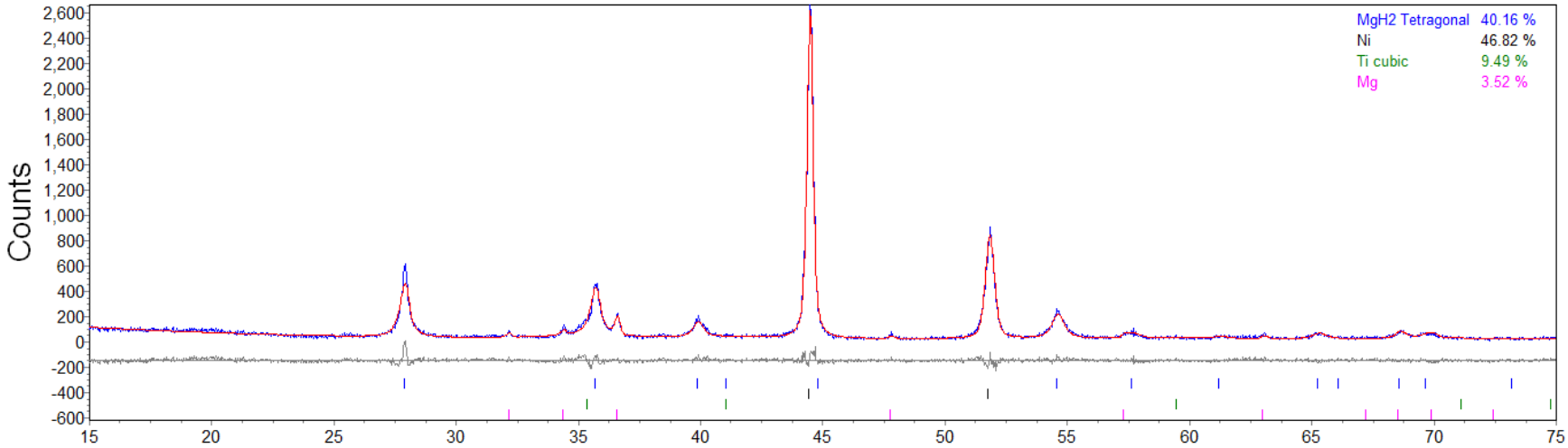

Figure 10-5 Rietveld refined XRD pattern of as-ball-milled MgH_2-Ni-Ti sample.

Figure 10-6 shows the Mg_2Ni, Ti, Mg and Ni phases in the sample after degassing. As expected, the MgH_2 phase has fully dehydrided after degassing. Moreover, Mg and Ni formed Mg_2Ni during degassing at 400 °C, although there was some remaining Mg and Ni in the sample. The Ti still did not form any alloys.

Rietveld refinement was performed on the Mg_2Ni, Ti, Mg and Ni phases. The Rietveld refined pattern had a goodness of fit (GOF) of 1.564. Figure 10-7 shows that the majority of the degassed sample was Mg_2Ni with small fractions of pure Mg, Ni and Ti.

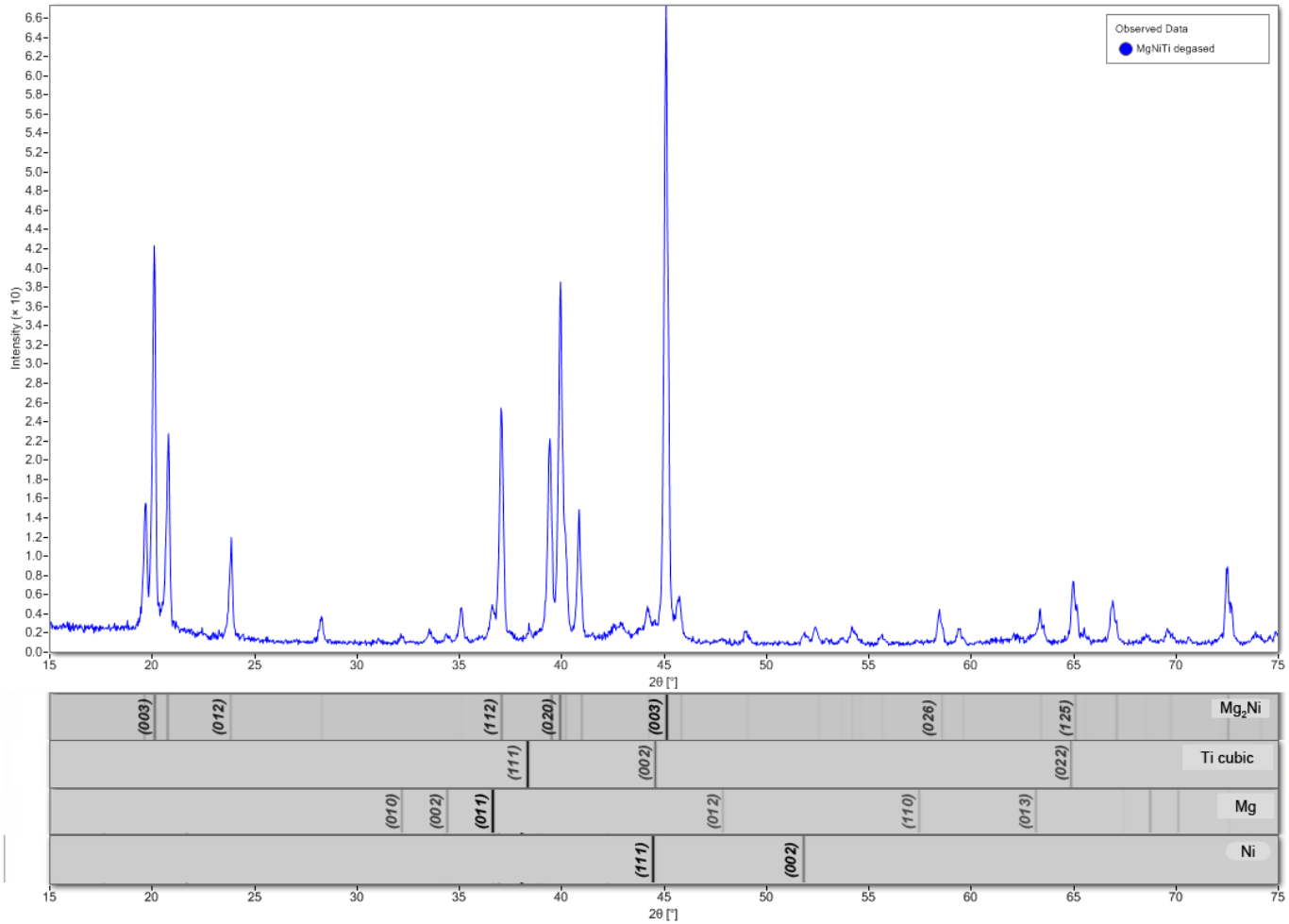

Figure 10-6 XRD pattern of degased Mg-Ni-Ti sample by ball milling.

Starting Ratio	Mass Ratio (%)				Mole Ratio (%)				End Ratio
	Mg_2Ni	Ni	Ti	Mg	Mg_2Ni	Ni	Ti	Mg	
$(MgH_2)_{69}Ni_{26}Ti_5$	76.24	6.95	13.83	2.98	57.28	9.54	23.29	9.89	$Mg_{58}Ni_{31}Ti_{11}$

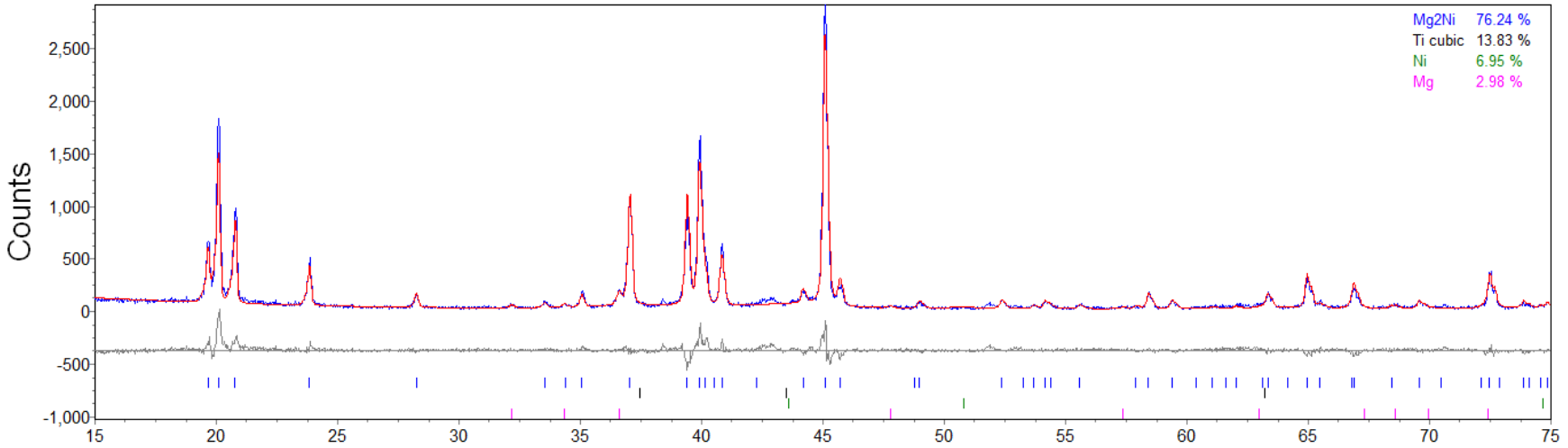

Figure 10-7 Rietveld refined XRD pattern of degased Mg-Ni-Ti by ball milling.

10.2.3. Melt spinning of Mg-Ni-Ti powder compressed sample

The degassed Mg-Ni-Ti powder was pressed into pellets before melt spinning in the same manner as that of the Mg-Ni samples. The compressed pellets were loaded inertly onto the melt spinner. The power on the induction heater was increased in this instance to 55%, in an attempt to get close to the melting point of Ti. The pyrometer lost the signal at a temperature of around 730 °C. On ejection of the melt, only two small ribbons were produced. The rest of the alloy remained in the crucible. The ribbons and remnants have been investigated by SEM.

Figure 10-8 shows the back scattered images of a cross section of the melt-spun ribbon with EDS analysis. The melt spun ribbon can be identified as pure Mg. This suggests that magnesium was the only phase that was molten before injection. However, there were only two ribbons collected, indicating that most of the magnesium had been vaporized, when the induction melting power went up to 55%. The remnant was supposed to have a low Mg content, and this has been confirmed by the SE M studies.

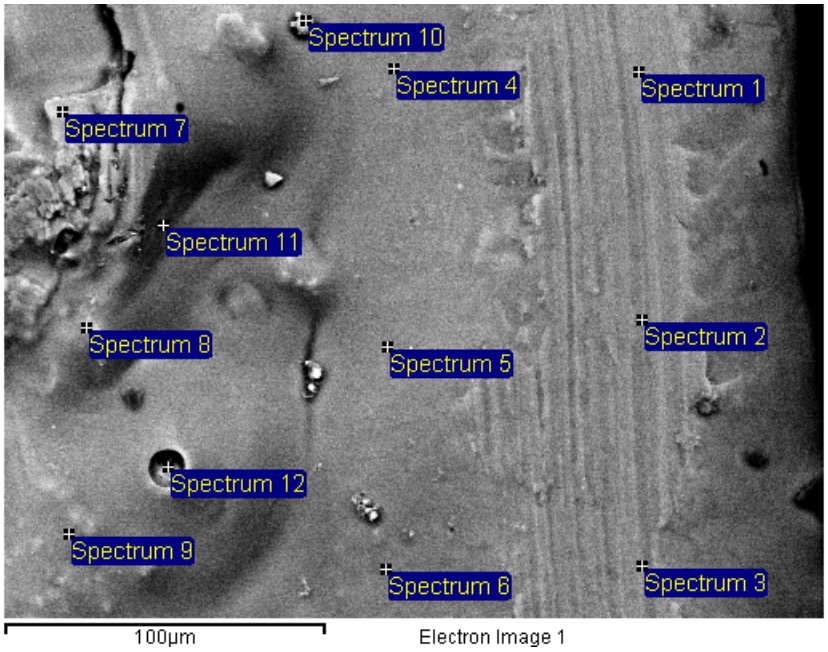

Spectrum	Mg
Spectrum 1	100.00
Spectrum 2	100.00
Spectrum 3	100.00
Spectrum 4	100.00
Spectrum 5	100.00
Spectrum 6	100.00
Spectrum 7	100.00
Spectrum 8	100.00
Spectrum 9	100.00
Spectrum 10	100.00
Spectrum 11	100.00
Spectrum 12	100.00
Max.	100.00
Min.	100.00

All results in atomic%

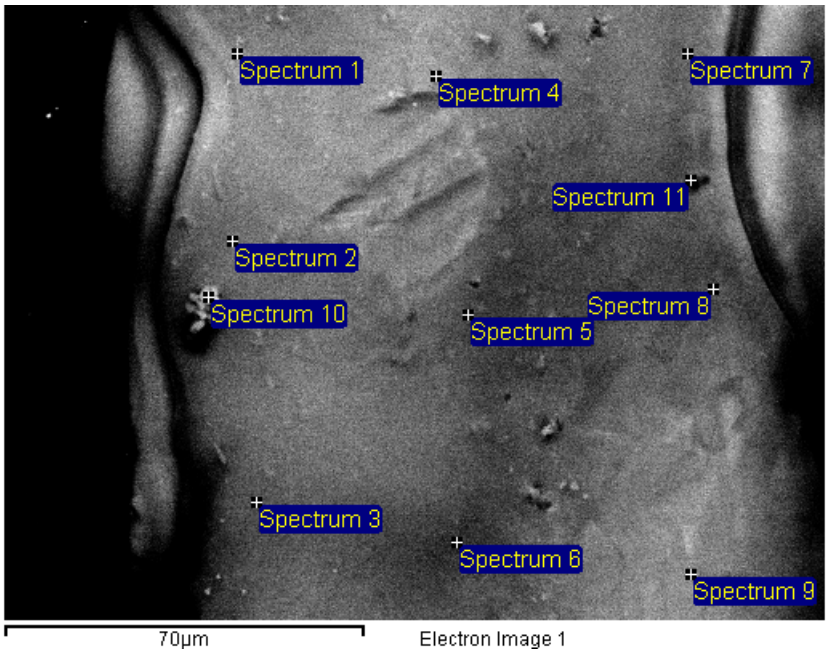

Spectrum	Mg
Spectrum 1	100.00
Spectrum 2	100.00
Spectrum 3	100.00
Spectrum 4	100.00
Spectrum 5	100.00
Spectrum 6	100.00
Spectrum 7	100.00
Spectrum 8	100.00
Spectrum 9	100.00
Spectrum 10	100.00
Spectrum 11	100.00
Max.	100.00
Min.	100.00

All results in atomic%

Figure 10-8 SEM & EDS of cross section of the ribbon collected after melt spinning of Mg-Ni-Ti alloy.

Two cross sections were prepared from the remnants, one from the top part of the melt, and the other from the bottom. Figure 10-9 shows the back scattered image with EDS of the cross section of the top part of the melt. It showed that Ti was fully alloyed to form the $TiNi_3$ phase (Spectrum 1, 2). The $TiNi_3$ phase contributed the majority of the melt, whereas the Mg content in all the SEM images was low, due to the significant losses of Mg during the melt spinning process.

Figure 10-10 shows the SEM result of the bottom part of the remnants. $TiNi_3$ could be observed once again (Spectrum 1-3) in the first image of Figure 10-10, and there were some areas which were Mg-rich. In general, the losses of magnesium in the bottom part of the melt were not as significant as that in the top part. Due to the sublimation of the magnesium, the evaporation occurs more significantly on the molten surface rather than that at the bottom of the melt. This means that the surface losses are mostly magnesium and the bottom losses the least. The SEM with EDS analysis confirms this picture.

The melting point of $TiNi_3$ is around 1200 °C which is unlikely to be achieved in the induction furnace on the melt spinner. It is also evident from this work and from the behaviour observed for the $Mg_{70}Ni_{30}$ sample, that above 700 °C, the magnesium sublimation is a major issue. This significantly limits the range of alloys which can be prepared using this arrangement.

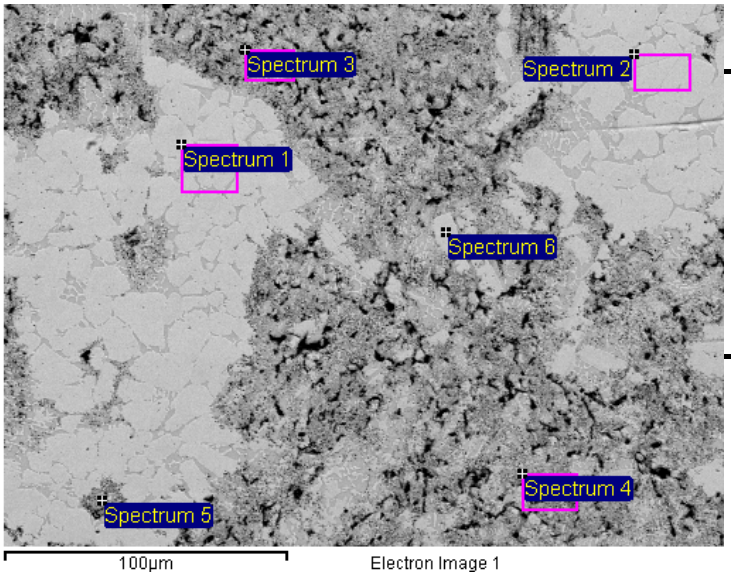

Spectrum	Mg	Ti	Ni
Spectrum 1	5.45	19.22	75.33
Spectrum 2	1.69	23.21	75.10
Spectrum 3	25.52	11.22	63.26
Spectrum 4	30.86	11.00	58.15
Spectrum 5	22.01	13.47	64.51
Spectrum 6	2.93	20.97	76.10
Max.	30.86	23.21	76.10
Min.	1.69	11.00	58.15

All results in atomic%

Figure 10-9 Back scattered images with EDS analysis of the cross section of the top part of the remnant in the crucible after melt spinning for the Mg-Ni-Ti alloy.

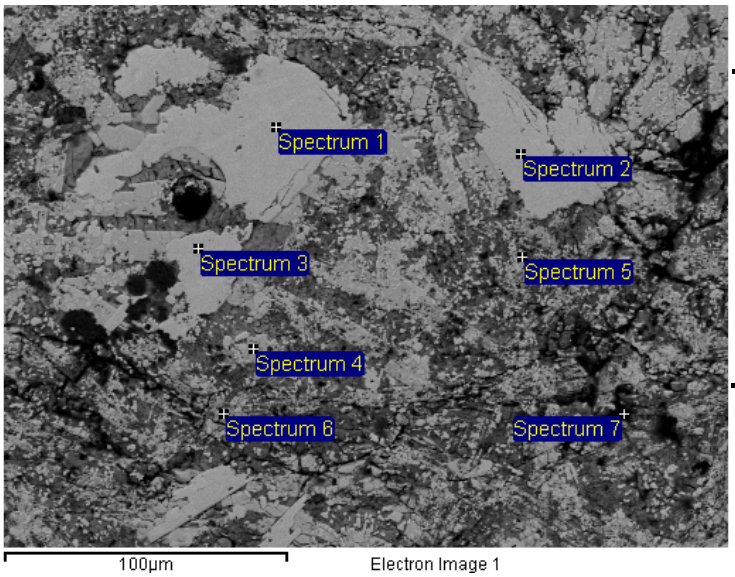

Spectrum	Mg	Ti	Ni
Spectrum 1	5.43	21.31	73.26
Spectrum 2	4.68	21.81	73.51
Spectrum 3	5.49	21.75	72.76
Spectrum 4	31.59	4.32	64.09
Spectrum 5	57.70	10.55	31.75
Spectrum 6	32.35	11.81	55.85
Spectrum 7	35.41	11.82	52.77
Max.	57.70	21.81	73.51
Min.	4.68	4.32	31.75

All results in atomic%

Figure 10-10 Back scattered images with EDS analysis of the cross section of the bottom part of the remnant in the crucible after melt spinning for the Mg-Ni-Ti alloy.

10.3. Enthalpy and Entropy

Reaction	Materials	ΔH (kJ mol^{-1}H$_2$)	ΔS (J·K^{-1}mol^{-1})	Reference
α-**MgH$_2$** → Mg	MS-Mg$_{85.7}$Ni$_{14.3}$	74.56		(Teresiak et al., 2009b)
	(Mg$_6$Ni)	74.05 ± 1.3		H.E. Kissinger, Anal.Chem. 29(1957) 1702
	MS-Mg$_{90}$Ni$_5$Ce$_5$	77.9	139.7	(Lin et al., 2012a)
	MS-Mg$_{88}$Ni$_{11}$Fe$_1$	77.6 ± 0.5		(Palade et al., 2006)
	MS-Mg$_{85}$Ni$_{10}$La$_5$	76.5	136	(Tanaka, 2008)
	Commercial MgH$_2$	74.4 ± 0.3	135.06 ± 1.9	(Stampfer et al., 1960)
	BM-Mg-10V-10Nb	76.8	136.9	(Tan et al., 2012)
	BM-Mg-50wtZrCrFe	71.42		(Jain et al., 2012)
	MS-Mg$_{80}$Ni$_{15}$Nd$_5$	76	136	(Tanaka et al., 1999)
	TF-Mg-4at.Fe	66.9 ± 4.1	102 ± 10	(Tan et al., 2011)
	TF-Mg-TM	80.5 ± 2.4	142 ± 4	(Fry et al., 2013)
Mg$_2$NiH$_4$ → Mg$_2$Ni		64.5		(Reilly and Wiswall Jr, 1968)
		69.3		(Liang et al., 1998)
	MS-Mg$_{88}$Ni$_{11}$Fe$_1$	71.3 ± 1.2		(Palade et al., 2006)
	MS-Mg$_{85}$Ni$_{10}$La$_5$	73.3	135	(Tanaka, 2008)
		69	129	(Tanaka et al., 1999)
	Mg$_{1.95}$NiAg$_{0.05}$	61 ± 7		(Li et al., 2004)
	Mg$_{1.9}$NiAg$_{0.1}$	50 ± 2		(Li et al., 2004)

* BM for ball milling; MS for melt spinning; TF for thin films

Table 10-2 Enthalpy and Entropy values for the hydrogen desorption of MgH_2 and Mg_2NiH_4 hydrides in the literature.

10.4. Variable temperature XRD traces for the $Mg_{90}Ni_{10}$ and $Mg_{73}Ni_{27}$ alloys

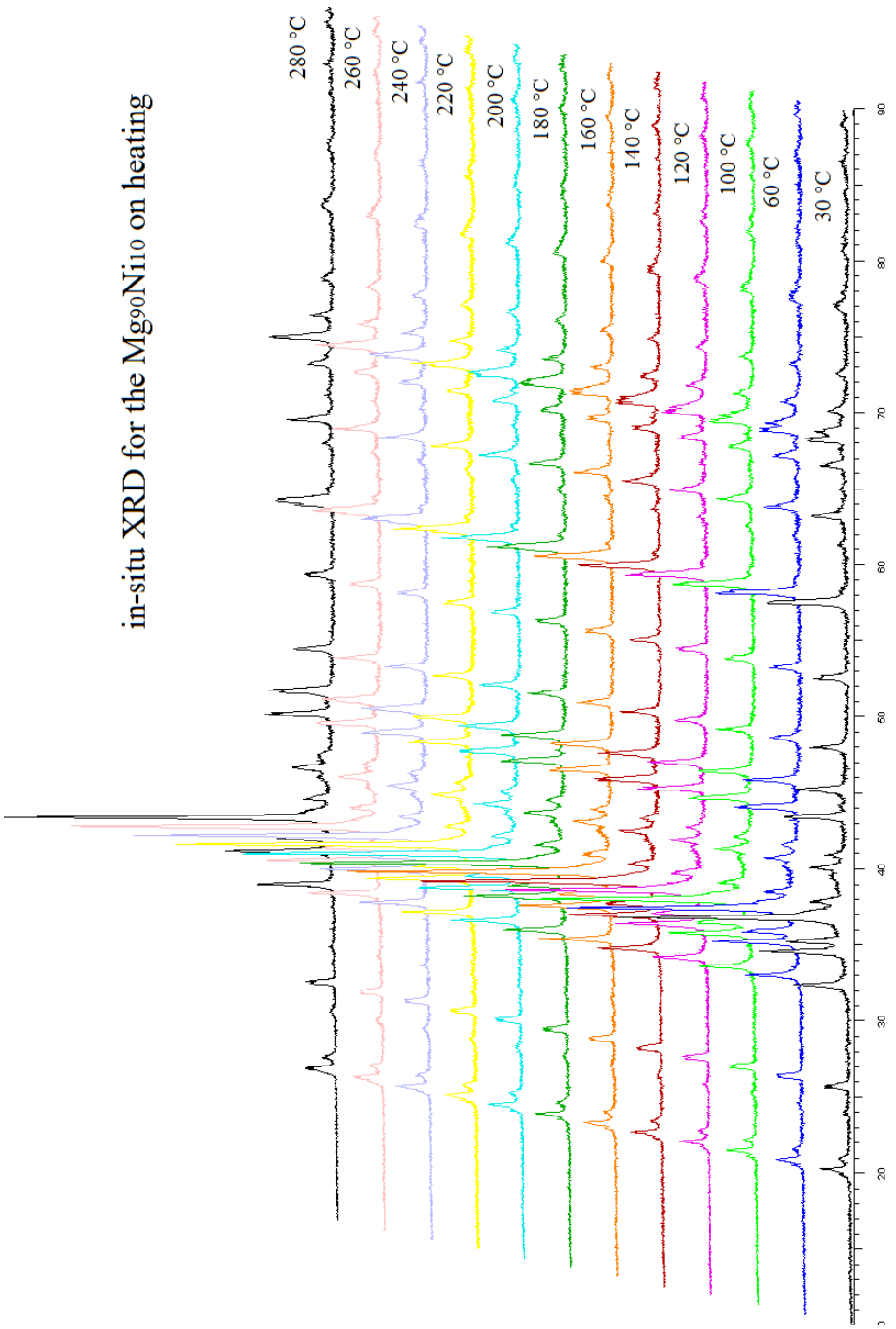

Figure 10-11 Variable temperature in-situ XRD for the melt-spun $Mg_{90}Ni_{10}$ cryo-milled powder from 25 °C to 280 °C.

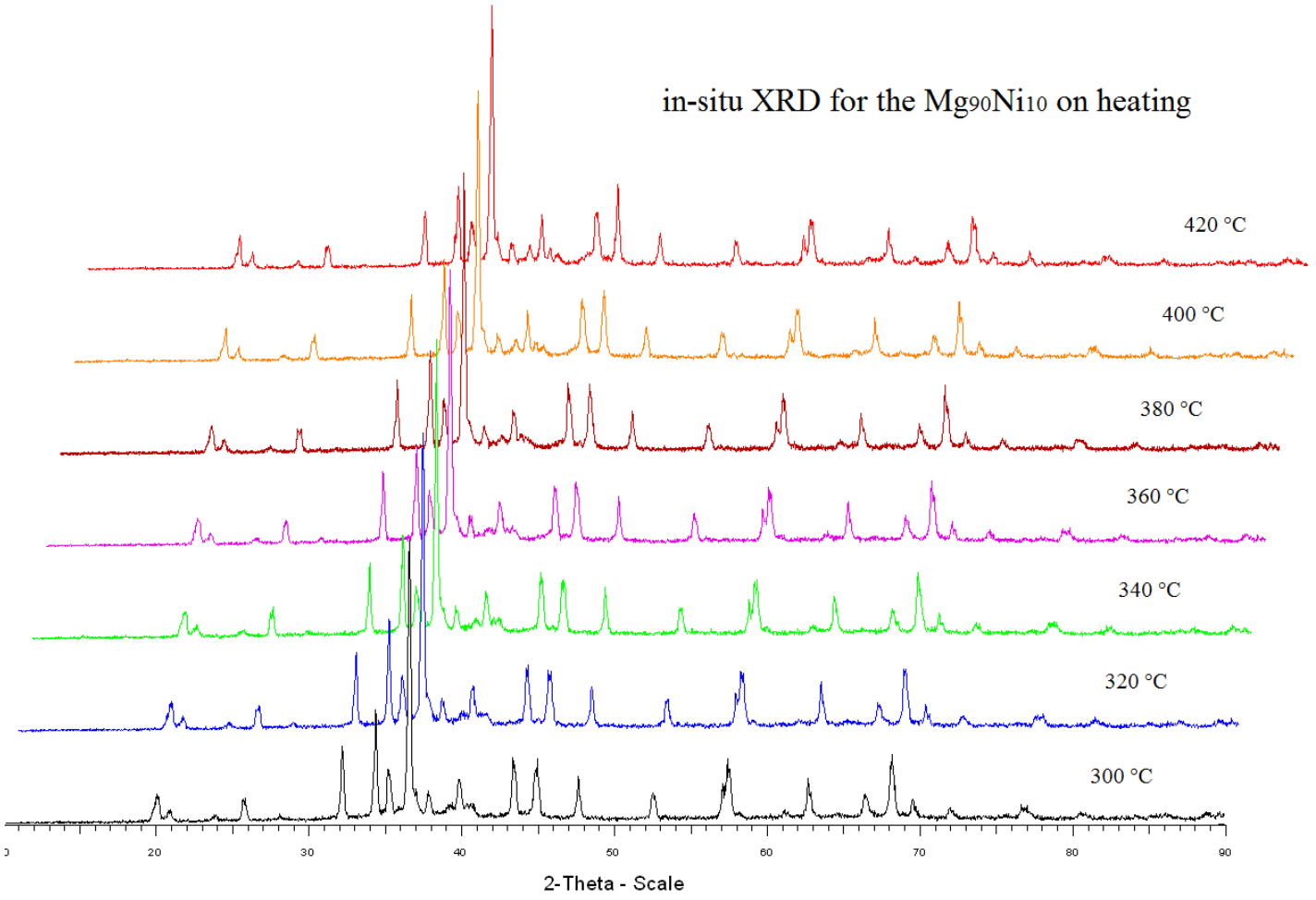

Figure 10-12 Variable temperature in-situ XRD for the melt-spun $Mg_{90}Ni_{10}$ cryo-milled powder from 300 °C to 420 °C.

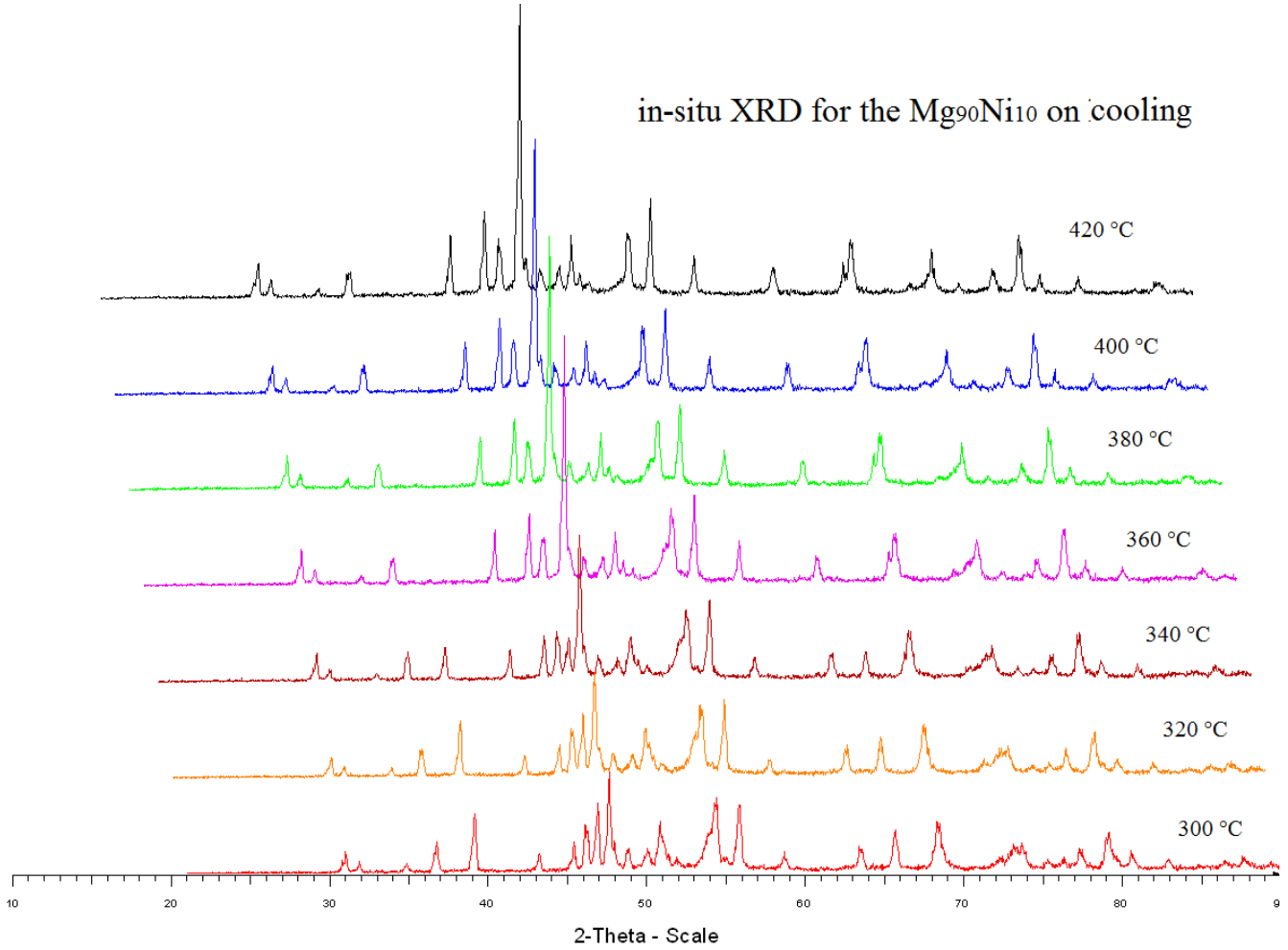

Figure 10-13 Variable temperature in-situ XRD for the melt-spun $Mg_{90}Ni_{10}$ cryo-milled powder from 420 °C to 300 °C.

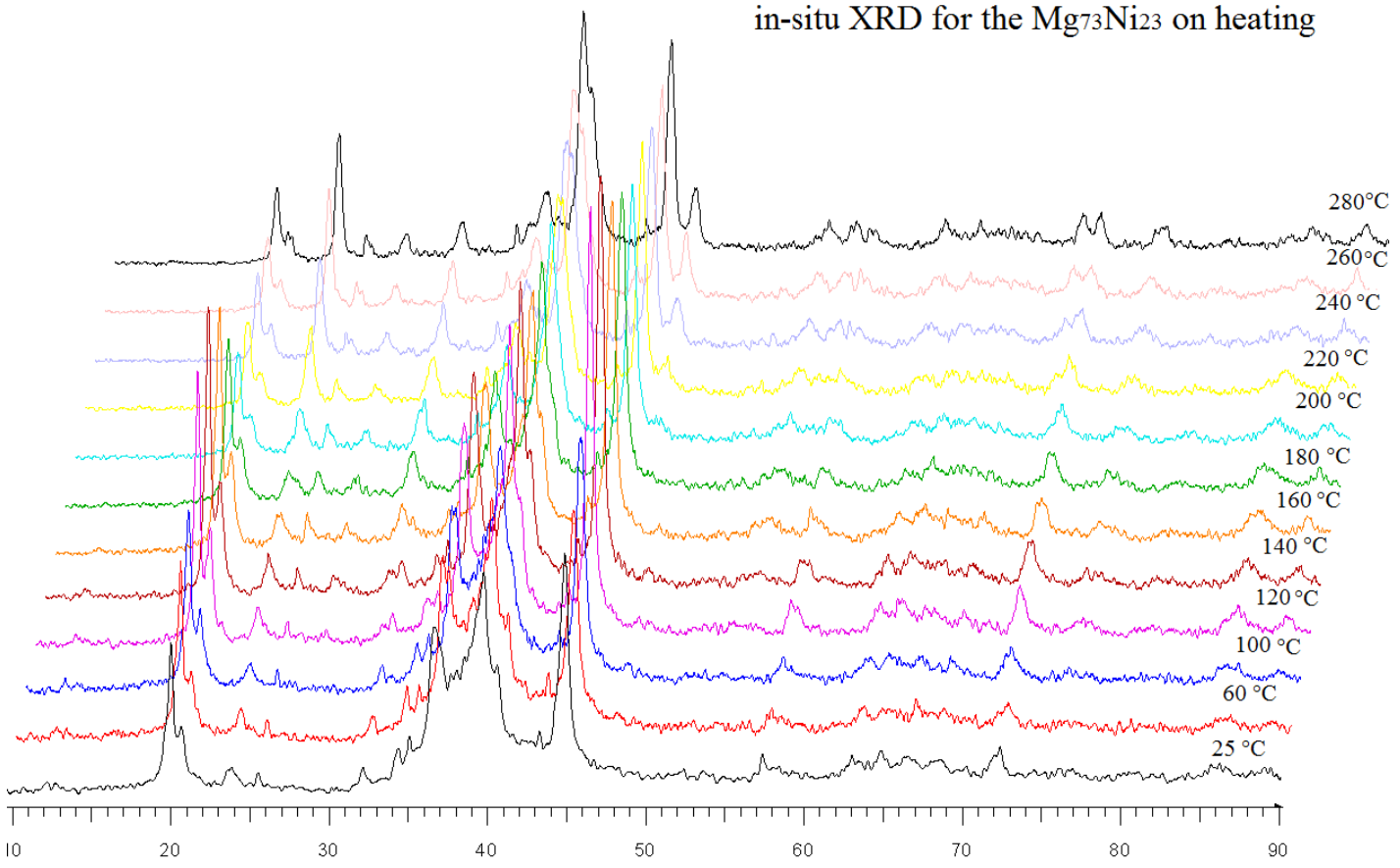

Figure 10-14 Variable temperature in-situ XRD for the melt-spun $Mg_{73}Ni_{27}$ cryo-milled powder from 25 °C to 280 °C.

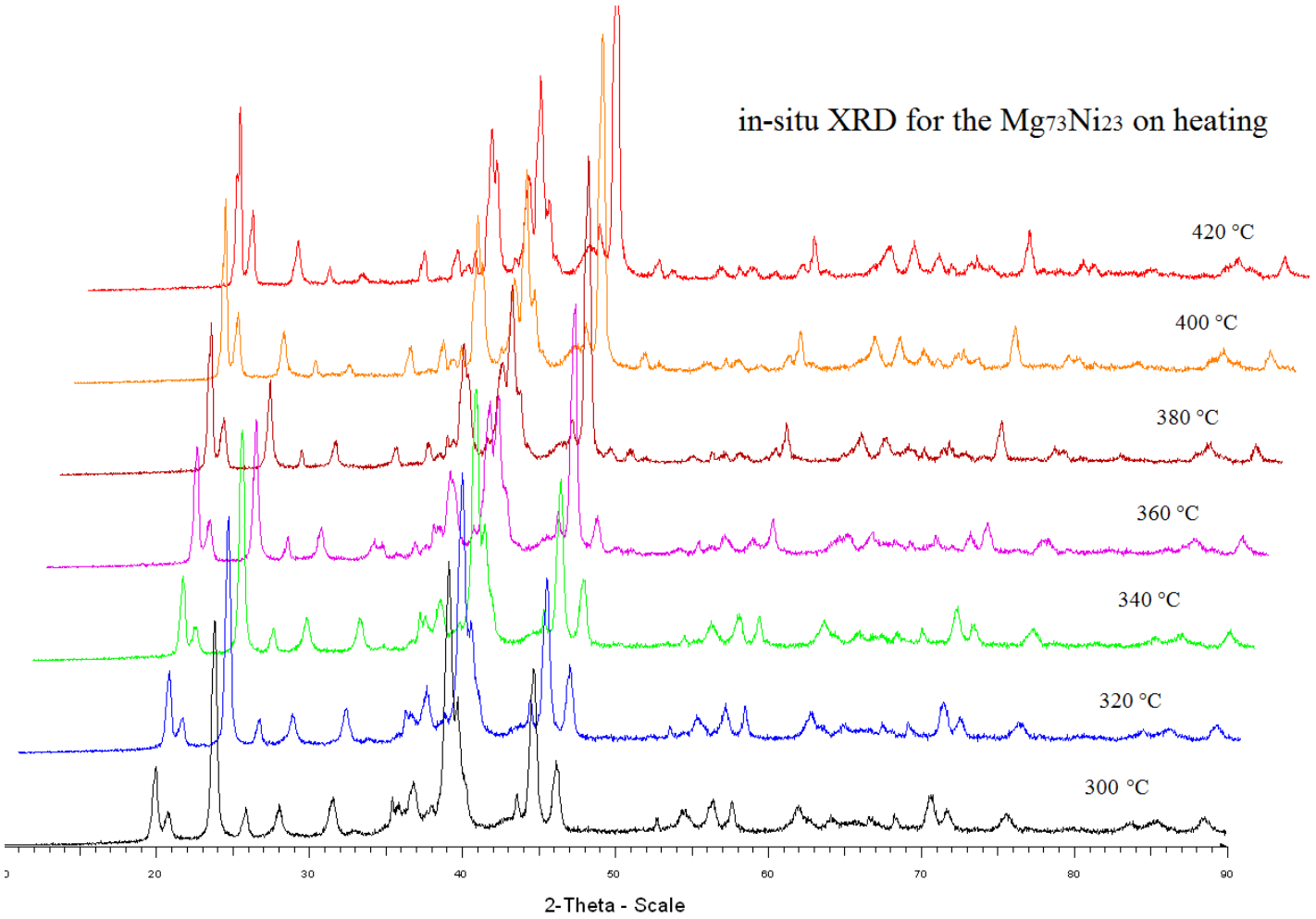

Figure 10-15 Variable temperature in-situ XRD for the melt-spun $Mg_{73}Ni_{27}$ cryo-milled powder from 300 °C to 420 °C.

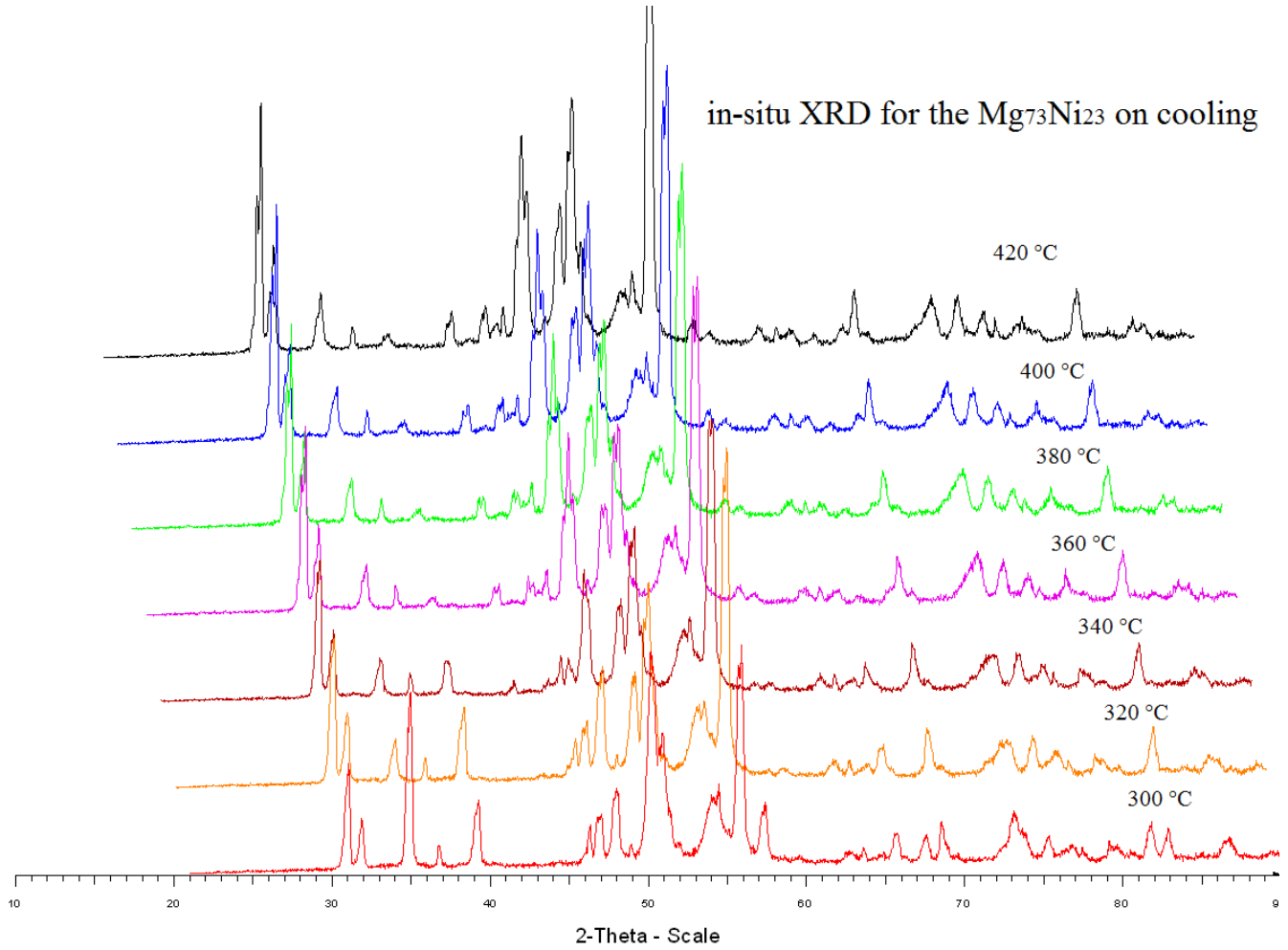

Figure 10-16 Variable temperature in-situ XRD for the melt-spun $Mg_{73}Ni_{27}$ cryo-milled powder from 420 °C to 300 °C.

List of References

Aguey-Zinsou, K.F., Ares Fernandez, J.R., Klassen, T., et al. (2007) Effect of Nb2O5 on MgH2 properties during mechanical milling. **International Journal of Hydrogen Energy,** 32 (13): 2400-2407

Andreasen, A. (2008) Hydrogenation properties of Mg-Al alloys. **International Journal of Hydrogen Energy,** 33 (24): 7489-7497

Baldi, A., Gremaud, R., Borsa, D.M., et al. (2009) Nanoscale composition modulations in MgyTi1-yHx thin film alloys for hydrogen storage. **International Journal of Hydrogen Energy,** 34 (3): 1450-1457

Ballirano, P. and Caminiti, R. (2001) Rietveld refinements on laboratory energy dispersive x-ray diffraction (EDXD) data. **Journal of Applied Crystallography,** 34 (6): 757-762

Barkhordarian, G., Klassen, T. and Bormann, R. (2004) Effect of Nb2O5 content on hydrogen reaction kinetics of Mg. **Journal of Alloys and Compounds,** 364 (1–2): 242-246

Bastide, J.-P., Bonnetot, B., Létoffé, J.-M., et al. (1980) Polymorphisme de l'hydrure de magnesium sous haute pression. **Materials Research Bulletin,** 15 (9): 1215-1224

Belin, E., Gupta, M., Zolliker, P., et al. (1987) An experimental and theoretical investigation of the densities of states of dimagnesium cobalt pentahydride. **Journal of the Less Common Metals,** 130 (0): 267-274

Bendersky, L.A., Chiu, C., Skripnyuk, V.M., et al. (2011) Effect of rapid solidification on hydrogen solubility in Mg-rich Mg–Ni alloys. **International Journal of Hydrogen Energy,** 36 (9): 5388-5399

Berlouis, L.E.A., Cabrera, E., Hall-Barientos, E., et al. (2001) Thermal analysis investigation of hydriding properties of nanocrystalline Mg-Ni- and Mg-Fe-based alloys prepared by high-energy ball milling. **Journal of Materials Research,** 16 (1): 45-57

Bobet, J.L., Grigorova, E., Khrussanova, M., et al. (2003) Hydrogen sorption properties of the nanocomposite 90 wt% Mg2Ni+10 wt% V. **Journal of Alloys and Compounds,** 356–357 (0): 593-597

Bogdanović, B., Bohmhammel, K., Christ, B., et al. (1999) Thermodynamic investigation of the magnesium-hydrogen system. **Journal of Alloys and Compounds,** 282 (1-2): 84-92

Bortz, M., Bertheville, B., Böttger, G., et al. (1999) Structure of the high pressure phase γ-MgH2 by neutron powder diffraction. **Journal of Alloys and Compounds,** 287 (1–2): L4-L6

Bortz, M., Bertheville, B., Yvon, K., et al. (1998) Mg3MnH7, containing the first known hexahydridomanganese(I) complex. **Journal of Alloys and Compounds,** 279 (2): L8-L10

Bronger, W., Jansen, K. and Auffermann, G. (1993) Mg3RuH6, a complex hydride containing two types of hydrogen atoms differing in their bonding. **Journal of Alloys and Compounds,** 199 (1-2): 47-51

Buschow, K.H. and Van Mal, H.H. (1972) Phase relations and hydrogen absorption in the lanthanum-nickel system. **Journal of the Less Common Metals,** 29 (2): 203-210

Černý, R., Joubert, J.M., Kohlmann, H., et al. (2002) Mg6Ir2H11, a new metal hydride containing saddle-like [IrH4]5- and square-pyramidal [IrH5]4- hydrido complexes. **Journal of Alloys and Compounds,** 340 (1-2): 180-188

Choi, Y.J., Lu, J., Sohn, H.Y., et al. (2008) Hydrogen storage properties of the Mg-Ti-H system prepared by high-energy-high-pressure reactive milling. **Journal of Power Sources,** 180 (1): 491-497

Cui, S., Feng, W., Hu, H., et al. (2008) Structural phase transitions in MgH2 under high pressure. **Solid State Communications,** 148 (9-10): 403-405

De Jongh, P.E., Wagemans, R.W.P., Eggenhuisen, T.M., et al. (2007) The preparation of carbon-supported magnesium nanoparticles using melt infiltration. **Chemistry of Materials,** 19 (24): 6052-6057

Ditze, A. and Scharf, C. (2008). **Recycling of Magnesium**: Papierfliger.

Dixon, R.K. (2007) Advancing towards a hydrogen energy economy: Status, opportunities and barriers. **Mitigation and Adaptation Strategies for Global Change,** 12 (3): 305-321

DOE. (2009) **DOE Targets for Onboard Hydrogen Storage Systems for Light-Duty Vehicles** [Online]. Available: http://www1.eere.energy.gov/hydrogenandfuelcells/storage/pdfs/targets_onboard_hydro_storage.pdf [Accessed 17-Jan 2013].

Dufour, J. and Huot, J. (2007) Rapid activation, enhanced hydrogen sorption kinetics and air resistance in laminated Mg-Pd 2.5 at.%. **Journal of Alloys and Compounds,** 439 (1-2): L5-L7

Ehlert, T.C., Hilmer, R.M. and Beauchamp, E.A. (1968) A mass spectrometric study of the vaporization of magnesium, calcium, magnesium hydride and calcium hydride. **Journal of Inorganic and Nuclear Chemistry,** 30 (11): 3112-3115

Ewan, B.C.R. and Allen, R.W.K. Year. The roads to hydrogen - A feasibility assessment. *In*, 2005 Glasgow, Scotland. 407.

Friedlmeier, G., Arakawa, M., Hirai, T., et al. (1999) Preparation and structural, thermal and hydriding characteristics of melt-spun Mg-Ni alloys. **Journal of Alloys and Compounds,** 292 (1-2): 107-117

Fry, C.M.P., Grant, D.M. and Walker, G.S. (2013) Improved hydrogen cycling kinetics of nano-structured magnesium/transition metal multilayer thin films. **International Journal of Hydrogen Energy,** 38 (2): 982-990

Fu, Y., Groll, M., Mertz, R., et al. (2008) Effect of LaNi5 and additional catalysts on hydrogen storage properties of Mg. **Journal of Alloys and Compounds,** 460 (1–2): 607-613

Gandhi, C. and Ashby, M.F. (1979) Overview no. 5: Fracture-mechanism maps for materials which cleave: F.C.C., B.C.C. and H.C.P. metals and ceramics. **Acta Metallurgica,** 27 (10): 1565-1602

Gennari, F.C., Castro, F.J. and Urretavizcaya, G. (2001) Hydrogen desorption behavior from magnesium hydrides synthesized by reactive mechanical alloying. **Journal of Alloys and Compounds,** 321 (1): 46-53

Goto, Y., Kakuta, H., Kamegawa, A., et al. (2003) Effect of synthesis pressure on hydride phases in Mg-M systems (M = Mn, Y). **Science and Technology of Advanced Materials,** 4 (4): 333-338

Graham, T. (1866) On the Absorption and Dialytic Separation of Gases by Colloid Septa. **Philosophical Transactions of the Royal Society of London,** 156 (ArticleType: research-article / Full publication date: 1866 /): 399-439

Gremaud, R., Broedersz, C.P., Borsa, D.M., et al. (2007) Hydrogenography: An optical combinatorial method to find new light-weight hydrogen-storage materials. **Advanced Materials,** 19 (19): 2813-+

Guo, Z.X., Shang, C. and Aguey-Zinsou, K.F. (2008) Materials challenges for hydrogen storage. **Journal of the European Ceramic Society,** 28 (7): 1467-1473

Häglund, J., Fernández Guillermet, A., Grimvall, G., et al. (1993) Theory of bonding in transition-metal carbides and nitrides. **Physical Review B,** 48 (16): 11685-11691

Hanada, N., Ichikawa, T. and Fujii, H. (2005) Catalytic effect of nanoparticle 3d-transition metals on hydrogen storage properties in magnesium hydride MgH2 prepared by mechanical milling. **Journal of Physical Chemistry B,** 109 (15): 7188-7194

Hanada, N., Ichikawa, T., Hino, S., et al. (2006) Remarkable improvement of hydrogen sorption kinetics in magnesium catalyzed with Nb2O5. **Journal of Alloys and Compounds,** 420 (1-2): 46-49

Higuchi, K., Kajioka, H., Toiyama, K., et al. (1999) In situ study of hydriding–dehydriding properties in some Pd/Mg thin films with different degree of Mg crystallization. **Journal of Alloys and Compounds,** 293–295 (0): 484-489

Hong, S.H., Kwon, S.N., Bae, J.S., et al. (2009) Hydrogen-storage properties of gravity cast and melt spun Mg-Ni-Nb2O5 alloys. **International Journal of Hydrogen Energy,** 34 (4): 1944-1950

Hong, S.H., Na, Y.S., Kwon, S., et al. (2008) Preparation and hydrogen-storage properties of 90(Mg-23.5Ni)-10Ta(2)O(5) alloy by melt spinning and oxide addition. **Journal of Alloys and Compounds,** 465 (1-2): 512-516

Huang, L.J., Liang, G.Y. and Sun, Z.B. (2006) Hydrogen-storage properties of amorphous Mg–Ni–Nd alloys. **Journal of Alloys and Compounds,** 421 (1–2): 279-282

Huang, L.j., Tang, J.g., Wang, Y., et al. (2009) Effects of microstructure on the electrode properties of melt-spun Mg-based amorphous alloys. **Journal of Alloys and Compounds,** 485 (1-2): 186-191

Huot, J., Liang, G. and Schulz, R. (2001) Mechanically alloyed metal hydride systems. **Applied Physics A: Materials Science and Processing,** 72 (2): 187-195

Hyunder. (2013) **D3.1 - Overview on all Known Underground Storage Technologies for Hydrogen - D3.1_Overview of all known underground storage technologies.pdf** [Online]. Available: http://www.hyunder.eu/images/Deliverables/D3.1_Overview%20of%20all%20known%20underground%20storage%20technologies.pdf [Accessed].

IEA. (2012) **WEO 2012 Executive Summary - English.pdf** [Online]. Available: http://www.iea.org/publications/freepublications/publication/English.pdf [Accessed 21-Feb 2013].

Imamura, H., Tabata, S., Shigetomi, N., et al. (2002) Composites for hydrogen storage by mechanical grinding of graphite carbon and magnesium. **Journal of Alloys and Compounds,** 330-332 579-583

IPCC. (2007) Fourth Assessment Report: Climate Change 2007.

Isogai, K., Shoji, T., Kimura, H., et al. (2000) Increase in thermal stability of Mg 62Ni 33Ca 5 amorphous alloy by absorption of hydrogen. **Materials Transactions, JIM,** 41 (11): 1486-1489

Jain, A., Agarwal, S., Jain, P., et al. (2012) Hydriding behavior of Mg-50 wt% ZrCrFe composite Prepared by high energy ball milling. **International Journal of Hydrogen Energy,** 37 (4): 3665-3670

Jain, I.P., Vijay, Y.K., Malhotra, L.K., et al. (1988) Hydrogen storage in thin film metal hydride—a review. **International Journal of Hydrogen Energy,** 13 (1): 15-23

Janot, R., Aymard, L., Rougier, A., et al. (2003) Enhanced hydrogen sorption capacities and kinetics of Mg2Ni alloys by ball-milling with carbon and Pd coating. **Journal of Materials Research,** 18 (8): 1749-1752

Kalinichenka, S., Röntzsch, L., Baehtz, C., et al. (2010) Hydrogen desorption kinetics of melt-spun and hydrogenated Mg90Ni10 and Mg80Ni10Y10 using in situ synchrotron, X-ray diffraction and thermogravimetry. **Journal of Alloys and Compounds,** 496 (1-2): 608-613

Kalinichenka, S., Röntzsch, L., Baehtz, C., et al. (2011a) Hydrogen desorption properties of melt-spun and hydrogenated Mg-based alloys using in situ synchrotron X-ray diffraction and TGA. **Journal of Alloys and Compounds,** 509 (SUPPL. 2): S629-S632

Kalinichenka, S., Röntzsch, L. and Kieback, B. (2009) Structural and hydrogen storage properties of melt-spun Mg-Ni-Y alloys. **International Journal of Hydrogen Energy,** 34 (18): 7749-7755

Kalinichenka, S., Röntzsch, L., Riedl, T., et al. (2011b) Hydrogen storage properties and microstructure of melt-spun Mg 90Ni 8RE 2 (RE = Y, Nd, Gd). **International Journal of Hydrogen Energy,** 36 (17): 10808-10815

Khrussanova, M., Terzieva, M., Peshev, P., et al. (1991) Hydriding of mechanically alloyed mixtures of magnesium with MnO2, Fe2O3 and NiO. **Materials Research Bulletin,** 26 (7): 561-567

Komura, Y. and Tokunaga, K. (1980) Structural studies of stacking variants in Mg-base Friauf-Laves phases. **Acta Crystallographica Section B,** 36 (7): 1548-1554

Kumar, S., Reddy, G.L.N. and Raju, V.S. (2009) Hydrogen storage in Pd capped thermally grown Mg films: Studies by nuclear resonance reaction analysis. **Journal of Alloys and Compounds,** 476 (1–2): 500-506

Kyoi, D., Sato, T., Rönnebro, E., et al. (2004) A new ternary magnesium-titanium hydride Mg7TiHx with hydrogen desorption properties better than both binary magnesium and titanium hydrides. **Journal of Alloys and Compounds,** 372 (1-2): 213-217

Léon, A., Knystautas, E.J., Huot, J., et al. (2002) Hydrogenation characteristics of air-exposed magnesium films. **Journal of Alloys and Compounds,** 345 (1–2): 158-166

Langmi, H.W., Walton, A., Al-Mamouri, M.M., et al. (2003) Hydrogen adsorption in zeolites A, X, Y and RHO. **Journal of Alloys and Compounds,** 356–357 (0): 710-715

Li, Q., Chou, K.-C., Lin, Q., et al. (2004) Hydrogen absorption and desorption kinetics of Ag–Mg–Ni alloys. **International Journal of Hydrogen Energy,** 29 (8): 843-849

Liang, G., Boily, S., Huot, J., et al. (1998) Hydrogen absorption properties of a mechanically milled Mg–50 wt.% LaNi5 composite. **Journal of Alloys and Compounds,** 268 (1–2): 302-307

Liang, G., Huot, J., Boily, S., et al. (1999a) Catalytic effect of transition metals on hydrogen sorption in nanocrystalline ball milled MgH2–Tm (Tm=Ti, V, Mn, Fe and Ni) systems. **Journal of Alloys and Compounds,** 292 (1–2): 247-252

Liang, G., Huot, J., Boily, S., et al. (1999b) Hydrogen storage properties of the mechanically milled MgH2–V nanocomposite. **Journal of Alloys and Compounds,** 291 (1–2): 295-299

Lin, H.J., Ouyang, L.Z., Wang, H., et al. (2012a) Hydrogen storage properties of Mg–Ce–Ni nanocomposite induced from amorphous precursor with the highest Mg content. **International Journal of Hydrogen Energy,** 37 (19): 14329-14335

Lin, H.J., Wang, W.H. and Zhu, M. (2012b) Room temperature gaseous hydrogen storage properties of Mg-based metallic glasses with ultrahigh Mg contents. **Journal of Non-Crystalline Solids,** 358 (11): 1387-1390

Liu, C., Fan, Y.Y., Liu, M., et al. (1999) Hydrogen storage in single-walled carbon nanotubes at room temperature. **Science,** 286 (5442): 1127-1129

Ma, S. and Zhou, H.C. (2010) Gas storage in porous metal-organic frameworks for clean energy applications. **Chemical Communications,** 46 (1): 44-53

Malka, I.E., Błachowski, A., Ruebenbauer, K., et al. (2011) Iron fluorides assisted dehydrogenation and hydrogenation of MgH 2 studied by Mössbauer spectroscopy. **Journal of Alloys and Compounds,** 509 (17): 5368-5372

Mishima, R., Miyamura, H., Sakai, T., et al. (1993) Hydrogen storage alloys rapidly solidified by the melt-spinning method and their characteristics as metal hydride electrodes. **Journal of Alloys and Compounds,** 192 (1–2): 176-178

Molinas, B., Ghilarducci, A.A., Melnichuk, M., et al. (2009) Scaled-up production of a promising Mg-based hydride for hydrogen storage. **International Journal of Hydrogen Energy,** 34 (10): 4597-4601

Moriwaki, T., Akahama, Y., Kawamura, H., et al. (2006) Structural phase transition of rutile-type MgH 2 at high pressures. **Journal of the Physical Society of Japan,** 75 (7):

Moser, D., Bull, D.J., Sato, T., et al. (2009) Structure and stability of high pressure synthesized Mg-TM hydrides (TM = Ti, Zr, Hf, V, Nb and Ta) as possible new hydrogen rich hydrides for hydrogen storage. **Journal of Materials Chemistry,** 19 (43): 8150-8161

Nagengast, D.G., Van Gogh, A.T.M., Kooij, E.S., et al. (1999) Contrast enhancement of rare-earth switchable mirrors through microscopic shutter effect. **Applied Physics Letters,** 75 (14): 2050-2052

Noréus, D. and Werner, P.-E. (1982) Structural Studies of Hexagonal Mg2NiHx. **Acta Chemica Scandinavica, Series A,** 36 847-851

Oelerich, W., Klassen, T. and Bormann, R. (2001) Metal oxides as catalysts for improved hydrogen sorption in nanocrystalline Mg-based materials. **Journal of Alloys and Compounds,** 315 (1-2): 237-242

Ong, M.S., Li, Y., Blackwood, D.J., et al. (1998) Effect of heat treatment on the corrosion behaviour of amorphous Mg-18 at% Ni alloy. **Journal of Alloys and Compounds,** 279 (2): 252-258

Orimo, S. and Fujii, H. (2001) Materials science of Mg-Ni-based new hydrides. **Applied Physics A: Materials Science and Processing,** 72 (2): 167-186

Orimo, S., Fujii, H. and Ikeda, K. (1997) Notable hydriding properties of a nanostructured composite material of the Mg2Ni-H system synthesized by reactive mechanical grinding. **Acta Materialia,** 45 (1): 331-341

Ouwerkerk, M. (1998) Electrochemically induced optical switching of Sm0.3Mg0.7Hx thin layers. **Solid State Ionics,** 113-115 431-437

Ouyang, L.Z., Yang, X.S., Dong, H.W., et al. (2009) Structure and hydrogen storage properties of Mg3Pr and Mg3PrNi0.1 alloys. **Scripta Materialia,** 61 (4): 339-342

Palade, P., Sartori, S., Maddalena, A., et al. (2006) Hydrogen storage in Mg–Ni–Fe compounds prepared by melt spinning and ball milling. **Journal of Alloys and Compounds,** 415 (1–2): 170-176

Pan, L., Sander, M.B., Huang, X., et al. (2004) Microporous Metal Organic Materials: Promising Candidates as Sorbents for Hydrogen Storage. **Journal of the American Chemical Society,** 126 (5): 1308-1309

Patah, A., Takasaki, A. and Szmyd, J.S. (2009) Influence of multiple oxide (Cr2O3/Nb2O5) addition on the sorption kinetics of MgH2. **International Journal of Hydrogen Energy,** 34 (7): 3032-3037

Porutsky, S.G., Zhurakovsky, E.A., Mogilevsky, S.A., et al. (1990) Electronic structure of Mg2FeH6 and Mg2CoH5 hydrides and binding role of hydrogen in them. **Solid State Communications,** 74 (7): 551-553

Pranevicius, L., Milcius, D., Pranevicius, L.L., et al. (2006) The role of grain boundaries in the mechanism of plasma immersion hydrogenation of nanocrystalline magnesium films. **Applied Surface Science,** 252 (12): 4202-4208

Quantum (2005) News: In brief: Quantum looking to transfer H2 storage technology to Japanese automakers. **Fuel Cells Bulletin,** 2005 (6): 7

Rönnebro, E., Kyoi, D., Blomqvist, H., et al. (2004) Structural characterization of Mg3CrH~6 - A new high-pressure phase synthesized in a multi-anvil cell at 8 GPa. **Journal of Alloys and Compounds,** 368 (1-2): 279-282

Révész, Á., Kis-Tóth, Á., Varga, L.K., et al. (2012) Hydrogen storage of melt-spun amorphous Mg65Ni20Cu5Y10 alloy deformed by high-pressure torsion. **International Journal of Hydrogen Energy,** 37 (7): 5769-5776

Rangelova, V. and Spassov, T. (2002) Primary crystallization kinetics in rapidly quenched Mg-based Mg–Ni–Y alloys. **Journal of Alloys and Compounds,** 345 (1–2): 148-154

Ranjbar, A., Guo, Z.P., Yu, X.B., et al. (2009) Hydrogen storage properties of MgH2–SiC composites. **Materials Chemistry and Physics,** 114 (1): 168-172

Raupach, M.R., Marland, G., Ciais, P., et al. (2007) Global and regional drivers of accelerating CO 2 emissions. **Proceedings of the National Academy of Sciences of the United States of America,** 104 (24): 10288-10293

Reda, M.R. (2009) The effect of organic additive in Mg/graphite composite as hydrogen storage materials. **Journal of Alloys and Compounds,** 480 (2): 238-240

Reguera, L., Balmaseda, J., Krap, C.P., et al. (2008) Hydrogen storage in zeolite-like hexacyanometallates: Role of the building block. **Journal of Physical Chemistry C,** 112 (44): 17443-17449

Reilly, J.J. and Wiswall Jr, R.H. (1968) The reaction of hydrogen with alloys of magnesium and nickel and the formation of Mg2NiH4. **Inorganic Chemistry,** 7 (11): 2254-2256

Reilly, J.J. and Wiswall, R.H. (1967) The reaction of hydrogen with alloys of magnesium and copper. **Inorganic Chemistry,** 6 (12): 2220-2223

Ren, H.p., Zhang, Y.h., Li, B.w., et al. (2009) Influence of the substitution of La for Mg on the microstructure and hydrogen storage characteristics of Mg20-xLaxNi10 (x = 0-6) alloys. **International Journal of Hydrogen Energy,** 34 (3): 1429-1436

Richardson, T.J., Slack, J.L., Armitage, R.D., et al. (2001) Switchable mirrors based on nickel-magnesium films. **Applied Physics Letters,** 78 (20): 3047-3049

Rosi, N.L., Eckert, J., Eddaoudi, M., et al. (2003) Hydrogen Storage in Microporous Metal-Organic Frameworks. **Science,** 300 (5622): 1127-1129

Sandí, G. (2004) Hydrogen storage and its limitations. **Electrochemical Society Interface,** 13 (3): 40-44

Schlapbach, L. and Zuttel, A. (2001) Hydrogen-storage materials for mobile applications. **Nature,** 414 (6861): 353-358

Selvam, P., Viswanathan, B., Swamy, C.S., et al. (1986) Magnesium and magnesium alloy hydrides. **International Journal of Hydrogen Energy,** 11 (3): 169-192

Selvam, P., Viswanathan, B., Swamy, C.S., et al. (1988) Thermal studies on Mg2NiH4: Existence of additional hydride phase in the Mg2Ni-Hydrogen system. **Thermochimica Acta,** 125 (0): 1-8

Shang, C.X. and Guo, Z.X. (2004) Effect of carbon on hydrogen desorption and absorption of mechanically milled MgH2. **Journal of Power Sources,** 129 (1): 73-80

Skripnyuk, V.M., Rabkin, E., Estrin, Y., et al. (2009) Improving hydrogen storage properties of magnesium based alloys by equal channel angular pressing. **International Journal of Hydrogen Energy,** 34 (15): 6320-6324

Song, M., Kwon, S., Bae, J.-S., et al. (2009) Hydrogen-storage properties of melt spun Mg-23.5 wt%Ni milled with nano Nb2O5. **Journal of Alloys and Compounds,** 478 (1-2): 501-506

Song, M., Yim, C.-D., Kwon, S., et al. (2008a) Preparation of Mg–23.5Ni–10(Cu or La) hydrogen-storage alloys by melt spinning and crystallization heat treatment. **International Journal of Hydrogen Energy,** 33 (1): 87-92

Song, M.Y., Kwon, S.N., Bae, J.-S., et al. (2008b) Hydrogen-storage properties of Mg–23.5Ni–(0 and 5)Cu prepared by melt spinning and crystallization heat treatment. **International Journal of Hydrogen Energy,** 33 (6): 1711-1718

Song, M.Y. and Park, H.R. (1998) Pressure–composition isotherms in the Mg2Ni–H2 system. **Journal of Alloys and Compounds,** 270 (1–2): 164-167

Spassov, T. and Koster, U. (1998) Thermal stability and hydriding properties of nanocrystalline melt-spun Mg63Ni30Y7 alloy. **Journal of Alloys and Compounds,** 279 (2): 279-286

Spassov, T. and Koster, U. (1999) Hydrogenation of amorphous and nanocrystalline Mg-based alloys. **Journal of Alloys and Compounds,** 287 (1-2): 243-250

Spassov, T., Lyubenova, L., Koster, U., et al. (2004) Mg-Ni-RE nanocrystalline alloys for hydrogen storage. **Materials Science and Engineering a-Structural Materials Properties Microstructure and Processing,** 375-77 794-799

Spassov, T., Rangelova, V. and Neykov, N. (2002a) Nanocrystallization and hydrogen storage in rapidly solidified Mg–Ni–RE alloys. **Journal of Alloys and Compounds,** 334 (1–2): 219-223

Spassov, T., Solsona, P., Suriñach, S., et al. (2002b) Nanocrystallization in Mg83Ni17−xYx (x=0, 7.5) amorphous alloys. **Journal of Alloys and Compounds,** 345 (1–2): 123-129

Stampfer, J.F., Holley, C.E. and Suttle, J.F. (1960) The Magnesium-Hydrogen System1-3. **Journal of the American Chemical Society,** 82 (14): 3504-3508

Sugamata, M., Hanawa, S. and Kaneko, J. (1997) Structures and mechanical properties of rapidly solidified Mg-Y based alloys. **Materials Science and Engineering: A,** 226–228 (0): 861-866

Tan, X., Zahiri, B., Holt, C.M.B., et al. (2012) A TEM based study of the microstructure during room temperature and low temperature hydrogen storage cycling in MgH2 promoted by Nb–V. **Acta Materialia,** 60 (16): 5646-5661

Tan, Z., Chiu, C., Heilweil, E.J., et al. (2011) Thermodynamics, kinetics and microstructural evolution during hydrogenation of iron-doped magnesium thin films. **International Journal of Hydrogen Energy,** 36 (16): 9702-9713

Tanaka, K. (2008) Hydride stability and hydrogen desorption characteristics in melt-spun and nanocrystallized Mg–Ni–La alloy. **Journal of Alloys and Compounds,** 450 (1–2): 432-439

Tanaka, K., Kanda, Y., Furuhashi, M., et al. (1999) Improvement of hydrogen storage properties of melt-spun Mg-Ni-RE alloys by nanocrystallization. **Journal of Alloys and Compounds,** 295 521-525

Taylor, A. (1950) Lattice Parameters of Binary Nickel-Cobalt Alloys. **J. Inst. Met,** 77 585-594

Teresiak, A., Gebert, A., Savyak, M., et al. (2005) In situ high temperature XRD studies of the thermal behaviour of the rapidly quenched Mg77Ni18Y5 alloy under hydrogen. **Journal of Alloys and Compounds,** 398 (1-2): 156-164

Teresiak, A., Uhlemann, M., Gebert, A., et al. (2009a) Formation of nanostructured LaMg2Ni by rapid quenching and intensive milling and its hydrogen reactivity. **Journal of Alloys and Compounds,** 481 (1–2): 144-151

Teresiak, A., Uhlemann, M., Thomas, J., et al. (2009b) The metastable Mg∼6Ni phase—Thermal behaviour, crystal structure and hydrogen reactivity of the rapidly quenched alloy. **Journal of Alloys and Compounds,** 475 (1–2): 191-197

Terzieva, M., Khrussanova, M. and Peshev, P. (1998) Hydriding and dehydriding characteristics of Mg-LaNi5 composite materials prepared by mechanical alloying. **Journal of Alloys and Compounds,** 267 (1-2): 235-239

Tkatch, V.I., Limanovskii, A.I., Denisenko, S.N., et al. (2002) The effect of the melt-spinning processing parameters on the rate of cooling. **Materials Science and Engineering: A,** 323 (1–2): 91-96

Todorova, S. and Spassov, T. (2009) Mg6Ni formation in rapidly quenched amorphous Mg–Ni alloys. **Journal of Alloys and Compounds,** 469 (1–2): 193-196

Tsirelson, V.G., Avilov, A.S., Abramov, Y.A., et al. (1998) X-ray and Electron Diffraction Study of MgO. **Acta Crystallographica Section B,** 54 (1): 8-17

Vajeeston, P., Ravindran, P., Fichtner, M., et al. (2012) Influence of crystal structure of bulk phase on the stability of nanoscale phases: Investigation on MgH 2 derived nanostructures. **Journal of Physical Chemistry C,** 116 (35): 18965-18972

Van Der Sluis, P., Ouwerkerk, M. and Duine, P.A. (1997) Optical switches based on magnesium lanthanide alloy hydrides. **Applied Physics Letters,** 70 (25): 3356-3358

Vermeulen, P., Niessen, R.A.H. and Notten, P.H.L. (2006) Hydrogen storage in metastable MgyTi(1 - Y) thin films. **Electrochemistry Communications,** 8 (1): 27-32

Vijay, R., Sundaresan, R., Maiya, M.P., et al. (2004) Characterisation of Mg–x wt.% FeTi (x = 5–30) and Mg–40 wt.% FeTiMn hydrogen absorbing materials prepared by mechanical alloying. **Journal of Alloys and Compounds,** 384 (1–2): 283-295

Wagemans, R.W.P., Van Lenthe, J.H., De Jongh, P.E., et al. (2005) Hydrogen storage in magnesium clusters: Quantum chemical study. **Journal of the American Chemical Society,** 127 (47): 16675-16680

Wang, J.C.F. and Ronnebro, E.C.E. (2005). "An overview of hydrogen storage for transportation application" In **2005 TMS Annual Meeting. San Francisco, CA,**pp.21-24

Wei, G. and Cantor, B. (1989) The effect of heat treatment and surface treatment on the crystallisation behaviour of amorphous Fe40Ni40B20. **Acta Metallurgica,** 37 (12): 3409-3424

Wu, C.Z., Wang, P., Yao, X., et al. (2006) Effect of carbon/noncarbon addition on hydrogen storage behaviors of magnesium hydride. **Journal of Alloys and Compounds,** 414 (1–2): 259-264

Wu, Y., Lototsky, M.V., Solberg, J.K., et al. (2009) Microstructure and novel hydrogen storage properties of melt-spun Mg–Ni–Mm alloys. **Journal of Alloys and Compounds,** 477 (1–2): 262-266

Wu, Y., Solberg, J.K. and Yartys, V.A. (2007) The effect of solidification rate on microstructural evolution of a melt-spun Mg-20Ni-8Mm hydrogen storage alloy. **Journal of Alloys and Compounds,** 446-447 178-182

Yermakov, A.Y., Mushnikov, N.V., Uimin, M.A., et al. (2006) Hydrogen reaction kinetics of Mg-based alloys synthesized by mechanical milling. **Journal of Alloys and Compounds,** 425 (1–2): 367-372

Yim, C.D., You, B.S., Na, Y.S., et al. (2007) Hydriding properties of Mg-xNi alloys with different microstructures. **Catalysis Today,** 120 (3-4): 276-280

Yoshimura, K., Yamada, Y. and Okada, M. (2004) Hydrogenation of Pd capped Mg thin films at room temperature. **Surface Science,** 566–568, Part 2 (0): 751-754

Züttel, A. (2003) Materials for hydrogen storage. **Materials Today,** 6 (9): 24-33

Züttel, A. (2004) Hydrogen storage methods. **Naturwissenschaften,** 91 (4): 157-172

Züttel, A., Sudan, P., Mauron, P., et al. (2002) Hydrogen storage in carbon nanostructures. **International Journal of Hydrogen Energy,** 27 (2): 203-212

Zahiri, B., Danaie, M., Tan, X., et al. (2011) Stable Hydrogen Storage Cycling in Magnesium Hydride, in the Range of Room Temperature to 300 °C, Achieved Using a New Bimetallic Cr-V Nanoscale Catalyst. **The Journal of Physical Chemistry C,** 116 (4): 3188-3199

Zaluska, A., Zaluski, L. and Ström-Olsen, J.O. (1999) Synergy of hydrogen sorption in ball-milled hydrides of Mg and Mg2Ni. **Journal of Alloys and Compounds,** 289 (1-2): 197-206

Zaluska, A., Zaluski, L. and Ström-Olsen, J.O. (2001) Structure, catalysis and atomic reactions on the nano-scale: A systematic approach to metal hydrides for hydrogen storage. **Applied Physics A: Materials Science and Processing,** 72 (2): 157-165

Zhang, J., Zhou, D.W., He, L.P., et al. (2009a) First-principles investigation of Mg2Ni phase and high/low temperature Mg2NiH4 complex hydrides. **Journal of Physics and Chemistry of Solids,** 70 (1): 32-39

Zhang, Y., Zhao, D., Ren, H., et al. (2009b) Hydriding and dehydriding characteristics of nanocrystalline and amorphous Mg 20-xLa xNi 10(x=0-6) alloys prepared by melt-spinning. **Journal of Rare Earths,** 27 (3): 514-519

Zhang, Y.H., Ren, H.P., Guo, S.H., et al. (2009c) Electrochemical hydrogen storage characteristics of nanocrystalline and amorphous Mg20Ni10-xCox (x=0-4) alloys prepared by melt spinning. **Journal of Alloys and Compounds,** 480 (2): 750-755

Zhou, C., Fang, Z.Z., Ren, C., et al. (2013) Effect of Ti Intermetallic Catalysts on Hydrogen Storage Properties of Magnesium Hydride. **The Journal of Physical Chemistry C,** 117 (25): 12973-12980